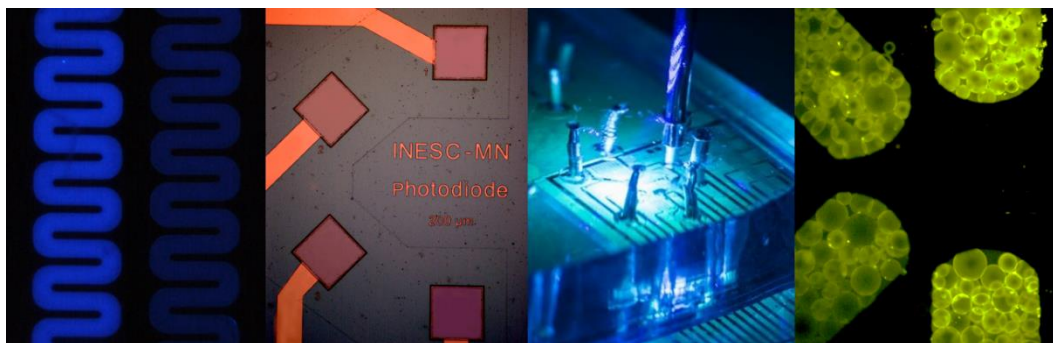


UNIVERSIDADE DE LISBOA
INSTITUTO SUPERIOR TÉCNICO



**Development of an Integrated Microfluidic Mycotoxin Screening
Chip for Point-Of-Need Food Safety Applications**

Rúben Rafael Gonçalves Soares

Supervisor: Doctor João Pedro Estrela Rodrigues Conde

Co-supervisor: Doctor Maria Raquel Múrias dos Santos Aires Barros

**Thesis approved in public session to obtain the PhD degree in
Biotechnology and Biosciences**

Jury final classification: Pass with Distinction and Honour

UNIVERSIDADE DE LISBOA
INSTITUTO SUPERIOR TÉCNICO

**Development of an Integrated Microfluidic Mycotoxin Screening
Chip for Point-Of-Need Food Safety Applications**

Rúben Rafael Gonçalves Soares

Supervisor: Doctor João Pedro Estrela Rodrigues Conde

Co-supervisor: Doctor Maria Raquel Múrias dos Santos Aires Barros

**Thesis approved in public session to obtain the PhD degree in
Biotechnology and Biosciences**

Jury final classification: Pass with Distinction and Honour

Jury

Chairperson: Doctor Duarte Miguel de França Teixeira dos Prazeres, Instituto Superior Técnico da Universidade de Lisboa

Members of the Committee:

Doctor José António Teixeira, Escola de Engenharia da Universidade do Minho

Doctor João Pedro Estrela Rodrigues Conde, Instituto Superior Técnico da Universidade de Lisboa

Doctor Ana Cecília Afonso Roque, Faculdade de Ciências e Tecnologia da Universidade Nova de Lisboa

Doctor Margarida Maria Portela Correia dos Santos Romão, Instituto Superior Técnico da Universidade de Lisboa

Doctor Ana Margarida da Costa Macedo Fortes, Faculdade de Ciências da Universidade de Lisboa

Doctor Ricardo Manuel Marques Caleiro Cabeça, Biosurfit

Funding Institution

Fundação para a Ciência e Tecnologia (FCT) – PhD Grant SFRH/BD/97354/2013

*To my grandmother Ema,
you deserve more than anybody could ever give you*

“It always seems impossible until it’s done”

Nelson Mandela

Acknowledgements

The journey of the PhD student is far beyond a mere intellectual challenge. The hurdles of a PhD span beyond solving difficult problems and engineering intricate tools. Actually, having a clear problem to solve is the easy part. Finding a solution to go from “A” to “B” is not difficult. Difficult is having to go from “A” to “Z” (with “Z” being the main goal of the thesis) without knowing any of the letters in between, nor their logical order, neither if they indeed exist! Difficult is finding the motivation to do so. Difficult is to be humble, assume failure and learn beyond our initial preconceptions (in science, assuming “C” comes after “B” is only good enough if you can prove it). Difficult is to go back to “A” if “D” does not exist after “C” (maybe you can find “E” some other way). Difficult is failing to reach “Z”, being happy finishing halfway, and motivating others to move on from the top of your shoulders. Difficult is to be patient, knowing that others can find the way to “Z” before you. If they do, difficult is keeping confident and finding a better way to do it. The journey of a PhD student is certainly driven on intellect, but the fuel is emotion, and emotion does not always come cheap, nor it is used only to drive the intellect forward.

Like everything in life, random chance also helps (a lot), and I was fortunate enough to have a great project, great supervisors, great colleagues and friends, a great family and a perfect life companion to fuel my intellect and my journey. Having in mind the possibility of forgetting someone important (and for that my apology) I want to try my best at enumerating everyone that had a critical role in my own journey as a PhD student.

Firstly, I would like to express my deepest gratitude to my supervisor Prof. João Pedro Conde and to Dr. Virginia Chu, with whom I have been having the great pleasure to work with for the past 6 years. They are two extremely professional individuals who contributed tremendously to my growth as a researcher and were always available to discuss my project and provide their helpful insights. I would also like to sincerely thank my co-supervisor Prof. Raquel Aires-Barros for always finding time to discuss the progress of my project, for all the invitations to write review articles and for the introduction to the world of peer-review, along with a great deal of motivation and trust put in my work. Besides my formal supervisors, I would also like to acknowledge Prof. Ana Azevedo and Prof. Pedro Fernandes for their availability and for always providing their helpful insights during our meetings.

I would also like to acknowledge all my colleagues and friends at INESC MN that contributed both professionally and personally for the success of my project. The first acknowledgement must be given to Narayanan Madaboosi Srinivasan, my full-time colleague and teacher in the “Biolab” for more than three years and now a good friend. Words cannot describe the extraordinary researcher and person he is. Pedro Novo and João Tiago Fernandes, two extraordinarily talented researchers, are acknowledged for all the microfabrication and microfluidic lessons as my first role models in the lab. A pronounced acknowledgement also to my talented colleague and friend Denis Santos, with whom I shared countless scientific discussions and troubleshooting sessions in the optics room. Without our common perseverance, a major part of my thesis would not have been possible. A pronounced acknowledgement also to Diogo Ramadas and António Cascalheira, with whom I shared endless frustrating moments at Lumisense optimizing an ochratoxin A immunoassay. They are some of the most dedicated and competent professionals I have ever met, and, without their perseverance, it would have been impossible to achieve a working prototype. An acknowledgement to my colleague Daniel Silva, my conference partner and “general knowledge teacher” on so many occasions. I wish him all the best for his future. An acknowledgement also to Eduardo Brás, whom I have helped supervise as a summer student back in 2014 and have since been my colleague and friend. He is a creative and talented researcher that has grown a lot as a researcher in the past years (never forget there is still a long way to go and a lot to learn). I am sure he will finish as a highly successful PhD student and will be able to fulfil his career goals. Finally, an acknowledgement to all my colleagues at INESC MN that have been contributing to create a fantastic work environment, which is critical for the success of any research lab, particularly Catarina Caneira, Catarina Bombaça, Tatiana Arriaga, Rui Pinto and Ricardo Fradique. You are all amazing colleagues and extremely talented, I wish you all the best for the rest of your doctoral studies.

The success of a researcher is founded on pillars that lie beyond the research lab, and for that I want to express my deepest gratitude to my family, particularly my parents, for all the love and support at every stage throughout my life. Last but absolutely not the least, an endless “thank you” to my wife-to-be Inês Fernandes Pinto, whom I was lucky enough to have as my research partner throughout my PhD project. She is an incredible life partner and researcher, with whom I have went through more personal and work challenges than could ever be written down on paper. With you, “every little thing gonna be alright”, always.

Resumo

Garantir a segurança alimentar, incluindo a identificação e análise de múltiplos contaminantes biológicos e químicos, é uma prioridade para o bem-estar da população e um desafio considerável, tendo em conta o ritmo crescente em que bens alimentares são produzidos e comercializados a uma escala global. As micotoxinas em particular são metabolitos secundários de fungos, prevalentes em todo o mundo, podendo contaminar bens agrícolas não só no terreno, mas também durante o armazenamento e transporte. Estes contaminantes estão associados a efeitos nefastos para a saúde humana e animal, induzindo efeitos carcinogénicos, teratogénicos, hepatotóxicos, entre outros. Assim sendo, a sua presença numa grande variedade de bens alimentares direcionados a humanos e animais tem sido alvo de restritos limites legais impostos em particular pela União Europeia. A existência destes limites legais motiva uma exigência por parte das agências regulatórias e empresas de produção alimentar de um dispositivo detetor de micotoxinas rápido, portátil, simples, de baixo custo e adequado à finalidade.

Esta tese reporta o desenvolvimento de vários módulos miniaturizados de um dispositivo portátil para deteção de micotoxinas incluindo (1) extração, preparação da amostra e pré-concentração do analito de interesse, (2) imunoensaio competitivo em microfluídica para deteção simultânea de vários analitos, (3) miniaturização de transdutores óticos para aquisição de sinal e (4) eletrónica portátil para endereçar os transdutores e providenciar uma resposta quantitativa. Como resultado, combinando os módulos 2 a 4, concentrações na ordem das ng/mL de três micotoxinas, nomeadamente ocratoxina A, aflatoxina B1 e deoxinivalenol, foram detetadas simultaneamente em aproximadamente 60 segundos numa variedade de alimentos sólidos e líquidos. Tal deteção foi efetuada depois de um processo simples de extração e tratamento da amostra baseado em sistemas aquosos de duas fases em menos de 20 min.

Estas características contribuíram significativamente para o estado-da-arte e abriram caminho para o desenvolvimento de um dispositivo integrado de operação simples e potencialmente disruptivo, capaz de detetar rapidamente várias micotoxinas diretamente no terreno.

Palavras-chave: Micotoxinas, microfluídica, integração, preparação da amostra, fotossensores

Abstract

The assurance of food and feed safety, including the identification and effective screening of multiple biological and chemical hazards, is a societal priority and a major challenge, given the increasing pace at which food commodities are demanded, produced and traded across the globe. Mycotoxins in particular are globally widespread secondary fungal metabolites, which can contaminate crops either in the field or during storage and transport. These contaminants are associated with serious human and animal health impacts such as carcinogenic, teratogenic and hepatotoxic effects. Therefore, their presence in a wide range of foods and feeds has been subjected to increasingly strict regulations, particularly in the European Union. Such regulations motivate an increasing demand by regulatory agencies and food producers for a rapid, portable, simple, cost-effective and fit-for-purpose device to detect mycotoxins.

This thesis reports the development of several miniaturized modules of a portable point-of-need mycotoxin screening chip including (1) analyte extraction, sample preparation and pre-concentration, (2) microfluidic and multiplexed competitive immunodetection, (3) miniaturized optical transducers for signal acquisition and (4) portable electronics to address the transducers and provide a quantitative response. Ultimately, combining modules 2 to 4, ng/mL concentrations of three mycotoxins, namely ochratoxin A, aflatoxin B1 and deoxynivalenol, could be detected in multiple solid and liquid food matrices in approximately 60 seconds. The detection was performed after a previous simple aqueous two-phase extraction and pre-concentration procedure performed in less than 20 min.

These achievements contributed significantly to the state-of-the-art and pave the way towards the development of a potentially disruptive integrated device, operated by non-specialists and allowing the rapid detection of mycotoxins directly on the field.

Keywords: Mycotoxins; microfluidics; integration; sample preparation; photosensors

Table of contents

List of acronyms and abbreviations	xvii
List of figures.....	xxi
List of tables	xxv
Motivation and outline of the thesis	xxvii

Chapter 1. Introduction	1
1.1. Fundamental aspects of microfluidic immunoassays	1
1.2. Recent advances and trends in the development of microfluidic immunoassays.....	5
1.3. Mycotoxins and point-of-need screening: Relevance, demand, challenges and opportunities	13
1.4. Aqueous two-phase systems: a simple and biocompatible approach to isolate target biomolecules	37
1.5. Thin-film silicon photodetectors for optical signal transduction in portable microfluidic devices.....	47

Chapter 2. General Microfabrication and Microfluidic Device Handling Methodologies.....	53
2.1. Fabrication of microfluidic devices: a general overview.....	53
2.2. Hard-mask fabrication	54
2.3. SU-8 mold fabrication	54
2.4. PDMS mold-replication, punching of access holes and sealing.....	56
2.5. Fabrication of a-Si:H photoconductors and <i>p-i-n</i> photodiodes.....	56
2.6. Liquid handling and imaging of chemiluminescent and fluorometric signals using standard optical or fluorescence microscopy	58

Chapter 3. Microfluidic Aqueous Two-Phase Systems for On-Chip Integration of Sample Preparation	61
3.1. Materials and experimental methods	61
3.2. Partition of OTA and AFB1 in PEG-phosphate salt systems	65
3.3. Optimization of ATPS composition to extract mycotoxins from wine	67
3.4. General concept of integrated extraction and immunodetection	72
3.5. Optimization of the microfluidic FLISA	73

3.6. Optimization of the microfluidic ATPE module.....	75
3.7. Integration of ATPE in series with the optimized FLISA for simultaneous sample preparation and detection	79
3.8. Chapter conclusions	83

Chapter 4. Aqueous Two-Phase Systems for the Simultaneous Extraction and Concentration of Mycotoxins in Solid Samples.....85

4.1. Materials and experimental methods	85
4.2. Aqueous two-phase extraction coupled to a microfluidic immunoassay for detecting mycotoxins in feeds.....	89
4.3. Concentration of AFB1, OTA and DON in PEG-phosphate ATPSs.....	90
4.4. Optimization of the tie-line length (TLL) and PEG molecular weight for enhancing extraction and immunodetection	93
4.5. Optimization of the dilution factor for minimizing matrix interference	95
4.6. Benchmarking of ATPS-based extraction for sample processing and microfluidic immunodetection	97
4.7. Mycotoxin calibration curves using the optimized PEG-phosphate ATPS	98
4.8. Mycotoxin calibration curves using a biodegradable PEG-sodium citrate ATPS .	100
4.9. PEG-sodium citrate ATPS for processing multiple types of feed matrices	101
4.10. Chapter conclusions	103

Chapter 5. Rapid and Regenerable Microfluidic Immunoassay with Integrated Optical Signal Transduction105

5.1. Materials and experimental methods	106
5.2. Immunoassay design and photosensor integration.....	107
5.3. Systematic optimization of the immunoassay.....	110
5.4. OTA calibration curve and assay regeneration	115
5.5. Detection of OTA in red wine at the regulatory limits	116
5.6. Integration of the immunoassay in a portable biosensor prototype	118
5.7. Chapter conclusions	120

Chapter 6. Immunoassay Multiplexing Coupled with a Microarray of Photoconductors121

6.1. Materials and experimental methods	121
---	-----

6.2. Multiplexing concept and microchannel design	127
6.3. Spatially resolved adsorption of BSA fluorescent conjugates.....	128
6.4. Simultaneous calibration and immunodetection of the mycotoxins OTA, AFB1 and DON.....	129
6.5. Simultaneous detection of OTA, AFB1 and DON using a multiplexed array of a-Si:H photoconductors.....	133
6.6. Chapter conclusions.....	137

Chapter 7. Capillary Microfluidic Immunoassays for Mycotoxin Detection Coupled with Smartphone Signal Acquisition..... 139

7.1. Materials and experimental methods	139
7.2. Multiplexed competitive immunoassay design	144
7.3. Evaluation of cross-reactivity	147
7.4. Calibration curves for OTA, AFB1 and DON	148
7.5. Detection of mycotoxins in spiked corn feed samples	150
7.6. Chapter conclusions.....	152

Chapter 8. Bead-Based Microfluidic Immunoassays to Improve Assay Speed and Sensitivity..... 155

8.1. Materials and experimental methods	155
8.2. Microfluidic bead-based biosensing strategies to detect mycotoxins, proteins and oligonucleotides	159
8.3. Integration of <i>p-i-n</i> a-Si:H photodiodes in bead-based microfluidics to transduce fluorescence, chemiluminescence and colorimetry	163
8.4. Chapter conclusions.....	167

Chapter 9. Capillary Bead-Based Microfluidic Immunoassay for Ultrarapid Mycotoxin Detection..... 169

9.1. Materials and experimental methods	169
9.2. Capillary device design and operation.....	171
9.3. Optimization of a competitive immunoassay for deoxynivalenol (DON) quantification and an anti-BSA internal control	173
9.4. Ultrarapid detection of DON using the double-chamber device	174
9.5. Chapter conclusions.....	176

Chapter 10. Multiplexed Microfluidic Immunoassay Addressed by a Photodetector Array for Point-of-Need and Sub-Minute Detection of Mycotoxins	177
10.1. Materials and experimental methods	178
10.2. Design of the microbead-based microfluidic device for immunoassay multiplexing with an internal reference.....	180
10.3. Development and optimization of a competitive immunoassay for sub-minute mycotoxin quantification in model solutions	182
10.4. Simultaneous detection of AFB1, OTA and DON using the multiplexed device	184
10.5. Point-of-need compatible fluorescence signal acquisition with an integrated photodiode array.....	188
10.6. Multiplexed detection of mycotoxins in corn extracts as a model food matrix ...	192
10.7. Chapter conclusions	195
Chapter 11. Conclusions and Outlook.....	197
11.1. Novelty and main improvements to the state-of-the-art	197
11.2. Future research towards a fully integrated and portable mycotoxin screening device	200
11.3. Extension of the analytical device for the pre-emptive detection of mycotoxigenic fungi in foods and feeds	202
Bibliography	207
Appendix A	233
Curriculum Vitae	239

List of acronyms and abbreviations

AC – Alternating current

ADC – Analog-to-digital converter

AFB1 – Aflatoxin B1

APCI – Atmospheric pressure chemical ionization

APTES – (3-Aminopropyl) triethoxysilane

a-Si:H – Hydrogenated amorphous silicon

a-SiC:H – Hydrogenated amorphous silicon carbide

ATPE – Aqueous two-phase extraction

ATPS – Aqueous two-phase system

AuNPs – Gold Nanoparticles

BP – Band Pass

BSA – Bovine serum albumin

CAD – Computer-aided design

CB – Conduction band

CC – Control chamber

CCD – Charge-coupled device

CDI – Carbonyldiimidazole

cDNA – Complementary DNA

CE – Counter-electrode

CHO – Chinese hamster ovary

CL – Chemiluminescence

CM – Colorimetry

CMOS – Complementary metal-oxide-semiconductor

COC – Cyclic olefin copolymer

c-Si – Crystalline silicon

CV – Coefficient of variation

D μ ID – Microfluidic immunoarray device

DC – Direct current

DLLME – Dispersive liquid-liquid microextraction

DNA – Deoxyribonucleic acid

DOL – Degree of labeling

DON – Deoxynivalenol

DPF – Pressure difference
DPL – Laplace pressure
DWL – Direct write lithography
EDC – 1-Ethyl-3-(3-dimethylaminopropyl) carbodiimide
EEA – European Economic Area
EIS – Electrochemical impedance spectroscopy
ELISA – Enzyme-linked immunosorbent assay
EOPO – Ethylene oxide / propylene oxide copolymer
EQE – External quantum efficiency
ESI – Electrospray ionization
EU – European Union
EWOD – Electrowetting-on-dielectric
FAO – Food and Agriculture Organization of the United Nations
FB – Fumonisin
FITC – Fluorescein isothiocyanate
FLISA – Fluorescence-linked immunosorbent assay
f-PSA – Free prostate specific antigen
GC/MS – Gas Chromatography – mass spectrometry
GCE – Glassy carbon electrode
GOPTES – (3-Glycidyloxypropyl) trimethoxysilane
GPIB – General purpose interface bus
GUI – Graphical user interface
HCP – Host cell proteins
HPLC – High-performance liquid chromatography
HRP – Horseradish peroxidase
IAC – Immunoaffinity column
IARC – International Agency for Research on Cancer
icELISA – Indirect competitive enzyme-linked immunosorbent assay
IgG – Immunoglobulin G
IL – Ionic liquid
IPA – Isopropanol
IR – Infrared
ITO – Indium tin oxide
ITS – Internal transcribed spacer

IUPAC - International Union of Pure and Applied Chemistry
LAMP – Loop-mediated isothermal amplification
LC/MS – Liquid chromatography / mass spectrometry
LED – Light emitting diode
LFIA – Lateral-flow immunoassay
LoD – Limit of detection
LP – Low-pass
LSPR – Localized surface plasmon resonance
mAb – Monoclonal antibody
ME – Matrix effect
MIP – Molecularly imprinted polymer
MOF – Metal-organic framework
mRNA – Messenger ribonucleic acid
MUDA – 11-mercaptoundecanoic acid
MW – Molecular weight
MWCO – Molecular weight cut-off
NASBA – Nucleic acid sequence-based amplification
NC – Nitrocellulose
ncDNA – non-complementary deoxyribonucleic acid
ND – Neutral density
NHS – N-hydroxysuccinimide
NIPAM – *N*-Isopropylacrylamide
OTA – Ochratoxin A
PAA – Polyacrylate
PBS – Phosphate buffered saline
PCB – Printed circuit board
PCR – Polymerase chain reaction
PDMS – Polydimethylsiloxane
pDNA – Plasmid DNA
PECVD – Plasma-enhanced chemical vapor deposition
PEG – Polyethylene glycol
PGMEA – Propylene glycol monomethyl ether acetate
PHEMA – Poly(2-hydroxyethyl methacrylate)
PLA – Polylactic acid

PMTDI – Provisional maximum tolerable daily intake
PP – Polyphenols
PRP – polyethylene glycol-rich phase
PtNPs – Platinum nanoparticles
QD – Quantum dots
RCA – Rolling circle amplification
RE – Reference electrode
RIE – Reactive ion etching
ROI – Region of interest
RT – Room temperature
SAM – Self-assembled monolayer
SDA – Strand displacement amplification
SOD – Superoxide dismutase
SPE – Solid phase extraction
SPR – Surface plasmon resonance
SPRi – Surface plasmon resonance imaging
SRP – Salt-rich phase
SRW – Salt-rich red wine
ssDNA – Single-stranded deoxyribonucleic acid
SUA – Sample under analysis
TBA – Toxin-bovine serum albumin-Alexa 430 conjugate
TC – Test chamber
TEG - Triethylene glycol
TIA – Transimpedance amplifier
TLL – Tie-line length
TMB – 3,3',5,5'-tetramethylbenzidine
tRNA – Transfer ribonucleic acid
USB – Universal serial bus
UV – Ultraviolet
VB – Valence band
VGND – Virtual ground
WE – Working electrode
WHO – World Health Organization
ZEN – Zearalenone

List of figures

Figure 1.1 - Microfluidic immunoassay schematics	2
Figure 1.2 - Summary of strategies to develop microfluidic immunosensors	7
Figure 1.3 - Microfluidic immunosensors coupled with optical transducers.....	9
Figure 1.4 - Microfluidic immunosensors coupled with electrochemical transducers ..	11
Figure 1.5 - Microfluidic immunosensors coupled with label-free sensing	13
Figure 1.6 - Schematics of immunoassay designs used in well plates or lateral flow devices	20
Figure 1.7 - Schematics of the main components of a typical chemical measurement process	22
Figure 1.8 - Schematic summary of main components and trends on mycotoxin analytical assay development	26
Figure 1.9 - Phase diagram, analyte partition and concentration effects in aqueous two-phase separation	39
Figure 1.10 - Critical parameters of aqueous two-phase separation in microtubes and microchannels	47
Figure 1.11 - Band diagram in semiconductor devices.....	48
Figure 1.12 - Band diagrams in doped semiconductor devices	49
Figure 1.13 - Schematics and band diagram of p-i-n Si photodiodes.....	50
Figure 1.14 - Electrical bias and optical measurements using Si photodiodes.....	51
Figure 1.15 - General schematics of a transimpedance amplification circuit.....	52
Figure 2.1 - Schematics of the microfabrication procedure to obtain PDMS microfluidic devices	53
Figure 2.2 - Schematics of thin-film photoconductors and photodiodes	538
Figure 3.1 - Partition of ochratoxin A and aflatoxin B1 in PEG-phosphate ATPS	67
Figure 3.2 - Schematics of the ATPE sample processing strategy and main optimization parameters	68
Figure 3.3 - Effect of ATPE parameters on OTA detection performance	69
Figure 3.4 - Comparison of ELISA sensitivity using raw or processed samples	71
Figure 3.5 - ELISA results for AFB1 spiked in red wine using increasing TLLs	71
Figure 3.6 - Conceptual schematics of the integrated microfluidic ATPE strategy for matrix neutralization and concentration	72

Figure 3.7 - Schematics of the microchannel FLISA protocol and methodology used for OTA quantification	73
Figure 3.8 - Optimization of the microfluidic FLISA to detect OTA	75
Figure 3.9 - Optimization of OTA and polyphenol partition in microfluidic ATPE	76
Figure 3.10 - Schematics of the microfluidic device optimized to perform an integrated ATPE in line with a FLISA.....	80
Figure 3.11 - Schematics of the main control steps used to perform the integrated ATPE-FLISA assay	81
Figure 3.12 - Microscopy images and schematics of the ATPE-FLISA assay	82
Figure 3.13 - Results of the ATPE-FLISA assay obtained for red and white wines.....	83
Figure 4.1 - Schematics of the ATPE to extract and concentrate target mycotoxins from a dried feed material, followed by microfluidic immunodetection	90
Figure 4.2 - Quantification of absolute chemiluminescence signals and relative signals using ImageJ.....	91
Figure 4.3 - Partition and concentration of mycotoxins in PEG-salt ATPSs	92
Figure 4.4 - Cross-reactivity in mycotoxin immunodetection	94
Figure 4.5 - Optimization of PEG molecular weight and salt concentration	94
Figure 4.6 - Optimization of top-phase dilution ratio	96
Figure 4.7 - Estimation of extraction yield.....	96
Figure 4.8 - Benchmarking of the ATPE extraction procedure	98
Figure 4.9 - Calibration curves for OTA, AFB1 and DON using PEG-phosphate ATPE for sample preparation.....	99
Figure 4.10 - Calibration curves for OTA, AFB1 and DON using PEG-citrate ATPE for sample preparation	102
Figure 4.11 - Microfluidic immunodetection performance using different solid feed matrices	103
Figure 5.1 - Schematics of the microfluidic competitive immunoassay design used for OTA quantification	109
Figure 5.2 - Schematics of the measurement setup used to acquire the photoluminescent signal emitted from the microchannel	110
Figure 5.3 - Optimization of the OTA-BSA concentration.....	112
Figure 5.4 - Optimization of anti-OTA-HRP concentration in the SUA, total incubation time and flow rate of the solution through the microchannel	114

Figure 5.5 - Calibration curves for increasing OTA concentrations using the optimized conditions without and with regeneration.....	115
Figure 5.6 - Voltage measurements of three reference wine samples or spiked with 2 ng/mL OTA.....	117
Figure 5.7 - Integrated biosensor prototype co-developed in collaboration with Lumisense Lda.	11719
Figure 5.8 - Schematics of the PDMS device coupled with the integrated prototype	11720
Figure 6.1 - Schematics of the micropatterning-based microfluidic structure for immunoassay multiplexing	123
Figure 6.2 - General operation schematics of the multiplexing device	124
Figure 6.3 - Detailed operation schematics for the multiplexed assays.....	126
Figure 6.4 - Characterization of the photoconductor array.....	127
Figure 6.5 - Proof-of-concept of the multiplexed by generating micropatterns using fluorophore labeled BSA	129
Figure 6.6 - Schematics of the direct competitive immunoassays and results of the cross-reactivity tests	130
Figure 6.7 - Molecular patterning and BSA blocking.....	132
Figure 6.8 - Calibration curves for single and multiplexed measurements of OTA, AFB1 and DON	134
Figure 6.9 - Schematics, photographs and addressing of the photoconductor array ...	135
Figure 6.10 - Microfluidic immunoassay signal currents of the 9 integrated photosensors for the detection of 9 discrete spots	136
Figure 6.11 - Multiplexed chemiluminescence detection of mycotoxins with integrated calibration using the thin film amorphous photoconductors array	137
Figure 7.1 - Schematic representation of the capillary-driven competitive ELISA.....	141
Figure 7.2 - Selection of an area centered in the colorimetric spot and analysis performed in ImageJ.....	142
Figure 7.3 - Colorimetric signal acquired with an optical microscope.....	142
Figure 7.4 - Colorimetric signal acquired with smartphone camera using different lighting conditions	143
Figure 7.5 - TMB conversion kinetics	144
Figure 7.6 - Detailed schematics of the capillary device, including the liquid insertion and pumping modules.....	145

Figure 7.7 - Characteristic flow rate profile in the capillary device and corresponding average residence times.....	147
Figure 7.8 - Data acquired with smartphone camera from a sample contaminated with one or two mycotoxins and respective quantification.....	148
Figure 7.9 - Calibration curves obtained for OTA, AFB1 and DON.....	149
Figure 7.10 - Comparison of velocity profiles measured with the autonomous sequential structure or manual insertion of each sample.....	151
Figure 7.11 - Results for the analysis of mycotoxins spiked in solid feed samples.....	151
Figure 8.1 - Schematics of the microchannel designed for trapping beads and assays to detect mycotoxins, ssDNA and PSA.....	161
Figure 8.2 - Results of the bead-based assays for the detection of mycotoxins, ssDNA and PSA.....	162
Figure 8.3 - Coupling of photodiodes with bead-based assays to detect fluorescent, chemiluminescent and colorimetric signals.....	166
Figure 9.1 - Schematics and photos of the capillary bead-based device showing the chamber where the beads are packed and the capillary pump.....	172
Figure 9.2 - Optimization of the DON immunodetection assay, calibration curve and kinetic profile.....	175
Figure 9.3 - Fluorescence emission of the DON competitive immunoassay measured in the double chamber structure with an internal maximum signal control.....	176
Figure 10.1 - Schematics of the bead-based multiplexed immunoassay.....	182
Figure 10.2 - Optimization of antibody and BSA conjugate concentration.....	183
Figure 10.3 - Calibration curves and kinetic profiles for OTA, AFB1 and DON.....	184
Figure 10.4 - Optimization of anti-BSA concentration.....	186
Figure 10.5 - Results for the multiplexed detection of OTA, AFB1 and DON.....	187
Figure 10.6 - Schematics of the photodiode array and respective electronics.....	189
Figure 10.7 - Characterization of the photodiode array.....	190
Figure 10.8 - Raw voltage measurements measured over time using MATLAB.....	191
Figure 10.9 - Multiplexed detection of OTA, AFB1 and DON using the integrated photodiode array.....	192
Figure 10.10 - Multiplexed detection of mycotoxins spiked in corn after an ATPE-based sample processing.....	194
Figure 10.11 - Non-specific signal due to adsorption of matrix interferents.....	194

List of tables

Table 1.1 - Summary of relevant chemical and toxicological data for the most prevalent mycotoxins.....	14
Table 1.2 - Summary of the regulatory limit ranges in the EU for multiple toxins and foodstuffs	15
Table 1.3 - Summary of regulations concerning aflatoxin B1 in animal feed	15
Table 1.4 - Summary of recommended limit ranges in the EU for multiple toxins and animal feeds	16
Table 1.5 - A sample of commercially available solutions for point-of-need mycotoxin analysis.....	25
Table 1.6 - Summary of mycotoxin measurement processes published between 2013 and 2017	27
Table 1.7 - Summary of response parameters for various types of ATPE aimed at biomolecule purification	42
Table 4.1 - Summary of the results obtained for the partition of AFB1, OTA and DON in PEG-salt ATPSs.....	87
Table 5.1 - Summary of recent OTA biosensing strategies published between 2014 and 2015	118
Table 7.1 - Summary of mycotoxin biosensing strategies published between 2015 and 2017	153

Motivation and outline of the thesis

The global population had an increase of more than 4-fold in the past 100 years and is expected to double in the next 100, surpassing 10 billion. One of the most fundamental requirements to sustain such rapidly increasing number of human lives is an adequate supply of water and food. However, such supply is only effective at assuring an acceptable degree of quality of life if appropriate food safety standards are adequately enforced. The fundamental nature of food to sustain human life is the main motivation to invest in research directed at improving food security and safety. Mycotoxins as harmful food and feed contaminants are a major modern challenge since there is an expanding need for increasing the throughput of food production, long distance trade and medium to long-term storage. In all sections of the food production train there is a significant risk of fungal and mycotoxin contamination, unless adequate screening methods are available for routine monitoring at every stage of the process.

This thesis aimed at improving the state-of-the-art methods for rapid screening of mycotoxins by combining the expertise in micro/nanotechnologies and microfluidics held by INESC Microsystems and Nanotechnologies (INESC MN) and the expertise in biomolecule purification and sample preparation held by the Institute of Bioengineering and Biosciences (IBB) at Instituto Superior Técnico (IST). This document is organized as follows. The **first introductory chapter** discusses mainly the fundamental principles of analytical assays performed in microfluidics, followed by an introduction to mycotoxins and the standard methods for their detection in food materials. A brief introduction followed by the state-of-the-art on the use of aqueous two-phase extraction is also included, as the method of choice to pre-process the sample prior to analysis, followed by a brief theoretical introduction to silicon photodetectors. The **second chapter** compiles the main methods employed for the microfabrication and operation of microfluidic devices. From the **third to the seventh chapters**, the development of sample preparation, immunodetection (including multiplexing strategies) and signal transduction modules are discussed. From the **eight to the tenth chapters**, several improvements to the assay related to assay speed and minimization of the number of steps are reported, achieved by coupling nanoporous microbeads with the microfluidic device. Finally, the **last chapter** wraps up the main achievements of the thesis and discusses further research projects towards (1) the achievement of full integration and sample-to-answer analysis and (2) integration of an analytical module to detect mycotoxigenic fungi.

Chapter 1

Introduction

This introductory chapter describes and discusses (1) the fundamental theoretical background supporting the experimental results compiled in this thesis, (2) the relevance of engineering fit-for-purpose biosensors to detect panels of mycotoxins in foods and feeds within the scope of food safety and (3) the potential of microtechnologies to pave the way towards fully integrated, simple to operate and portable analytical devices. A primary focus will be directed to microfluidic immunoassays in general, as the main analytical technique explored for mycotoxin detection. Furthermore, an emphasis is placed on the principles, applications and advances in aqueous two-phase extraction (ATPE) methods, since this liquid-liquid (L-L) separation methodology showed significant potential in sample preparation and pre-concentration for mycotoxin analysis in real samples including wines, beer, maize and other solid feed materials. A few of the subsequent sections are reproduced with appropriate adaptation from two review articles published during my doctoral studies [1, 2].

1.1. Fundamental aspects of microfluidic immunoassays

In the past couple of decades, there has been a dramatic development in microfluidic technologies applied to analytical assays by many research groups [3]. Such developments owe greatly to the advent of polydimethylsiloxane (PDMS) soft lithography [4], allowing the rapid and versatile prototyping of intricate device designs integrating actuators (e.g. microvalves [5]) and different signal transduction strategies (e.g. optical sensors [6]), controlled using portable electronic devices. Furthermore, developments in 3D-printing [7] and micromilling [8] technologies have also been extending microfluidics to other cost-effective materials such as cyclic olefin copolymer (COC) and polystyrene.

In the simplest setup, microfluidic immunoassays involve a controlled flow of solution through a confined microchannel. The main critical variables and physical properties having an impact on immunoassay performance are highlighted in **Figure 1.1**. It is important to highlight that although the experimental setup discussed here focuses

on immunoassays in particular (i.e. using antibodies as molecular probes), the same principles are applicable to any probe molecule (e.g. aptamer, peptide, low molecular weight organic ligand, lectin) immobilized in a microchannel.

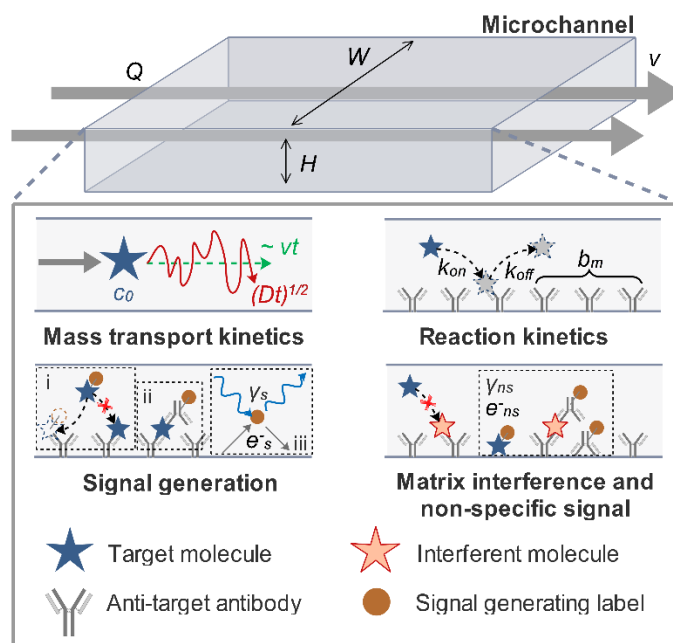


Figure 1.1 – Schematics of a generic microfluidic immunoassay and critical variables. The target molecules with a concentration c_0 flow through a confined microchannel with a cross-section area $H \times W_c$ (height \times width) and a linear velocity U , dependent on the imposed flow rate (Q). The molecules are transported along the channel proportionally to Ut and move across the channel only by diffusion, according to $(Dt)^{1/2}$, in which D is the diffusion coefficient of the target molecule and t is the time. These target molecules flow over a capture region on the surface of the channel with dimensions $L \times W_s$, containing a surface density b_m of capturing molecules such as monoclonal antibodies. These molecules are then captured according to the dissociation constant K_d intrinsic of the antibody, defined as the ratio of the kinetic constants k_{on} over k_{off} . After molecular capture, the signal can be generated via a competitive (i) or non-competitive (e.g. sandwich) (ii) immunoassay, followed by signal generation (iii) based on, for example, photon (γ_s) or current generation (e_s). Possible matrix interference effects may result in the absence of signal, while non-specific interactions may result in non-specific signal (γ_{ns} or e_{ns}). Therefore, appropriate sample preparation and surface passivation procedures must be evaluated to minimize such effects.

In microfluidic assays, the liquid flow occurs mostly in a laminar regime ($Re < 1$), meaning that mass transport perpendicular to the flow direction is governed by diffusion alone according to the intrinsic diffusion coefficient (D) of the molecule under analysis. Therefore, in flow conditions providing residence times significantly below the time required for the molecules to reach the capture region by diffusion, these will be lost downstream [9]. On the other hand, to minimize assay times it is necessary to supply molecules at a sufficient rate towards the capture region to minimize any mass transport limitations. This ensures that the assay is limited only by the intrinsic reaction kinetics between the target molecule and the capture antibody, even if such molecular supply rate inevitably implies wasting the majority of target molecules downstream of the capture

region [10]. To achieve such conditions, the Peclet numbers relative to the channel (Pe_H , **Equation 1.1**) and sensor (Pe_S , **Equation 1.2**) must be $\gg 1$, meaning that the target molecule depletion zone above the sensing region is relatively thin, thus maximizing the total flux of molecules (J_D) towards the capture region [9]. The parameter J_D , which assumes that every molecule that comes in contact with the capture region is effectively captured, can be estimated using **Equation 1.3**, where δ is the thickness of the depletion zone [9]. On the other hand, it should be noted that higher flow rates imply wasting high amounts of reagents, which are limited in real conditions. In this context, a third regime, additional to mass-limited and reaction-limited conditions, designated as “reagent-limited” was defined by Parsa and co-workers [11], highlighting the need to optimize the flow rate in order to balance analyte capture rate and total reagent volumes required.

$$Pe_H = \frac{H^2/D}{H^2W_c/Q} \sim \frac{Q}{DW_c} \quad (1.1)$$

$$Pe_S = 6 \left(\frac{L}{H}\right)^2 Pe_H \quad (1.2)$$

$$J_D \sim \frac{Dc_0}{\delta} W_S L \quad (1.3)$$

Focusing on the capture region, since the capture molecule is thermodynamically limited by an intrinsic dissociation constant (K_d), i.e. the ratio between the dissociation (k_{off}) and association (k_{on}) rates, not every target molecule that reaches the capture surface is effectively captured, neither remains captured indefinitely. Considering assay conditions which are limited only by the chemical reaction ($c_s \approx c_0$, with c_s being the concentration of targets at the sensor surface), the capture rate of targets can be assumed to follow first order Langmuir kinetics, according to **Equation 1.4**. Integrating **Equation 1.4** between $t = 0$ and t , **Equation 1.5** is obtained, from which the fraction of antibodies occupied in equilibrium ($t \rightarrow \infty$) is obtained according to **Equation 1.6** [9].

$$\frac{\partial b}{\partial t} = k_{on}c_0(b_m - b) - k_{off}b \quad (1.4)$$

$$\frac{b(t)}{b_m} = \frac{c_0/K_d}{1+c_0/K_d} (1 - e^{-(k_{on}c_0+k_{off})t}) \quad (1.5)$$

$$\frac{b_{eq}}{b_m} = \frac{c_0/K_d}{1+c_0/K_d} \quad (1.6)$$

The latter equation highlights that while concentrated target solutions ($c_0 \gg K_d$) result in all antibodies being occupied in equilibrium ($b_{eq} \approx b_m$), very dilute solutions ($c_0 \ll K_d$) result in only a small fraction of antibodies actually capturing the target molecule. This often-overlooked property of immunosensors results in a critical

limitation, significantly affecting miniaturized sensors in particular, as is highlighted by **Equation 1.7**, with c^* being the critical concentration. The parameter c^* quantifies the target concentration in solution resulting in only one target binding to the sensing region of area A , in equilibrium [9]. Therefore, at concentrations lower than c^* the molecular binding events will be singular and discontinuous over time. From this equation it is clear that to improve the assay sensitivity one can either (1) increase the affinity of the target molecule to the target analyte, (2) increase the surface density of antibodies or (3) increase the available surface area per unit volume, resulting in a higher number of probes aligned with the plane of the capture region. The latter strategy implies that the generated signal can still be effectively captured, despite the out-of-plane conformation of the capture region.

$$c^* = \frac{K_d}{b_m A} \quad (1.7)$$

As is highlighted in **Figure 1.1**, relying only on optimizing the mass transport and reaction kinetics may not be sufficient to achieve a target assay performance. Another critical parameter is the magnitude of signal generated per captured molecule. Such signal can either be generated by the molecular binding per se (label-free) or by an appropriate label. Thus, the possibility of quantifying the fraction of signal generated per captured molecule is of utmost importance to select the appropriate signal transduction method and adequately optimize a compromise between sensitivity and complexity/cost-effectiveness for a particular application. Several examples of improving the signal-to-noise ratio generated per molecule to achieve a target sensitivity have been reported for optical [12, 13] and electrochemical [14, 15] signal transduction for example. A thorough compilation of these strategies has been recently reviewed elsewhere [16]. Differently, resorting to a competitive approach (**Figure 1.1-i**), i.e. maximum measured signal obtained in the absence of target molecule, requires a different optimization approach compared with “sandwich” assays (**Figure 1.1-ii**). In this case the (1) stability of the signal acquisition and (2) concentration of antibody in solution relative to the target molecule, as modelled by Fu and co-workers [17], are major optimization factors to effectively induce and accurately measure a downshift in the binding kinetics.

Finally, the minimization of non-specific signal or matrix interference is equally critical and is perhaps the most challenging parameter when dealing with the detection of a target analyte in any complex sample comprising a mixture of hundreds of different

compounds. On one hand the non-specific signal implies an increase in the noise background, which limits the potential minimum detectable limits achievable with a given microfluidic immunoassay architecture [12]. Thus, the careful selection of adequate surface passivation strategies is necessary, although often significantly challenging [18]. On the other hand, matrix interference may simultaneously increase the noise background through the unwanted recognition of contaminant molecules and/or the decrease in the specific signal by the blocking of antibody binding sites, changes in molecular conformation or hindered effective diffusion of target molecules to the capture region due to increased viscosity [19]. Therefore, the often overlooked optimization and integration of effective and rugged sample preparation procedures is of capital importance to bring out the full potential of the developed biosensor [20]. Furthermore, to facilitate the sample preparation procedure without limiting rapid analysis times in the order of a few minutes [21, 22], the integration of the sample preparation procedure in-line with the assay should be considered whenever possible [23-25].

1.2. Recent advances and trends in the development of microfluidic immunoassays

Recent developments in microfluidic immunoassays in general, applied either within the scope of food safety or other highly relevant fields such as biomedical and environmental monitoring applications, can be categorized in six main modules, namely (1) the type of sensing surface where the probe, i.e. antibody or antigen, is immobilized; (2) the way in which the liquid is driven through the device; (3) the degree of process integration in a single microfluidic device; (4) the number of analytes that are simultaneously tested; (5) the way in which a measurable signal, correlated with the analyte concentration, is generated and; (6) the liquid manipulation as a continuous flow (analog) or in discrete micro droplets (digital). Each of these categories, schematized in **Figure 1.2**, are subsequently explored and coupled with relevant examples recently published in the literature.

Concerning the sensing surface, it can be either planar, such as the surface of a microchannel [26] or a non-porous bead (static as is the case of trapped polystyrene beads [27] and dynamic as is the case of magnetically actuated superparamagnetic beads [28]), or tridimensional, comprising for example a porous bead matrix [18, 29] (e.g. cross-linked agarose or controlled pore glass), a nano/micropatterned surface [30] or a porous

membrane [31] (e.g. electrospun fibers). Planar surfaces are well spatially defined, tend to facilitate the mass transport to the sensing area and are, in general, significantly simpler to model in terms of balancing mass transport and reaction kinetics, as discussed in **Section 1.1**. On the other hand, despite possible mass transport limitations in highly cross-linked nanoporous matrices, which can hinder the effective usage of the full probe surface coverage [32], this strategy intrinsically provides a dramatically increased surface to volume ratio, typically resulting in higher signal to noise ratio assuming an effective surface passivation [18]. Furthermore, by tuning the pore size it is possible to balance analyte diffusion and available surface area to maximize the molecular capture rate and overall signal output [29]. With the exception of devices relying on the mechanical actuation of micro particles through discrete liquid compartments to perform the immunochemical reaction [28], the way in which the solution is driven relative to the sensing surface is a critical design consideration. The liquid flow is typically driven using (1) a positive or negative pressure source [21] (e.g. syringe pump, pressure flow controller or peristaltic pump), (2) hydrophilic surfaces providing capillary-driven flow [33, 34] or (3) centrifugal force [35, 36]. While a pressure-driven flow allows a high and precise degree of fluidic control towards the development of minimally user-operated microfluidic immunoassays, comparable performances were already achieved with minimally instrumented capillary-flow based devices and standard optical disc drive-based centrifugal platforms. Notable examples are the development of automated sequential flow-injectors and versatile capillary pumps [37, 38] to control flow rate in the case of capillary-driven flow and fully integrated fluidic actuating components such as in-plane valves, meters and mixers relying only on sequential rotation frequency shifts [35]. Differently from microfluidic immunoassays based on a continuous liquid flow (i.e. analog), there have been considerable advances in digital microfluidics in recent years, based on manipulating discrete microdroplets. This manipulation, applied to microfluidic immunoassays, is typically performed using droplet generators [39] or electrowetting-on-dielectric (EWOD) platforms [40], the latter showing significant potential for automation, process integration and portability [41].

Depending on the application, either single or multiple target analytes may need to be detected simultaneously. For the simultaneous immunodetection of several target molecules, two main strategies have been reported, namely the (1) spatial confinement of detection regions, comprising an array of different antibodies or antigens [42] or (2) discriminating the immunodetection based on the specific label/ barcode alone [43].

While the early typically resorts to bi-directional micromosaic patterning [26], the latter is typically based on immobilizing specific molecules on barcoded microparticles using fluorophores [44], chromophores [43] or other optically active materials such as photonic crystals [45]. The specific target analyte is then detected using either a labeled detector molecule, covalently bound to an enzyme, fluorophore or optically active nanoparticle such as gold nanoparticles or quantum dots, or resorting to a label-free signal transduction [46]. In the scope of microfluidic immunoassays, the latter has most often been reported based on impedance or surface plasmon resonance (SPR) sensors. Both label-based and label-free modes of signal transduction integrated in microfluidic immunoassays are further explored in the next section.

Finally, there have been increasing efforts to integrate multiple process modules in the same device towards sample-to-answer operation, namely (1) extraction and/or sample preparation, including cell lysis and target analyte pre-concentration/ amplification (2) immunodetection and (3) optical/ electrochemical/ electrical signal acquisition using integrated sensors. This integration aims at facilitating device operation by non-specialized personnel, improving times of analysis, minimizing reagent consumption, increasing reproducibility and, ultimately, allowing true portability. The integration of signal transducers is explored in the subsequent sections.

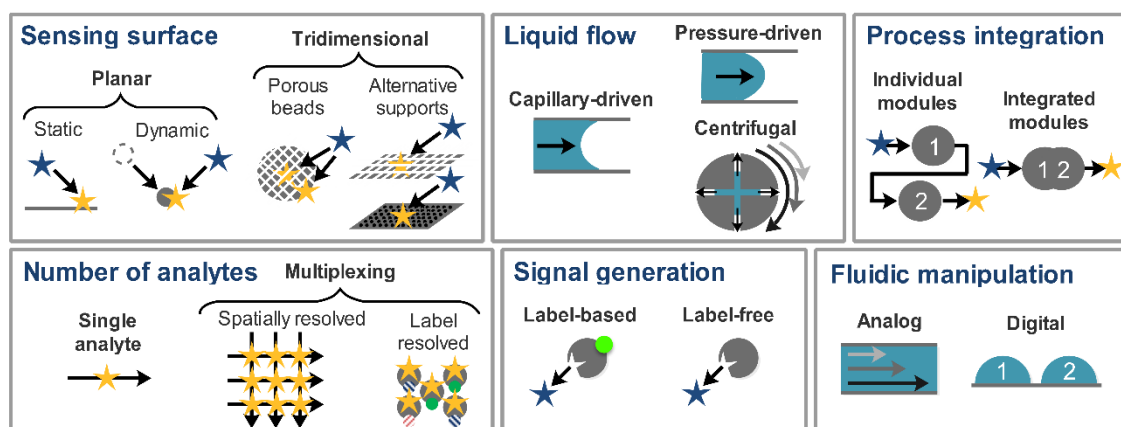


Figure 1.2 – Summary of the main strategies currently employed in the development of microfluidic immunosensors. The (1) blue (dark) and (2) yellow (light) stars refer to the (1) free target molecule in solution or (2) to the same molecules after immunoaffinity-based capture.

1.2.1. Optical to electrical signal transduction

Optical to electrical signal transducers integrated in microfluidics allow non-contact operation upon an efficient optical coupling, particularly in the case of miniaturized light sensors with sizes comparable to those of the microchannels [47]. The non-contact operation implies that no direct physical contact between the immunosensing

surface and the sensor is required. This characteristic allows the design of disposable fluidic devices while reusing the sensor indefinitely without cross-experiment contamination. Optical sensors coupled to microfluidic immunoassays have been mostly reported for the detection of (1) light absorbance [48], (2) fluorescence [49] or (3) chemiluminescence [50], using enzymatic or fluorophore labels. Recently reported devices resorting to each of these modes of detection are summarized in **Figure 1.3**. **Figure 1.3-A** schematizes an automated and multiplexed microfluidic device reported by Hu and co-workers [50], coupled with a portable and customized instrument for chemiluminescence signal acquisition. The instrument contains a peristaltic pump to drive the solutions through the microchannels, actuators for the mechanical valves integrated in the microfluidic device and a CCD camera coupled to a reflector and lens to collimate and focus the emitted light. According to the schematics in **Figure 1.3-B**, Novo and co-workers [34] reported a different strategy aiming at tackling the same integration challenge. Instead of using a CCD camera to acquire the chemiluminescence signal, the prototype equipment integrates a thin-film photodiode array to acquire the signal from a disposable capillary microfluidic chip. The capillary chip was engineered with a sequential capillary pump to allow an automated operation after inserting the samples in the respective inlets. **Figure 1.3-C** schematizes a microparticle-based lab-on-disk device developed by Zhao and co-workers [35] containing pre-stored reagents, providing a fully automated immunoassay in a single step. In this case, the signal is provided by an HRP-streptavidin conjugate, which converts the TMB substrate into a colored product. The absorbance of the product was measured outside of the LabDisk player platform for a direct comparison with standard microtiter plates but, in principle, a spectrophotometric cell could be easily integrated. Finally, integrated fluorescence measurements, schematized in **Figure 1.3-D**, were also reported by Pinto and co-workers [51] by coupling a fluorescent label with a large Stokes shift and a photodiode covered by an integrated absorption filter. By aligning a device containing agarose nanoporous beads with the sensors and performing the excitation with a standard 405 nm laser diode, continuous fluorescence measurements were achieved. This setup allows the development of ultra-rapid sub-minute immunoassays based on analyte binding kinetics [49].

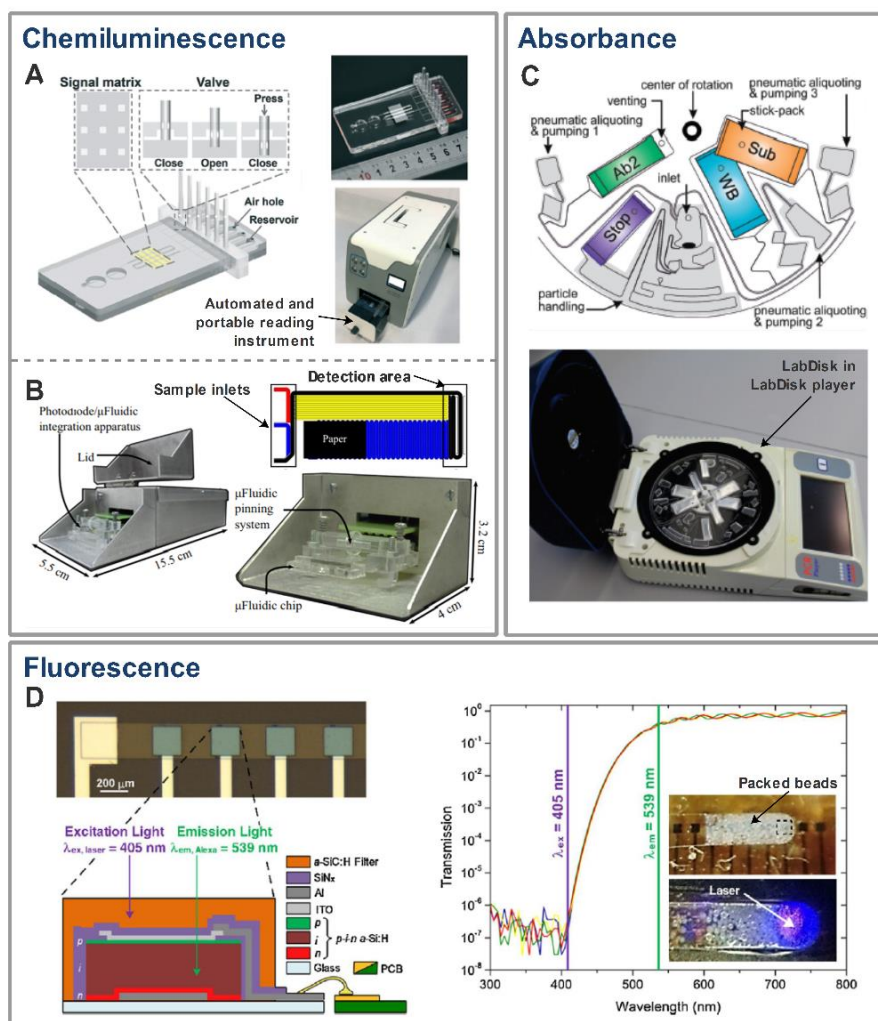


Figure 1.3 – Microfluidic immunosensors coupled with optical transducers. **A-** Disposable microfluidic chip with integrated valves to perform an array of immunoassays coupled to a portable instrument to for performing (1) valve actuation, (2) liquid handling and (3) optical signal acquisition. Adapted from ref. [50]. **B-** Disposable capillary-based microfluidic chip to perform multiple immunoassays after performing the microspotting of the antibodies in the microchannels. The chemiluminescence signals are acquired by thin-film a-Si:H photodiodes integrated in a fully portable prototype addressed by a laptop computer. Adapted from ref. [34]. **C-** Lab-on-disk device using anti-target functionalized microparticles and integrating stored reagents in a dried form. All liquid handling steps are performed automatically by changing the rotation frequency. Adapted from ref. [35]. **D-** Microfluidic channel containing commercial agarose beads aligned on top of an a-Si:H photodiode with an integrated fluorescence filter (spectral properties plotted on the right). Adapted from ref. [51].

1.2.2. Electrochemical signal transduction

Microfluidic immunoassays coupled with electrochemical transducers are typically based on having antibodies or antigens directly immobilized on the surface of electrodes. However, there are also reports of microfluidic assays where the antibodies are immobilized upstream of the electrode [52]. Compared to optical sensors, electrochemical sensors are typically simpler to fabricate, requiring only a thin layer of conductive and stable material patterned on the surface of the device such as gold, platinum or carbon-

based materials. Strategies have also been developed to increase the surface area of the electrodes, e.g. via nanopatterned features [53], following the same rationale as the nanoporous bead-based assays. Furthermore, the potentiostat instrumentation required to perform electrochemical measurements, typically based in DC amperometry, is relatively simple and cost-effective for integration in portable platforms [54]. On the other hand, differently from optical-based measurements, direct contact between the solution and electrodes is required, implying either the disposability [55, 56] or efficient regeneration of the electrodes [57]. The latter is a significant challenge and often limited to a few cycles to avoid compromising the assay performance [58]. Two recently reported examples of microfluidic immunoassays are schematized in **Figure 1.4**. **Figure 1.4-A** illustrates the assay developed by Oliveira and co-workers [59] comprising a pre-concentration step using magnetic particles conjugated to an anti-target antibody and HRP. The particles are then loaded into a disposable microfluidic immunoarray device (D μ ID) containing antibodies immobilized on screen printed carbon ink electrode arrays with a nanostructured surface (1.4 μ m average roughness), which is intrinsic to graphite ink. The current is then continuously measured at 200 mV while flowing a mixture of hydroquinone substrate and hydrogen peroxide. A different electrochemical assay design was reported by Kling and co-workers [52] (**Figure 1.4-B**), based on immobilizing antibodies on the channel surface via capillary pumping spatially defined by hydrophobic regions, upstream of planar Pt electrodes. The antibodies in this case are not used to detect the target molecule directly, but rather to immobilize a DNA strand bound to a repressor protein labelled with biotin, working as the actual biosensor. Streptavidin labelled with glucose is then used as label and glucose as substrate. Using a strategy based on stop-flow to accumulate hydrogen peroxide in the immobilization region, the authors achieve significant amperometric signals downstream in the Pt electrode, polarized to 450 mV against a reference Ag/AgCl on-chip reference electrode.

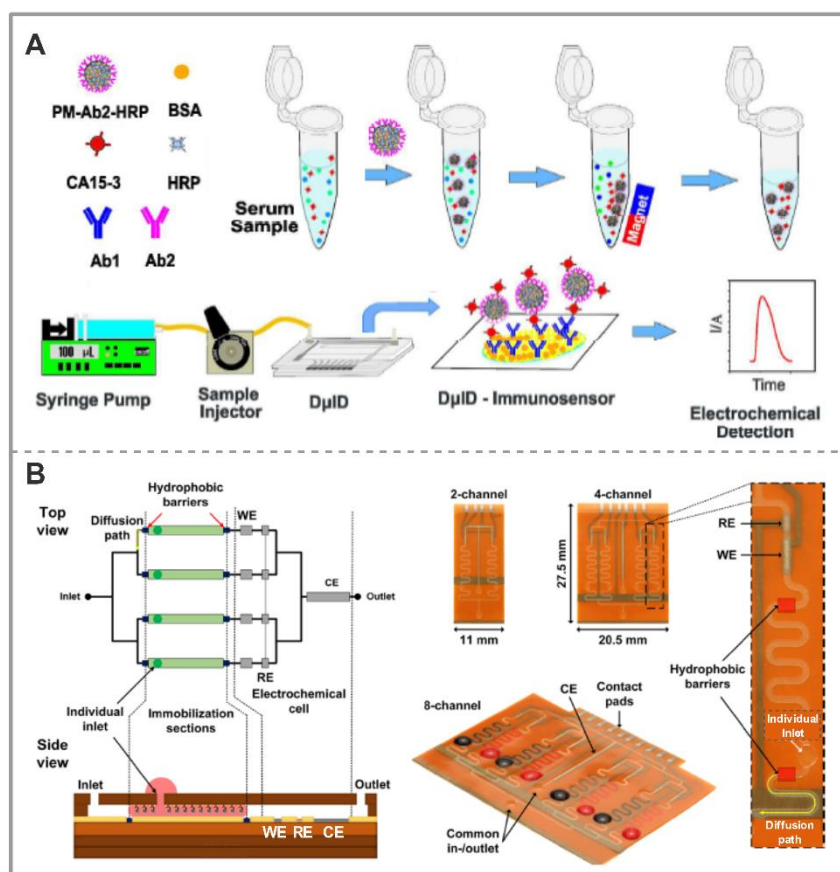


Figure 1.4 – Microfluidic immunosensors coupled with electrochemical transducers. **A-** Inexpensive polystyrene-based disposable microfluidic immunoarray device (D μ ID) comprising screen printed carbon ink electrodes. Prior to injection into the D μ ID the sample containing the target molecules was pre-concentrated using magnetic particles functionalized with the secondary antibody and an enzymatic label. Adapted from ref. [59]. **B-** Cost effective polymeric multiplexed microfluidic device comprising integrated Pt electrodes to perform the immunodetection of multiple target molecules using glucose oxidase as label. The antibodies are immobilized in defined regions upstream of the electrodes using capillary flow and hydrophobic barriers. WE, RE and CE refer to working electrode, reference electrode and counter-electrode, respectively. Adapted from ref. [52].

1.2.3. Label-free transduction

Label free detection integrated in microfluidic immunoassays has mostly been reported based on impedimetric or surface plasmon resonance measurements. The early requires a setup similar to that of electrochemical measurements, where the antibodies or antigens are typically immobilized on top or in close proximity to planar electrodes. The impedance measurements are then performed between the electrodes, at AC frequencies typically in the range of kHz to MHz and voltages below 1 V, allowing the electric field to propagate into the medium [60]. Different frequencies can first be tuned using electrochemical impedance spectroscopy (EIS) in order to identify the frequency regime providing the highest specific impedimetric signal, the latter allowing the continuous monitoring of the target analyte at a single frequency [60, 61]. Two examples of

microfluidic immunoassays coupled with impedance measurements for signal transduction are schematized in **Figure 1.5**, developed by Mok and co-workers [62] (**Figure 1.5-A**) and Nwankire and co-workers [63] (**Figure 1.5-B**). The device schematized in **Figure 1.5-A** [62] comprises a microchannel containing a capture region with immobilized anti-target antibodies ($300\ \mu\text{m}$ wide \times $30\ \mu\text{m}$ tall) and an electrochemical impedance sensor aligned with a $40 \times 10\ \mu\text{m}$ micropore. The detection is based on flowing magnetic microbeads functionalized with anti-target antibodies to perform a sandwich assay in the capture region, followed by elution and counting using the impedance sensor excited with a 700 kHz, 300 mV AC signal. The output digital signal is directly proportional to the target concentration in solution. The electrochemical lab-on-a-disk device schematized in **Figure 1.5-B** [63] allows integrated sample preparation using a ficoll gradient to effectively isolate the target cells from blood, followed by a single step immunoassay allowing the label-free impedimetric detection of the immobilized target cells. The impedimetric signal is measured by applying a 117.2 Hz 50 mV AC signal between the working (immobilized anti-target antibodies) and counter-electrodes. Alternative to impedimetric measurements, label-free optical SPR measurements are currently the gold standard to extract thermodynamic information using high-precision, high-throughput commercial equipments such as Biacore from GE Healthcare [64]. There have been considerable efforts in simplifying and miniaturizing these towards cost-effective integration with microfluidic devices using SPR reflectivity measurements based on prism light coupling or gratings, SPR imaging (SPRi) or localized SPR (LSPR) [65]. As a remarkable example, the strategy reported by Guner and co-workers [66], schematized in **Figure 1.5-C**, comprises a portable platform attachable to a smartphone camera to perform SPRi of a disposable microchannel, integrating a light source, optics and microfluidic chip holder. In order to be disposable, the microfluidic device was sealed against a standard Blu-ray disk patterned with gold, in order to cost-effectively provide a grating with a pitch width of 320 nm and depth of 20 nm for light coupling. The acquired images can then be analyzed in terms of reflectivity change (linearly correlated with the refractive index) to continuously monitor molecular capture on the gold surface.

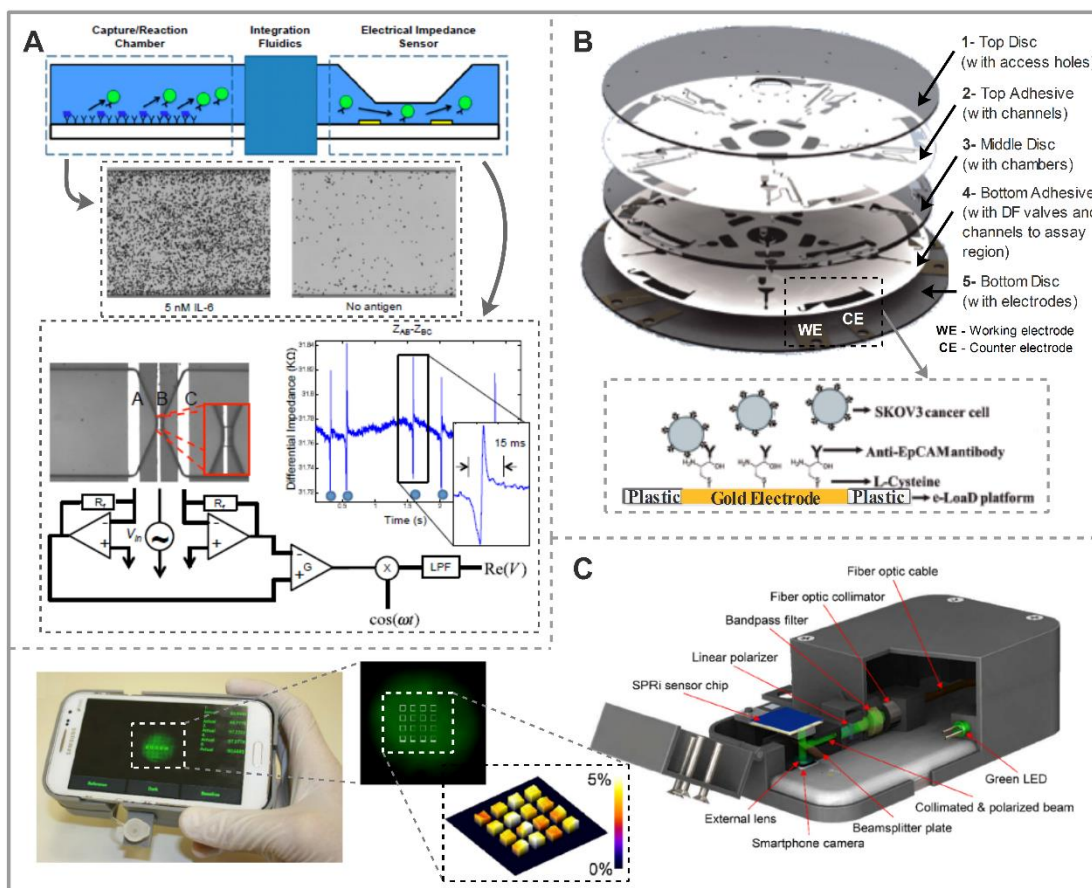


Figure 1.5 – Microfluidic immunosensors coupled with label-free impedance-based or surface plasmon resonance (SPR)-based transducers. **A-** Microfluidic device comprising two gold electrodes to perform the digital counting of $2.8 \mu\text{m}$ magnetic beads functionalized with anti-target antibodies. Upstream of the micropore, the beads flow through a capture chamber also containing immobilized anti-target antibodies. Adapted from ref. [62]. **B-** Fully automated lab-on-disk device for the label-free detection of cells directly from whole blood, integrating a density gradient-based centrifugation sample preparation/ pre-concentration step. Anti-target cell antibodies are immobilized on the surface of gold working electrodes, measured against a counter electrode in an adjacent chamber without target cells. Adapted from ref. [63]. **C-** Miniaturized SPR imaging instrument coupled to a standard smartphone, allowing label-free measurements of an immunoassay performed on a disposable microfluidic device sealed against a gold patterned standard Blu-ray disk. The percent values relate the reflectivity change above the baseline after adsorbing BSA on the gold surface. Adapted from ref. [66].

1.3. Mycotoxins and point-of-need screening: Relevance, demand, challenges and opportunities

1.3.1. Relevance and regulatory aspects of mycotoxin analysis

Mycotoxins are prominent among fungal secondary metabolites with a negative impact on human and animal health. As many as 1,000 fungal compounds have been given this label, including aflatoxins (AF), trichothecenes, fumonisins (FB), ochratoxin A (OTA), and various indole-terpene tremorgenic compounds. These are major threats to

the health and life of humans and livestock, since the most relevant of these are found in food [67]. Their biosynthesis by the producing fungi can occur throughout the entire food chain, from the crops in the field to the end-product in storage, from the transportation of food commodities to the processing and storage of food and feed [68, 69]. The toxic effects of mycotoxins on humans and animals have been extensively studied for the last several decades and are summarized in **Table 1.1**.

Table 1.1 – Summary of relevant chemical and toxicological data for the most prevalent mycotoxins.

Mycotoxin	Fungal species (examples)	Effects	Target organ and mechanism of toxicity	Ref.
Aflatoxins (B1, B2, G1, G2)	<i>Aspergillus flavus</i> , <i>A. parasiticus</i> , <i>A. nomius</i>	Carcinogen, immune suppressor	Liver; alteration of p53-target gene expression and mutations, necrosis	Williams <i>et al.</i> , 2004 [70] IARC, 2002 [71]
Ochratoxin A	<i>Aspergilli</i> section <i>nigri</i> , <i>circumdati</i> , <i>flavi</i> ; <i>Penicillium</i> section <i>viridicata</i>	Suspected carcinogen, nephrotoxic, hepatotoxic	Kidney; inflammation of proximal tubule cells, altered cellular signaling. Liver; interleukin-6 decrease, superoxide dismutase (SOD) increase	El Khoury <i>et al.</i> , 2010 [72]
Trichothecenes B (deoxynivalenol, nivalenol)	<i>Fusarium graminearum</i> , <i>F. culmorum</i> ,	Vomiting, feed refusal, anemia	Alimentary and hematopoietic system; DNA damage and cell cycle arrest, alteration of cell membrane integrity and function	Pestka, 2007 [73] Sudakin, 2003 [74]
Trichothecenes A (T-2, HT-2)	<i>F. sporotrichioides</i> , <i>F. langsethiae</i>			
Zearalenone	<i>F. graminearum</i> , <i>F. oxysporum</i> , <i>F. culmorum</i>	Infertility, abortion	Endocrine system; hormonal imbalances	Zinedine <i>et al.</i> , 2007 [75]
Fumonisin	<i>F. verticillioides</i> , <i>F. proliferatum</i>	Suspected carcinogen equine leucoencephalomalacia	Central nervous system; ceramide synthase inhibitors, cytotoxic	Soriano <i>et al.</i> , 2005 [76]
Patulin	<i>Penicillium expansum</i>	Gastric ulcer, alteration of renal function.	Gastrointestinal tract, kidney; DNA damage, proteotoxicity	Puel <i>et al.</i> , 2010 [77]

Regulations relating to mycotoxins have been established in many countries to protect the consumer from their harmful effects. As an example, in the EU, precise limits for the possible presence of some mycotoxins in food and feedstuff have been established [78-80] in accordance with the provisional maximum tolerable daily intake (PMTDI) as a guideline for preventing and controlling contamination (**Table 1.2**). Since Commission regulations and directives are binding legislative acts, they must be applied across the EU as well as the European Economic Area (EEA) including Iceland, Liechtenstein, and Norway.

Table 1.2 – Summary of the regulatory limit ranges in the EU for multiple toxins and foodstuffs. In particular, Regulation 165/2010 concerning aflatoxins [78], Regulation 1881/2006 concerning ochratoxin A [79], and Regulation 1126/2007 concerning deoxynivalenol [80].

Commodity	Maximum limit (µg/kg)		
	B1	B1/2 G1/2	M1
Aflatoxins (AF)			
Foods to be subjected to physical treatment before human consumption	5-12	10-15	-
Foods for direct human consumption or use as an ingredient in foodstuffs	2.0	4.0	-
Processed cereal-based and dietary foods for infants, babies and young children.	0.10	-	0.025
Raw milk, heat-treated milk and milk for the manufacture of milk-based products.	-	-	0.050
Infant milk, follow-on milk. and follow-on formulae	-	-	0.025
Ochratoxin A (OTA)			
Unprocessed cereals and derived products for direct human consumption	3.0-5.0		
Dried vine fruit (currants, raisins and sultanas), soluble (instant) coffee	10.0		
Wine and aromatized wine excluding liqueur wine with an alcoholic strength >15% vol. Grape juice, nectar intended for direct human consumption.	2.0		
Piper spp., <i>Myristica fragrans</i> (nutmeg), <i>Zingiber officinale</i> (ginger), <i>Curcuma longa</i> (turmeric), Capsicum spp., liquorice root and extract.	15.0-80		
Processed cereal-based foods, dietary and baby foods for infants	0.50		
Deoxynivalenol (DON)			
Unprocessed cereals, and milling fractions of maize (particle size ≤ 500 µm) not used for direct human consumption	1250-1750		
Cereals and cereal products intended for direct human consumption	500-750		
Processed cereal-based foods and baby foods for infants and young children.	200		

The toxic effects of certain mycotoxins on many livestock animals including reduced growth and reproduction rates, hemorrhagic phenomena and death have also been documented [81]. These findings have led to the development of a regulation concerning the tolerable level of certain mycotoxins in feed (

Table 1.3), both to control environmental contamination and economic losses resulting from contamination of feed and products derived from livestock (e.g., meat and milk). Although current feed regulations cover only AF, limits have been recommended for other mycotoxins (**Table 1.4**), which are not binding but create policies that can result in regulation.

Table 1.3 – Summary of the Regulation 574/2011 concerning aflatoxin B1 in animal feed [82].

Commodity	Maximum limit (µg/kg)
All feed materials. Compound feed for cattle, sheep, goats, pigs and poultry (except young and dairy animals)	20
Compound feed for dairy cattle, sheep, goats, calves, lambs, piglets and young poultry animal	5
Compound feed for cattle (except dairy cattle, calves, sheep, goats), pigs and poultry (except young animals)	20

Table 1.4 – Summary of recommended limit ranges in the EU for multiple toxins and animal feeds[83, 84].

Toxin	Commodity	Maximum Limit (ppm)
OTA	Feed materials	0.25
	Complete feeds	0.05 - 0.1
FB1+FB2	Feed materials	60
	Complete feeds	5 - 50
DON	Feed materials	8 - 12
	Complete feeds	0.9 - 5
ZEN	Feed materials	2 - 3
	Complete feeds	0.1 - 0.5

Mycotoxin diffusion and distribution reflects the synthesis of these secondary toxic metabolites by different fungal species in various environments [85]. The most recent validated predictive models for mycotoxin contamination in climate-change hot spots such as the Mediterranean area [86-88], suggest that environmental conditions will promote the development of mycotoxin producing fungi [89-92] and therefore negatively affect agricultural production in those areas. The importance of crop contamination is thus crucial to assessing general contamination, because most mycotoxins come from the field, even if their content in crop-derived products can rise dramatically due to improper post-harvest management. The ability of mycotoxins to move through different levels of the food pyramid (carry-over) constitutes another aspect of the risk they represent. As an example, the carry-over of aflatoxin B1 (AFB1) excreted as aflatoxin M1 (AFM1) in cow's milk is a well-known phenomenon. Furthermore, different studies indicate that mycotoxin contamination is often detectable in different organs of the livestock fed with contaminated feed or in their products [93, 94].

The globalization of agricultural trade without commensurate legislative harmonization demands the fostering of increased awareness of the presence of mycotoxins in the food chain. Aside from health risks, such contamination has important economic and trade implications [95, 96] including (1) reduced crop and livestock production, (2) contaminated food and feedstuffs disposal, (3) loss of human and animal life, and (4) increased costs associated with human and animal health care, analytical and regulatory efforts, and research investment. Given the breadth and diversity of the economic implications, the costs and impact of mycotoxin contamination on international trade are difficult to assess in a consistent, uniform way and impossible to determine accurately [96]. However, estimates indicate that total annual losses can be as high as 2.5 billion USD in the United States of America and more than one billion in Europe, accounting for market, livestock and human health losses [95, 96]. To reduce the presence

and impact of mycotoxins requires an integrated understanding of crop biology, agronomy, fungal ecology, harvesting methods, storage conditions, food processing, and detoxification strategies. In this context, it is critical to highlight that any strategy must be based on reliable quantitative determination of mycotoxins in the relevant raw materials.

1.3.2. Standard analytical methods for mycotoxin quantification

The detection and quantification of potential mycotoxin contaminants of a bulk of a food commodity are crucial for determining whether that bulk is acceptable for human consumption. Mycotoxin concentration is usually estimated by testing small portions (samples) of a bulk lot; if the sample concentration does not accurately reflect the lot concentration, then the lot may be misclassified and there may be undesirable economic and/or health consequences [97]. The mycotoxin test consists of (1) sampling (milling and sub-sampling), (2) preparation (extraction and purification), and (3) analysis. Although each step may involve variation and uncertainty, sampling is the most critical [98] and an accurate and precise sampling design is mandatory for minimizing bulk-lot misclassification risk.

Contaminated particles may not be distributed uniformly throughout the lot, due to, e.g., a local moisture leak or increased temperature due to environmental exposure. Thus, the sample should be a composite of many small portions taken from different locations throughout the lot. The FAO/WHO recommends that one portion of about 200 g be taken for every 200 kg of product [99]. The collection of all portions taken should constitute the bulk sample. Studies on sampling in agricultural products, such as peanuts and shelled corn [100, 101] suggest that even if a very small percentage (0.1%) of the kernels in the lot are contaminated, the concentration on a single kernel may be extremely high. For shelled corn for example, it is estimated that in a lot with contamination of 20 ng/g, only six kernels out of 10,000 may actually be contaminated [102]. This accounts for large variation among replicated samples within the same lot and the difficulty of designing effective and efficient sampling plans. Although sampling variance trends for different commodities and mycotoxins must be described by specific equations, sampling variance generally increases with an increase in mycotoxin concentration and decreases with an increase in sample size.

After sampling, sample preparation can be accomplished with different procedures depending on the food matrix and toxins considered. An extraction by solvent

mixtures is usually performed. The raw extract is then cleaned up using (1) solid phase extraction (SPE) columns (with stationary phase materials such as silica gel or activated charcoal) or (2) immunoaffinity columns (IAC) (with a stationary phase gel with immobilized antibodies specific to certain mycotoxins). In each case, the raw extract is placed at the top of the column, which is washed with the appropriate solvent (e.g., water or organic solvent), thereby allowing the separation of most interfering compounds. Thus, a purified extract is obtained, which can be further analyzed for a quantitative determination of a possibly present mycotoxin. The difficulty and complexity of sample preparation depends on the food or feed matrix considered, the chemical characteristics of the mycotoxin, its concentration in the sample, and the potential presence of different mycotoxins. After extraction and sample preparation, the analysis is typically performed resorting to chromatographic or immunochemical methods, as discussed below.

Chromatography coupled with different detection principles has become a widely used reference method for unambiguously confirming samples determined to be positive after screening assays based on immunochemical methods, and for enabling exact quantification when needed. From the mid-90s onwards, atmospheric pressure chemical ionization (APCI) and electrospray ionization (ESI) LC/MS became available [103]. These allow a soft ionization and improved analytical performance due to their robustness, easy handling, high sensitivity, accuracy, and their compatibility with almost the whole range of compound polarities [104-106]. These methods have been largely used to determine mycotoxins in biological and environmental matrices and their sensitivity and selectivity have enabled considerable reduction in sample preparation or/and derivatization processes. In general, GC/MS and LC/MS are commonly accepted by authorities as highly reliable analyte confirmation tools in residue analysis in the course of regulatory and legal proceedings [107, 108].

However, these techniques have also several drawbacks that may significantly reduce quantification accuracy and precision: ionization efficiencies are not equal for all analytes and signal suppression/enhancement can be observed. Due to the complexity and diversity of food samples these matrix effects (ME) vary in different sample matrices. To control ME consequences, methods such as matrix-matched calibration or use of internal standard can be used. Besides, extensive validation efforts must be undertaken, such as calibration curves set up in the matrix together with an internal standard [109]. Furthermore, chromatography-based techniques also require lengthy sample pretreatment and execution times, expensive instruments and skilled technicians, resulting in high

determination costs. These methods therefore are of limited practicality for rapid on-site analysis by importers, traders, and food and feed companies.

As an alternative to chromatography-based methods for the fast screening of mycotoxins, immunochemical methods can be used. The basis of any immunoassay is an antibody-antigen interaction (in this case, with mycotoxins). Regarding the production of antibodies, it is important to highlight that mycotoxins do not have their own immunogenicity due to their very small molecular weights. Consequently, it is necessary to bind them to a carrier molecule, usually a protein, such as bovine serum albumin (BSA) or ovalbumin before immunization to achieve immunogenicity [110], although the conjugation process can also be responsible for a decrease in assay selectivity [111]. The methods used for coupling the mycotoxins with a carrier are specific for each mycotoxin. For example, ochratoxins can be conjugated with the protein directly, without preliminary modification through the interaction of the ochratoxin carboxyl group with the protein amine group via EDC (1-Ethyl-3-(3-dimethylaminopropyl) carbodiimide) [112]. Ochratoxins and DON can also be directly activated using CDI (carbonyldiimidazole) via carboxyl or hydroxyl groups for direct covalent coupling with amine groups in proteins [113]. On the other hand, AF do not have chemically active groups for the direct binding to the carrier protein and, therefore, require preliminary activation through the formation of a 3-(O-carboxymethyl) oxime reactive group for covalent binding to the protein [114].

If a conjugate of the enzyme-coupled mycotoxin is mixed with an extract containing free mycotoxin, and added to a well coated with specific antibodies, the enzyme-coupled mycotoxin will compete with the free mycotoxin present in the extract for antibodies binding sites (**Figure 1.6-A**). After removing any excess enzyme-coupled and free mycotoxin, the substrate of the enzyme is added and reacts with the enzyme-coupled mycotoxin, whose concentration is inversely proportional to the concentration of the mycotoxin in the sample, such that the absence of color indicates analyte presence while coloration indicates a negative result. The same concept can be applied by having instead the antigen immobilized on the surface and labelled antibodies in the sample. In this case, the surface concentration of bound labelled antibodies is also inversely proportional to the free mycotoxin concentration in the sample. These are examples of competitive ELISA that are best suited for low molecular weight compounds such as mycotoxins, which typically cannot bind two antibodies simultaneously.

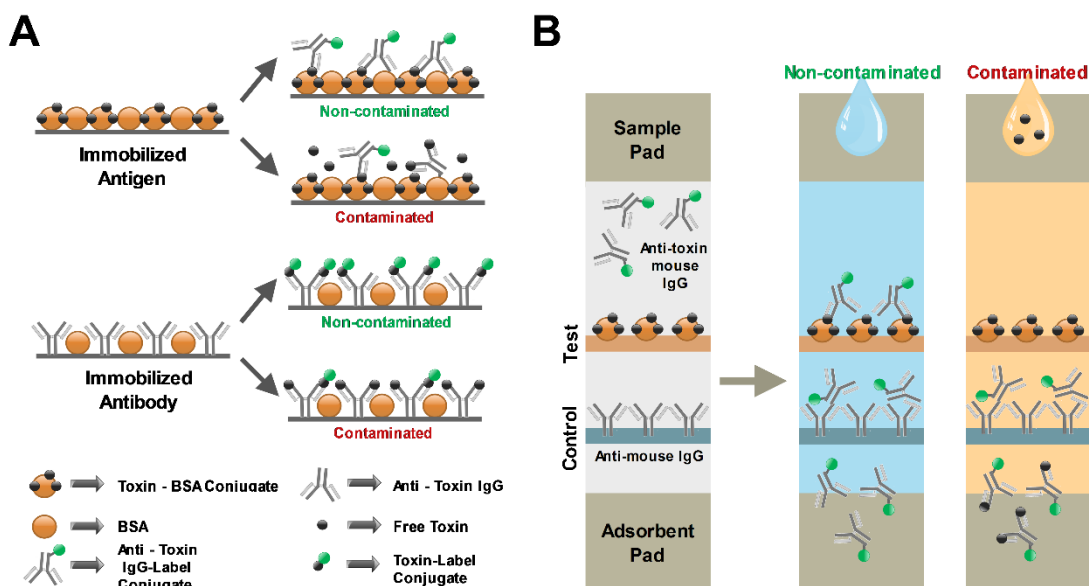


Figure 1.6 – Schematics of competitive immunoassay designs typically used in **A**- well plates or **B**- lateral flow devices. Bovine serum albumin (BSA) is given as an example of a typical protein scaffold used to immobilize the antigen. BSA alone at relatively high concentrations (i.e. above 1 mg/mL) is typically used for blocking purposes. The labels employed in standard immunoassays are typically enzymes such as horseradish peroxidase (HRP) or alkaline phosphatase, used to catalyze reactions generating a colored product. Alternatively, gold nanoparticles are also often used as colorimetric labels in lateral flow immunoassays.

Similar to a well plate ELISA, lateral flow immunoassays (LFIA) are a method of analysis where a liquid sample containing the analyte is placed on an absorbing pad, moving via capillary action towards different zones of the pad (**Figure 1.6-B**). In the first zone, label-antibody conjugates are present and get hydrated by the flowing sample, subsequently moving to the test line, which contains pre-immobilized mycotoxin (the same to be detected) which is specifically recognized by the label-antibody conjugate. There is also a control line containing pre-immobilized secondary antibody having the ability to bind to the labeled antibody. If the target analyte in sample solution is absent, both the test and the control lines show signal, on the other hand, if the target analyte is present in the sample solution, it will compete with the immobilized antigen, reducing the signal intensity in the test line [115].

Based on the specific antigen–antibody reaction, traditional immunoassays, especially ELISA performed in a well plate and LFIA, are easy to perform and have been extensively used in the screening of different mycotoxins as commercial kits, as will be discussed ahead in **Section 1.3.4**. However, there are some disadvantages, such as the difficulty of automating the process, or low sensitivity and cross-reactivity. In recent years, many novel biosensors were developed based on antibody-mycotoxin interactions

[116], aiming at tackling drawbacks associated with traditional methods for performing these assays, including several improvements to conventional LFIA (e.g. multiplexing capabilities, enhanced sensitivity and precise signal quantification), as will be discussed in detail in **Section 1.3.5**.

1.3.3. Assay requirements and fit-for-purpose analytical performance

This section briefly summarizes the fundamentals of standard procedures in analytical chemistry to evaluate if an assay is fit-for-purpose for a specific mycotoxin detection threshold. This is particularly important to subsequently discuss the tradeoffs between performance and other considerations such as simplicity of use and cost when developing a point-of-need analytical device. As an overview, Figure 1.7 schematically shows the main components of a mycotoxin measurement process and the subsequent interpretation of the response. For in-depth discussions of the analytical standards involved in quantitative and qualitative assays, the reader is referred to reviews by Lloyd Currie [117, 118] and Macarthur and von Holst [119].

The measurement of mycotoxin content includes all the steps from sample preparation to signal transduction. It is fundamental in a chemical measurement for analytical purposes to have statistical control, meaning that its imprecision and bias are fixed at a particular measurement condition (i.e. a particular analyte in a particular matrix). Along these lines, after bringing the uncertainty to within acceptable bounds, it is also important to guarantee a high degree of ruggedness, so that the precision and accuracy of the method are relatively insensitive to minor changes in environment or procedure. While the statistical quality of the sampling process is critical to provide an accurate estimation of the safety of a batch of feed – as discussed in the previous section, this step is not taken in account when discussing the measurement process. Only the real analyte concentration “ x ” present in the tested sample is considered, regardless of its origin. The response is the output estimation of the analyte concentration “ \hat{x} ”, related to the measured signal, typically via a linear response in which the slope is the sensitivity “ A ” and the intercept is the signal of the blank. This linear response is affected by the measurement error, including bias and random error. To calibrate the signal and characterize the response in terms of accuracy and precision, it is critical to include high quality standard reference materials in the measurement process.

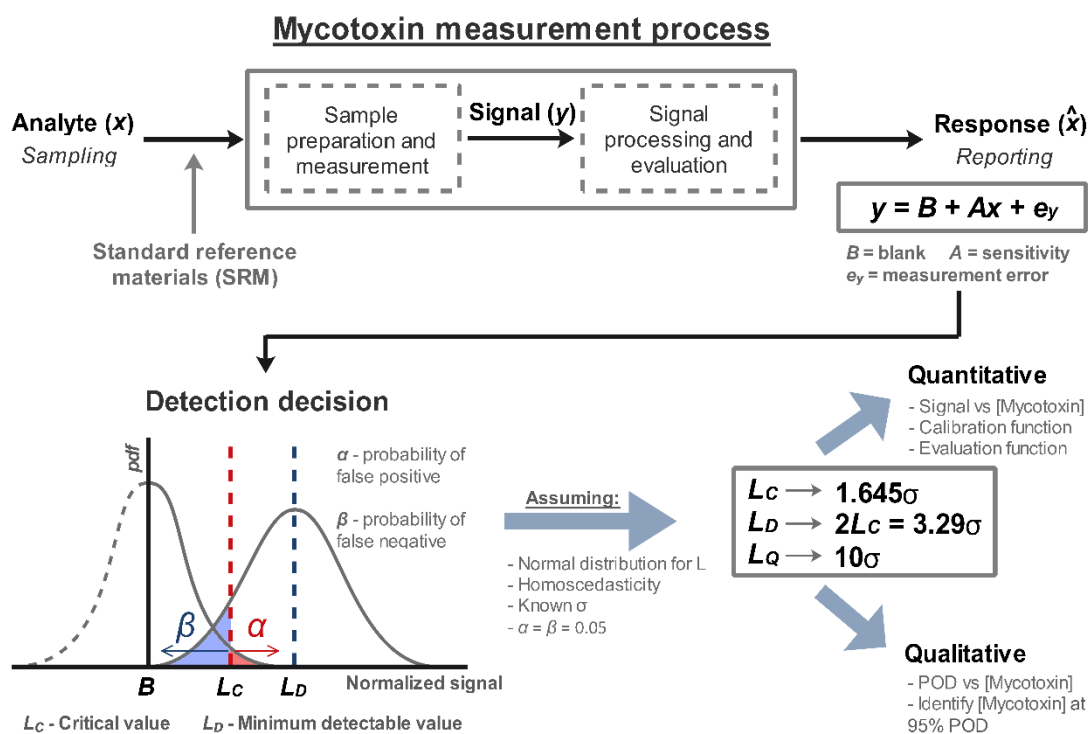


Figure 1.7 – Schematics of the main components of a typical chemical measurement process aimed at mycotoxin detection, fundamentals on detection decision after the response and main features of quantitative [117] and qualitative [119] data interpretation. L_C , L_D and L_Q refer to critical value, minimum detectable value and quantification limit, respectively. POD and *pdf* refer to probability of detection and probability density function, respectively.

It is also essential to statistically define the detection decision to confidently determine if a certain sample is above or below a certain critical threshold (i.e. detection or non-detection). Before discussing the detection criteria, it is important to remind the reader that the null hypothesis (H_0), i.e. non-detection, indicates that the analyte concentration falls below the detection limit of the system and does not suggest that the analyte is absent (zero concentration). A measurement of zero concentration is impossible to achieve [118]. In the case of mycotoxins, considering the presence of established regulatory limits, one can instead consider H_0 equal to this target concentration, below which it can be considered that the mycotoxin concentration is acceptable. According to IUPAC recommendations [117], the detection capability of a measurement process should be defined by two values, the critical value (L_C) and the minimum detectable value (L_D). Both these values are defined based on the distribution and standard deviation (σ) of the blank, highlighting the importance of an accurate determination of these parameters to the evaluation of the analytical method. The definition of L_C and L_D is related with two types of error, type I or false positive and type II or false negative errors. Type I error means rejecting the null hypothesis when the analyte is not present above the critical

threshold and type II means accepting the null hypothesis when the analyte is present above the critical threshold. The probabilities associated with incurring type I or II errors are referred to as α and β , respectively, for which default values recommended by IUPAC are 0.05 (i.e. 5%) for each. **Figure 1.7** illustrates α (red shaded region) and β (blue shaded region) for two hypothetical probability functions in the measurements of the blank and of a sample with a mycotoxin concentration at the minimum detectable value (L_D). By assuming a set of conditions in this scenario, in particular (1) the standard deviations being homoscedastic, (2) known for the blank and (3) following a normal distribution, the L_C and L_D can be easily calculated according to the formulas shown in **Figure 1.7**. The determination of the measurement performance and establishment of a detection decision is then followed by the classification of the method as quantitative or qualitative. For a quantitative assay, the signal magnitude “y” is correlated with the concentration of mycotoxin via a calibration function to subsequently allow the determination of an unknown mycotoxin titer via an evaluation function. In this case, the limit of quantification (L_Q) is generally accepted as 10σ and the estimates should typically have a relative standard deviation of 10% [117]. Regarding qualitative assays, the probability of detection (POD) is correlated with the mycotoxin concentration and the concentration of mycotoxin that generates 95% POD should be accurately determined [119]. This scenario is fit-for-purpose when it is sufficient to simply know if sample has an analyte concentration that is above or below a certain threshold (blank or a predefined limit). This is typically the case of quick point-of-need screening applications to determine whether it is necessary to send a sample for quantification using a reference method at a certified laboratory.

1.3.4. Shortcomings of commercially available solutions for point-of-need mycotoxin analysis

Due to its economic relevance and worldwide spread, several instrumentation companies have considered mycotoxin detection a very significant market. The current instruments on the market can be divided into two general types: the first kind addresses the needs of accredited laboratories while the second kind satisfies the requirements of private customers. The accredited laboratories include all governmental and public administration organizations, both at European and national/local level as well as private, specialized laboratories providing quality certificates. The aim of governmental and public organizations is to provide a network for food security safeguard, both through

controls on production and through research. These public entities have the following aims such as: (i) making certified checks, of proven accuracy, based on validated methodologies; (ii) certifying the validity of innovative methods of detection; and (iii) carrying out research on the methods of detection of mycotoxins, on the prevention of their spread and, finally, on methods of purification of toxins. Private laboratories provide instead mainly certified checks with a proven accuracy.

As previously discussed, the most common analytical procedures used for mycotoxin analysis in accredited laboratories include high-performance liquid chromatography (HPLC), gas chromatography (GC) and mass spectrometry (MS). The main companies producing these equipments are Shimadzu, Cecil Instrumentation Ltd., Gilson Inc., JASCO, SCIEX, Thermo Fisher Scientific and Waters Corporation. All these instruments cost more than 10,000 € and trained personnel is needed to carry out the analysis. On the other hand, private customers include producers of agri-foods subjected to mycotoxin contamination. Within these users, it is important to distinguish between those who directly produce the goods subject to contamination from those who use them as intermediate product to make derivatives or other agri-food products. Private parties are generally motivated by the need to ensure and certify the quality of their products as well as regulatory constraints (e.g., the obligation to comply with the law for self-control of production). Due to its low cost, their preferred analysis method is the dipstick lateral-flow assay based on a competitive immunoassay format (LFIA) as shown previously in **Figure 1.6-B**. Depending on the company and on the mycotoxin, the method features a water-based or a methanol-based extraction, which enable users to test for single or multiple mycotoxins from the same prepared sample. Furthermore, the LFIA is often coupled to an optical reader to convert the line densities into a quantitative result, displayed in ppb or ppm.

Table 1.5 summarizes key features of the main commercially available point-of-need compatible systems for detection and quantification of different mycotoxin. It is possible to see that all systems have similar performances, comply with the regulation limits and present analysis times in the 5-30 min range after sample preparation. However, most of the kits are available only for solid matrices and the extraction protocol is still quite laborious, and require steps such as grinding, centrifugation, filtering, weighting and pipetting. Furthermore, the extraction times are in general not specified. Concurrently with methods which rely on a reader for the quantification of the mycotoxin concentration, some companies have developed visible screening test able to provide a

yes/no response with respect to a threshold value. These systems are based on a competitive direct ELISA where samples are compared to a control or color chart.

Table 1.5 – A sample of commercially available solutions for point-of-need mycotoxin analysis.

Name of company (type)	Analytical procedure	Tested toxins	Detection range	Limit of detection	Testing time (minutes)	Ref.
NEOGEN (Reveal Q+)	LFIA	Aflatoxin	2-300 ppb			
		Ochratoxin	2-100 ppb	2 ppb	5	[120]
		T-2/HT-2	5-3,000 ppb			
		Zearalenone	25-1,500 ppb			
CHARM (Rosa Mycotoxin Strips)	LFIA	Aflatoxin	Up to 150 ppb	2 ppb		
		DON/vomitoxin	Up to 6 ppm	0.1 ppm		
		Fumonisin	Up to 6 ppm	0.25 ppm		
		Ochratoxin in feed	Up to 150 ppb	2 ppb	2-10	[121]
		Ochratoxin in beverages	Up to 5 ppb	0.1 ppb		
		T2/HT2	Up to 2,500 ppb	10 ppb		
ROMER LABS AgraStrip/Quant	LFIA	Zearalenone	Up to 1,500 ppb	-----		
		Aflatoxin	4-40 ppb	3 ppb		
		Zearalenone	25-1,000 ppb	20 ppb		
		Ochratoxin	2-40 ppb	1.9 ppb	15	[122]
		T-2/HT-2	37-500 ppb	29 ppb		
		DON	250-5,000 ppb	200 ppb		
NEOGEN Veratox	ELISA	Fumonisin	250-5,000 ppb	200 ppb		
		Aflatoxin	5-50 ppb	2.5 ppb		
		Zearalenone	25-500 ppb	5 ppb		
		Ochratoxin	2-25 ppb	1 ppb	10-20	[123]
		T-2/HT-2	26-250 ppb	25 ppb		
		DON	0.5-5 ppm	0.1 ppm		
		Fumonisin	1-6 ppm	0.2 ppm		

1.3.5. State-of-the-art toolbox towards an integrated point-of need device

In this section, the recent advances towards detection of mycotoxins at the point-of-need are reviewed by looking at emerging trends and the individual tools being developed for mycotoxin assay development. Along these lines, **Figure 1.8** shows a conceptual summary of a general toolbox for developing a mycotoxin-sensing assay based on recent developments and trends reported in the literature. Overall, the development of a mycotoxin sensing assay can be divided into five major components: 1) sample interface and overall assay architecture; 2) engineering of the sensing surface and 3) molecular recognition; 4) extraction and sample preparation; and 5) signal generation and transduction. As highlighted in **Figure 1.8**, only the sample interface and signal transduction modules are fundamental to fabricate a mycotoxin sensor. However, to adequately enable a point-of-need and fit-for-purpose approach, the integration of the

other three modules in the assay is often critical towards versatility, sensitivity, specificity and ease-of-use, as will be discussed ahead in this section. Each of the individual assay components shown in **Figure 1.8** are discussed below together with specific examples, as compiled in **Table 1.6**, and evaluated for potential integration in effective point-of-need mycotoxin detection strategies.

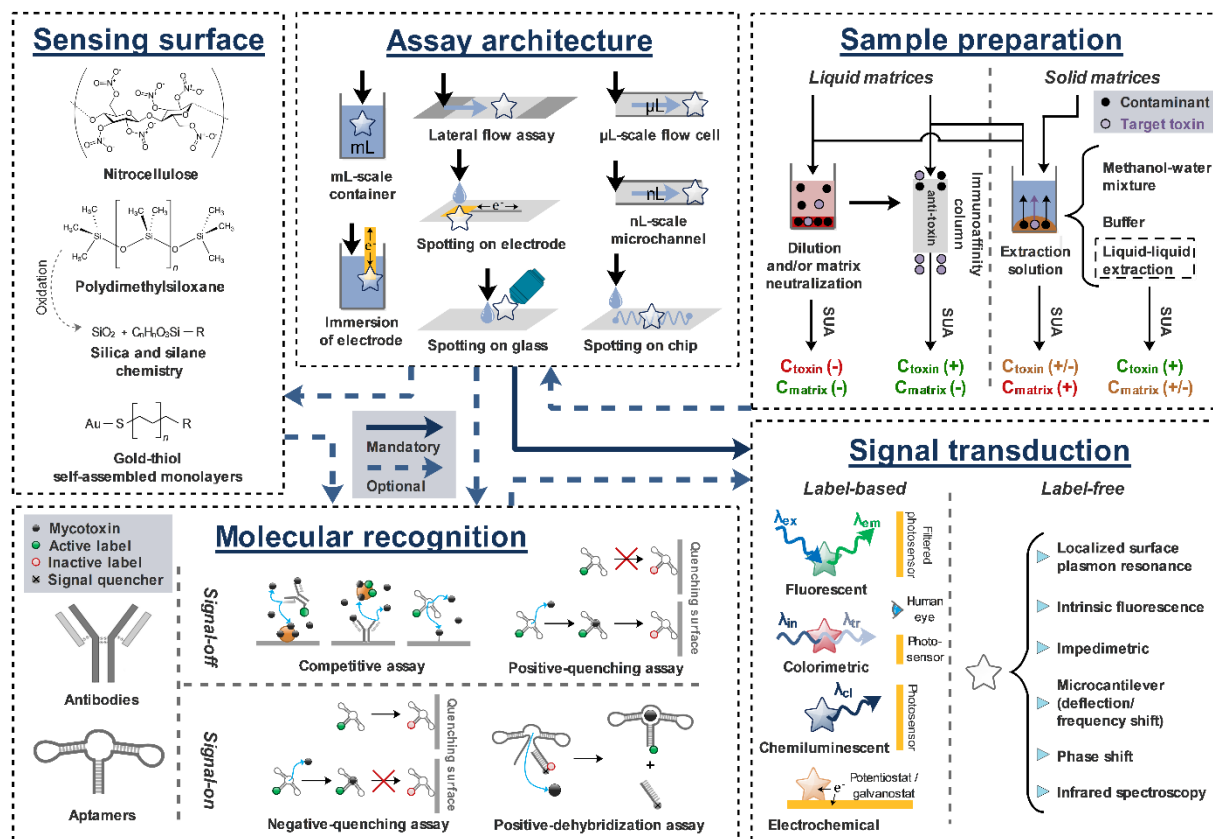


Figure 1.8 – Schematic summary of the main components and recent trends on mycotoxin analytical assay development. Dashed arrows indicate an optional sequence of assay elements, while continuous arrows indicate the fundamental elements to build a functional mycotoxin analytical assay. λ_{ex} , λ_{em} , λ_{in} , λ_{tr} and λ_{cl} refer to excitation light, emission light, incident light, transmitted light and chemiluminescent light, respectively. SUA refers to sample under analysis.

Table 1.6 – Summary of mycotoxin measurement processes published between 2013 and 2017. Key qualifiers were listed for each assay, in accordance with the schematics in **Figure 1.8**. *(1) indicates that the immobilized molecule is the molecular probe itself. S and $[M]$ refer to the output signal of the assay and mycotoxin concentration, respectively.

Assay Architecture	Solid-phase material	Molecular probe	Immobilized molecule*	Immobilization chemistry	Output signal	$\frac{\delta S}{\delta [M]}$	Signal acquisition	Analytical performance (maximum sensitivity)	Approx. assay time	Assay steps	Tested sample(s)	Sample preparation	Ref.
mL-scale container	None	Aptamer conjugated to fluorescein	None	None	Fluorescence (quenching mediated by graphene oxide)	-	Spectrofluorimeter	Quantitative (ng/mL range)	40 min	Single-step	Rice seeds	Extraction with 50% methanol	Joo <i>et al.</i> , 2017[124]
mL-scale container	None	Aptamer conjugated to fluorescein and hybridized with ssDNA-quencher	None	None	Fluorescence (quenching mediated by quencher-fluorescein proximity)	+	Spectrofluorimeter	Quantitative (ng/mL range)	30 min	Single-step	Rice cereal	Extraction with 60% methanol and dilution (5x)	Chen <i>et al.</i> , 2017[125]
mL-scale container	None	Aptamer conjugated to quantum dots (QD)	None	None	Fluorescence (quenching mediated by molybdenum disulfide nanosheets)	+	Spectrofluorimeter	Quantitative (ng/mL range)	40 min	Single-step	Red wine	Extraction with toluene	Lu <i>et al.</i> , 2017[126]
mL-scale container	None	Aptamer	None	None	Fluorescence (mediated by SYBR Gold binding before digestion with ExoI)	+	Spectrofluorimeter	Quantitative (ng/mL range)	45 min	Multi-step	Red wine and beer	Dilution (100x)	Lv <i>et al.</i> , 2017[127]
mL-scale container	None	Aptamer	None	None	Colorimetric (modulated by aggregation of gold nanoparticles (AuNPs))	+	Smartphone camera (light transmission)	Quantitative (ng/mL range)	15 min	Multi-step	Honey and milk	Dilution (100x)	Liu <i>et al.</i> , 2017[128]
mL-scale container	None	Anti-toxin IgG Fab fragment	None	None	Fluorescence (Label-free)	-	Spectrofluorimeter	Quantitative (ng/mL range)	20 min	Single-step	Grains	Extraction with 60% methanol and dilution (10x)	Li <i>et al.</i> , 2013[129]
mL-scale container	None	Molecular imprinted polymer (MIP)-QD conjugate	None	None	Phosphorescence (quenching mediated by toxin binding)	-	Spectrofluorimeter	Quantitative ($\mu\text{g/mL}$ range)	30 min	Single-step	Apple juice	Extraction with ethyl acetate, drying and resuspension in buffer	Zhang <i>et al.</i> , 2017[130]
mL-scale container	None	Luminescent metal-organic framework (MOF)	None	None	Fluorescence	-	Spectrofluorimeter	Quantitative ($\mu\text{g/mL}$ range)	<1 min	Single-step	Not tested	Not applicable	Hu <i>et al.</i> , 2015[131]
mL-scale container	None	None	None	None	Fluorescence (Intrinsic toxin fluorescence)	+	CMOS sensor + LED light + microcontroller board	Quantitative (ng/mL range)	<1 min	Single-step	Beer and wine	IAC	Hernández <i>et al.</i> , 2017[132]
mL-scale container	None	None	None	None	Fluorescence (Intrinsic toxin fluorescence)	+	Spectrofluorimeter	Quantitative (ng/mL range)	<1 min	Single-step	Red wine	Dilution (2x) with PEG 1% and NaHCO_3 5% + IAC	Arduini <i>et al.</i> , 2016[133]
Lateral flow assay	Nitrocellulose	Anti-toxin IgG conjugated to AuNPs or desert rose-AuNPs	Toxin-BSA conjugates	Physisorption	Colorimetric	-	Visual interpretation	Qualitative (ng/mL range)	10 min	Single-step	Maize flour	Extraction with 50% methanol and dilution (2x)	Di Nardo <i>et al.</i> , 2017[134]
Lateral flow assay	Nitrocellulose	Anti-toxin IgG conjugated to AuNPs or QDs	Toxin-BSA conjugates	Physisorption	Colorimetric or Fluorescence	-	Visual interpretation	Qualitative (ng/mL range)	25 min	Single-step	Wheat	Extraction with 80% methanol and dilution (8x)	Foubert <i>et al.</i> , 2017[135]

Lateral flow assay	Nitrocellulose	Anti-toxin IgG conjugated to QD beads	Toxin-BSA conjugates	Physisorption	Fluorescence	-	Optical reader	Quantitative (pg/mL range)	15 min	Single-step	Maize	Extraction with 70% methanol and dilution (60x)	Ren <i>et al.</i> , 2014[13]
Lateral flow assay	Nitrocellulose	Anti-toxin IgG	Toxin-BSA conjugates	Physisorption	Chemiluminescence (anti-rabbit-HRP mediated)	-	CCD scanner	Quantitative (ng/mL range)	24 min	Multi-step	Maize	Extraction with PBS buffer and heat inactivation at 100 °C	Zangheri <i>et al.</i> , 2015[136]
μL-scale flow cell	Carboxylated magnetic beads	Anti-toxin IgG	(1)	Covalent (EDC-NHS chemistry)	Photoelectrochemical (Toxin-BSA-glucose oxidase conjugate mediated)	+	3-electrode electrochemical cell	Quantitative (ng/mL range)	75 min	Multi-step	Peanuts	Extraction with 80% methanol and dilution (4x)	Lin <i>et al.</i> , 2017[137]
μL-scale flow cell	Glass	Anti-toxin IgG	ovalbumin-toxin conjugate	Electrostatic (APTES silanization)	Phase shift (Label-free)	+	Spectrometer coupled to an array of Mach-Zehnder interferometers	Quantitative (ng/mL range)	120 min	Multi-step	Beer	Dilution (8x)	Pagkali <i>et al.</i> , 2017[138]
μL-scale flow cell	Gold with mercaptoundecanoic acid (MUDA) self-assembled monolayer (SAM)	Anti-toxin IgG	(1)	Affinity (protein A)	Amperometric (toxin-HRP mediated)	-	Electrochemical analyzer	Quantitative (ng/mL range)	20 min	Multi-step	Wheat	Extraction with water and filtration (0.44 μm pore)	Olcer <i>et al.</i> , 2014[57]
μL-scale flow cell	Gold with MUDA SAM	Anti-toxin IgG	(1)	Affinity (protein A)	Amperometric (toxin-HRP mediated)	-	Portable electrochemical analyzer	Quantitative (ng/mL range)	20 min	Multi-step	Dry fig and wheat	Extraction with 70% methanol, dilution (3x) and IAC	Uludag <i>et al.</i> , 2016[139]
μL-scale flow cell	Gold	Thiolated anti-toxin IgG	(1)	Covalent (Thiol-Au chemistry)	Microcantilever mechanical deflection	+	Laser and position sensitive detector	Quantitative (ng/mL range)	150 min	Single-step	Peanuts	Extraction with PBS buffer	Zhou <i>et al.</i> , 2016[140]
μL-scale flow cell	Silica	Aptamer conjugated to Cy5.5	OTA	Covalent (APTES and EDC-NHS chemistry)	Fluorescence	-	Photodiode, band-pass filter and pulsed laser	Quantitative (ng/mL range)	2 min	Single-step	Wheat	Not disclosed	Liu <i>et al.</i> , 2015[141]
nl-scale microchannel	PDMS	Anti-toxin IgG conjugated to HRP	Toxin-BSA conjugates	Physisorption	Chemiluminescence (Luminol mediated)	-	c-Si photodiode + microcontroller board	Quantitative (ng/mL range)	5 min	Multi-step	Red wine	PEG-salt aqueous two-phase extraction	Soares <i>et al.</i> , 2016[21]
nl-scale microchannel	PDMS	Anti-toxin IgG	Toxin-BSA conjugates	Physisorption	Fluorescence (anti-mouse-FITC mediated)	-	Fluorescence microscope	Quantitative (ng/mL range)	30 min	Multi-step	Red and white wine	Integrated PEG-salt aqueous two-phase extraction	Soares <i>et al.</i> , 2014[24]
nl-scale microchannel	PDMS-polycarbonate	Anti-toxin IgG	Toxin-BSA conjugates	Physisorption	Colorimetry (Silver staining and Streptavidin-nanogold mediated)	-	Smartphone	Quantitative (ng/mL range)	60 min	Multi-step	Corn samples	Extraction with 70% methanol + 4% NaCl and dilution (2x)	Li <i>et al.</i> , 2017[142]
nl-scale microchannel	Agarose	Anti-toxin IgG	(1)	Affinity (protein A)	Fluorescence (toxin-BSA-Alexa 430 mediated)	-	a-Si:H photodiode coupled to an integrated a-SiC:H absorption filter	Qualitative (ng/mL range)	1 min	Single-step	Not tested	Not applicable	Soares <i>et al.</i> , 2016[143]
nl-scale microchannel	Glass-PHEMA-streptavidin	Aptamer	(1)	Covalent (EDC-NHS chemistry)	Chemiluminescence (aptamer-biotin and streptavidin-HRP mediated)	+	Array of a-Si:H photosensors	Quantitative (μg/mL range)	40 min	Multi-step	Beer	Extraction with ethyl acetate, drying and resuspension in buffer	Costantini <i>et al.</i> , 2016[144]

Immersion of electrode	Carbon nanotube on electrodes-Au/PtNPs	Anti-toxin IgG	(1)	Affinity (protein A)	Amperometric (Label-free)	-	Electrochemical workstation	Quantitative (pg/mL range)	20 min	Single-step	Corn	Extraction with 70% methanol and dilution (5x)	Liu <i>et al.</i> , 2017[145]
Immersion of electrode	Gold coated with AuNPs	Anti-toxin IgG	Toxin-BSA conjugates	Physisorption	Impedimetric (Label-free)	-	Electrochemical workstation	Quantitative (ng/mL range)	50 min	Single-step	Rice, corn and ground nuts	Extraction with 80% methanol and dilution (5x)	Chen <i>et al.</i> , 2015[146]
Spotting on electrode	Gold	Aptamer	Thiolated ssDNA	Hybridization	Amperometric (ssDNA-carbon nanotubes and methylene blue)	-	Portable potentiostat	Quantitative (ng/mL range)	45 min	Multi-step	Grape juice and rat serum	None	Abnous <i>et al.</i> , 2017[147]
Spotting on electrode	Gold	Aptamer	Thiolated ssDNA	Hybridization	Amperometric (alkaline phosphatase-Streptavidin conjugate mediated)	+	Electrochemical workstation	Quantitative (pg/mL range)	>180 min	Multi-step	Corn	Extraction with 80% methanol and dilution (5x) + IAC	Qing <i>et al.</i> , 2017[148]
Spotting on electrode	Thionine film electrodeposited on printed electrodes plus nanoparticles	Aptamer-NH ₂	(1)	Electrostatic	Impedimetric (Label-free)	+	Potentiostat/ Galvanostat	Quantitative (pg/mL range)	90 min	Single-step	White wine	None	Rivas <i>et al.</i> , 2015[149]
Spotting on electrode	AuNPs electrodeposited on printed electrodes	Aptamer-SH	(1)	Covalent (Thiol-Au chemistry)	Impedimetric (Label-free)	+	Electrochemical workstation	Quantitative (ng/mL range)	30 min	Single-step	Corn	Extraction with 80% methanol and dilution (ratio not disclosed)	Ren <i>et al.</i> , 2017[150]
Spotting on electrode	Glassy carbon electrode (GCE) coated with chitosan	Anti-toxin IgG conjugated to AuPtNPs	toxin-BSA conjugates	Glutaraldehyde cross-linking	Amperometric (p-nitrophenol and NaBH ₄ mediated)	-	Electrochemical workstation	Quantitative (pg/mL range)	60 min	Multi-step	Red wine	None or not disclosed	Zhang <i>et al.</i> , 2017[151]
Spotting on electrode	GCE-rutile TiO ₂ mesocrystals-polydopamine	Anti-toxin IgG	(1)	Adsorption	Amperometric (Anti-toxin IgG-ordered mesoporous cobalt oxide mediated)	-	Electrochemical workstation	Quantitative (pg/mL range)	>60 min	Multi-step	Peanuts	Extraction with 80% methanol + 4% NaCl and dilution (2.5x)	Liu <i>et al.</i> , 2017[152]
Spotting on chip	Polyacrylamide-ssDNA conjugate	Aptamer	(1)	Hybridization	Colorimetric (modulated by PtNPs and H ₂ O ₂)	+	Visual interpretation	Quantitative (ng/mL range)	90 min	Multi-step	Beer	IAC	Ma <i>et al.</i> , 2016[153]
Spotting on chip	PDMS	Anti-toxin IgG	Toxin-BSA conjugates	Physisorption	Colorimetry (TMB blotting solution mediated)	-	Smartphone	Quantitative (ng/mL range)	10 min	Multi-step	Corn-based feed	PEG-salt aqueous two-phase extraction	Machado <i>et al.</i> , 2018[154]
Spotting on glass	Gold nanorods immobilized on thiol- SiO ₂	Aptamer-SH	(1)	Covalent (Thiol-Au chemistry)	Localized surface plasmon resonance (LSPR, Label-free)	+	Spectrophotometer	Quantitative (ng/mL range)	20 min	Single-step	Corn	Extraction with 30% methanol and 2% NaCl	Park <i>et al.</i> , 2014[155]
Spotting on glass	Silica microspheres (photonic crystals)	Anti-toxin IgG conjugated to FITC	Toxin-BSA conjugates	Covalent (GOPTES silanization)	Fluorescence	-	Array scanner or fluorescence microscope	Quantitative (pg/mL range)	60 min	Multi-step	Corn, wheat, peanut, rice and soybean	Extraction with methanol, drying and resuspension in buffer	Deng <i>et al.</i> , 2013[45]
Spotting on glass	GaAs waveguide	None	None	None	Infrared spectroscopy (Intrinsic mid IR-spectrum of toxins)	+	Thermoelectrically cooled photoconductive mercury cadmium telluride detector	Qualitative (ng/g range)	2-3 min	Single-step	Maize, wheat and peanuts	Extraction with methanol	Sieger <i>et al.</i> , 2017[156]

Sampling interface and overall architecture

The majority of assay architectures being developed for mycotoxin detection in recent years (2013-2017) can be divided into eight main categories: (1) assays performed in mL-scale containers, such as a cuvette or a plastic well, typically requiring volumes above 100 μL ; (2) lateral flow assays, comprising a porous hydrophilic material such as nitrocellulose, which pumps the sample under analysis (SUA) via capillary forces through discrete regions containing suspended and immobilized molecules; (3) μL -scale and (4) nL-scale flow cells comprising confined channels made of various materials with dimensions ranging from mm down to μm (in the latter case, designated as microfluidics), through which the liquids are flowed; electrochemical assays involving (5) the spotting of the SUA on an electrode or (6) immersion of bulk or thin-film electrodes in the SUA; (7) spotting of the SUA on a surface such as a glass slide, followed by imaging using microscopy or a scanner and; (8) spotting of the sample on a standalone fluidic chip containing a channel network, without coupling an external pumping system. These different architectures are the major qualifier of the assay and define most of the required components for mycotoxin analysis. Therefore, the assay architecture was used to classify recently published detection strategies, listed in **Table 1.6**.

For point-of-need detection of mycotoxins, all of these assay architectures could, conceptually, be engineered to be portable and user friendly, however, most advances to this end have been achieved for the ubiquitous lateral-flow immunoassays [157]. This can be justified by the relative simplicity, versatility and ease of multiplexing [135, 136, 158, 159] associated with these devices, coupled to the visual signal transduction [160], easily integrated in a standalone device. While still not being fully point-of-need compatible, several lateral flow assays for mycotoxin detection are already being commercialized.

Other assay architectures are also being successfully developed towards improved simplicity. For example, ultra-rapid and single-step assays using mL-scale containers have already been performed based on intrinsic mycotoxin fluorescence, measured by coupling integrated and portable imaging setups [132], although this method is limited to mycotoxins that exhibit auto-fluorescence. Assays using flow cells are also being improved by reducing the dimensions of the fluidic path down to a few tens to hundreds of μm [42, 142]. An increasing number of mycotoxin assays based on microfluidics have been reported in the literature, following the growing trend of microfluidics observed for biosensing applications in the biomedical arena [3, 161-163]. The pronounced scale down to the μm -range is particularly useful for 3 important reasons: (1) lower volumes of

solution required to make the analysis; (2) faster assays due to reduced diffusion times and possibility of using very high linear velocities, considerably minimizing mass transfer limitations [9]; and (3) possibility of integrating complex sequential multi-module fluidic networks in a very small foot print towards a sample-to-answer analysis [24, 46, 164, 165]. Electrochemical assays are also being simplified by integrating the required potentiostat/ galvanostat electronics in compact devices [139, 147], similar to standard glucose meters. Finally, mycotoxin assays are also being developed requiring only a droplet of liquid, placed in a standalone fluidic chip, autonomously driven by capillarity [154] or a simple manual operation [153]. This is advantageous in particular to avoid the use of external liquid pumping mechanisms, while still taking advantage of versatile and precise fluidic manipulations [34].

Surface engineering and molecular recognition

To improve the selectivity and sensitivity of the assay, a specific mycotoxin recognition probe is immobilized on a solid surface. The more typically used solid phase materials and biomolecules to perform the specific recognition of mycotoxins (i.e. IgG antibodies and aptamers) are represented in **Figure 1.8**. However, it is important to highlight that other emerging non-biological recognition strategies are also being developed, as discussed ahead in this section. To achieve an adequate molecular surface density and a robust and reproducible probe immobilization, it is necessary to optimize the appropriate immobilization method depending on the material and the type of molecule being used as probe. The most typical surface materials being used for mycotoxin measurement processes are (1) nitrocellulose, the workhorse of lateral-flow-immunoassays; (2) polydimethylsiloxane (PDMS), typically used for the fast-prototyping of microfluidic devices and easily coupled, together with other silicon oxides (i.e. glass), with versatile silane chemistries and; (3) gold thin-films, compatible with electrochemical assays and providing highly selective and versatile immobilizations via thiol (sulfhydryl) chemistry. On the other hand, the immobilization procedure can generally be performed reversibly or irreversibly by (1) physisorption, (2) electrostatic interactions or (3) covalent bonding, either directly or intermediated by a (4) specific affinity interaction. Recently, a very extensive and detailed review on the subject of surface functionalization was compiled by Dohyun Kim and Amy E. Herr [166].

Using electrostatic interactions and physisorption, in particular as molecular immobilization procedures, are much simpler methods compared to the generation of

covalent bonds, since the modification/activation of the surface and/or the target molecule are typically not required [21]. However, this type of adsorption, used ubiquitously in standard well plate ELISAs to immobilize, for example, IgG and BSA-conjugated antigens, tends to be weaker and prone to dissociation as it is generally sensitive to changes in ionic force or pH in solution and also to the high shear stress observed in microchannels. Nevertheless, it has been reported that on some hydrophobic materials such as PDMS, polymeric materials such as nitrocellulose membranes and even glass, some proteins such as BSA are able to bind very strongly to the surface, even under harsh conditions of shear stress, viscosity and the presence of small titers of organic solvents [166]. Therefore, physisorption is a particularly relevant strategy in signal-off competitive assay designs where a mycotoxin-BSA conjugate is immobilized on the surface, and this is validated by the large number of publications using this approach spanning most assay architectures (**Table 1.6**). Nevertheless, an important caveat is that lateral diffusion of BSA on the surface should be taken into account when relatively long assay times and precise spatial resolution are required [167]. On the other hand, using physisorption to immobilize antibodies on a surface tends to be more cumbersome, particularly due to the lack of orientation and a reported tendency for adsorption via the Fab regions, responsible for antigen recognition, particularly on hydrophobic surfaces [168, 169]. The same applies to aptamers, for which an immobilization based on electrostatic and physisorption effects is typically inefficient due to changes in their functional tridimensional structure [170] and intrinsic high negative charge (low hydrophobicity), resulting in relatively poor adsorption to hydrophobic surfaces [171]. Overall, despite the relative complexity of covalent bonding protocols, these tend to be preferred in integrated point-of-need devices due to enhanced stability over time, robustness to regeneration protocols, improved tridimensional conformation, decreased stereochemical hindrance and improved ruggedness. Furthermore, the wide variety of commercially available silane (i.e. APTES, GOPTES) and thiol conjugates (i.e. MUDA) to mediate the direct covalent coupling via i.e. EDC-NHS chemistry, or affinity mediated coupling (protein A, protein G, biotin-streptavidin), greatly facilitates research and optimization of novel biosensing strategies.

Regarding the molecular recognition, it is important to highlight beforehand that some emerging single-step strategies are based on responsive materials working as standalone molecular recognition agents, combining the sensing surface with molecular recognition. Examples of this are molecular imprinted polymers conjugated with quantum dots, resulting in fluorescence quenching upon binding of a specific mycotoxin [130] and

photoluminescent metal organic frameworks (MOF) providing a similar effect [131]. However, more commonly, the molecular recognition is achieved using IgG antibodies or its fragments (i.e. scFv) [172] in competitive signal-off assays, or aptamers both in signal-off and innovative signal-on approaches, the latter highlighting the versatility of these molecules for developing novel biosensing strategies. Many examples of these are given in **Table 1.6**. These novel strategies, as schematically shown in **Figure 1.8**, include simple signal-off and signal-on single step quenching assays in mL-containers upon binding of the aptamer to the specific target. Alternatively, the binding event can also induce the release of a quenching molecule blocking the fluorescence of a fluorophore functionalized on the aptamer. As an extension to these simple and single-step modes of detection, the binding of the aptamer to the target has also been engineered to initiate complex chains of events aimed at amplifying the signal (e.g. rolling circle amplification and hybridization chain reactions), providing ultra-sensitive assays in order of pg/mL [148, 173, 174]. However, this arguably advantageous improvement in limit-of-detection comes at the cost of lengthier, higher complexity and multi-step assays, compromising their suitability for point-of-need applications.

Extraction and sample preparation

To perform an assay to detect mycotoxins in a real sample, sample preparation refers to the processing of solid or liquid samples after the appropriate sampling procedures in the field. The schematics in **Figure 1.8** list the major sample preparation steps typically followed in the literature, starting either from liquid or solid samples.

Considering liquid samples (e.g. wines and beer), the sample preparation procedure comprises either dilution and/or matrix neutralization, typically by adding a polymer with high affinity to interferents [19, 133, 160] or by flowing the sample through an immunoaffinity column [132, 139, 148] which selectively binds the mycotoxin, thus providing a simultaneous concentration and matrix neutralization effect after elution. In cases where the interferents are observed to reduce the performance of the immunoaffinity column, both these procedures can also be performed in series.

In the case of solid samples (e.g. corn, wheat and spices), the first step is to effectively solubilize the mycotoxin dispersed in the solid matrix. Then, considering the typically limited selectivity of the extraction procedure against possible interferents and/or requirement of relatively high concentrations of organic solvents (i.e. methanol or acetonitrile in the case of highly hydrophobic mycotoxins such as AFB1), the extracted

sample often follows the same sample processing procedure as the liquid samples. There are however some emerging methodologies aiming at improving and simplifying the sample processing procedure focusing on (1) using alternative non-organic solvents to effectively and selectively solubilize the mycotoxins such as surfactant [175] or polymer additives [176], ionic liquids [177] or supramolecular complexes with selectivity to small molecules [178]; (2) using liquid-liquid separations to simultaneously extract and concentrate the target mycotoxin comprising either low concentrations of organic solvents (dispersive liquid-liquid microextraction, DLLME) [179] or fully organic solvent-free extractions using aqueous two-phase systems (ATPS) [19, 180].

Overall, each sample preparation methodology provides a variable concentration of mycotoxins and interferents in the processed SUA, which needs to be tailored to the subsequent mycotoxin measurement process to provide a fit-for-purpose quantification. According to **Table 1.6**, the clear majority of sample processing procedures comprise the extraction of the mycotoxins from solid samples using an aqueous solution of methanol at concentrations ranging from 50-80%, followed by dilution to reduce the methanol concentration down to 10-20%, sometimes with the addition of 2-4% NaCl. This approach seems to be generally compatible with all assay architectures using either antibodies or aptamers as molecular recognition probes. Some noteworthy alternative approaches include (1) the extraction procedure being performed with water or a buffer solution for the analysis of AFB1 [140], FB [136] and DON [57], an approach also increasingly implemented in commercial lateral-flow devices for AFB1 and FB for example [181, 182]; (2) the extraction being performed with aqueous two-phase systems, providing a simultaneous concentration effect either in a mL-scale container for solid samples [180] or integrated in-line with a nL-scale microchannel for liquid samples [24]; and (3) the analytical method not requiring any sample preparation procedure in specific electrochemical assays dealing with liquid samples including grape juice [147], white wine [149] and red wine [151].

In conclusion, to develop a point-of-need detection system, it is extremely important to always consider the fit-for-purpose sample preparation method for a certain required sensitivity, while guaranteeing the ruggedness of the entire methodology. Therefore, efforts must be invested in simplifying the sample preparation process in terms of handling, number of steps and total required time, optimally involving some degree of automation and minimizing the use of toxic and/or non-environmentally friendly reagents in the process.

Signal generation and transduction

According to the schematics in **Figure 1.8**, the signal transduction mechanisms currently under investigation for integration in mycotoxin measurement processes follow the same trend as the biosensors community in general. These can be divided into two main categories, label-based and label-free. Within label-based systems, the signal transduction is mediated mostly by optically (fluorescence, colorimetry and chemiluminescence) and electrochemically active labels. In this case, the signal is transduced to an electrical signal often via photosensors in the case of optically active labels or an appropriate potentiostat/ galvanostat circuitry in the case of electrochemically active labels. Alternatively, colorimetric signals are also widely used to allow a simple visual interpretation of the signal in qualitative assays, particularly in lateral flow immunoassays. On the other hand, label free methods are mostly based on optical, electrical and mechanical shifts which are specific either to the presence of the target toxin in solution (e.g. intrinsic fluorescence) or induced upon the interaction of the target toxin with a specific surface and/or probe.

From the reported sensitivities found in the literature, it is clear from **Table 1.6** that the majority of ultra-low limits of detection in the range of pg/mL are achieved using electrochemical methods, both label-based (amperometric) and label-free (impedimetric), utilizing either antibodies or aptamers as molecular probes. This implies that these high sensitivities arise from the transduction method itself rather than intrinsic chemical properties of the probe (i.e. dissociation constant) or the label. Exceptions to this are optical methods coupled to an amplification mechanism such as using quantum dot impregnated beads [183] or the enhancement of fluorescence or chemiluminescence by photonic crystals [184, 185], also providing detection limits down to the pg/mL range. These extremely low limits of detection, despite being orders of magnitude below current regulatory limits for mycotoxins in foods and feeds, not necessary for most point-of-need applications, can however be particularly useful in simplifying sample preparation by simply allowing the use of extreme dilutions.

While most of the recent literature has been focused on the sensing mechanism itself (both label-based and label-free), there has been fewer reports on the simplification and integration of the electronics used to address the sensor. An exception to this are colorimetric lateral flow assays. Therefore, based on **Table 1.6**, one can observe that the signal acquisition is mostly performed using bulky lab equipment, although it is reasonable to assume that most if not all would be amenable to integration in a portable

platform, particularly in the case of optical and electrochemical signals. Nevertheless, some achievements can be highlighted in this context, in particular (1) the use of a smartphone camera to measure light transmittance in a mL-scale container [128]; (2) integration of a CMOS sensor and an LED excitation source for fluorescence measurements in a mL-scale container, coupled to a microcontroller board for subsequent processing using the appropriate software[132]; (3) integrated optical readers and CCD scanners to measure quantitatively colorimetric, fluorescence and chemiluminescence signals in lateral flow assays [13, 136, 160]; (4) addressing of the sensing area with portable electrochemical analyzers [139, 147]; (5) integration of mm sized c-Si photodiodes for optical signal acquisition, coupled to a microcontroller board [21] and (6) acquisition of colorimetric signals using a standard smartphone camera either with [142] or without [154] a magnification setup for subsequent quantification.

As with sample preparation, the signal transduction method and electronic apparatus must be rugged and fit-for-purpose to achieve the required sensitivities, while maximizing portability and simplicity and minimizing costs. Along these lines, it can be assumed that for label-based methods, signal-off strategies tend to facilitate these objectives since the maximum sensitivity is derived from variations in the maximum signal of high label concentrations, rather than having to detect very weak signals above a noise threshold. The latter is also the case for label-free methodologies, regardless of whether the sensing mechanism is based on signal-off or signal-on strategies, since the detection is based on a small positive or negative shift in an initial baseline. On the other hand, while still in its infancy for mycotoxin detection, highly sensitive and versatile impedimetric label free methods, in particular, are relatively simple in terms of required apparatus and amenable to integration in a portable measurement setup [186-188]. Thus, these have recently become very promising for portable biosensing in general [189], possibly leading the label-free arena in terms of technology readiness for point-of-need mycotoxin biosensing applications.

1.4. Aqueous two-phase systems: a simple and biocompatible approach to isolate target biomolecules

1.4.1. A brief introduction to aqueous two-phase systems

Aqueous two-phase extraction (ATPE) is a liquid-liquid (L-L) separation technique based on the formation of two immiscible water-rich phases above certain critical concentrations of two mutually incompatible solutes, henceforth referred to as aqueous two-phase system (ATPS). There are many different types of solutes that can generate ATPSs of which the most widely explored in the literature are polymer-salt systems, namely polyethylene glycol (PEG)-phosphate and polymer-polymer systems, such as PEG-dextran. The phase separation behavior of ATPSs can be described by a phase diagram, as schematized in **Figure 1.9-A**, comprising a binodal curve (B) and tie lines (T) with a specific tie line length value (TLL, with units of w/w). The accurate determination of this diagram and a fit-for-purpose determination of the tie-lines are of critical importance to investigate a particular system. The binodal curve defines the threshold below which the concentration of the solutes is not sufficient to form an ATPS, while the tie-lines connect pairs of points in the binodal curve representing the equilibrium compositions of the bottom and top phases of each system with the total compositions following the points in the line. This occurs because specific phase compositions are energetically or entropically more favorable than all the others and thus along the same tie-line only the volume ratio between these two immiscible phases changes [190]. The longer the tie-line, the more different the phase compositions are between each other in terms of physical (e.g. viscosity and surface tension) and chemical (e.g. hydrophobicity, ionic strength and overall charge) properties. It is also important to highlight that the phase diagram is also sensitive to other intrinsic and extrinsic factors such as the temperature, the pH, the molecular weights of the polymers used and the presence of additives in solution other than the ATPS forming solutes [191].

Considering the general properties of ATPSs described above, these systems have been under investigation for more than three decades towards the selective partition of target biomolecules contained in complex mixtures. The strong interest in this type of L-L extraction arises from the large water content of each phase, in contrast to the generally bioincompatible water-organic L-L separations. This selective partition takes advantage of the wide range of parameters that can be manipulated in order to confer a selective affinity of the target molecule to one phase with the impurities partitioning to

the other phase [192]. The affinity to one of the phases is evaluated by the partition coefficient (K), calculated as the quotient between the concentration of the solute in the top and bottom phases. Since the preferential partition arises from chemical differences between the two phases, it can be generally assumed that the K values tend to become more extreme, meaning higher or lower, as the TLL of the system increases. These extreme TLLs may have the drawback of promoting precipitation, in conditions where the target molecule reaches a solubility limit in the target phase, resulting in a less pronounced K , meaning closer to 1.

With regards to selectivity, much effort has been put into modelling and predicting the K values based either on the properties of each phase [193-196] or on the chemical properties of the target molecules themselves such as size, charge, molecular weight and concentration in solution [192, 197, 198]. In particular, Zaslavsky *et al.* have described the partition of molecules using the Kamlet and Taft parameters of hydrogen bond acidity, basicity and dipolarity/polarizability [199]. However, in many cases, the optimization of these systems still relies on empirical optimization processes based on design of experiments [200] and/or high-throughput platforms [201, 202]. Upon optimization ATPE can confer a remarkable selectivity even for very similar peptides, small biomolecules and proteins, as recently reviewed by Zaslavsky *et al* [203]. In addition to the potential of these systems for purification, a concentration effect is also noteworthy, as simulated in **Figure 1.9-B**, assuming no case-specific precipitation and/or phase saturation effects. Here it is shown that very pronounced concentration factors of two to three orders of magnitude can be achieved by reducing the volume of the phase to which the target analyte has more affinity. Regarding this property it is important to highlight that for a given K , it is only advantageous to increase the volume ratio until a certain point, above which the concentration factor reaches a plateau.

Taking advantage both of its experimental simplicity and its high selectivity potential, the vast majority of the ATPS-related literature is currently directed towards separation performed at the micro-tube (>1 mL) scale and above, either in batch or, more recently, in continuous setups [204-207]. There has been however a relatively recent trend to combine these systems with microfluidic technologies. Indeed, studies of ATPSs at nanoliter-scale are further extending the range of applications of these systems by taking advantage of rapid diffusion times, increased degree of control of individual liquid streams and droplets and the integration of multi-dimensional separation modes.

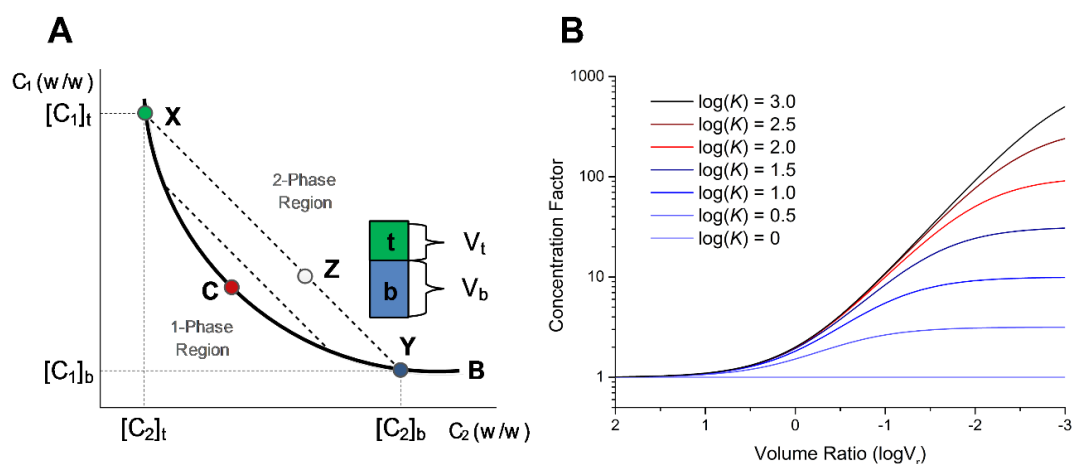


Figure 1.9 – **A-** Schematics of a typical phase diagram for an ATPS composed of two phase forming compounds C_1 and C_2 , comprising the binodal curve “B” which separates system compositions which form one single phase or two immiscible phases and tie-lines (XY). The abbreviations t and b refer to the top and bottom phases, respectively All points located on the tie line XY, including “Z”, have top and bottom phase compositions of X and Y, respectively. The point “Z”, since it is closer to Y, will provide a smaller top phase relative to the total volume of the system according to the mass balance described as **Equation 1.8**, where V is the volume and ρ is the density. The point “C” refers to the critical point. **B-** Theoretical simulation of the effect of K over the concentration factor of a biomolecule for increasing V_r values. It is assumed here that this biomolecule has affinity to the top phase.

$$\frac{\overline{AY}}{\overline{AX}} = \frac{V_t \rho_t}{V_b \rho_b} \quad (1.8)$$

1.4.2. Main applications and separation performance in batch mode

Purification of biomolecules and particulates from cell fermentation broths

The concept of using ATPSs to separate and purify biological compounds from cell fermentation broths has been under investigation for three decades since it was introduced by Albertsson [191]. With the combined purpose of simplifying the downstream processing after fermentation, there are three main approaches (A1 to A3) with an increasing degree of complexity to perform the aqueous-two-phase extraction (ATPE) of the target molecule: A1 - ATPE of the target product from pre-purified solutions or cell culture supernatants after centrifugation and/or filtration; A2 - ATPE of the target product from the raw broth containing suspended cells and other particulates; and A3 - continuous extraction of the target product by performing the fermentation directly on an ATPS, known as extractive fermentation. The first approach is the most widely reported since it provides a simpler and more general means of optimizing the partition behavior and selectivity of the system towards a certain compound of interest. However, considering the differences in densities between each phase and the adjustable liquid-liquid surface tensions obtained with different biphasic systems, some ATPSs have

shown great potential for the primary purification of fermentation broths, i.e., the ability to process a cell suspension directly without any prior processing. These systems are thus able to simultaneously remove cells and other particulates without resorting to centrifugation, which is a highly desired approach due to the high costs and low scalability of industrial centrifugation processes. Finally, if the ATPS is compatible with cell proliferation and biosynthesis, the potential of performing an extractive fermentation is also very attractive since this process would allow not only a combination of production with primary downstream processing, but also the reduction of both product inhibition and product degradation and the easy recycling of the cell rich phase for further bioconversions. A summary of relevant purification results obtained using approaches A1 to A3, explored by several research groups, is presented in **Table 1.7**.

Considering the target compounds alone, ATPE performed at mL-scale has been tested, with various levels of success, for the partition of virtually all types of biological molecules and particles including small organic compounds such as metabolites and antibiotics [19, 208], small (≈ 10 kDa) to large (≈ 150 kDa) size proteins, plasmids [209], large macromolecular complexes such as virus-like particles [210] and also animal cells [211]. The most explored types of system in recent years are the classic polymer-salt (P-S) and polymer-polymer (P-P), ionic-liquid containing systems (either used as phase forming components or adjuvants) (IL-X) and systems formed by responsive-polymer systems (RP). **Table 1.7** highlights the versatility and potential selectivity of these ATPS systems. P-S systems, particularly PEG-salt, have been overall the most explored due to the large and adjustable hydrophilicity (type of salt and polymer), charge difference (type of salt, pH, TLL), salting in- or out properties (type of anion/cation) and size exclusion degree (molecular weight of polymer), which together with the addition of neutral salts allow the selective and pronounced partition of a wide range of molecules either to the bottom or to the top phase. On the other hand, this large number of variables also serves to highlight the challenge of empirically optimizing a given P-S system for a particular target, thus justifying a demand for good modelling and high-throughput screening approaches. Within the P-S class, the purification of monoclonal antibodies from Chinese hamster ovary (CHO) and hybridoma cell supernatants have revealed remarkable achievements with $>70\%$ HCP removal and $>75\%$ high-performance liquid chromatography (HPLC) purities being achieved with yields above 95% in a single step [212]. Moreover, further improvements of up to 99% protein recovery and 97% total impurities removal from a CHO cell supernatant could be achieved using a continuous

process performed in a countercurrent mixer-settler battery [205]. P-S systems also proved to be compatible with type 2 separations for the purification of antibiotics [213] and virus-like-particles [214] directly from feedstocks containing whole cells or cell debris, respectively, where the full separation of whole cells was achieved with 99.6% DNA depletion. These systems also proved to have a high potential towards selectivity as demonstrated using similar molecules such as a mixture of *P. sapidus* and *T. versicolor* laccases [215] and pDNA plus mRNA and tRNA [202]. Regarding P-P systems, the most frequently employed polymers are PEG and dextran, in which the latter can be replaced by less expensive polysaccharides without a significant loss in the intrinsic properties of the system [216, 217]. Unlike P-S systems, the driving forces for partition in P-P systems are much smaller, particularly for molecules with low molecular weights [192]. Therefore, to confer more extreme K and better selectivity, it is possible to modify the polymers with molecular tags [218] or replace dextran by a polyelectrolyte such as polyacrylate [219, 220], providing an increased electrostatic contrast between the immiscible phases. Using polyelectrolytes, it is already possible to provide a K of 9.15 for a small molecule such as clavulanic acid, which partitions preferably to the less negatively charged top PEG-rich phase [221]. Despite the low selectivity of plain PEG-dextran systems, Chien *et al.* demonstrated a type 3 application for these systems using a very high volume ratio in which the cells were contained in a small dextran-rich bottom phase while extracellular lipase was continuously collected in the PEG-rich top phase [222]. Another focus of intense research are ATPE methodologies based on ionic liquids (ILs), either used as phase forming compounds or adjuvants. Similarly to A-S, IL-X systems using ILs as phase forming compounds or adjuvants have been widely used to extract small molecules from complex matrices [223]. Besides the advantageous hydrotropic properties of this class of solvents [224], they have also shown a high selectivity potential [225, 226]. However, the use of these systems for the separation of proteins and other large biomolecules is scarcely reported due to problems of low stability and precipitation [227]. Finally, responsive polymers, used either alone [228] or as a phase forming compound together with other polymers [229] or salts [230], confer a unique property compared to other ATPSs, which is the inverse thermal solubility of the polymer. This phenomenon allows the separation of the responsive polymer from the solution into a highly polymer-enriched aqueous phase above a critical cloud temperature (T_c). Polymers such as ethylene oxide-propylene oxide co-polymers (EOPO) and those formed using N-isopropylacrylamide (NIPAM) have low T_c values in the range of

20-40 °C [231, 232] which are compatible with biotechnological applications. Like P-S systems, RP systems can also potentially provide good selectivity with purification factors >13 reported for CGTase and lipase either as type 2 or type 3 extraction and are easily amenable to polymer recycling [233]. Given the potential of these systems for primary clarification and extractive fermentation, several patents have been filed by GE Healthcare for applications of thermoresponsive polymers in the downstream processing of monoclonal antibodies (MAbs), viral particles and enzymes [234, 235].

Table 1.7 – Summary of response parameters for various types of ATPE aimed at the purification of a wide range of biomolecules. The acronyms P-S, P-P, IL-X and RP refer to systems composed of polymers and salts, two polymers, ILs and temperature-responsive polymers, respectively.

	System	Additive	Target	Source matrix	K	Y (%)	Purity	Ref.
P-S	17.2% PEG 2000 6% Phosphate pH 6	None	MAB	CHO Cell culture supernatant (A1)	0.009	95.5	Purification factor of 3.3	[236]
	10% PEG 6000, 20% Phosphate pH 6	None	Retamycin	<i>S. olindensis</i> broth (A2)	8.2	91.3	Full separation from whole cells	[213]
	22.06% PEG 400, 6.8% Phosphate pH 8.5	7.5% NaCl	Virus-like-particles	Crude Sf9 cell lysate (A2)	Affinity to top PEG-rich phase	102	16.8% HPLC purity and 99.6 DNA depletion	[214]
	8% PEG 3350, 8% Citrate pH 6	15% NaCl 5% NaCl for back extraction	MAB	Hybridoma cell culture supernatant (A1)	>5 with 15% NaCl and <0.2 without NaCl	99	76% HPLC purity and an IgG/protein ratio of 0.96	[212]
	17.7% PEG 818 (avg.), 10.3% Phosphate pH 7.5	None	Plasmid DNA	Mixture of pDNA from <i>E.coli</i> with mRNA and tRNA from yeast (A1)	< 0.01	97.4	13.6% RNA yield in bottom phase	[202]
P-P	9.6% PEG 8000, 1.0% Dextran 500 kDa	None	Extracellular Lipase	<i>B. pseudomallei</i> fermentation broth (A3)	0.90	92.1	Cells contained in the bottom dextran-rich phase	[222]
	10% PEG 4000, 20% sodium polyacrylate 8000	6% Sodium sulphate pH 6.5	Clavulanic acid	<i>S. clavuligerus</i> culture supernatant (A1)	9.15	55	Contaminant proteins partition also to the top phase	[221]
IL-X	15% PEG 1500, 15% Phosphate at pH 7	5% [C6mim]Cl	Lipase	<i>Bacillus</i> sp. ITP-001 supernatant (A1)	0.15	77.6	Purification factor of 103.5	[226]
	53% PEG 2000, 27% [C2mim]Cl pH 6.15	None	1- Caffeine 2- Nicotine	Purified molecules (A1)	1- 0.24 2- 1.40	100 %	Maximum selectivity of 19	[225]
R	EPOPO 3900, Phosphate at pH 7	None	CGTase	<i>B. cereus</i> feedstock (A2)	>10	87%	Purification factor of 13.1	[230]
	10% EPOPO 3900 at pH 8.5	Heating above 50°C	Lipase	<i>Burkholderia cepacia</i> fermentation broth (A3)	23.3	99.3	Purification factor of 14, 100% cells in bottom EPOPO-rich phase	[228]

Extraction, purification and concentration of compounds from complex matrices

Besides the many successful applications of ATPE reported in the literature for the purification of biomolecules from fermentation broths within the downstream processing train, there has also been a considerable interest in using these systems to extract biomolecules from complex solid matrices. This process typically has two purposes: (1) to efficiently extract and perform a primary purification of natural bioproducts of commercial interest [237, 238] and (2) to perform a sample preparation and pre-concentration step in-line with an analytical technique [239-241]. It is relevant to highlight that such pre-concentration effects can be very pronounced using the principle of dispersive liquid-liquid microextraction (DLLME) [242]. This principle is based on the addition of a very small (i.e. 1 part per 100) volume of the immiscible phase to which the target analyte has affinity. This approach has been explored in several novel experimental setups, mainly using systems composed of water and organic solvents rather than ATPS, as recently reviewed by Leong *et al.* [179]. The systems that are most often employed for both types of applications (1) and (2) are A-S and IL-X since they provide considerable differences in the chemical properties of each phase namely the charge, the solubility and the polarity, thus providing extreme partition behaviors for small molecules. Furthermore, these systems also have low viscosity compared to P-S and P-P systems, making them more amenable to further processing and analysis.

To extract natural products, a number of examples can be found in the literature, including: a serine protease from mangoes using an A-S system composed of 2-propanol and potassium phosphate, where a K of 64.5 and a purification factor of 11.6 were achieved [243]; the antioxidant lithospermic acid B from plant roots with a purity of 55% using a sulphate-ethanol system [244]; gallic acid from grape juice using a system composed of ethanol and potassium phosphate with 99.26% yield and 75% removal of sugars [245]; and flavonoids and stilbenes from pigeon pea leaves using an ethanol-ammonium sulphate system [246]. IL-X systems have been used for the extraction of vanillin with very high K (> 98) using a system composed of potassium phosphite and [C₄mim]Cl [247], or for separation of *Cordyceps sinensis* polysaccharides from proteins with high separation efficiencies [248].

For analytical applications of ATPE, IL-X systems have been the prevalent choice when coupled to HPLC and spectrophotometric types of analysis. In particular, these systems have been applied to extract, concentrate and enhance the analysis of parabens in water samples [241], quinine in human plasma [249] and testosterone/epitestosterone

in human urine [250]. Other analytical techniques such as immunoassays have also been reported to take advantage of ATPE in order to enhance sensitivity, in particular, using P-S systems to process wine and beer samples for the detection of the mycotoxins ochratoxin A and aflatoxin B1 [19]. As a different approach and going towards miniaturization, ATPE has also been used together with lateral-flow immunoassays for sample processing and concentration in order to enhance the detection of target molecules such as proteins and virus-like particles [251-253].

1.4.3. Aqueous two-phase extraction at the microscale

In order to miniaturize the previously discussed L-L separation methodologies for applications within the field of microfluidics, it is important to highlight that at the microscale there are some physical phenomena that gain a larger magnitude, and others that become negligible [254]. One of the most interesting physical proprieties of microfluidics for ATPE in particular is the general absence of turbulence, and the establishment of a laminar flow regime [255]. The importance of this phenomenon results from the observation that without turbulence there is no convective mixing of the solution and molecular transport processes perpendicularly to the flow direction occur by diffusion only, according to Fick's first law, **Equation 1.9**, where N is the solute flux, D is the diffusion coefficient, x is the distance of diffusion, Δc is the molar concentration difference between two points in space at x distance from each other. The diffusion at the interface between phase 1 and 2 occurs according to **Equation 1.10** where c_1 is the molar concentration in the top phase, c_2 is the molar concentration in the bottom phase and K is the partition coefficient of the solute in a ATPS [256]. It is important to highlight that in conformity with the designation used for the mL-scale, here the top and bottom phases refer only to less and more dense phases, respectively.

$$N = D \left(\frac{\Delta c}{x} \right) \quad (1.9)$$

$$N = D \left(\frac{c_1 - c_2 \times K}{x} \right) \quad (1.10)$$

In **Figure 1.10** the main differences between the critical parameters of ATPE performed in microchannels (**Figure 1.10-A**) or microtubes (**Figure 1.10-B**) are highlighted. In a mL-scale container of dimensions $L \times W \times H$, the partition of a compound between two immiscible phases 1 and 2 with volumes V_t and V_b , respectively, is very slow occurring via diffusion only, taking several hours to days to complete. This is due to the very small ratio of interfacial area to total volume of approximately 0.05 mm^{-1} for 1.5 mL

of total ATPS in a typical microtube, assuming that the interface is located above the conical region. Therefore, in order to speed up the partition of the molecule from one phase to the other, convective mixing is required [257], generated by mechanically agitating the solution in order to generate small droplets of one phase dispersed in the other phase, dramatically increasing the total interfacial area. While this process is fast, the separation of the droplets back to the initial position of each phase which occurs by gravity and flotation forces is typically very slow [257], and may be limited by the often low surface tension between the phases [258-260] and by the high viscosities of concentrated polymer solutions [257]. There have been successful attempts at decreasing this separation time to a few minutes without resorting to centrifugation by using wider ($> L \times W$) and shorter ($< H$) containers [257]. It is also important to highlight that in the case of ATPE performed in a mL-scale container, the concentration effect is conferred by the volume ratio.

When ATPE is performed in a microchannel, the phases partition exclusively through diffusion since the ratio of interfacial area to total volume is 10 mm^{-1} for a channel of $200 \times 0.02 \times 0.1$ ($L \times H \times W$) mm dimensions, more than 2 orders of magnitude larger than that obtained for the microtube. In this case, besides the difference in channel dimensions, the critical parameters for separation are significantly different from the mL-scale. Firstly, since this is an intrinsically continuous process, meaning that each phase is continuously pumped parallel to each other through the channel (**Figure 1.10-A**), liquid flow velocities are the critical variables as opposed to phase volumes and total volume in the micro-tube case. In addition, the laminar flow characteristics of microfluidics allow for a multiphase formation and stabilization with more than 2 inlets ($n > 2$) which can potentially be useful for several applications. In addition, unlike the mL-scale, the interfacial effects are much more important at the microscale, such as a lower Bond (Bo) number, **Equation 1.11**, $\Delta\rho$ being the difference in densities, g the acceleration of gravity, L the characteristic length scale and σ the surface tension), which implies that gravity related effects are negligible, and adjustable Weber (We), **Equation 1.12**, with v being the linear velocity of the liquid) and Capillary (Ca), **Equation 1.13**, μ being the dynamic viscosity) numbers, so that inertial and viscous forces can be either significant or negligible. The manipulation of We and Ca is responsible for important phenomena such as droplet formation versus stable parallel flows [261] or for the preferential wetting of the surface by one of the phases, in conditions where the inertial forces are not sufficiently high to maintain a planar interface

(**Figure 1.10-A**). Thus, it is very important that the flow velocities and channel dimensions are optimized for a particular system to provide a stable flow-regime.

$$Bo = \frac{\Delta\rho \cdot g \cdot L^2}{\sigma} \quad (1.11)$$

$$We = \frac{\rho \cdot v^2 \cdot L}{\sigma} \quad (1.12)$$

$$Ca = \frac{\mu \cdot v}{\sigma} \quad (1.13)$$

To provide further insights on the molecular partition behavior between two parallel co-flowing streams of liquid, the partition of molecules with increasing molecular weight from a salt-rich phase to a PEG-rich phase was simulated according to the procedure described and validated by Silva *et al.* [256] (**Figure 1.10-C**). The diffusion coefficients of 50 and 200 $\mu\text{m}^2 \cdot \text{s}^{-1}$ for the PEG and salt-rich phases, respectively, correspond approximately to those measured for an IgG molecule, with a MW of approximately 150 kDa. Briefly, the simulation is based on Fick's first law for the general mass transfer and a modification to Fick's first law for the mass transfer across interfaces, according to **Equations 1.9 and 1.10**, respectively. The simulation consists of a 2D matrix divided into cells, each representing a defined area of the microchannel with the desired degree of resolution, in which the previous equations are used to calculate the solute molar concentration at each point along the matrix. Given that at micrometer-scale the flow of liquid is generally well below the turbulent flow threshold and the mass transfer occurs only by diffusion regardless of the T-juncture angle and geometry, it can be observed that the lower the diffusion coefficient of the target compound, the longer it takes for 90% of the molecules to partition to the PEG-rich phase (higher t_{90}). Thus, the length of the channel has to be designed accordingly to provide sufficient residence time at the required liquid velocities to complete the extraction. A second simulation was performed (**Figure 1.10-D**) to visualize the local concentration of molecules across the width of the microchannel at different positions along the length of the microchannel for a fixed diffusion coefficient. In this plot a concentration effect occurs in the PEG-rich phase, originating from the lower speed of this phase relative to the salt-rich phase. Thus, the flow rate ratio between each co-flowing phase in a continuous process is analogous to the volume ratio in batch conditions providing a concentration effect. It can also be noticed in **Figure 1.10-D** that the interface is not positioned in the center of the microchannel. This is due to the pressure difference (DPF) between the two phases as a function of the contact length and the flow velocity, together with the Laplace pressure (DPL), caused by the interfacial tension between two phases [262]. The balance between

these effects results in the interface stable at a certain position across the width of the microchannel.

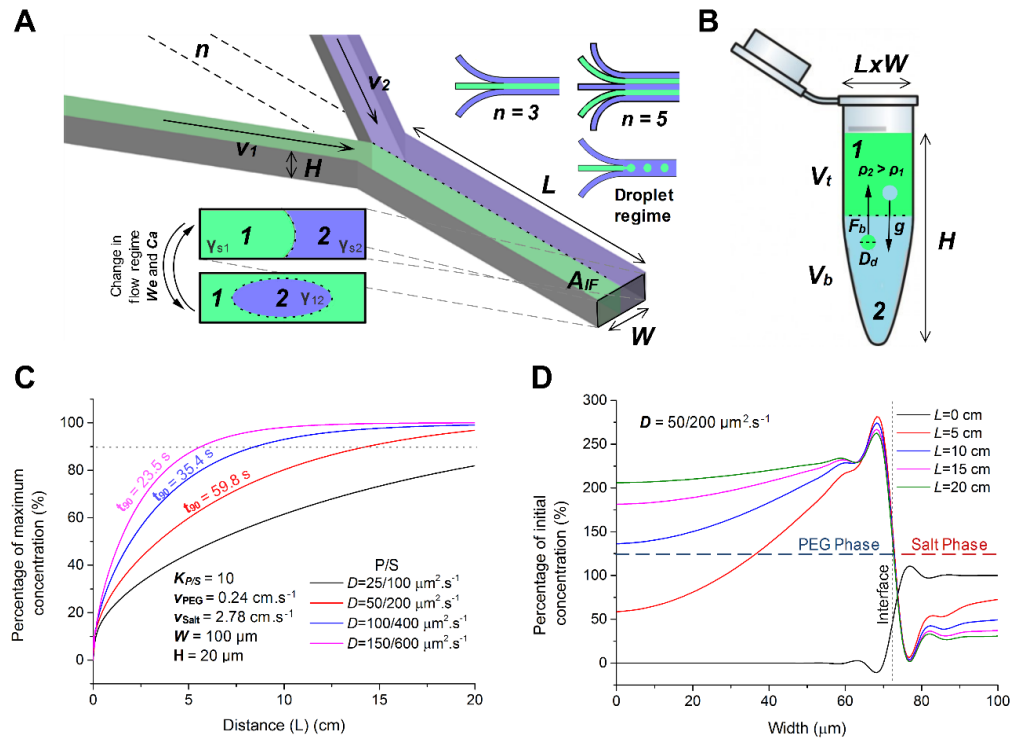


Figure 1.10 – Comparison between the critical parameters inherent to ATPE performed in a microfluidic channel (A) or in a mL-scale container such as a microtube (B) and simulation of the partition of molecules with increasing diffusion coefficients along (C) and across (D) a microfluidic channel. **A-** L - length of the microchannel; W - width of the microchannel; H - height of the microchannel; n - number of inlets converging into the main separation channel; v_1 and v_2 - liquid velocities of each of the immiscible phases 1 and 2; A_{IF} - total interfacial area between the phases, identified as a dotted line; γ_{S1} - surface tension between phase 1 and the surface of the channel; γ_{S2} - surface tension between phase 2 and the surface of the channel; γ_{12} - surface tension between phases 1 and 2. We and Ca refer the Weber and Capillary numbers. **B-** $L \times W$ - area of the container; H - height of the container; V_t - volume of the top immiscible phase; V_b - volume of the bottom immiscible phase; ρ_1 and ρ_2 - densities of each phase 1 and 2; D_d - average diameter of the droplets of one immiscible phase within the bulk of the other; generated after convective mixing; F_b - buoyancy force and g - gravity force. **C-** Simulation of the partition of compounds with increasing diffusion coefficients from a salt-rich (S) to a PEG-rich (P) phase along a 20×100 ($H \times W$) μm microchannel. The t_{90} values refer to the time it takes for 90% of the molecules to partition from the S to the P phases. **D-** Simulation of the partition of compounds with a diffusion coefficient of 50 and $200 \text{ }\mu\text{m}^2.\text{s}^{-1}$ for the P and S phases, respectively, across the microchannel width at increasing lengths of the channel (proportional to the residence time). The interface location is marked as a dotted line. The assumed values for flow velocities and widths of the channel occupied by each phase are based on experimental observations previously reported by Soares and Silva *et al* [24, 256].

1.5. Thin-film silicon photodetectors for optical signal transduction in portable microfluidic devices

Unlike metals, semiconductors such as crystalline and amorphous silicon are characterized by having an energy gap in their quantum energy levels, between the

valence band and the conduction band (**Figure 1.11-A**). This energy barrier fundamentally results in a reduced number of free electrons, thus reducing the conductivity when compared to metals, in which the valence and conduction bands are superimposed, given that in semiconductors there is a relatively lower number of electrons at the bottom of the conduction band ($n_E(E)$) at a certain temperature (**Figure 1.11-B**). This number of electrons is given by the product between the Fermi-Dirac probability function ($f(E)$) and the density of states in the CB ($g(E)$). On the other hand, the energy barrier of the band gap ($E_g = E_c - E_v$) can be overcome if the electrons are excited thermally or by photons with an energy $h\nu$ larger than E_g . In the case of the semiconductor being intrinsic (undoped), meaning that there are no acceptor or donor impurities (dopants) present in the material that add additional electrons or holes, the Fermi level (E_F) is located in the middle of the energy gap and the concentration of electrons in the conduction band is given by **Equation 1.14** in which N_c is the effective density of states in the conduction band and m_e^* is the effective mass of the electron in the conduction band. From the number of electrons in the conduction band, the conductivity of the material is given by **Equation 1.15**, where n and p are the electron and hole concentrations and μ_e and μ_h are the mobilities of electrons and holes as area per volt per time [263]. Since the conductivity is dependent on the number of electrons in the conduction band, simply measuring the conductivity of the semiconductor at a certain applied voltage can be used as a means of detecting incident photons (photoconductor).

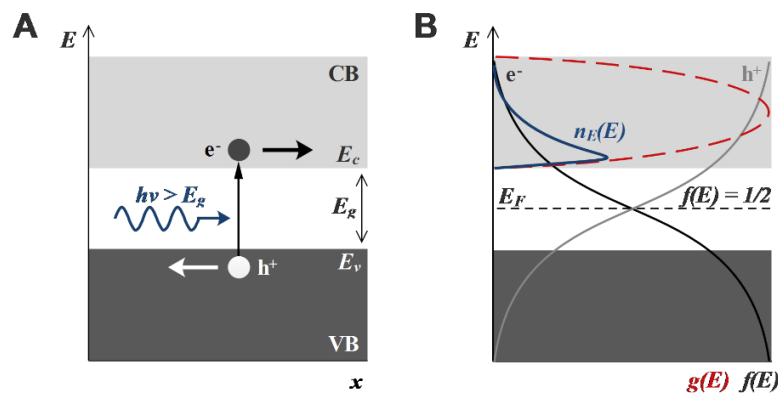


Figure 1.11 – A- Band diagram for a crystalline semiconductor material, highlighting the conduction band (CB) and the valence band (VB), which are separated by the band gap (E_g), calculated as $E_c - E_v$. A photon with sufficient energy, meaning larger than E_g , can excite an electron (e^-) into the CB, leaving a hole (h^+) in the VB. **B-** Schematic representation of the Fermi-Dirac probability function ($f(E)$) at $T \gg 0$ K, describing the probability of occupancy of a state by electrons and holes ($1 - f(E)$), the density of states in the CB ($g(E)$) per unit volume and the product of $g(E) \times f(E)$, representing the number of electrons per unit energy per unit volume ($n_E(E)$). The Fermi level (E_F), related to the electrical work input or output of the system, is located at $f(E) = 1/2$, considering that at this energy level there are no states available for the electrons to occupy.

$$n = N_c e^{\left[-\frac{(E_c - E_F)}{k_B T}\right]}, \quad N_c = 2 \left(\frac{2\pi m_e^* k_B T}{h^2}\right)^{3/2} \quad (1.14)$$

$$\sigma_i = e(n\mu_e + p\mu_h) \quad (1.15)$$

Many silicon devices such as transistors and photodiodes rely on a modification of the intrinsic Si material by the addition of impurities (doping) that change the electrical properties of the material, by selectively increasing the concentration of electrons in the conduction band (*n*-type) or holes in the valence band (*p*-type). This is achieved by adding electron donor atoms such as phosphorus (group V) or acceptor atoms such as boron (group III), resulting in the Fermi level shifting towards the conduction band or the valence band, respectively (**Figure 1.12-A**) and making, in general, the material relatively more conductive, depending mainly on the donor or acceptor concentration (**Equation 1.16**). Both the *p* and *n*-type material can then be used to create a *p-n* junction, which occurs at the metallurgical (*M*) junction between the two doped materials. At the junction, the electrons from the *n*-type will flow into the *p*-type and recombine with holes in the valence band, while the reciprocal occurs with holes in the *p*-type. This process is stopped by the opposite charge of the boron (B^-) and phosphorus (P^+) impurities in the solid lattice preventing further diffusion of electrons and holes. Overall, this results in a depletion region being formed at the interface between the *p* and *n*-doped regions. From the energy band in **Figure 1.12-B** it is possible to see that a built-in potential (eV_0) is generated at the junction and any excited electron-hole pairs in this region will be drifted according to the electrical field [263].

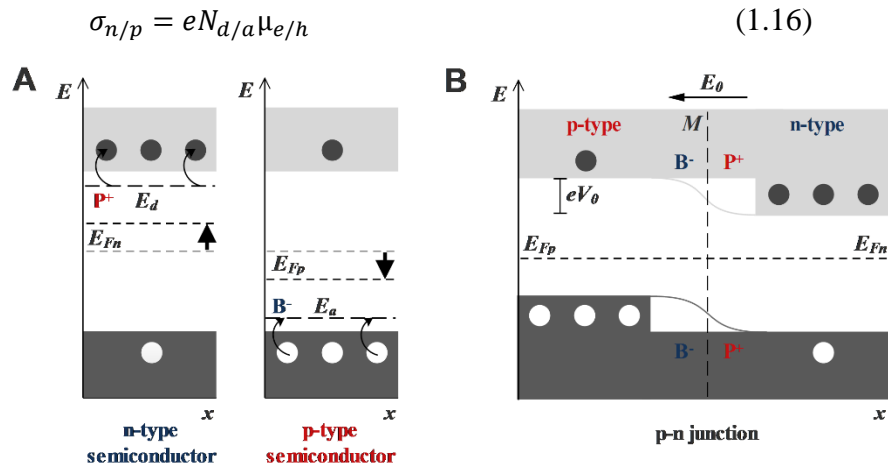


Figure 1.12 – **A**- Energy band diagrams for a *n*-doped and a *p*-doped semiconductor, using phosphate (P^+) and boron (B^-) atoms as donors and acceptors, respectively. **B**- Energy band diagram of a *p-n* junction. V_0 refers to the built-in potential and *M* refers to the junction (metallurgical) between the two layers.

To design a photosensor it is advantageous to include a relatively thick intrinsic layer in between the *p*-doped and *n*-doped layers, as shown in **Figure 1.13**. The reason

for this is that the p - n junction alone provides a too narrow depletion region, which hinders the efficient photodetection, considering that the absorption of light at any other section of the device does not contribute to the generated current since there is no electrical field to separate the electrons from the holes and drift them apart. By including a thick intrinsic layer, the field extends uniformly through its entire extension, providing a wider absorption region. In **Figure 1.13-A** the schematics of a thin-film p - i - n photodiode are shown, in which three design considerations can be highlighted. Firstly, the side walls of the p - i - n stack need to be adequately passivated with an insulator to eliminate surface defects, namely dangling bonds, and prevent short circuits between the top and bottom doped layers. Secondly, the top electrode needs to be both conductive and provide a high optical transmission to the target wavelength and thirdly, the p - i - n configuration, rather than n - i - p , has the advantage of generating electron-hole pairs closer to the p -type layer, facilitating the drift of holes, which in undoped silicon have a lower mobility than electrons, towards the respective electrode [263].

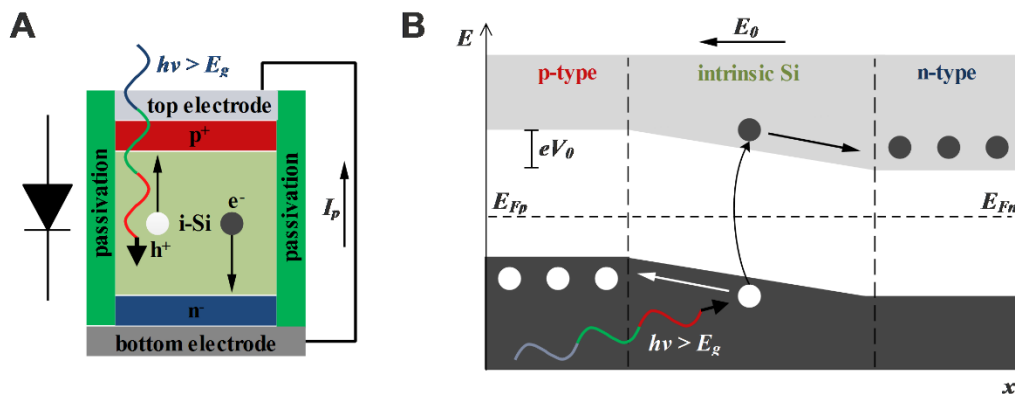


Figure 1.13 – **A**- Cross-section schematics of a thin-film p - i - n Si photodiode, addressed by a bottom electrode and a top transparent electrode. c-Si photodiodes can be optimized to absorb light across the visible spectrum, which generates electron-hole pairs and consequently a photocurrent between the n and p layers. I_p is the generated photocurrent upon light illumination. **B**- Energy band diagram for a p - i - n junction during the generation of electron-hole pairs.

While **Figure 1.13-B** shows the behavior of the energy band diagram of the p - i - n photodiode when no voltage is applied on the electrodes, **Figure 1.14-A** and **B** show the behavior of the energy band diagram when under a forward bias or reverse bias conditions, applying a voltage V . Under reverse bias, the voltage across the junction adds to the applied voltage and the energy barrier in the intrinsic layer increases, not allowing current (positive) to flow from the n to the p layer. Nevertheless, electron-hole pairs can still be collected, generating a negative current. On the other hand, applying a forward bias, the energy levels become closer and electrons can flow freely across the intrinsic layer, generating a positive current. This can be clearly observed in a typical I - V curve in

the dark or under increasing light intensities (**Figure 1.14-C**), which generate a proportionally higher current (**Figure 1.14-D**). The application of an external field can be of particular relevance to improve the response time of the photosensor, which in this case is limited by the drift of electron-hole pairs across the intrinsic region. Nevertheless, it complicates the electronic addressing, compared to using the sensor and 0 V Bias.

Regarding how sensitive the photodiode is to light, two critical parameters can be highlighted, (1) the external quantum efficiency (η), directly related to the responsivity (R), which are dependent on a certain wavelength and (2) the photoresponse at a fixed wavelength, meaning the output current at increasing photon fluxes. The first set of parameters are calculated using **Equations 1.17 and 1.18**, respectively, relating the number of free electron-hole pairs generated and collected per number of incident photons and the generated photocurrent per incident power, at a given wavelength [263].

$$\eta = \frac{I_p/e}{P_0/h\nu} \quad (1.17)$$

$$R = \frac{I_p}{P_0} = \eta \frac{e\lambda}{hc} \quad (1.18)$$

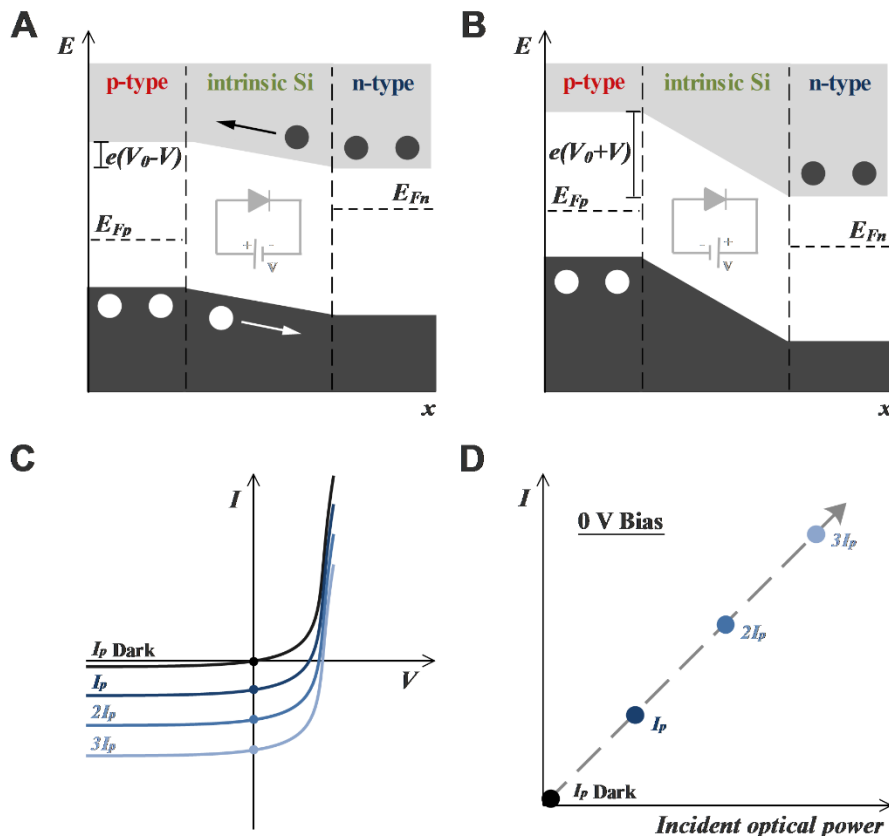


Figure 1.14 – **A-** Energy band diagram of a forward biased *p-i-n* Si photodiode. **B-** Energy band diagram of a reversed biased photodiode. **C-** Characteristic *I-V* curve for photodiodes in the dark and exposed to incremental intensities of light, generating a proportionally higher photocurrent. **D-** Characteristic measured photocurrent at 0 V bias under increasing incident optical power (W).

Finally, when discussing the integration of Si photodiodes in biosensors, these are often required in very small dimensions, ranging from tens of micrometers to few millimeters. Considering mm-size commercial c-Si photodiodes, these generate dark currents in the order of tens of pA. While these currents can be easily measured using a picoammeter, such complex and bulky equipment is surely not adequate for portability, simplicity and cost reduction demanded in the development of biosensors. Therefore, a common and relatively simple opamp-based amplifier circuit to measure the current output of a photodiode is the transimpedance amplifier, schematized in **Figure 1.15**. The *n*-doped layer of the photodiode is connected to the negative input of the opamp and both the positive input and *p*-doped layer are connected to the ground. The output current of the photodiode (I_p) is then converted into an output voltage (V_{out}), proportionally to the feedback resistance (R_f) in accordance with **Equation 1.19**. Therefore, by selecting a sufficiently large R_f and an appropriate opamp, very small currents in the order of pA can generate easily measurable voltages in the order of mV to V. It is also important to highlight that transimpedance amplifiers typically also require a feedback capacitance (C_f) to compensate and minimize oscillations in signal at high frequencies due to the internal capacitance of the photodiode, which is connected in parallel with the opamp inputs.

$$V_{out} = I_p \times R_f \quad (1.19)$$

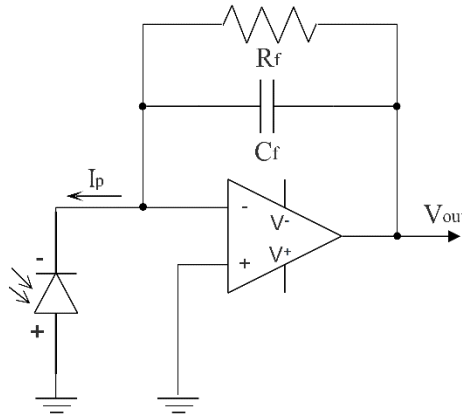


Figure 1.15 – General circuit schematics of a transimpedance amplifier, here used to amplify the current generated by a photodiode at 0 V bias. R_f and C_f refer to the feedback resistance and capacitance, respectively.

Chapter 2

General Microfabrication and Microfluidic Device Handling Methodologies

This chapter describes the general microfabrication methods optimized to fabricate PDMS microfluidic devices, namely (1) hard mask fabrication, (2) SU-8 mold fabrication, (3) mold-replication of PDMS and, (4) processing and sealing. Experimental details on the handling of microfluidic devices, including optical signal acquisition using standard optical or fluorescence microscopy, are also provided. Furthermore, the microfabrication of thin-film a-Si:H photoconductors and photodiodes is also described. A few detailed descriptions are reproduced with appropriate adaptations from publications co-authored with PhD students Inês Pinto [18] and Denis Santos [42, 49].

2.1. Fabrication of microfluidic devices: a general overview

In general, the fabrication of PDMS microfluidic devices was performed in three steps, namely (1) hard-mask fabrication, (2) SU-8 mold fabrication and (3) mold replication. These steps are schematically summarized in **Figure 2.1**.

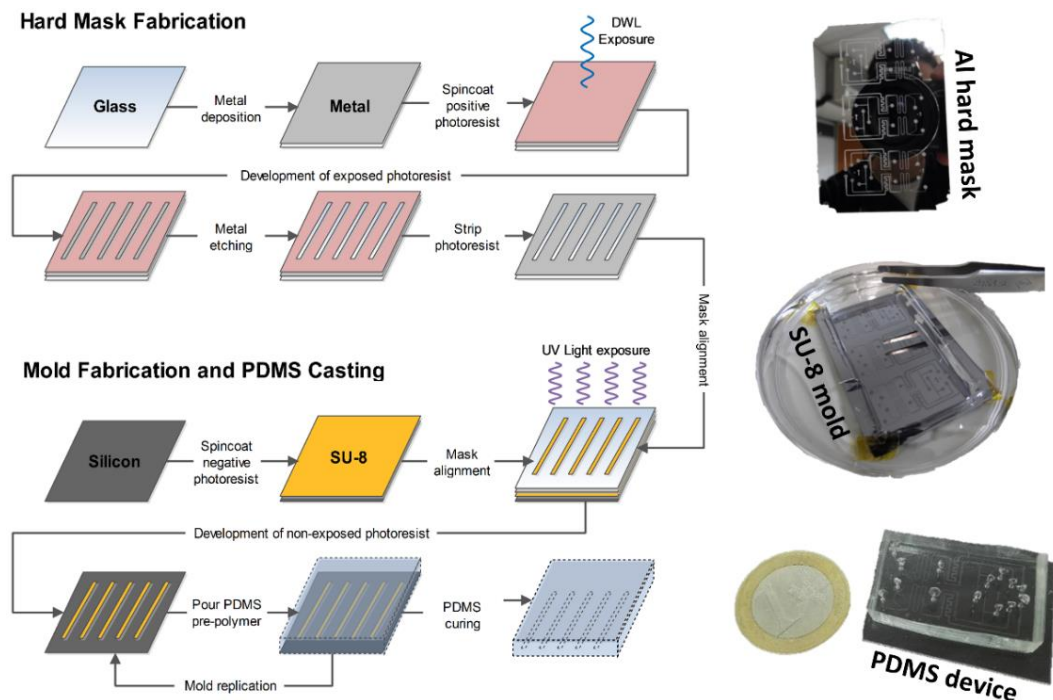


Figure 2.1 – Schematics of the microfabrication procedure used to obtain PDMS microfluidic devices. Photos on the right show an example of the intermediate stage after each main fabrication step.

2.2. Hard-mask fabrication

The microchannel patterns in the aluminium masks were first designed using AutoCAD software (Autodesk Inc., Mill Valley, CA/USA). A glass substrate was cleaned by sequentially rinsing with acetone (LabChem Inc. Zelienople, PA/USA), deionized (DI) water, followed by immersion in an Alconox® detergent solution (Alconox Inc. White Plains, NY/USA) for 15 min at 65 °C, and a thorough rinse with DI water followed by drying with compressed air. The thorough rinsing with DI water after Alconox® is critical to remove any detergent residues before drying. Otherwise, these dried residues may compromise the adhesion of subsequent materials deposited on the surface. Subsequently, a 200 nm Aluminium (Al) layer was deposited using a Nordiko 7000 magnetron sputtering system (Nordiko Technical Services Ltd. Havant, Hampshire, UK). A positive photoresist layer of 1.5 µm (PFR 7790G, JSR, Sunnyvale, CA/USA) was spin-coated onto the deposited Al layer. The AutoCAD file was then converted and transferred to a Heidelberg DWLii direct write laser photolithography system (Heidelberg Instruments, Heidelberg, DE) using a 405 nm laser diode, used to transfer the pattern to the photoresist. The resist was then developed (TMA238WA, JSR, Sunnyvale, CA/USA) and later removed by wet etching using a standard aluminium etchant acid mixture (TechniEtch Al80 Aluminium etchant, Microchemicals, Ulm, DE). Finally, the remaining photoresist was stripped away with acetone, resulting in a patterned Al mask on the glass substrate. The previous microfabrication steps were all performed under class 100 clean-room conditions, except for the photolithography step, which was performed in class 10 conditions.

2.3. SU-8 mold fabrication

The master molds were fabricated on Si substrates (University Wafer, South Boston, MA/USA) using SU-8 negative photoresist (2015 or 50 formulations, Microchem Corp, Newton, MA/USA) for a total height of 20 µm or 100 µm. Some molds were also fabricated using two superimposed SU-8 layers with 20 and 100 µm, deposited in this respective order. In all cases, a Si substrate was first cleaned by sequential rinsing with acetone, isopropanol (IPA, 99.9%, LabChem Inc. Zelienople, PA/USA) and DI water to remove any residues of photoresist (used during the dicing process) or other organic contaminants on the surface. Then, the substrate was immersed in an Alconox® detergent solution for 15 min at 65 °C, followed by a thorough rinse with DI water and drying with

compressed air. The substrate was then placed in a UVO cleaner (1444AX-220, Jelight Company, Inc. Irvine, CA/USA) for 15 min to remove any remaining organic contaminants. To fabricate the mold with a height of 20 μm , SU-8 2015 was spin-coated (Laurell Technologies Corp. North Wales, PA/USA) onto the clean silicon substrate for 10 s at 500 rpm with an acceleration of 100 rpm/s, followed by 34 s at 1700 rpm with an acceleration of 300 rpm/s. After a 4 min pre-exposure bake at 95 $^{\circ}\text{C}$ using a hot plate (Digital hotplate, Stuart, Staffordshire, UK), the substrate was allowed to cool down for 1 min and the hard mask with the design for the 20 μm channels was placed over the SU-8 layer with the aluminium surface facing down, to prevent a loss in resolution due to light scattering effects. The stack was exposed to a 400 W UV light (UV Light Technology Limited, Birmingham, UK) with an energy per unit area of 178 mJ/cm^2 and baked for 5 min at 95 $^{\circ}\text{C}$ followed by a cool down to room temperature for 2 min. The development of the non-exposed photoresist was achieved by immersion of the SU-8 in a propylene glycol monomethyl ether acetate (PGMEA) solution (> 99% v/v) for 2 min with manual orbital agitation. After the development, the substrate was rinsed with IPA and dried with compressed air. To fabricate the mold with a height of 100 μm , SU-8 50 was spin-coated onto the clean silicon substrate for 10 s at 500 rpm with an acceleration of 100 rpm/s, followed by 30 s at 1000 rpm with an acceleration of 300 rpm/s. A pre-exposure bake process was then performed by baking the substrate at 65 $^{\circ}\text{C}$ for 10 min, followed by a gradual ramping-up of the temperature to 95 $^{\circ}\text{C}$, where it was baked for 30 min and then allowed to cool for 1 min. The mask and substrate stack were then exposed to UV light for a total energy per unit area of 416 mJ/cm^2 . A post-exposure bake was performed at 65 $^{\circ}\text{C}$ for 1 min, followed by 10 min at 95 $^{\circ}\text{C}$ and 2 min of cooling down. The photoresist layer was developed in PGMEA for 10 min with manual orbital agitation (see Table 4), rinsed with IPA, and dried. Finally, in all cases, the mold was hard baked for 15 min at 150 $^{\circ}\text{C}$ and left to slowly cool down on top of the hot plate until the temperature dropped below 50 $^{\circ}\text{C}$. The slow cooling process is critical to avoid cracking the hardened SU-8 due to rapid contraction. Molds comprising two layers with different heights were fabricated in the same way as described above by spincoating the thickest layer on top of the thinner layer. No washing or hard bake steps were performed between the two layers. The alignment between the second mask and the mold features on the first layer was performed manually with the aid of a stereomicroscope (AmScope, Irvine, CA/USA) with a total amplification of 20 \times to 40 \times .

2.4. PDMS mold-replication, punching of access holes and sealing

The SU-8 mold was first taped to the bottom of a Petri dish, with the patterned surface facing up. To prepare the PDMS elastomer, a 10:1 weight ratio of PDMS to curing agent was mixed (Sylgard 184 poly(dimethyl)siloxane, Dow Corning, Midland, MI/USA), degassed for 30 min and poured into the Petri dish containing the mold to a total height of 0.5-1 cm. The liquid pre-polymer was then left to cure at 70 °C for 90 min in a convection oven (Oven loading model 100-800 (70 °C), Memmert, Schwabach, DE). The cured PDMS was then cut using a scalpel and peeled off from the mold using tweezers. Access holes were punched with blunt 20 or 18 ga needles (Instech Laboratories, Inc. Plymouth Meeting, PA/USA). Holes punched with 20 ga needles were used to fit 20 ga metallic adapters (purchased also from Instech Solomon), while holes punched with 18 ga needles were used to fit 0.1-20 μL or 1-200 μL pipette tips. After punching access holes, the PDMS devices were then sealed against PDMS membranes with different thicknesses controlled by a spincoating procedure or microscope glass slides (100 μm or 700 μm thick). 500 μm thick PDMS membranes were prepared by spin coating the PDMS pre-polymer on top of a silicon wafer at 250 rpm for 25 s and an acceleration of 100 rpm/s. This membrane was then baked as described above for the PDMS devices and cut into pieces of appropriate size. In the case of the device being sealed against glass, the glass slide was previously cleaned as described in **Section 2.2**. The PDMS structures were sealed against the respective substrate by first oxidizing both sides using an oxygen plasma cleaner (800 mTorr oxygen pressure) at the medium power setting (11 W applied to the radiofrequency coil) for 60 s (Expanded oxygen plasma cleaner PDC-002-CE, Harrick Plasma, Ithaca, NY/USA). The substrate was placed in contact with the PDMS structure immediately after the plasma treatment. After sealing, the PDMS becomes relatively hydrophilic for a few hours due to the plasma treatment. To allow hydrophobic recovery and stabilization by diffusion of the unreacted siloxane oligomers to the surface, the PDMS structures were stored for at least 24 h before usage.

2.5. Fabrication of a-Si:H photoconductors and *p-i-n* photodiodes

The side view schematics and microscopy photos of the thin-film photoconductors and photodiodes fabricated at INESC MN are shown in **Figure 2.2**. The microfabrication of the photoconductors started with the deposition of aluminum by DC magnetron sputtering over a clean glass substrate (Corning® 1737) and its patterning into parallel

electrodes through photolithography and wet chemical etching using Gravure Aluminum Etchant. All photolithography steps are made using a direct-write photolithography system. The intrinsic 500 nm thick a-Si:H photoconductive layer was deposited by radio frequency Plasma-Enhanced Chemical Vapor Deposition (rf-PECVD), in a custom-built capacitively coupled radio-frequency reactor, at 100 mTorr deposition pressure, 250 °C of deposition temperature and 13.56 MHz RF power. This deposition system has been described in detail elsewhere [264]. The a-Si:H islands were defined by photolithography followed by Reactive Ion Etching (RIE) (Lam Research Rainbow 4520, Lam Research Corporation, USA). A final transparent SiN_x passivation layer was deposited by rf-PECVD and vias were opened by lift-off at the contact pads to allow wire-bonding. The photoconductor chip was then diced, die-bonded and wire-bonded to custom designed printed circuit boards.

To fabricate the photodiodes, a 200 nm aluminum back contact was first deposited by magnetron sputtering and patterned using direct write optical lithography. The a-Si:H *p-i-n* junction, with a 10 nm thick layer of *n*⁺-a-Si:H, a 500 nm thick layer of undoped *i*-a-Si:H, and a 10 nm thick layer of *p*⁺-a-Si:H, was deposited by rf-PECVD at a deposition pressure of 100 mTorr and a deposition temperature of 250 °C. Each layer was deposited through the decomposition of silane (SiH₄), *n*-type dopant phosphine (PH₃) or *p*-type dopant diborane (B₂H₆). Mesa junctions with 200 × 200 μm were defined by photolithography and etched by reactive ion etching using sulfur hexafluoride (SF₆) and trifluoromethane (CHF₃). Then, a 100 nm thick passivation layer of SiN_x was deposited by rf-PECVD, at a deposition pressure of 100 mTorr and a deposition temperature of 100 °C, to achieve passivation of the lateral walls of the junction. To allow electric contact between the *p*⁺-a-Si:H layer and the indium tin oxide (ITO) transparent top contact layer, a via was opened by lift-off of the passivation layer. A 50 nm thick ITO layer was deposited by magnetron sputtering and defined by lift-off. To electrically connect the ITO top contact, 200 nm thick aluminum lines were deposited by magnetron sputtering and defined by lift-off. A second 200 nm thick SiN_x passivation layer was deposited by rf-PECVD and vias were opened at the contact pads also by lift-off to allow wire bonding. In the case of the photodiodes used for fluorescence measurements, an extra 1.8 μm thick layer of a-SiC:H was deposited by rf-PECVD, at a deposition pressure of 100 mTorr and deposition temperature of 100 °C, working as an integrated high-pass absorption filter.

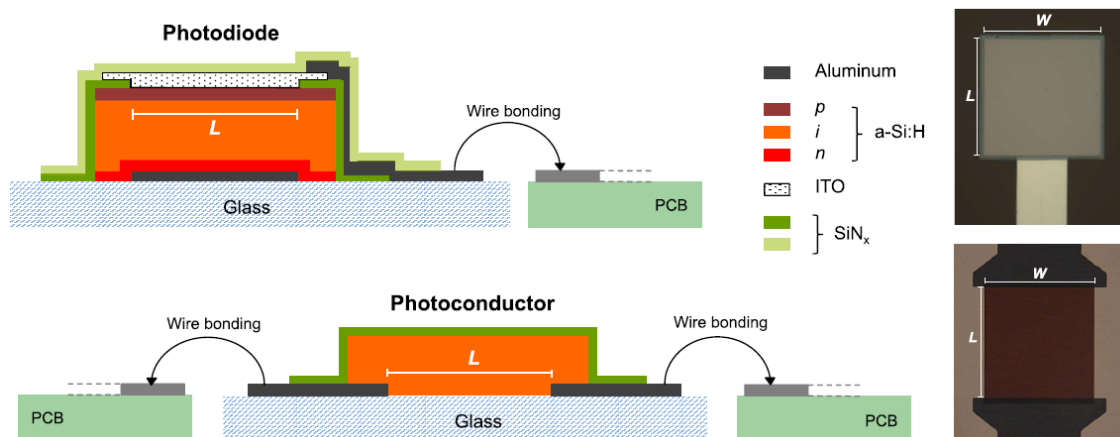


Figure 2.2 - Schematics of the thin-film a-Si:H photodiodes and photoconductors fabricated at INESC MN. The images on the right are microscopy photos of the fabricated sensors. Dimensions W and L in this thesis range from 50 to 200 μm . This figure was adapted from ref. [47], co-authored with PhD student Denis Santos.

2.6. Liquid handling and imaging of chemiluminescent and fluorometric signals using standard optical or fluorescence microscopy

The liquids were flowed through the microchannels applying either a positive or negative pressure using a syringe pump. To exert a positive pressure, the syringe pump model was a NE-300 from New Era Pump Systems, Inc. (Farmingdale, NY/USA), while in the case of the negative pressure, NE-1200 (12-channel) or NE-4000 (2-channel) syringe pumps were used. In both cases, 1 mL syringes (Insulin syringe 1 mL U-100 Luer-Lock, Codan, Lensahn, DE) were used, previously coupled with polyethylene capillary tubing (0.864 mm of inner diameter, BTPE-90, purchased from Instech Solomon) and filled with PBS buffer or double distilled water from a MilliQ purification system. In the case of positive pressure being used, the solution of interest was pulled into the capillary tubing, leaving an air spacer with a length of ~ 1 cm (~ 5.86 μL in volume) to allow a separation from the solution contained inside the syringe and capillary tubing. The small size of the air gap is critical to minimize the delay in syringe pump responsiveness due to gradual air compression, allowing the system to rapidly achieve the required equilibrium pressure to drive the liquid into the microchannels at the intended input flow rate defined on the pump. The interface between the capillary tubing and the microfluidic devices was established using a 20 ga metallic adapter (SC 20/15 stainless steel catheter coupler from Instech Solomon) with a total volume of approximately 4.28 μL (15 mm long with an internal diameter of 0.603 mm). Since the holes in the

PDMS device were punched using also a 20 ga blunt needle, the elastomeric properties of the material were sufficient to provide an air tight sealing against the adapter. In the case of sequential flow steps being required, it was critical to assure that the liquid inside the adapter contacts the liquid inside the access hole of the PDMS device without leaving a small air gap in between, otherwise the flowing air bubble can potentially compromise the assay integrity. In the alternative case of using a negative pressure, the syringe pump was operated in a pulling motion coupled to the outlet hole of the device. A pipette tip (0.1-20 μL or 1-200 μL) was then used as a liquid reservoir at the inlet by first pipetting a certain volume of solution and then releasing the tip after insertion in the inlet hole. In this case it was often critical to first fill the entire fluidic channel network with liquid before exerting a negative pressure, to avoid preferential wetting and unequal flow velocity when multiple inlets were used. As previously described for the use of a positive pressure, in this case it was also critical to ensure fluidic contact inside the punched holes when replacing the pipette tips to avoid an irregular flow velocity and trapped air-bubbles.

The imaging of the microfluidic devices (bright field and fluorescence microscopy) was performed using either a Leica DMLM fluorescence microscope (Leica Microsystems, Wetzlar, DE) equipped with a DFC300FX digital color camera and a 100 W short arc mercury vapor lamp or an Olympus CKX41 inverted fluorescence microscope (Olympus, Shinjuku, Tokyo, JP) equipped with a XC30 CCD color camera and a 50 W short arc mercury vapor lamp. All chemiluminescence measurements were performed using the Leica microscope, while the fluorescence measurements were performed in both microscopes depending on the sensitivity requirements (i.e. 100 W excitation source from Leica provides a more intense fluorescence emission). Three filter cubes were available in each microscope, namely D, I3 and TX2 for the Leica and U, B and G for Olympus. The spectral characteristics of each filter are described as follows (BP stands for band pass and LP for long pass): D – Excitation: BP 355-425, Emission: LP 470; I3 – Excitation: BP 450-490, Emission: LP 515; TX2 – Excitation: BP 560/40, Emission: BP 645/75; U – Excitation: BP 360-370, Emission: LP 420; B – Excitation: BP 460-490, Emission: LP 520; G – Excitation: BP 480-550, Emission: LP 590. All acquired images were quantified in terms of grayscale using the software ImageJ from the National Institute of Health (Bethesda, MD, USA).

Chapter 3

Microfluidic Aqueous Two-Phase Systems for On-Chip Integration of Sample Preparation

This chapter reports the development of an aqueous two-phase system (ATPS) based methodology for the simultaneous concentration of mycotoxins and neutralization of matrix interference. Polyethylene glycol (PEG)-phosphate salt ATPSs were used to enhance the detection sensitivity of ochratoxin A (OTA) and aflatoxin B1 (AFB1) in wines and beer by an indirect competitive enzyme-linked immunosorbent assay (ELISA) performed in a standard microtiter plate format. This methodology was further integrated in a microfluidic device to perform sample preparation in series with a microfluidic immunoassay. The microfluidic device was composed of two modules in series, the first performing an aqueous two-phase extraction (ATPE) for matrix neutralization and analyte pre-concentration, and the second a competitive fluorescence-linked immunosorbent assay (FLISA) for mycotoxin quantification. In this case, OTA was used as a model analyte spiked in red and white wines. Using this strategy, a limit of detection (LoD) of 0.26 ng/mL was obtained for red wine spiked with OTA, well below the regulatory limit for OTA in wines of 2 ng/mL set by the European Union. The contents of this chapter are summarized and reproduced with appropriate adaptations from two original research articles [19, 24], based on experimental results obtained during my MSc project [265] and beginning of the PhD project.

3.1. Materials and experimental methods

3.1.1. Chemicals and biologicals

PEG with 2, 6 or 10 kDa average molecular weight (MW), NaH₂PO₄, K₂HPO₄, OTA, AFB1, phosphate buffered saline (PBS) tablets, methanol (99,9%), OTA-bovine serum albumin (BSA) conjugate, AFB1-BSA conjugate, Tween 20, 3,3',5,5'-tetramethylbenzidine (TMB) ready-to-use liquid substrate (super-slow) for ELISA, BSA and fluorescein isothiocyanate (FITC) conjugated goat polyclonal anti-mouse antibody (whole molecule) were purchased from Sigma Aldrich. Ultrapure water was obtained from a MilliQ purification system from Millipore (Billerica, MA, USA). OTA and AFB1

stock solutions were prepared with an equal concentration of 100 µg/mL in 25% (v/v) and 50% (v/v) methanol in PBS respectively. The monoclonal anti-OTA IgG (3C5) and monoclonal anti-AFB1 IgG (AFA-1) were purchased from Abcam (Cambridge, UK). Horseradish peroxidase (HRP) conjugated polyclonal goat anti-mouse IgG (whole molecule) was purchased also from Abcam. Generic Portuguese red wine (11% v/v ethanol), white wine (11% v/v ethanol) and beer (5.2% v/v ethanol), were purchased from a local store.

3.1.2. ATPS preparation to evaluate mycotoxin partition

The ATPSs were prepared for a total of 1 g in 1.5 mL microtubes. Aqueous solutions of PEG 50% (w/w) (2, 6 or 10 kDa average MW) and NaH₂PO₄/K₂HPO₄ 40% (w/w) (adjusted to a final pH of 6, 7 or 8 by changing the ratio of monosodic to dipotassic salts) were added depending on the conditions chosen and adjusted to the total mass of the system using ultrapure water. Then, each tube was agitated in a vortex for 10 to 15 s. Finally, to obtain clear separated phases the microtubes were centrifuged at 6,000 g for 2 min. The analytical balance used was a Mettler Toledo (Columbus, OH, USA) XS205 Dual Range. The statistical analysis of the results was performed using the computer software Statistica 7 from StatSoft (Tulsa, OK, USA).

3.1.3. Quantification of mycotoxins in ATPS using a spectrofluorimeter

Analyte quantification in both phases of 1 µg/mg analyte spiked ATPS was performed using a Varian (Palo Alto, CA, USA) Cary Eclipse plate reader spectrofluorimeter. All experiments were performed using a high voltage (800 V) setting for the photomultiplier tube and the excitation/ emission slits were set at 5 nm. The readings were averaged from 5 consecutive measurements with a 0.5 s interval in white polystyrene Corning® (Corning, NY, USA) 96 well plates. The excitation and emission wavelengths for OTA and AFB1 quantification were set at 333/ 446 nm and 370/ 439 nm respectively. A single point calibration of the fluorescence emission was performed by adding a known amount of analyte (2.5 µg/mL) to both top and bottom phases of a second ATPS prepared for each condition. This addition was performed after separating each phase to individual microtubes. A third ATPS was also prepared to subtract the background fluorescence value for each phase.

3.1.4. ATPS sample processing prior to immunodetection in microtiter plates

Undiluted red wine, white wine and beer were first adjusted to pH 6 using 10 M NaOH before any further processing. Then NaH₂PO₄ / K₂HPO₄ were added at a mass ratio of 1.27 or 0.43 for a final pH of 6 or 7, respectively, and weighed together with wine or beer to the intended final mass concentration. This mixture was then agitated in a vortex for 20-30 s for complete salt dissolution. Then, 1,881 µL of this solution were transferred to individual 2 mL microtubes and spiked with 19 µL of an OTA or AFB1 solutions prepared in PBS, at a concentration 100 times higher than the intended final concentration in wine. For the reference solutions, 19 µL of PBS were added instead of OTA or AFB1. A 50% (w/w) aqueous solution of the second phase forming component (PEG with 1, 8 or 20 kDa) was then added, 4-5 mg at a time, with intermittent agitations for 20-30 s in a vortex and 2 min of centrifugation at 6,000 g. This process was stopped when a collectable amount of top phase was obtained and was only performed the first time a new system was used, or a new top phase volume was required. The collected top phase was then diluted with a PBS solution containing anti-OTA or anti-AFB1 IgG, yielding the final IgG concentration of 50 or 100 ng/mL, respectively. Depending on the experiment, in cases where polyphenol precipitation occurred after the dilution step, the solution was centrifuged a second time under the above-mentioned conditions. This final solution was then used as SUA (sample under analysis) for the wellplate icELISA.

3.1.5. Competitive ELISA for mycotoxin detection in microtiter plates

MaxiSorp® flat-bottom 96 well microtiter plates from Nunc (Roskilde, Denmark) or Bio-one PS medium bind ELISA plates from Greiner (Kremsmünster, Austria) were used for the OTA and AFB1 experiments respectively. The shaker-incubator used was a StatFax 2200 incubator/shaker from Bio-Rad (Hercules, CA, USA) set at a shaking speed of 5. First, 100 µL of a 10 µg/mL solution of OTA-BSA in carbonate buffer (100 mM) at pH 9.2 or AFB1-BSA in PBS were added to each well. The plate was then incubated at 37°C with shaking for 1 h. After this coating step, the solution was discarded. Then, each well was washed twice with 100 µL of PBS containing 0.1% (v/v) Tween 20 (PBST). In each washing step, the plate was agitated for 30 s and the liquid was discarded. After the second wash and removal of the liquid, 150 µL of a 0.5% (w/v) BSA solution prepared in PBS was added to the wells to block the uncoated areas on the polystyrene surface. This solution was incubated for 30 min at room temperature (RT) with shaking. After washing three times, 100 µL of the SUA, containing 50 ng/mL anti-OTA IgG or

100 ng/mL anti-AFB1 IgG, were added to the wells and incubated for 45 min at RT with shaking. Four washing steps with PBST followed the primary antibody step. The final step comprised the addition of 100 μ L of a secondary antibody labeled with HRP, at a concentration of 100 ng/mL in PBST. The plate was incubated for 30 min with shaking at RT. Four final washing steps were performed also with PBST and the plate was tapped on blotting paper to ensure maximum removal of the remaining washing solution. Finally, 100 μ L of a commercial TMB solution, containing hydrogen peroxide, were added to the wells, followed by 1-5 min incubation at RT without shaking, depending on the time taken for color development. The reaction was stopped by adding 100 μ L of 250 mM HCl solution. The plate was then inserted into the spectrophotometer within 5-10 min of stopping the reaction and the absorbance was measured at a wavelength of 450 nm. The absorbance value obtained for each SUA is normalized in respect to a reference solution with the same matrix and IgG composition but without OTA or AFB1 spiking.

3.1.6. Microfluidic competitive FLISA

The immunoassays were carried out in straight PDMS microchannels 9 mm long, 20 μ m tall and 200 μ m wide. Two assays were carried simultaneously in 2 separate channels, one for the reference solution (0 ng/mL OTA) and the other for the OTA spiked solution. The immunoassay was carried out by first pumping a 50 μ g/mL OTA-BSA solution prepared in PBS into the channel for 10 min at a flow rate of 0.2 μ L/min followed by a washing step. All washing steps consisted of flowing pure PBS solution at 4 μ L/min for 1.5 min. The solutions of the reference or the sample under analysis (SUA) (spiked with OTA at concentrations of 0.1-100 ng/mL), both containing 1.25-3.75 μ g/mL anti-OTA IgG, were pumped into each respective channel for 15 min at a flow rate of 0.4 μ L/min. After a second wash, a solution of 50 μ g/mL anti-mouse IgG-FITC, prepared in PBS, flowed at 0.4 μ L/min for 10 min, followed by a final washing step.

3.1.7. Microfluidic aqueous two-phase extraction (ATPE)

A microfluidic channel design comprising two 50 μ m wide channels converging at an angle of 30° into a primary separation channel was used. For the OTA partition experiments, a system with a total composition of 14% PEG 8,000, 8% NaH₂PO₄/K₂HPO₄ (pH 7) was prepared in a microtube and each phase was separated. Then, 19 μ L of the bottom salt-rich phase (SRP) were spiked with 1 μ L of a 100 μ g/mL OTA stock solution, yielding a concentration of 5 μ g/mL OTA. Each of the spiked SRP and PEG-rich phase (PRP) were inserted into each inlet at a flow rate of 1 μ L/min and

0.2 $\mu\text{L}/\text{min}$ respectively. Alternatively, when PEG 20,000 was used, a solution of 12.5% $\text{NaH}_2\text{PO}_4/\text{K}_2\text{HPO}_4$ at pH 7 (SRP) or a solution containing 18.5% PEG 20,000 and 4.5% $\text{NaH}_2\text{PO}_4/\text{K}_2\text{HPO}_4$ at pH 7 (PRP) were spiked with OTA to a final concentration of 2 $\mu\text{g}/\text{mL}$. In one experiment, the OTA spiked SRP was converged with the non-spiked PRP and in another, while maintaining the same flow rates and PEG/ Salt compositions, the OTA is spiked in the PRP instead. In both cases the OTA behavior was monitored under the Leica microscope using the D filter. The polyphenol (PP) partition experiments were performed by converging red wine containing 12.5% $\text{NaH}_2\text{PO}_4/\text{K}_2\text{HPO}_4$ (pH 7) and a PRP prepared by dissolving 18.5% PEG 20,000 and 4.5% $\text{NaH}_2\text{PO}_4/\text{K}_2\text{HPO}_4$ (pH 7) in ultrapure water, using multiple flow rate combinations for each of the solutions, ranging from 0.02 $\mu\text{L}/\text{min}$ to 2 $\mu\text{L}/\text{min}$. The behavior of the PPs was monitored using both bright field and fluorescence microscopy (D filter).

3.2. Partition of OTA and AFB1 in PEG-phosphate salt systems

To develop a clean-up and concentration strategy based on ATPS, the partition coefficient (K) of the target analytes was first analyzed. The molecular structure of both OTA and AFB1 is presented in **Figure 3.1-A** and B. A face centered central composite design of experiments (DoE) was used to evaluate three key variables for each analyte [244, 266-268], which are the pH, PEG MW and the tie-line length (TLL). Briefly, the TLL represents the variation in the composition of the top PEG-rich and bottom salt-rich phases and the larger the difference in the composition of the phases, the longer the TLL [269]. The TLL values were considered as approximate unitary values from 1 to 3, which correspond to equal and linearly increasing total PEG and salt concentrations which is a reasonable trend indication for the K values and avoids the time-consuming quantification of the PEG and salt mass fractions in each of the phases. The results are summarized in **Figure 3.1-A** and B.

For the same set of factors and conditions tested, tenfold higher average values of K are obtained for OTA ($K \approx 267$) than for AFB1 ($K \approx 22$), while in both cases the average extraction yields are close to 100% in the top PEG rich phase. Several literature reports claim a good correlation between molecular partition to top phase in PEG-salt ATPS and increasing experimental/calculated octanol-water partition coefficient ($\log P_{ow}$) values [270-273], which arises from the intrinsic difference in hydrophobicity between the more hydrophilic salt-rich phase (water-like), and the more hydrophobic PEG-rich phase

(octanol-like). These reports and the higher K obtained for OTA correlate with the fact that OTA and AFB1 have calculated [274] $\log P_{OW}$ values of 4.61 and 1.58, respectively. However, at the pH values tested, the major OTA microspecies have either a mononegative or dinegative charge, with the calculated [274] pH dependent $\log P_{OW}$ ranging between 1 and 2, while AFB1 remains neutral. Thus, a significant difference in lipophilicity does not seem to exist between both molecules in the pH range tested. Alternatively, the difference in K values may possibly be related with the inherent positive electrochemical potential generated in the top phase of PEG-phosphate systems [192]. To maintain electroneutrality at equilibrium, the system might favor the partition of negatively charged molecules to the top phase. Such hypothesis is supported by the results obtained by Bora and co-workers, regarding the partition of the cephalosporins 7-ADCA and cephalixin in multiple PEG-salt systems [275]. The overall electric charge of these molecules shifts with pH, in a given range of pH [274]. Accordingly, the partition gradually shifts from the more hydrophilic salt phase to the PEG phase, as observed here for the mono/dinegative OTA, in opposition to the neutral AFB1.

OTA partition displays a very strong dependence on the TLL and a weaker, but significant ($p < 0.05$), dependence on the pH. A longer TLL as a promoter of more extreme K values has been previously reported [192, 270, 276]. The more pronounced difference in phase composition may enhance both the electrochemical and polarity gradients present at the interface, thus further emphasizing the entropic and enthalpic contributions for molecular partition [192]. The pH effect may be explained by the increasing concentration of the dinegative form of OTA in the pH range tested [274], in tune with the previously discussed hypothesis that the negative charge promotes the partition to the PEG rich phase. As for AFB1, the TLL factor weakly affects the K value, (**Figure 3.1-B**), while pH has no significant effect on partition, which is expected as AFB1 remains with a neutral charge in the tested pH range.

Thus, our system is neither significantly sensitive to temperature, nor requires the use of additional molecules to enhance the K of the target analytes, unlike results previously reported involving the use of water-surfactant systems to concentrate proteins and virus to enhance detection in lateral flow immunoassays [253, 277]. Furthermore, the separation times are reduced from several hours to a few minutes.

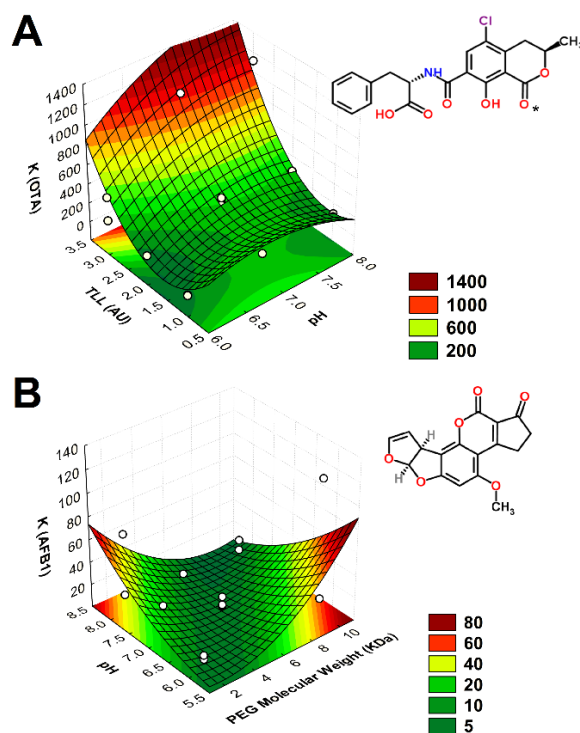


Figure 3.1 - Molecular structure and K surface tendency charts of each OTA (**A**) and AFB1 (**B**) molecules in PEG-NaH₂PO₄/KH₂PO₄ ATPSs. The OTA phenol moiety labeled with an asterisk has a pK_a of 7.1. The factors plotted in each tendency chart provide the most significant effect on the variable K.

3.3. Optimization of ATPS composition to extract mycotoxins from wine

Both analytes partition strongly to the top PEG rich phase, thus, an ATPS concentration strategy (**Figure 3.2-A**) was developed, based on the generation of systems with a small V_r . Under these conditions the colored compounds in wine and beer, which include a large fraction of the polyphenols [278], tend also to concentrate on the PEG rich phase, as can be visualized in **Figure 3.2-B**. However, a preferential affinity of the polyphenols to PEG [279], responsible for reducing the effect of interference on immunoassays has been reported [160, 280, 281]. Furthermore, since the competitive ELISA having the antigen immobilized as schematized in **Figure 1.6-A** requires both the target analyte and an analyte-specific antibody to be present in solution, the partition behavior and affinity of IgG must be assessed under different PEG concentrations, MW and salt concentrations. Depending on the PEG MW and TLL present in the system, the IgG molecules partition preferably to either of the phases or precipitate at the interface above a certain maximum TLL threshold, in accordance with previous results [282-284]. To minimize these effects, the antibody was added after phase separation together with the diluting solution to provide a reproducible mass of IgG in the PEG rich phase solution.

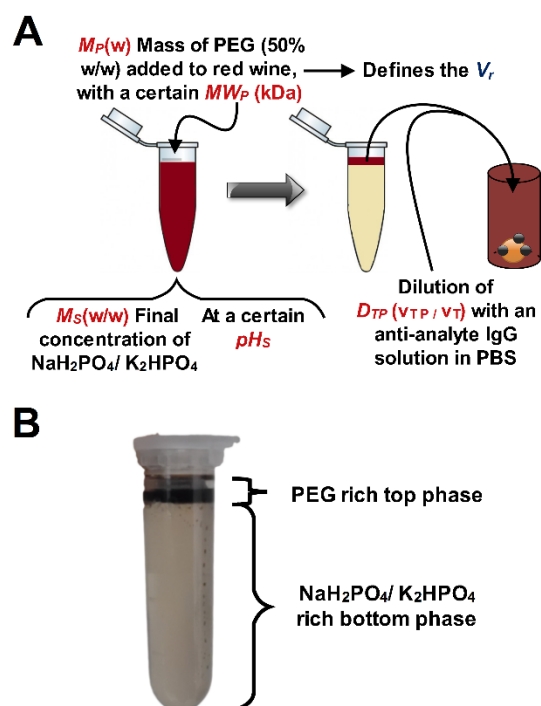


Figure 3.2 - Schematics of the ATPS mediated concentration strategy and main optimization parameters, highlighted in red. **A**- The grey arrow refers to phase separation after centrifugation. The cylinder on the right represents a well after previous adsorption of analyte-BSA conjugate. **B**- Photograph of a tube after addition of 55 mg of a PEG 20000 (50% w/w) solution to red wine in which 12.5% (w/w) of NaH_2PO_4/K_2HPO_4 were previously dissolved, for a final pH of 7.

The highest detection interference for both analytes was observed for immunodetection in red wine, with a negligible signal to noise below 100 ng/mL of analyte and a very low absolute signal. This matrix was thus selected as a worst-case scenario and was used for further ATPS concentration optimization studies. The effect of salt mass concentration (M_S), final pH (pH_s), mass (M_P) and MW_P of PEG and the dilution of top PEG rich phase with IgG solution (D_{TP}) on the LoD and half maximal inhibitory concentration (IC_{50}) for OTA was assessed and the results are presented in **Figure 3.3**. The obtained LoD and IC_{50} values were determined using the logarithmic fit shown as **Equation 3.1**, with S_R being the signal ratio obtained at a given analyte concentration $[A]$.

$$S_R = m \times \ln([A]) + b \quad (3.1)$$

From **Figure 3.3** it can be concluded that M_S does not affect significantly neither the LoD nor the IC_{50} at concentrations up to 18% (w/w), but at higher concentrations of 25%, the detection performance is severely impaired. On the other hand, the pH_s has a statistically significant impact on the IC_{50} only, in the range of tested values. The decrease of M_P , which defines the V_r of the system and therefore the extent of the concentration

effect, seems to have a positive impact on both the IC_{50} and LoD. Finally, the MW_P , together with the D_{TP} seem to have the greatest impact in both the LoD and IC_{50} values obtained. While the MW_P provides a significant improvement in both variables at higher values, the D_{TP} seems to have an optimum range between 0.1 and 0.4 parts PEG rich phase in 0.9 to 0.6 parts diluting solution.

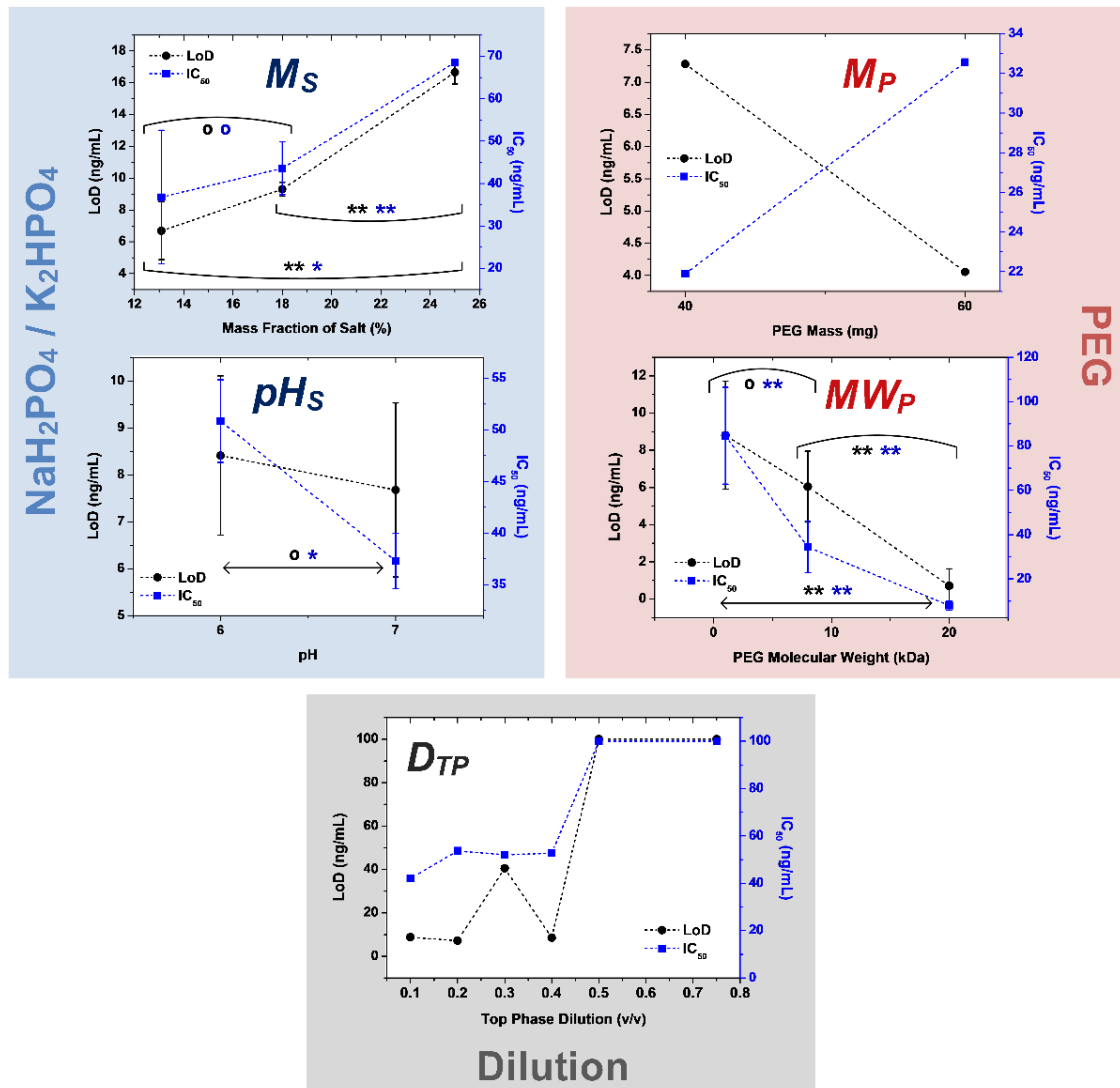


Figure 3.3 - Effect of salt/ PEG related parameters and top phase dilution on the icELISA LoD and IC_{50} values obtained for OTA quantification. For the dilution effect plot, the values on the x-axis are calculated as the volume fraction of top phase per total volume of final solution. Red wine was used as SUA for all experiments. The asterisk code refers to a confidence level below 90% (o), between 90 and 99% (*) and above 99% (**), for the hypothesis of the average value of each sample group being independent. The symbols on the left (black) or right (blue) axis refer to the LoD and IC_{50} values respectively.

The extent of PEG concentration in the PEG rich phase thus plays a key role in preventing a further increase in detection sensitivity. Furthermore, the results also strongly suggest that increasing PEG MWs provide different interactions with BSA and/or IgG proteins, resulting in dramatic differences in sensitivity. Reports in the

literature are contradictory on this topic. While some authors have concluded that volume exclusion effects predominate and that protein interaction with PEG is negligible [285], Wu and co-workers, reported that there is a significant interaction of BSA with PEG with increasing ratios of protein to PEG, with a non-linear dependence on the MW [286]. The results suggest a low point in polyphenol binding using PEG 8,000. Such non-linear dependence, regarding PEG-tannin binding, was also observed by Makkar and co-workers [287]. While the generation of a smaller volume of PEG rich phase apparently provides lower IC_{50} values, the increase of the LoD is probably due to the practical limitation of collecting, without contamination with bottom salt rich phase, a larger fraction of the existent PEG rich phase.

Using a set of conditions directed towards increased detection sensitivity, the icELISA results from raw matrices, PBS buffer and ATPS concentrated solutions were compared. The results for both OTA and AFB1 are presented in **Figure 3.4**. Regardless of the matrix used, the quantification performance was very similar for each MW_P . PEG 20,000 in particular, allowed for a very sensitive detection and a linear range spanning three orders of magnitude were achieved. PEG 8,000 prevented detection at the regulatory limits, yet the response is more accurate, with a higher slope, covering a smaller range of analyte concentrations. Furthermore, the analyte concentration effect using PEG 20,000 was sufficient to provide a superior OTA detection sensitivity in red wine, when compared to PBS control conditions, but the same was not achieved for AFB1. Such difference can possibly be related to the lower K values inherent to AFB1 partition to the top PEG rich phase. Accordingly, and given the previously observed effect of the TLL on increasing the K values, M_S values of 15% and 17.5% NaH_2PO_4/K_2HPO_4 were also tested (**Figure 3.5**). Unexpectedly, when using PEG 8,000, the obtained curves overlap regardless of the M_S . Also, in conditions where PEG 20,000 is used, there is a loss of linearity in the log scale with increasing salt concentration, resulting in an increase of LoD from 0.035 ng/mL to 0.098 ng/mL and a decrease in IC_{50} from 1.02 ng/mL to 0.67 ng/mL, from 12.5% M_S to 15% M_S . This may be either due to an increased PEG 20,000 concentration in the PEG rich phase because of an increase in the TLL, or it may alternatively be related to a simultaneously increased concentration of polyphenols. In either case, these results are in accordance with the above-mentioned observation that an M_S up to 18% does not have a significant impact in detection performance.

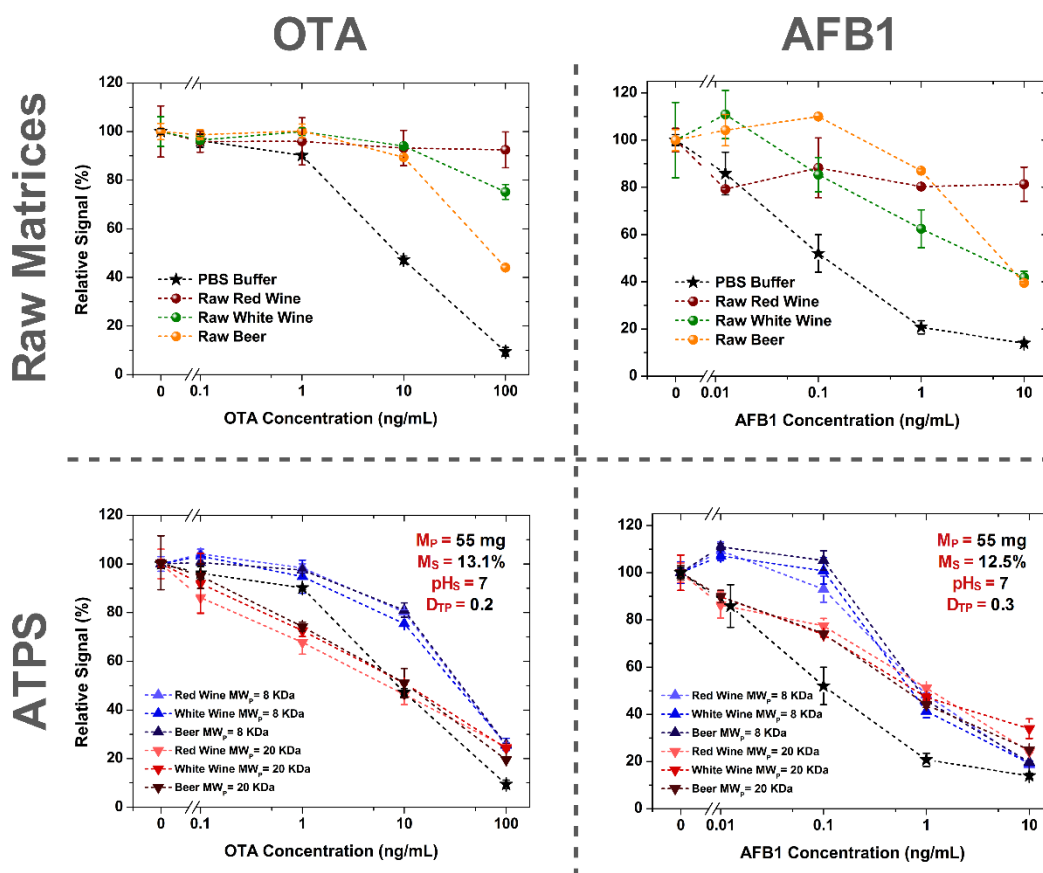


Figure 3.4 - Comparison of icELISA sensitivity using either raw red/white wines or beer matrices as SUA (top) or ATPS processed samples (bottom). The curve obtained in PBS buffer is represented in both conditions for direct visual comparison. The relative signal values are calculated as the ratio between the absorbance at a given analyte concentration and the average absorbance value of the blank (0 ng/mL analyte). All blank values are an average of four independent assays, while the remaining values are an average of two independent assays.

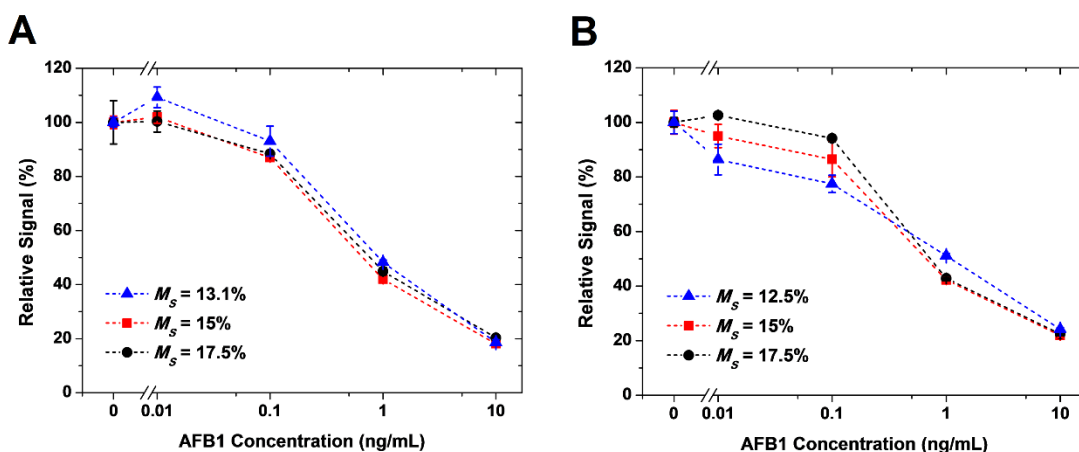


Figure 3.5 - icELISA results for AFB1 spiked in red wine, processed with ATPS with increasing M_S values. The remaining conditions are: $pH_S = 7$; $M_P = 60$ mg; $MW_P = 8$ kDa; $D_{TP} = 0.2$ (a) or $pH_S = 7$; $M_P = 60$; $MW_P = 20$ kDa; $D_{TP} = 0.3$ (b). The relative signal values are calculated as the ratio between the absorbance at a given analyte concentration and the average absorbance value of the blank (0 ng/mL analyte). All blank values are an average of four independent assays, while the remaining values were the average of two independent assays.

3.4. General concept of integrated extraction and immunodetection

The design principle of the microfluidic structure for an integrated ATPE sample processing and detection system using an icFLISA is shown in **Figure 3.6**. First, red wine spiked with salt (henceforth referred to as SRW), containing a given amount of OTA, converges with a PEG-rich phase (PRP). Then, by providing a sufficient length (L), the partition of both OTA and polyphenols (PPs), the latter representing a major part of the colored/ auto-fluorescent compounds in wine, occurs from the salt-rich phase (SRP) to the PEG-rich phase (PRP) [274] (extraction module). An anti-OTA IgG solution is simultaneously inserted through a third inlet and converges with the PRP downstream. This solution is then directed towards the OTA-BSA conjugate coated section of the channel, where the icFLISA is performed (detection module). Since in these conditions both OTA and PP partition to the PRP and PPs are known to have a major, albeit possibly not exclusive, role in protein binding and interference, the reported PP-protein interactions [288, 289] and the effect of PEG on preventing immunoassay interference [160, 280, 281] were assessed using protein-FITC conjugate coated microchannels and fluorescence microscopy. Based on quenching effects only, the obtained results strongly suggest that while the PPs are capable of binding with both BSA and IgG, the presence of PEG in solution at typical ATPS PRP concentrations ($\approx 20\%$ (w/w)) drastically reduces these unspecific interactions.

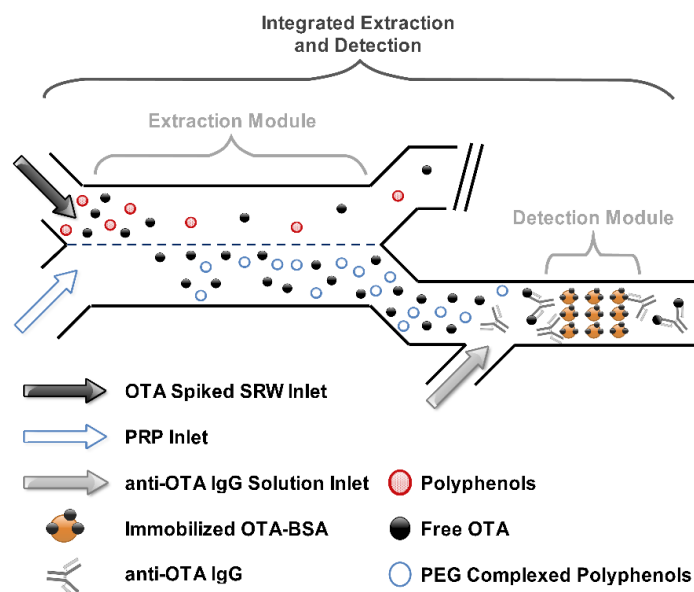


Figure 3.6 - Conceptual schematics of the integrated microfluidic ATPE strategy for matrix neutralization and OTA concentration in red wine samples. SRW refers to red wine spiked with salt and PRP to PEG-rich phase.

3.5. Optimization of the microfluidic FLISA

The first step in the design of a PDMS microfluidic structure for integrated ATPE for sample processing was to develop and optimize an immunoassay module for OTA quantification, allowing the further evaluation of the ATPE performance. For this purpose, a fluorescence-based icFLISA was developed, using plain PBS as model matrix (**Figure 3.7-A**). The ratio between the average fluorescence of each of the independent samples under analysis (SUA) and the reference channel (**Figure 3.7-B**) is used to estimate the OTA concentration present in the target SUA. Since this is a competitive assay, the generated signal is inversely proportional to the OTA concentration in solution.

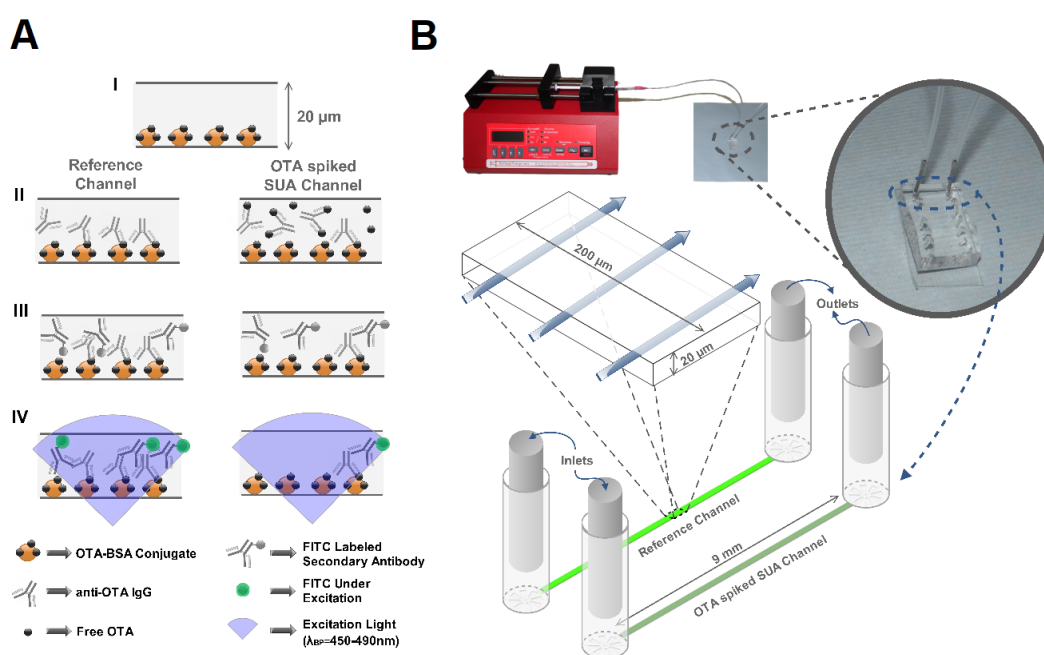


Figure 3.7 - Schematics of the microchannel icFLISA protocol (**A**) and methodology (**B**) used for OTA quantification. (I) Adsorption of OTA-BSA conjugate molecules on the inner channel surfaces. (II) Flow of a reference or OTA spiked solution. (III) Flow of a solution containing FITC labeled secondary antibody. (IV) Fluorescence quantification under the microscope. All previous steps are performed under continuous liquid flow, from the inlets to the outlets as schematized in (**B**).

To optimize the icFLISA, both the OTA-BSA concentration used to coat the channel surface, and the primary antibody (anti-OTA IgG) concentration added to the SUA were studied. For the study of the OTA-BSA concentration, conditions were optimized to allow saturation of the inner channel surfaces, ensuring that the surface coverage is reproducible between experiments, assuming that a multilayer is not formed. To select the appropriate concentration, an experiment was performed in which the OTA-BSA is inserted into the microchannels at increasing concentrations. The channels were then washed using PBS, prior to flowing the secondary antibody solution (anti-

mouse FITC-labeled IgG). As no primary antibody is present, the appearance of fluorescence is related to a non-specific binding of the secondary antibody due to insufficient coating of the surface of the channel with OTA-BSA. The results are shown in **Figure 3.8-A**. To minimize the background signal and reagent consumption, a concentration of 50 $\mu\text{g/mL}$ of OTA-BSA was selected. For the study of the anti-OTA IgG concentration in the SUA and reference solutions, increasing concentrations were tested. The obtained fluorescence ratios were then compared for the detection of 10 ng/mL of OTA spiked in PBS. The results are shown in **Figure 3.8-B**. It can be observed that as the concentration of anti-OTA IgG decreases, the fluorescence in the reference and SUA channels becomes increasingly similar. This observation may be due to the increasing proximity of both the reference and SUA channels to the lower fluorescence detection limit of the experimental setting used. On the other hand, if the concentration of anti-OTA increases above a threshold of 5 $\mu\text{g/mL}$, a plateau is reached for the fluorescence intensity in the reference channel, while the same was not observed for the SUA channel. Therefore, to avoid conditions in which a fluorescence intensity plateau is reached in the reference channel, while still obtaining a relatively good signal ratio, an anti-OTA IgG concentration of 3.75 $\mu\text{g/mL}$ was selected for further experiments.

The microfluidic icFLISA results obtained for increasing OTA concentrations in PBS using the previously optimized conditions are shown in **Figure 3.8-C**. After performing a logarithmic fit, a LoD of 0.15 ng/mL was obtained, which was calculated as the OTA concentration that provides a signal reduction that is 3 times the standard deviation of the average ratio between reference channels (3σ). It is important to highlight that the obtained LoD is more than one order of magnitude below the target regulatory limit for OTA in wines, which stands as a first validation of this immunoassay for OTA monitoring in food samples.

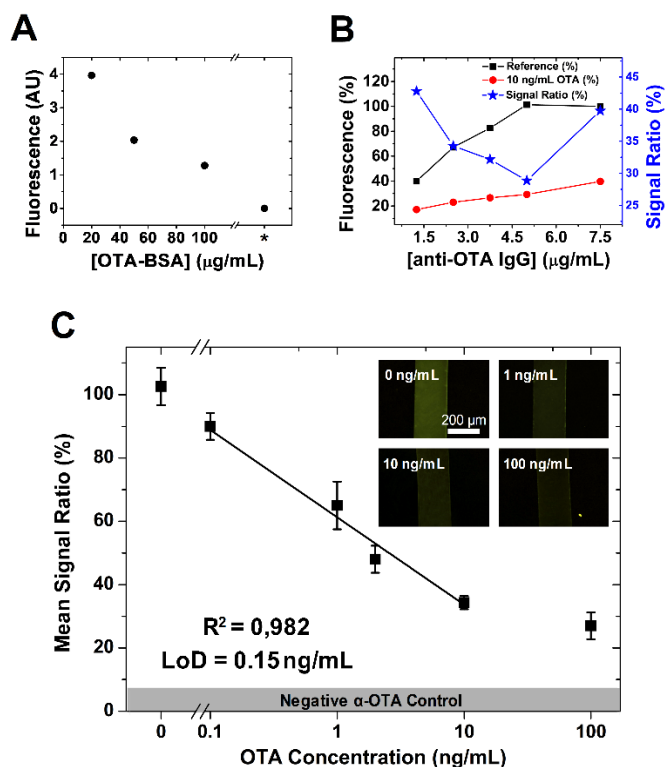


Figure 3.8 - Optimization of the OTA-BSA concentration used to coat the microchannels (A), optimization of anti-OTA IgG concentration added to the SUA (B), and quantification of OTA spiked in PBS, using the optimized conditions (C). For the last point in the plot (A), labeled with an asterisk (*), a solution of 1 mg/mL BSA in PBS buffer was flowed before the secondary antibody, after performing the adsorption step using 100 μg/mL of OTA-BSA solution to achieve a maximum in blocking efficiency. In (B), the fluorescence values for the reference and 10 ng/mL OTA are relative to the highest measured fluorescence intensity (reference channel when using 5 μg/mL anti-OTA IgG). The signal ratio was calculated by dividing the absolute fluorescence in the SUA channel by the fluorescence in the reference channel. In (C), the icFLISA assays were performed using concentrations of OTA-BSA and anti-OTA IgG of 50 μg/mL and 3.75 μg/mL, respectively. The signal ratios were calculated as in (B). All points are an average of three independent experiments, except for 0.1 ng/mL and 100 ng/mL OTA, which are an average of two independent experiments. The error bars relate to the standard deviation (\pm SD) for each set of measurements. The shaded area refers to the non-specific background fluorescence value when the anti-OTA antibody is not present in solution.

3.6. Optimization of the microfluidic ATPE module

The partition of OTA and the PP molecules was studied prior to the integration of the ATPE with the microfluidic icFLISA. Both OTA and PPs are naturally fluorescent under UV light, therefore using an UV filter coupled to the fluorescence microscope allows the imaging of their concentration across the channel in real time. The design shown in **Figure 3.9-A** was used in all subsequent experiments.

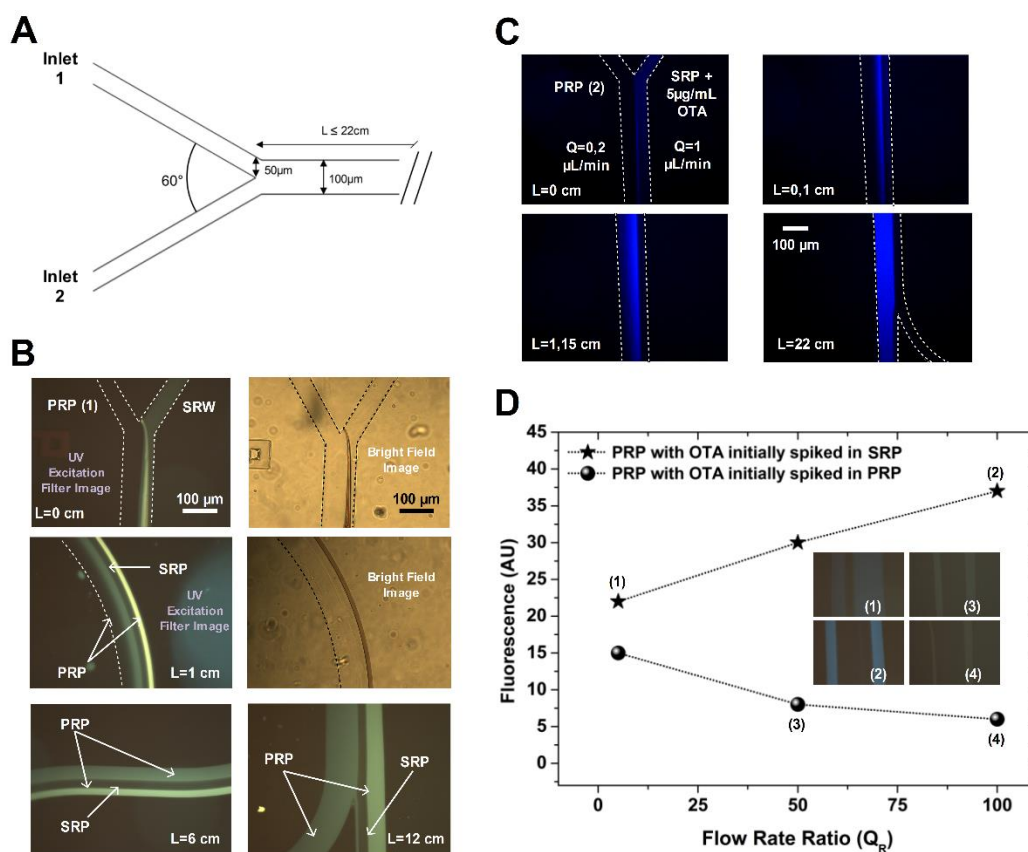


Figure 3.9 - General channel design used for the microfluidic ATPE experiments (**A**), bright field and fluorescence microscopy images of PP (**B**) and OTA (**C** and **D**) at increasing L along the separation channel. **B**- the PP partition was monitored using UV excitation or bright field microscopy. The PRP (18.5% PEG and 4.5% $\text{NaH}_2\text{PO}_4/\text{K}_2\text{HPO}_4$ (pH 7)) was flowed at 0.25 $\mu\text{L}/\text{min}$, while the SRW (red wine with 12.5% $\text{NaH}_2\text{PO}_4/\text{K}_2\text{HPO}_4$ (pH 7)) was flowed at 1 $\mu\text{L}/\text{min}$. The right and the bottom sides of all images correspond to the secondary PRP side. **C**- Fluorescence images of the OTA partition. The blue color was enhanced for improved visualization purposes. PEG 8,000 was used in this experiment, with the SRP and PRP being prepared by mixing a total of 14% PEG, 8% $\text{NaH}_2\text{PO}_4/\text{K}_2\text{HPO}_4$ (pH 6) in a microtube. **D**- Q_R and initial solution effects on OTA fluorescence intensity measured at $L=9$ cm in each of the primary PRP and SRP. The PRP and SRP are aqueous solutions containing 18.5% PEG 20,000 / 4.5% $\text{NaH}_2\text{PO}_4/\text{K}_2\text{HPO}_4$ (pH 7) and 12.5% $\text{NaH}_2\text{PO}_4/\text{K}_2\text{HPO}_4$ (pH 7) respectively. In images (1)-(4), the secondary and primary PRPs are on the left and right sides of the SRP, respectively.

3.6.1. Optimization of polyphenol extraction

The design used for the microfluidic ATPE requires the salt-rich phase (SRP) and PEG-rich phase (PRP) to each flow into channels already at near-equilibrium concentrations for both phase forming components. Therefore, for a concentration of 12.5% $\text{NaH}_2\text{PO}_4/\text{K}_2\text{HPO}_4$ (pH 7) in the SRP, the equilibrium PRP composition is approximately 18.5% PEG 20,000 and 4.5% $\text{NaH}_2\text{PO}_4/\text{K}_2\text{HPO}_4$ (pH 7), according to published binodal curves measured under similar conditions [190]. PEG 20,000 was used for all further experiments unless stated otherwise.

Under these conditions, it was observed that as the SRP, initially containing the interfering PPs, and the PRP were converged, two PRPs are formed at each side of the SRP. As expected, one flows on the side at which the PRP was inserted in the channel (henceforth referred to as primary PRP) and the other on the opposite side of the channel (henceforth referred to as secondary PRP). The formation of this secondary PRP, although unexpected, is highly advantageous as the PP molecules are concentrated in the secondary PRP and can be easily disposed of, thus removing them from the solutions of interest (**Figure 3.9-B** at $L=12$ cm) as will be discussed next. Nevertheless, even if this secondary phase had not formed, the matrix clean up effect still occurred as previously demonstrated by batch studies at lab scale [274].

Another phenomenon, observed in **Figure 3.9-B** at $L=0$ cm and $L=1$ cm, was the precipitation of PPs at the SRW-PRP interface possibility due to PRP saturation. These precipitates were not re-dissolved by the SRP, accumulating in the SRP insertion side of the channel, but were easily dissolved by the PRP, flowing as a highly rich PP solution in the secondary PRP that was being simultaneously formed at $L=0$. It should be noted that this secondary PRP was also formed without adding wine to the SRP, thus its formation is not related with the precipitation of the PPs. Curiously, this secondary PRP was not observed when PEG 8,000 was used under the same flow rate conditions. The formation of this secondary phase is possibly due to the PRP-PDMS interface having a more favorable molecular interaction than the SRP-PDMS, considering the observed contact angles of approximately 105.7° and 113.5° , respectively. Therefore, the hypothesis is that the PRP crosses the SRP as a thin liquid film, in contact with the bottom and top surfaces of the channel. This is strongly supported by (1) the gradual increase in width of this secondary PRP with increasing L ; (2) a very fast PP and OTA mass transfer from the SRW to the secondary PRP, justified by the increased contact area between the phases and (3) the gradual re-distribution of both PP and OTA molecules between the primary and secondary PRPs along the separation channel. Furthermore, in accordance to the contact angle hypothesis described above, it was also observed that when BSA was adsorbed on the channel surface, rendering it more hydrophilic than the native PDMS surface, the opposite effect was observed as the SRP crosses the PRP through the top and bottom sides of the channel, forming a secondary SRP. Interestingly, with an L up to 12 cm, the PP concentration in the primary and secondary PRP did not achieve an equal value, as shown in **Figure 3.9-B**, possibly due to the relatively high molecular weight and low diffusion coefficient of some PPs. This property presents an advantage when

collecting the primary PRP for further detection, since it is strongly depleted of PPs in comparison to the secondary PRP, particularly at a shorter L . Furthermore, by varying the flow rates of the SRW (Q_S) and PRP (Q_P), it could be concluded that to obtain a stable and collectable primary PRP, the flow rate ratio Q_R (Q_S/Q_P) is limited to a value in the range of 5-10 ($Q_S=1\mu\text{L}/\text{min}$), as at larger Q_R the PRP crosses the SRP almost completely to the opposite side of the separation channel, forming a relatively slow flowing and unstable secondary PRP, very concentrated in PPs.

3.6.2. Optimization of OTA extraction

It is shown in **Figure 3.9-C** that the partition of OTA from the SRP to the PRP is a very fast process with the SRP reaching an equilibrium OTA concentration at $L=2.5$ cm, which at the flow rates used for the SRP corresponds to a residence time of 3 s. A similar observation was also made when using PEG 20,000, despite the formation of a primary and secondary PRPs. This fast diffusion is due to the small molecular size of OTA, resulting in a high diffusion coefficient. In contrast, in the case an antibody, which has nearly 400 times the MW of OTA, it was reported by Silva and co-workers that at least 16 cm of channel is required for full partition under similar conditions [256]. It is important to highlight that PEG 8,000 was used for this experiment instead of PEG 20,000 (which does not have a significant effect in the partition behavior of OTA as previously observed [274]) since the formation of a secondary PRP would promote a quasi-instantaneous mass transfer in the beginning of the channel, obscuring the visualization of its inherent partition kinetics.

A pronounced concentration effect of OTA in the PRP could also be observed, as the fluorescence intensity obtained in the PRP after equilibrium is increased by nearly a factor of 3 in comparison to the initial concentration in the SRP. To evaluate whether this effect was dependent on the flow rates used, the Q_R was varied between 5 (Q_S and Q_P set to 1 and 0.2 $\mu\text{L}/\text{min}$ respectively) and 100 (Q_S and Q_P set to 2 and 0.02 $\mu\text{L}/\text{min}$ respectively), with OTA spiked initially in either the PRP or the SRP. The results are shown in **Figure 3.9-D**. When OTA was initially spiked in the SRP, the OTA concentration in the PRP at $L=9$ cm increased linearly with Q_R ($R^2=0.995$). On the other hand, when OTA was initially spiked in the PRP, the OTA concentration in the PRP, at $L=9$ cm, decreased with an increase in Q_R . Due to the strong partition of OTA to the PRP [274] no OTA could be measured in the SRP at $L=9$ cm in any of the previous conditions.

These previous observations can possibly be explained by introducing an extra factor defined according to **Equation 3.2**.

$$\gamma = \frac{v_P}{v_S} \quad (3.2)$$

v_P and v_S correspond to the velocities (independent of the channel cross-section area) of the PRP and SRP phases, respectively. Considering an extreme condition of $\gamma \ll 1$ and OTA spiked initially in the SRP phase with a concentration of β , this value will tend to be kept at a value of β in the SRP at a given L . On the other hand, the concentration of OTA in the PRP will tend to βK_{OTA} , with K_{OTA} being the partition coefficient for OTA, defined according to **Equation 3.3**.

$$K_{OTA} = \frac{[OTA]_t}{[OTA]_b} \quad (3.3)$$

$[OTA]_t$ and $[OTA]_b$ are the equilibrium concentrations of OTA in the top or bottom phases, when the system is prepared in batch conditions [269]. In a different situation in which the OTA is initially spiked in the PRP, the high speed of the SRP will tend to continuously dilute the PRP to maintain the equilibrium driven by K_{OTA} . Therefore, both concentrations will tend to 0. However, it is important to highlight that such extreme conditions are not feasible for testing, as there is a limited range of flows for which the interface stability can be maintained along the separation channel. For example, while it is possible to reach very high Q_R values for a PEG-salt system, as shown in this chapter, Q_R values lower than 1 do not provide a stable interface along the separation channel [290].

From both the PP and OTA microfluidic ATPE experiments it is possible to conclude that there is an optimum Q_R value that simultaneously guarantees the formation of a stable primary PRP and maximizes the OTA concentration in the PRP. Considering both constraints, a Q_R of 5 ($Q_P = 0.2 \mu\text{L}/\text{min}$, $Q_S = 1 \mu\text{L}/\text{min}$) was selected for the experiments presented in the following section.

3.7. Integration of ATPE in series with the optimized FLISA for simultaneous sample preparation and detection

Figure 3.10 shows the microchannel design consisting of the integration of the two previously optimized modules, for integrated extraction, concentration and detection of OTA. This structure comprises 5 key elements. First, the SRP and PRP are brought together in region I. Then, after molecular partition along the 2.72 cm long separation

channel, sufficient for full OTA partition to the PRP as previously discussed in **Section 3.6.2**, a fraction of the primary PRP is collected through a 40 μm wide channel (region II). The collected PRP is then converged with a solution containing primary antibody in region III. Downstream, after passing through a micromixing region of 90 $^\circ$ turns, 1/3 of the channel (on the side of the insertion of the primary antibody solution) is diverged (region IV) towards the icFLISA channel (IC), shown in region V, where the OTA-BSA conjugate was previously adsorbed. As a technical note, it can be noticed on **Figure 3.10** that in both regions II and IV, the waste (bottom) channels extend far downstream, instead of having an outlet hole close to the bifurcation. This has the purpose of increasing the amount of flow resistance in the waste channel, allowing the liquid to flow into the collection channels.

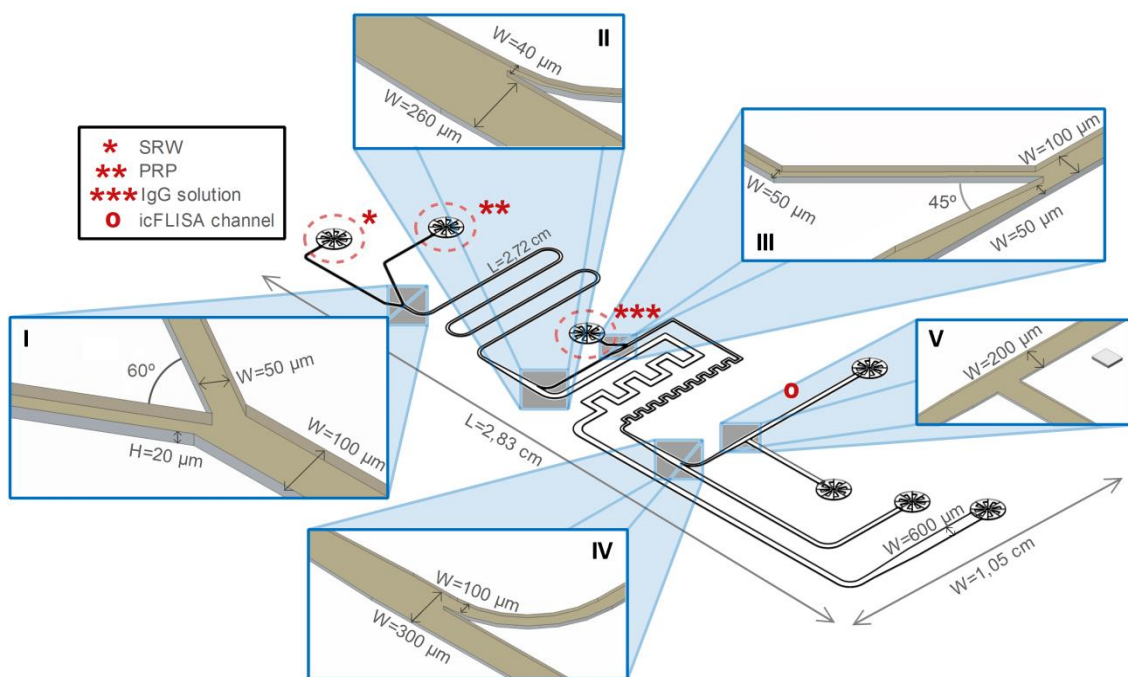


Figure 3.10 - Schematics of the PDMS structure optimized to perform an integrated microfluidic ATPE step followed by an icFLISA. L stands for length, W for width and H for height. The height is constant for the entire channel network.

Highlights on the main experimental steps to control the liquid flow in the microfluidic channel network are shown in **Figure 3.11**. Overall, this comprises A- OTA-BSA adsorption exclusively on the detection channel (o), B- stabilization of the biphasic interface along the separation channel and convergence of the SRP with the anti-OTA IgG solution, C- flow of the anti-OTA IgG spiked SRP solution into the detection channel and finally D- flow of a solution containing FITC conjugated secondary antibody.

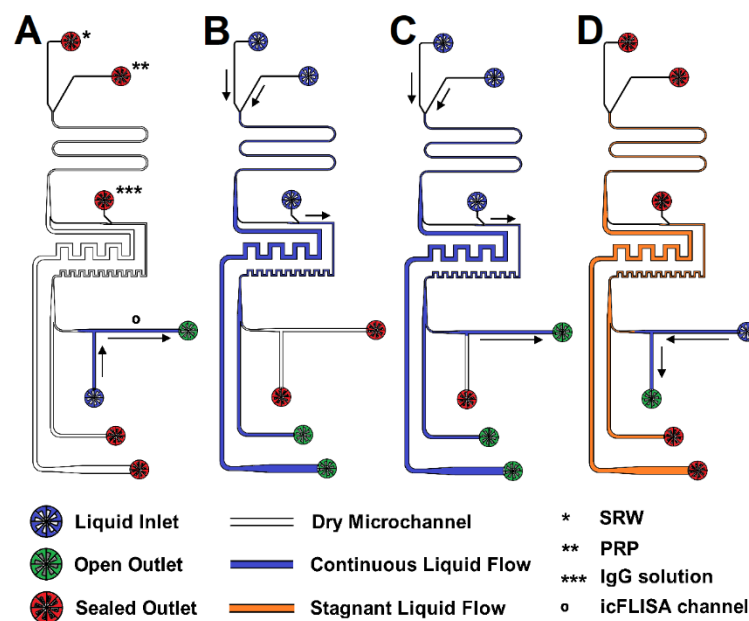


Figure 3.11 - Schematics of the main microfluidic control steps used to perform the integrated ATPE-icFLISA assay. **A**- Adsorption of OTA-BSA on the IC, followed by a washing step. **B**- Stabilization of both the biphasic interface and the flow of anti-OTA IgG solution through the center inlet. **C**- flow of OTA concentrated SUA through the IC. **D**- washing and subsequent flow of a secondary antibody solution.

Bright field images of the microfluidic structure during red wine processing are shown in **Figure 3.12**. Two of the structures shown in **Figure 3.10** were integrated in a single PDMS chip to allow easy comparison of the results obtained for each pair of either OTA spiked or non-spiked reference red wine solutions. The integrated microfluidic ATPE-FLISA is performed by flowing the OTA spiked SRW, the reference SRW and the PRP into inlets 1, 2 and 3 respectively. One important condition to consider is that SRW flows first in the microchannel and only then PRP is initiated in parallel with the already existing flow of SRW. Initiating either a concurrent flow, with both SRW and PRP being introduced at the same time, or flowing the PRP first, would cause the PRP to meet the SRP channel, inducing precipitation, which accumulates gradually, eventually disturbing the flow and interface position. Simultaneously with the PRP and SRW, the anti-OTA IgG solution is introduced into inlets 4 (**Figure 3.12**). The contact between the anti-OTA IgG solution and the PRP can be easily seen due to differences in light refraction. Therefore, the blue region in **Figure 3.12** is an adequate control point to assess both interface position and anti-OTA IgG solution insertion stability, before allowing the liquid to flow into the ICs.

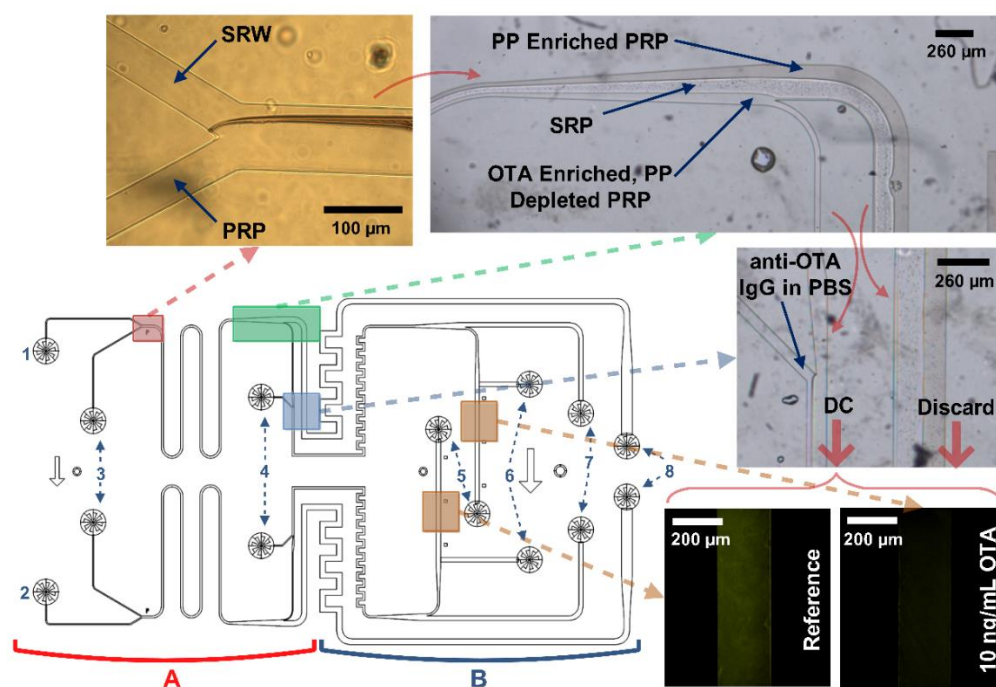


Figure 3.12 - Microscopy images and results obtained for the processing of a non-spiked reference and OTA spiked (10 ng/mL) SRW (12.5% $\text{NaH}_2\text{PO}_4/\text{K}_2\text{HPO}_4$, pH 7) samples. The PRP has a composition of 18.5% PEG and 4.5% $\text{NaH}_2\text{PO}_4/\text{K}_2\text{HPO}_4$, pH 7). “A” corresponds to the microfluidic portion responsible for the extraction of OTA, while “B” corresponds to the module responsible of performing iCLISA. The structure is composed of 2 independent channel networks with one being directed for the reference and the other for the OTA spiked SUA. The O-shaped structure (to the left of outlets 5) near the ICs labels the reference channel. The same applies to the arrow-like structures. (1) OTA spiked SRW inlet. (2) Reference SRW inlet. (3) PRP inlet. (4) anti-OTA IgG solution inlet. (5) IC outlets/ inlets (assay step dependent). (6) IC inlets/ outlets (assay step dependent). (7) anti-OTA IgG depleted solution outlet. (8) SRP and secondary PRP outlet.

The results obtained for the quantification of OTA spiked in red wine using the ATPE strategy are shown in **Figure 3.13**. It can be observed that the results are very similar to those obtained when performing the detection in plain PBS buffer and far superior to those obtained using raw red wine without integrated processing, in which an OTA concentration of 100 ng/mL is indistinguishable from the reference. The absolute signal intensities obtained for the reference channel using red wine are only slightly lower (19-23 AU) than those obtained when using PBS buffer (25-30 AU). Finally, to test the matrix-to-matrix robustness of the proposed method, white wine was analyzed using the same conditions. It is possible to observe that the slope of the obtained curve is comparable to the one obtained for red wine. This result supports the robustness of this technique to cope with wine matrixes of different compositions. Interestingly, no PP precipitates could be observed in the microchannel walls during white wine processing, possibly due to their considerably lower concentration [291]. Furthermore, the formation of a secondary PRP was not observed in this case, possibly due to a more comparable

affinity to the PDMS walls between the salt-spiked white wine and the PRP. Nevertheless, this further supports the claim that while the formation of the secondary PRP may be advantageous in reducing PP concentration in the primary PRP for red wine processing, the absence of its formation was not observed to significantly reduce OTA detection sensitivity for white wine.

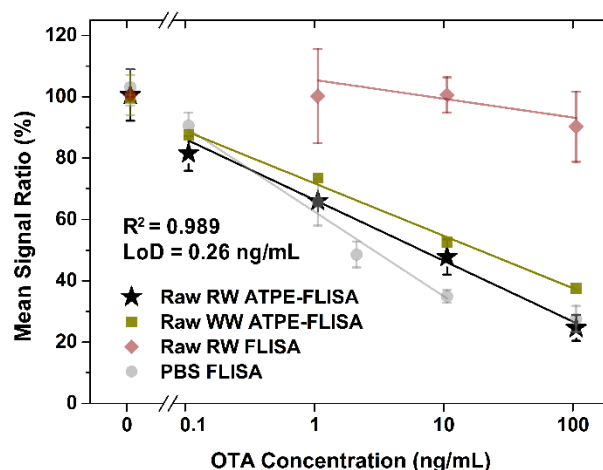


Figure 3.13 - icFLISA quantification of OTA spiked in red wine using a microfluidic integrated ATPE. For red wine (RW), the relative signal values with 0.1, 1 and 100 ng/mL OTA were obtained in duplicate, while the values for 0 and 10 ng/mL OTA were obtained in triplicate. For white wine (WW) the relative signal values are single experiments, except for the reference (0 ng/mL OTA), which was measured in triplicate. Error bars relate to \pm SD for each set of measurements. The measurements obtained for OTA spiked in raw red wine and PBS buffer are plotted for comparison.

3.8. Chapter conclusions

This work demonstrated the successful use of polymer-salt ATPS to enhance analyte detection sensitivity in immunoassays, allowing a simultaneous concentration and neutralization of matrix interference. Using a model icELISA to quantify two environmentally relevant mycotoxins in complex wine and beer matrices, the results were improved at least by one order of magnitude in comparison to the detection in raw matrices, providing either comparable or better results than those obtained using PBS control conditions. The MW_P had a significant impact on the detection curve. This allowed for either a more sensitive but less accurate quantification, which spans a large analyte concentration range ($MW_P = 20$ kDa) or a less sensitive, but more accurate quantification which can be directed towards “yes-no” types of response ($MW_P = 8$ kDa). The developed method proved to be robust in providing a high and similar sensitivity regardless of the analyte being spiked in PBS or polyphenol-rich wine.

Furthermore, an integrated microfluidic system comprising two modules was demonstrated to perform complex matrix clean-up and OTA concentration based on an ATPE, followed by the detection and quantification of OTA via icFLISA, respectively. This strategy allowed the quantification of OTA spiked in raw red wine with a LoD of 0.26 ng/mL and a linear range (in the log scale) spanning three orders of magnitude, from 0.1 to 100 ng/mL, using a microchannel icFLISA. In addition, this sensitivity was observed for different matrices making this system generalizable to a generic sample preparation and sensing platform.

While the model immunoassay used in this work required the use of a microscope for signal quantification, integrated optical detection of fluorescence can be achieved through on-chip fluorescence photodetectors [292]. Furthermore, by using a different molecule for signal generation such as HRP, similar sensitivities are expected. This would allow, by using luminol for chemiluminescence generation, the use of a similar strategy developed by Novo and co-workers [293], comprising the addition of integrated photodiodes for signal acquisition. Therefore, by including electronic addressing, integrated transduction of the molecular recognition event and designing automatic fluidic handling mechanisms, this same method for integrated sample processing and detection could provide a full sample-to-answer approach. Hence, to fully exploit the potential of this strategy, the automation of the process to minimize user input to perform the assay is required which is on-going research. Furthermore, it is expected that the strategy proposed can be extended to other relevant toxins, such as AFB1, and other food matrices, such as coffee, extracts of cereal based products, and extracts of chili pepper [280, 294, 295], which have also been observed to suffer from significant immunoassay matrix interference.

Chapter 4

Aqueous Two-Phase Systems for the Simultaneous Extraction and Concentration of Mycotoxins in Solid Samples

This chapter reports the extension of the ATPE-based sample preparation to solid samples of interest, which are significantly more common in the scope of food and feed safety than liquid samples according to **Table 1.2**, **Table 1.3** and **Table 1.4**. To achieve rapid mycotoxin detection, several biosensing strategies have been published, many reaching assay times of the order of a few minutes. However, the majority of these rely on sample preparation methods based on volatile organic solvents, often comprising complex multi-step procedures and do not provide any clean-up and/or concentration effects. Here, a novel sample preparation methodology based on a green, non-toxic and inexpensive polyethylene glycol-sodium citrate aqueous two-phase system is reported, providing single-step extraction and concentration of three target mycotoxins within 20 min: aflatoxin B1 (AFB1), ochratoxin A (OTA) and deoxynivalenol (DON). With point-of-need applications in mind, the extraction procedure was optimized and validated using a rapid multi-toxin microfluidic competitive immunoassay. The assay was successfully tested with spiked complex solid matrices including corn, soy, chickpea and sunflower-based feeds and limits of detection of $4.6 \text{ ng.g}^{-1} \pm 15.8\%$, $24.1 \text{ ng.g}^{-1} \pm 8.1\%$ and $129.7 \text{ ng.g}^{-1} \pm 53.1\%$ ($\pm\text{CV}$) were obtained in corn for AFB1, OTA and DON, respectively. The contents of this chapter are reproduced with appropriate adaptations from one original research article [180].

4.1. Materials and experimental methods

4.1.1. Chemicals and biologicals

Polyethylene glycol (PEG) with molecular masses of 3.5 kDa, 8 kDa and 20 kDa, sodium phosphate monobasic, potassium phosphate dibasic, sodium citrate tribasic dehydrate, sodium bicarbonate, phosphate buffered saline (PBS) tablets (137 mM NaCl, 2.7 mM KCl, 10 mM phosphate, pH 7), 1,1'-Carbonyldiimidazole (CDI), acetone (99%),

anhydrous ethanol, methanol and acetonitrile, bovine serum albumin (BSA), ochratoxin A (OTA), aflatoxin B1 (AFB1), deoxynivalenol (DON), OTA-BSA conjugates and AFB1-BSA conjugates were purchased from Sigma-Aldrich. DON-BSA conjugates were prepared in-house using CDI chemistry as described elsewhere [42]. The stock solutions of mycotoxins were prepared as follows: OTA was dissolved in 33% methanol in water ($100 \mu\text{g}\cdot\text{mL}^{-1}$), AFB1 was dissolved in anhydrous ethanol ($200 \mu\text{g}\cdot\text{mL}^{-1}$) and DON was dissolved in anhydrous methanol ($1 \text{ mg}\cdot\text{mL}^{-1}$). Affinity purified anti-OTA rabbit polyclonal antibodies conjugated with horse radish peroxidase (HRP) were purchased from Immunechem Pharmaceuticals (Burnaby, Canada), anti-AFB1 mouse monoclonal antibodies (AFA-1) were purchased from Abcam (Cambridge, UK) and anti-DON mouse monoclonal antibodies were purchased from Biotex (Berlin, Germany). The anti-AFB1 and anti-DON antibodies were conjugated with HRP using an HRP labeling kit, purchased also from Abcam, and performing the procedure provided by the supplier. Luminol was purchased as a SuperSignal™ West Femto Maximum Sensitivity Substrate, supplied by Thermo Fisher Scientific. All solutions were prepared using ultrapure water obtained from a MilliQ system from EMD Millipore. All feeds under study were kindly supplied by EWOS® Innovation (Dirdal, Norway) within the scope of the project DEMOTOX (FP7-SME-2013- 604752).

4.1.2. Spectrofluorometric and spectrophotometric quantification of AFB1, OTA and DON in the top phase of PEG-phosphate and PEG-citrate ATPSs

Each ATPS was prepared in duplicate by mixing 1.2 mL of the respective salt solution with a certain volume of PEG (50%), ranging from 55 to 100 μL according to **Table 4.1**, to generate a top PEG-rich phase with approximately 80 μL . Then, the mycotoxins were spiked in one of the ATPS duplicates, henceforth referred to as “sample tube” for a final concentration of $1 \mu\text{g}\cdot\text{mL}^{-1}$ for OTA and AFB1 and $10 \mu\text{g}\cdot\text{mL}^{-1}$ for DON. In the other ATPS duplicate, henceforth referred to as “calibration tube” the same volume of solution without mycotoxins was added. Both tubes for each condition were then vigorously mixed in a vortex mixer for 30 s and subsequently centrifuged at 2000 g for 1 min to separate the phases. The concentrations of AFB1 and OTA were measured through their intrinsic fluorescence ($\lambda_{\text{ex}} = 369 \text{ nm}$; $\lambda_{\text{em}} = 439 \text{ nm}$ for AFB1 and $\lambda_{\text{ex}} = 333 \text{ nm}$; $\lambda_{\text{em}} = 446 \text{ nm}$ for OTA) using a Varian Cary Eclipse plate reader spectrofluorimeter (800 V, 5 nm slits) and DON was measured by spectrophotometry ($\lambda = 230 \text{ nm}$) in a SpectraMax Plus 384 Microplate Reader from Molecular Devices. To perform the

measurement of the mycotoxin concentration in the top phase of each system, 20 μL of each top phase from the sample tubes were mixed with 80 μL of water and added to a well and compared in terms of fluorescence/absorbance with two other wells containing (1) 20 μL of the top phase of the calibration tube plus 80 μL of water (blank, used to subtract the background) and (2) the same composition as the blank plus 2 $\mu\text{g}\cdot\text{mL}^{-1}$ AFB1 or OTA and 20 $\mu\text{g}\cdot\text{mL}^{-1}$ of DON (single point calibration).

Table 4.1 - Summary of the results obtained for the partition of AFB1, OTA and DON in PEG-phosphate and PEG-citrate aqueous two-phase systems (ATPS). The final top phase volume for all systems was approximately 80 μL . The initial concentration of each mycotoxin in 1.2 mL of salt was 1 $\mu\text{g}\cdot\text{mL}^{-1}$ for AFB1 and OTA and 10 $\mu\text{g}\cdot\text{mL}^{-1}$ for DON. The estimated partition coefficients were calculated according to **Equation 4.1**, where $[M]$ and $m(M)_T$ refer to the concentration and total mass of each mycotoxin, V to the volume and the subscripts ATPS and TP to the total system or top phase, respectively. The extraction yield is calculated as the ratio of $m(M)_{TP}$ relative to $m(M)_T$.

System Composition	Mycotoxin concentration in the top phase ($\mu\text{g}\cdot\text{mL}^{-1}$)			Estimated partition coefficient (K)			Extraction yield (%)		
	AFB1	OTA	DON	AFB1	OTA	DON	AFB1	OTA	DON
100 μL PEG 3 350 (50% w/w) + 1.2 mL NaH ₂ PO ₄ /K ₂ HPO ₄ (13.75% w/w)	3.5 \pm 0.5	3.0 \pm 0.2	16.0 \pm 0.1	4.6 \pm 0.7	3.7 \pm 0.2	1.83 \pm 0.01	23 \pm 3	19.7 \pm 1.1	10.7 \pm 0.1
100 μL PEG 3 350 (50% w/w) + 1.2 mL NaH ₂ PO ₄ /K ₂ HPO ₄ (15% w/w)	5.7 \pm 0.6	6.1 \pm 0.2	17.3 \pm 0.1	9.3 \pm 1.0	10.4 \pm 0.4	1.99 \pm 0.02	38 \pm 4	40.5 \pm 1.6	11.5 \pm 0.1
55 μL PEG 8 000 (50% w/w) + 1.2 mL NaH ₂ PO ₄ /K ₂ HPO ₄ (12.5% w/w)	5.2 \pm 0.7	4.1 \pm 0.2	14.8 \pm 0.3	7.8 \pm 1.1	5.6 \pm 0.3	1.61 \pm 0.04	35 \pm 5	27.5 \pm 1.5	9.9 \pm 0.2
65 μL PEG 8 000 (50% w/w) + 1.2 mL NaH ₂ PO ₄ /K ₂ HPO ₄ (13.75% w/w)	7.9 \pm 0.7	4.3 \pm 0.2	16.9 \pm 0.3	16.3 \pm 1.4	5.9 \pm 0.2	1.88 \pm 0.03	52 \pm 4	28.5 \pm 1.1	11.2 \pm 0.2
75 μL PEG 8 000 (50% w/w) + 1.2 mL NaH ₂ PO ₄ /K ₂ HPO ₄ (15% w/w)	9.8 \pm 1.0	5.0 \pm 0.2	22.7 \pm 1.2	28.1 \pm 2.8	7.5 \pm 0.3	2.66 \pm 0.14	65 \pm 7	33.4 \pm 1.2	15.1 \pm 0.8
60 μL PEG 20 000 (50% w/w) + 1.2 mL NaH ₂ PO ₄ /K ₂ HPO ₄ (12.5% w/w)	5.3 \pm 0.3	4.0 \pm 0.2	14.8 \pm 0.3	8.0 \pm 0.5	5.5 \pm 0.2	1.62 \pm 0.03	35 \pm 2	27.0 \pm 1.1	9.9 \pm 0.2
70 μL PEG 20 000 (50% w/w) + 1.2 mL NaH ₂ PO ₄ /K ₂ HPO ₄ (13.75% w/w)	4.8 \pm 0.4	4.2 \pm 0.1	15.9 \pm 0.4	7.0 \pm 0.6	5.7 \pm 0.2	1.77 \pm 0.04	32 \pm 3	27.9 \pm 0.8	10.6 \pm 0.2
80 μL PEG 20 000 (50% w/w) + 1.2 mL NaH ₂ PO ₄ /K ₂ HPO ₄ (15% w/w)	6.6 \pm 0.5	4.6 \pm 0.2	17.2 \pm 0.2	11.7 \pm 1.0	6.6 \pm 0.3	1.94 \pm 0.02	44 \pm 4	30.4 \pm 1.3	11.4 \pm 0.1
75 μL PEG 8 000 (50% w/w) + 1.2 mL trisodium citrate (15% w/w)	4.4 \pm 0.6	3.1 \pm 0.2	15.2 \pm 3.2	6.1 \pm 0.8	3.8 \pm 0.2	1.69 \pm 0.35	29 \pm 4	20.4 \pm 1.1	10.2 \pm 2.1

$$K_p = \frac{[M]_{TP}}{\frac{m(M)_T - [M]_{TP} \times V_{TP}}{V_{ATPS} - V_{TP}}} \quad (4.1)$$

4.1.3. Sample processing using aqueous two-phase extraction

All feeds under study were manually ground to a fine powder using a marble mortar and pestle and stored at 4 °C until further processing. First, 400 ± 1 mg of feed were weighed in a 2 mL microtube using an analytical balance and spiked with either (1) 1 μ L mycotoxin solution prepared in absolute ethanol to the intended final concentration in $\mu\text{g}\cdot\text{g}^{-1}$ of feed or (2) 1 μ L absolute ethanol in the case of the feed used as reference. After adding 1 μ L of solution to the bulk of the feed, the sample was vigorously mixed with a vortex mixer and left open to the air at RT for 5 min, sufficient for ethanol to fully dry. This spiking method was validated to provide comparable results as those for a naturally contaminated sample, as discussed ahead in **Section 4.9**. The extraction solution comprising 1200 μ L salt solution (phosphate or citrate, 12.5-15% w/w) plus 55-100 μ L of PEG solution (50% w/w with a MW of 3.35 kDa-20 kDa) according to **Table 4.1**, was subsequently added to the feed and immediately subjected to a continuous vigorous mixing for 3 min at 2400 rpm in a vortex mixer. After the extraction, the tube was then centrifuged at 2000 g in a compact Labnet (Edison, NJ, USA) Spectrafuge™ mini-centrifuge for 15 min. After phase separation, if the feed under analysis had a low density, resulting in the accumulation of solid debris at the interface, 50 μ L of top phase were collected to a second 1.5 mL microtube and centrifuged again for 5 min to prevent the co-recovery of solid debris or bottom salt-rich phase. Finally, 2 μ L of top phase were collected to perform the subsequent immunoassay.

4.1.4. Microfluidic immunoassays

The microfluidic immunoassays were performed by sequentially pulling solutions from the outlets. The first step of the assay is the adsorption of the mycotoxin-BSA conjugates on the microchannel surface by flowing solutions prepared in PBS with a concentration of 50 $\mu\text{g}\cdot\text{mL}^{-1}$ for 5 min at a flow rate of 0.5 $\mu\text{L}\cdot\text{min}^{-1}$. To make the assay toxin-specific, each microchannel was coated with a single type of mycotoxin-BSA-conjugate. Then, the microchannels were blocked by flowing a solution of 4% (w/v) BSA in PBS for 5 min at 0.5 $\mu\text{L}\cdot\text{min}^{-1}$ and subsequently washed with PBS at a flow rate of 5 $\mu\text{L}\cdot\text{min}^{-1}$ for 1 min. The 2 μ L of top phase collected from the extraction procedure were diluted with an anti-mycotoxin IgG-HRP solution prepared in PBS for a total dilution of 10-20x, containing a final concentration of 5 $\mu\text{g}\cdot\text{mL}^{-1}$, 2.5 $\mu\text{g}\cdot\text{mL}^{-1}$ and 5 $\mu\text{g}\cdot\text{mL}^{-1}$ of antibody-HRP conjugate for AFB1, OTA and DON detection respectively. This sample-under analysis (SUA) was flowed through the microchannel at 0.5 $\mu\text{L}\cdot\text{min}^{-1}$ for 5 min.

4.2. Aqueous two-phase extraction coupled to a microfluidic immunoassay for detecting mycotoxins in feeds

The general concept of a single-step aqueous-two-phase extraction to simultaneously extract and pre-concentrate mycotoxins from a ground dried sample is schematically illustrated in **Figure 4.1-A** to **Figure 4.1-F**. To simplify the procedure, a biphasic extraction solution with a certain composition of two incompatible solutes, in this case a polymer (PEG) and a salt, is pre-prepared (A2), homogenized (B2), and added to a certain mass of target feed (B1). The extraction solution is prepared to form a small volume of top phase relative to the bottom phase (>10 times smaller). The top PEG-rich phase is the solution in which the target mycotoxins are concentrated in. Then, the mixture is agitated vigorously for a short time (C) and subsequently settled, and phase separated via a relatively weak centrifugation force of 2000 g. In the case of mycotoxins, their small molecular weights typically require a competitive immunoassay, and therefore the top phase is subsequently collected (E) and diluted with a solution containing a peroxidase labeled anti-mycotoxin antibody (F). The rapid and point-of-need compatible microfluidic competitive immunoassay, previously developed and optimized by Soares, Ramadas and co-workers [21], is described in **Figure 4.1-G** and **Figure 4.1-H**. To generate a signal, a continuous flow of luminol plus hydrogen peroxide solution through the channel produces a stable plateau of chemiluminescence, which is inversely proportional to the concentration of target mycotoxin present in the SUA. In order to always have a calibrated signal for all experiments, the measurements were performed relative to a reference feed sample, certified by HPLC-MS to contain very low concentrations ($\ll 1 \text{ ng.g}^{-1}$) of the target mycotoxins OTA, AFB1 and DON. An example of how the quantification procedure is performed in terms of absolute chemiluminescence and relative signal is shown in **Figure 4.2**.

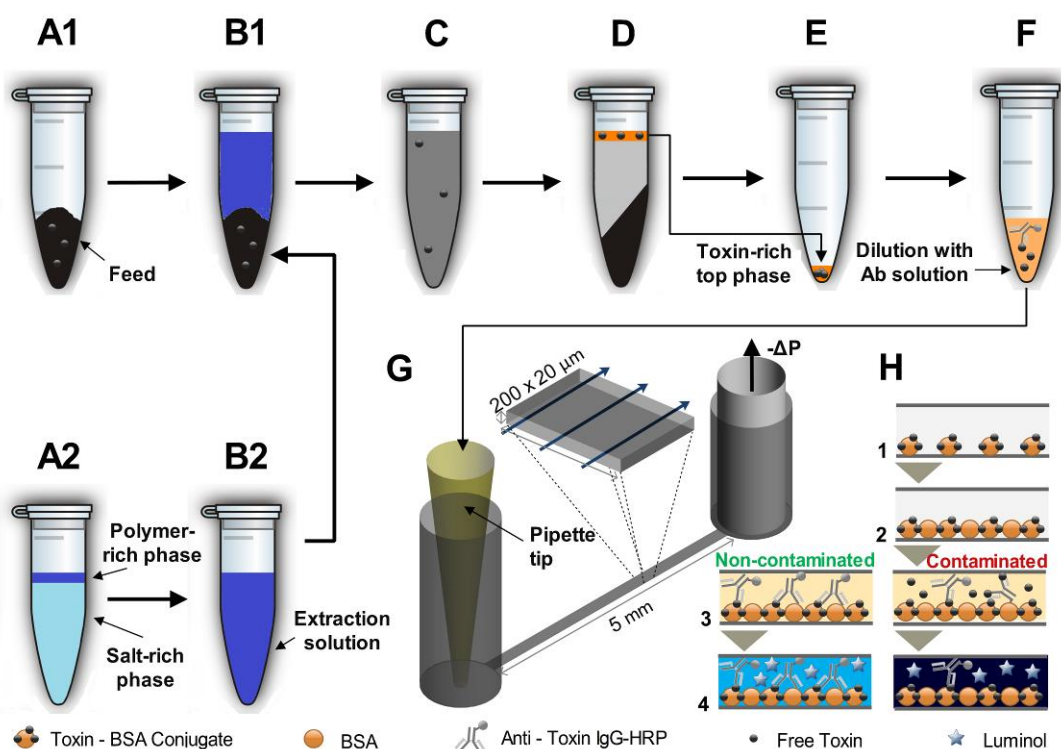


Figure 4.1 - Schematics of the ATPS-based procedure used to extract and concentrate target mycotoxins from a dried feed material and subsequent immunodetection using a miniaturized flow-based immunoassay. **A1**- sampling of a certain mass of ground target feed. **A2**- ATPS-based extraction solution composed of a top PEG-rich and a bottom salt-rich immiscible phase. **B2**- Homogenization of the extraction solution. **B1**- addition of the homogenized extraction solution to the feed sample. **C**- Vigorous mixing of the feed plus extraction solution. **D**- Phase separation via gravity settling or centrifugation. **E**- Separation of a certain volume of mycotoxin-enriched top PEG-rich phase and, **F**- subsequent dilution with a solution containing an HRP-labeled anti-mycotoxin antibody. **G**- The immunoassay is performed by flowing a sequence of solutions through a $200 \times 20 \mu\text{m}$ ($W \times H$) PDMS microchannel inserted in the device at the inlet using a standard 2-200 μL pipette tip. The liquid flow is driven by applying a negative pressure at the outlet using a syringe pump. **H**- The competitive immunoassay is performed by first adsorbing mycotoxin-BSA conjugates (1), performing a blocking step with BSA (2), flowing the sample-under analysis (SUA) containing the labeled anti-mycotoxin antibodies (3) and, finally, flowing luminol plus hydrogen peroxide solution to generate a chemiluminescence signal.

4.3. Concentration of AFB1, OTA and DON in PEG-phosphate ATPSs

The first step to validate the concept of ATPS for sample preparation and pre-concentration prior to mycotoxin analysis is to assess the equilibrium concentration of each toxin (molecular structures at neutral pH are shown in **Figure 4.3-A**) in the top phase after partition and phase separation. This was achieved by fluorescence (AFB1 and OTA) and absorbance (DON) measurements performed in several PEG-phosphate salt systems comprising increasing PEG molecular weights and tie-line lengths (TLL), which can be changed by increasing the salt concentration at a fixed top-phase volume. Systems composed of PEG-phosphate at a pH of 7 were initially selected to optimize the extraction

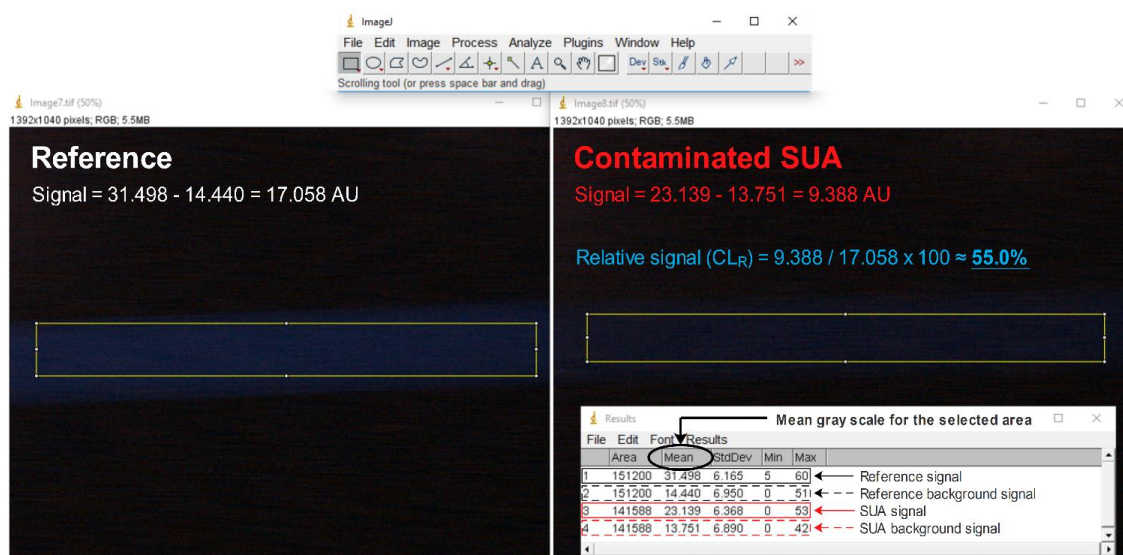


Figure 4.2 - Quantification of absolute chemiluminescence signals and relative signals using the software ImageJ, developed at the national institutes of health, USA. The output value in arbitrary units (AU) refers to the average gray scale in the selected region. All signals for all conditions are shown after first subtracting the respective background in the region outside the channel, with a selection area of the same size as that used for the channel (highlighted in the left panel). All images were acquired at half-length of the 200 μm wide microchannel (≈ 2.5 mm).

since these were previously observed to provide very pronounced partition coefficients (K) for OTA and AFB1 [19] and are compatible with a subsequent immunodetection step. The results obtained for the concentration factors (concentration of mycotoxin in the top phase relative to the total concentration of toxin present in the system) for systems with PEG MWs ranging from 3.35 to 20 kDa and salt concentrations ranging from 12.5 to 15% are shown in **Figure 4.3-B**. The results show that the PEG-phosphate systems could provide maximum concentration factors of 10.4 ± 1.04 (\pm standard deviation, σ), 6.59 ± 0.26 ($\pm\sigma$) and 2.41 ± 0.13 ($\pm\sigma$) for AFB1, OTA and DON, respectively. For each PEG MW, the concentration factors (and K) tend to increase with an increase in TLL, a well-known and expected behavior [192, 270] which is due to the generation of more extreme differences in charge and hydrophobicity between the two phases. The difference in affinities of the toxins towards the PEG-rich phase was expected since the more hydrophobic molecules tend to have a more pronounced partition to the more hydrophobic top phase. According to previous reports by several groups [271, 273, 296], this difference in polarity and respective partition behavior in ATPS can be evaluated by the calculated octanol-water distribution coefficient ($\log D$) at pH 7 for each molecule, which is 1.58, 1.21 and -0.97 for AFB1, OTA and DON, respectively [274]. It can thus be observed that the trend in $\log D$ matches the measured trend in concentration factors as well as that of the maximum calculated partition coefficients, where maximum $\log K$

values of $1.44 \pm 0.04 (\pm\sigma)$, $1.02 \pm 0.02 (\pm\sigma)$ and $0.43 \pm 0.02 (\pm\sigma)$ were obtained for AFB1, OTA and DON, respectively (all calculated K values are listed in **Table 4.1**). It is important to further highlight that although these results accurately match the polarity of the molecules, in previous reports by our group [19] it was observed, using the same methodology, that OTA had a significantly higher partition (≈ 10 -fold) to the top phase relative to AFB1. This difference can be related to the dramatically lower volume ratios (V_r) used in these previous studies, resulting in a pronounced increase in OTA concentration in the top phase, thus limiting the equilibrium concentrations for more extreme K values due to solubility constraints. Similar effects from extreme V_r values on the K have been previously reported in the literature for proteins [297], plasmid DNA [298] and small organic molecules [299]. Overall, based on the results in **Figure 4.3-B**, the PEG-phosphate system composed of 15% salt and PEG with a molecular weight of 8 kDa showed the most promising results for the simultaneous processing of all three target mycotoxins to maximize the concentration factor.

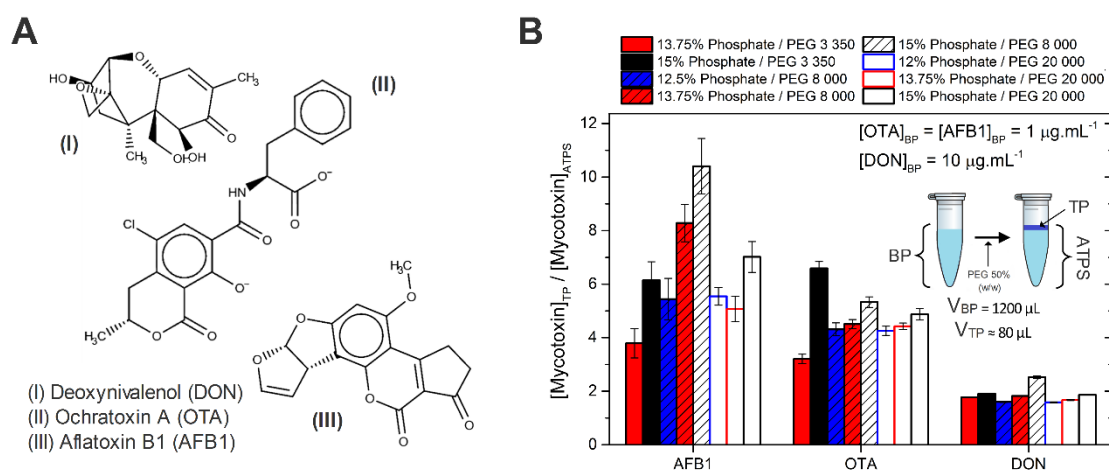


Figure 4.3 - A- Molecular structures of the major ($\geq 90\%$) microspecies of the tested target mycotoxins at a pH of 7. **B-** Results obtained for the concentration factor of each mycotoxin in the top phase of multiple PEG-phosphate systems at increasing PEG molecular weights (3.35 – 20 kDa) and salt concentrations (12.5 – 15 % w/w), relative to the theoretical concentration in the total ATPS volume. The acronyms TP, BP and ATPS refer to the top phase, bottom phase and total ATPS, respectively. The error bars refer to the standard deviation ($\pm\sigma$) from 5 repeated spectrofluorometric measurements in the case of AFB1 and OTA and 2 repeated spectrophotometric measurements in the case of DON. Other parameters calculated for each toxin (top phase concentrations, estimated K and extraction yields) are listed in **Table 4.1** for all tested systems.

4.4. Optimization of the tie-line length (TLL) and PEG molecular weight for enhancing extraction and immunodetection

After determining the concentration factors for each target mycotoxin in the top phase in the previous section, it was necessary to re-test each of the conditions in **Figure 4.3-B** to assess their ability to effectively extract the mycotoxins from a dried solid feed and minimize the simultaneous enrichment in potential interfering molecules during the subsequent immunodetection step. The optimization procedure was performed by spiking a mixture containing a known amount of each mycotoxin into a corn-based feed, performing the extraction procedure and subsequently analyzing the individual absolute chemiluminescence signals obtained for a 15× diluted top-phase as SUA, relative to a reference feed processed using the same conditions. The concentrations of each toxin used for the optimization procedure were 20, 50 and 500 ng.g⁻¹ for AFB1, OTA and DON, respectively, concentrations which are within or below the regulatory and recommended maximum limits for each toxin in the EU. The feasibility of analyzing a specific toxin in contaminated feed containing all three toxins was validated before-hand by performing cross-reactivity tests (**Figure 4.4**). The results obtained in terms of (1) the absolute chemiluminescence emission for each SUA and respective reference and (2) the calculated relative signal is shown in **Figure 4.5** for (A) AFB1, (B) OTA and (C) DON. Based on these results, two major conclusions can be drawn: (1) lower molecular weights of PEG have a high impact in reducing the measured absolute signals, possibly due to interference with the binding of antibodies in accordance with previous results by our group [19, 24] and (2) for AFB1 and OTA, higher concentrations of salt tend to decrease the obtained signal ratios, resulting in an increased sensitivity, thus correlating well with the previously measured concentration factors. Taking in account that the extraction procedure should ideally be a general method to extract all three mycotoxins, the single condition that provides the higher sensitivities for all three toxins is an ATPS composed of 1.2 mL 15% (w/w) phosphate salt and 75 µL PEG 8000 50% (w/w) added to 400 mg target feed. To further confirm that this condition could effectively detect the target concentrations of mycotoxins with signal ratios below the 3σ threshold, the extraction and immunodetection procedure was carried out in triplicate and the results are shown in **Figure 4.5-D** for the detection of 20 ng.g⁻¹ AFB1, 50 ng.g⁻¹ OTA and 500 ng.g⁻¹ DON in corn.

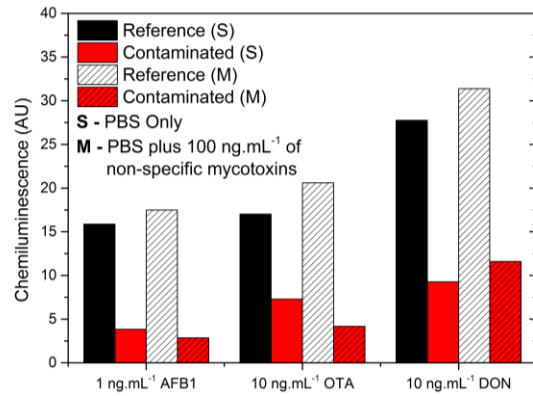


Figure 4.4 - Absolute chemiluminescence signals for reference (0 ng.mL^{-1} target mycotoxin) or contaminated (1 ng.mL^{-1} AFB1, 10 ng.mL^{-1} OTA or 10 ng.mL^{-1} DON) samples prepared in PBS buffer. (S) indicates the presence of only the target mycotoxin in the PBS solution in the contaminated sample. (M) indicates the presence of 100 ng.mL^{-1} of both nonspecific mycotoxins in solution. The results highlight that no significant antibody cross-reactivity could be observed by comparing conditions (S) and (M).

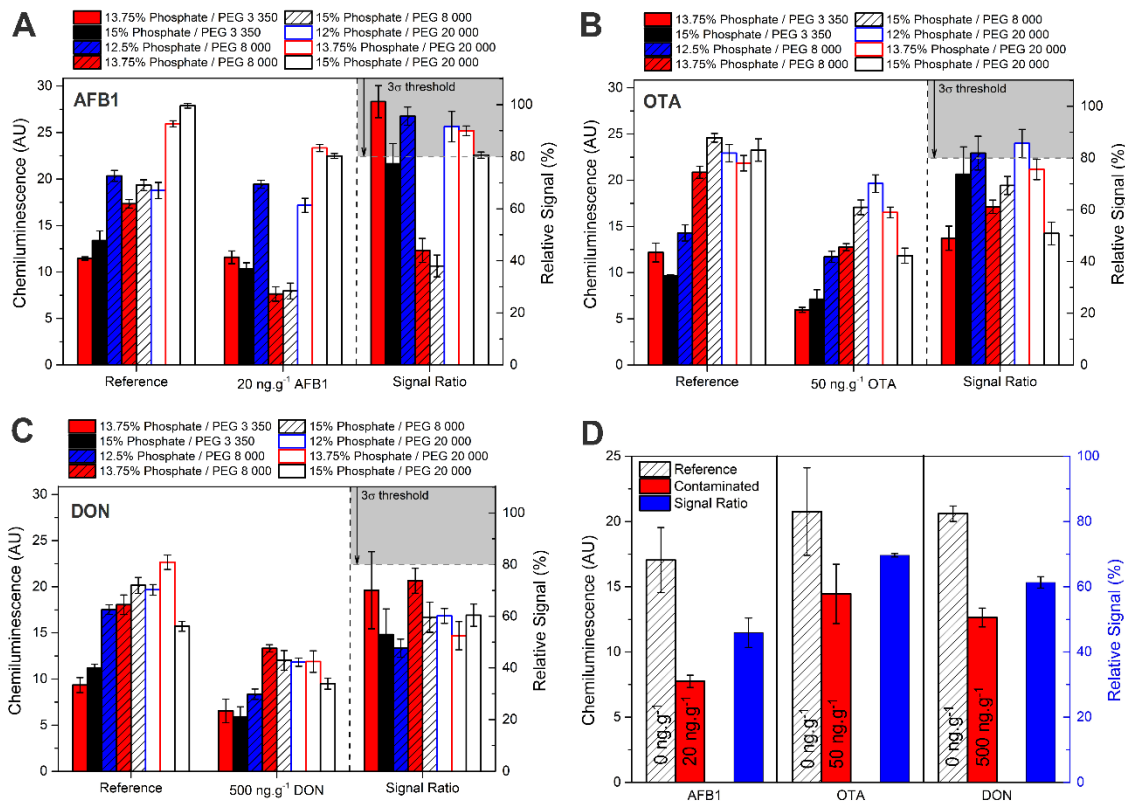


Figure 4.5 - Optimization of the PEG MW and salt concentration in respect to the relative chemiluminescence signals obtained between the reference samples and AFB1 (A), OTA (B) and DON (C) spiked corn samples. The shaded area represents the typical 3σ threshold associated with this type of microfluidic immunoassays as previously reported [21]. D – Results for the optimum condition for maximizing the relative signal for all toxins (PEG 8,000 and 15% salt). The error bars in (A), (B) and (C) refer to $\pm\sigma$ of 3 regions measured along the channel in single experiments, while in (D) the error bars refer to $\pm\sigma$ of the signals measured in triplicate.

4.5. Optimization of the dilution factor for minimizing matrix interference

After optimizing the ATPS composition to allow simultaneous detection of relevant toxin concentrations, the extraction procedure was further optimized to achieve a balance between minimizing matrix interference through dilution, arising from co-concentrated molecules in the top-phase and the ATPS forming components themselves, and the loss of sensitivity due to excessive dilution. This was done by testing different dilution ratios for the top phase in the PBS buffer solution containing the target antibodies, considering that low dilutions are limited by matrix interference and high dilutions are limited by low target mycotoxin concentrations.

Thus, it was expected that a low relative signal (high sensitivity) valley would occur in between these extreme conditions, where at the low dilution end, low sensitivity and repeatability can be expected and at the high dilution end, signal ratios falling within $\pm\sigma$ of the reference may occur. A minimum dilution of 5 \times was selected in order to (1) significantly minimize the viscosity of the top phase and (2) take into consideration that lower levels of dilution were previously shown to result in strong matrix interference in the case of wines [19]. The results obtained for each toxin after extraction, performing top phase dilutions ranging from 5 \times to 20 \times , are shown in **Figure 4.6**. Based on the results it is possible to conclude that the high sensitivity valley for the dilution ratio is achieved simultaneously for all toxins at a value of 10 \times dilution. Finally, to estimate the extraction efficiency of the dried mycotoxins from the solid feeds, the experiment was repeated using the optimum conditions by spiking the toxins directly in the extraction solution (**Figure 4.7**). The results showed that no statistically significant difference ($p > 0.05$) could be observed, which leads to the conclusion that when tailored to this immunoassay, the extraction efficiency (defined as the ratio between the mass of mycotoxins extracted from the feed and the mass of mycotoxins spiked in the feed) can be assumed to be virtually ~100%, whereas the effective extraction in the top phase is still limited by the intrinsic extraction yields listed in **Table 4.1**.

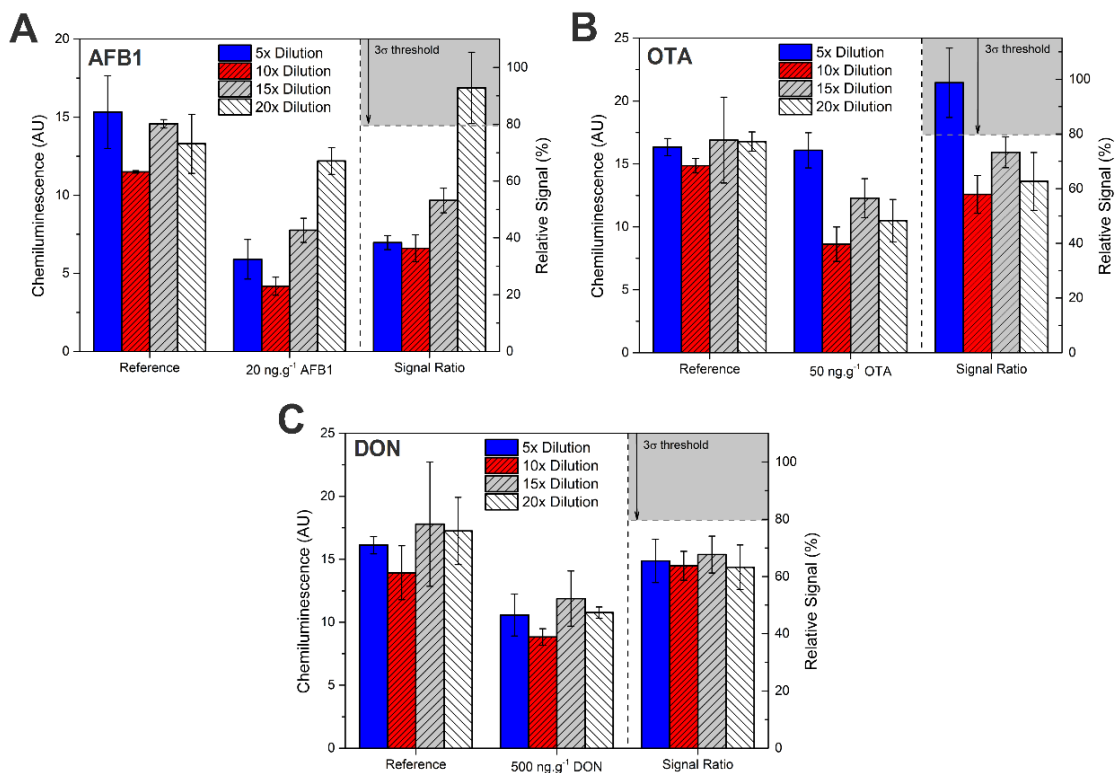


Figure 4.6 - Optimization of the top phase dilution ratio in respect to the relative chemiluminescence signals obtained between the reference samples and AFB1 (A), OTA (B) and DON (C) spiked corn samples. The error bars refer to $\pm\sigma$ of the signals, measured in duplicate.

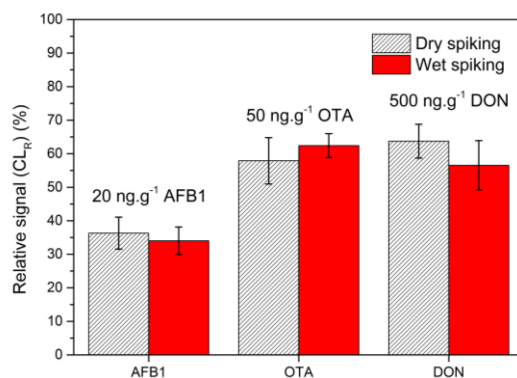


Figure 4.7 - Relative chemiluminescence signals measured in duplicate after spiking 20 ng.g⁻¹ AFB1, 50 ng.g⁻¹ OTA and 500 ng.g⁻¹ DON in corn either before (dry spiking) or after (wet spiking) performing the PEG-phosphate ATPS extraction procedure. The dry spiking procedure was performed in the same way as described in Section 4.1.3, while the wet spiking procedure was performed by adding 1 μ L of each mycotoxin solution prepared in ethanol directly to the ATPS system, instead of performing the addition to the feed and allowing the solution to dry. The average results obtained for each of the conditions were not statistically different with ($p > 0.1$ for the average signals between the two conditions being equal). The error bars in the plot indicate \pm SD.

4.6. Benchmarking of ATPS-based extraction for sample processing and microfluidic immunodetection

In order to compare the performance of the optimized ATPS-based method with standard organic solvent- or water-based extraction methods, the same sample processing and immunodetection procedure was replicated using the following solutions: (1) a solution of methanol and water at a ratio of 80:20 [300]; (2) a solution of acetonitrile and water at a ratio of 80:20 [301] and (3) a solution of 1% PEG 8,000 and 5% sodium bicarbonate in water [302]. The extraction procedure was carried in the exact same way as described in **Section 4.1.3**, considering that no extra PEG solution was added to 1.2 mL of extraction solution. The results obtained for reference and contaminated (20 ng.g⁻¹ AFB1, 50 ng.g⁻¹ OTA and 500 ng.g⁻¹ DON) corn-based feeds using each of the extraction solutions are shown in **Figure 4.8**. It can be observed that while some extraction solutions tested were comparable to ATPS for particular toxins, despite the absence of a concentration effect, as is the case of solutions (1) and (2) for AFB1 and solution (3) for DON, none of these solutions showed a general compatibility with the simultaneous analysis of all 3 toxins. In particular, the better performance of organic solvent-based solutions relative to ATPS for the analysis of AFB1 can be justified by the dramatically higher solubility of this toxin in organic solvents compared to water [303], considering its relatively high hydrophobicity as discussed in **Section 4.3**, thus favoring the effective desorption of the toxin from the feed material. The better performance of the aqueous solution (3) for extracting DON relative to ATPS may be simultaneously related with its relatively higher hydrophilicity (**Section 4.3**), and a relatively higher solute concentration in the tested ATPSs, which can limit the solubility of DON. On the other hand, the analysis of OTA using organic solvent-based solutions for extraction greatly reduced the measured absolute chemiluminescence signals, possibly due to matrix interference as previously observed by Novo and co-workers [293], while the analysis of AFB1 and OTA using the water based solution (3) resulted in insufficient sensitivity due to the absence of a simultaneous concentration effect.

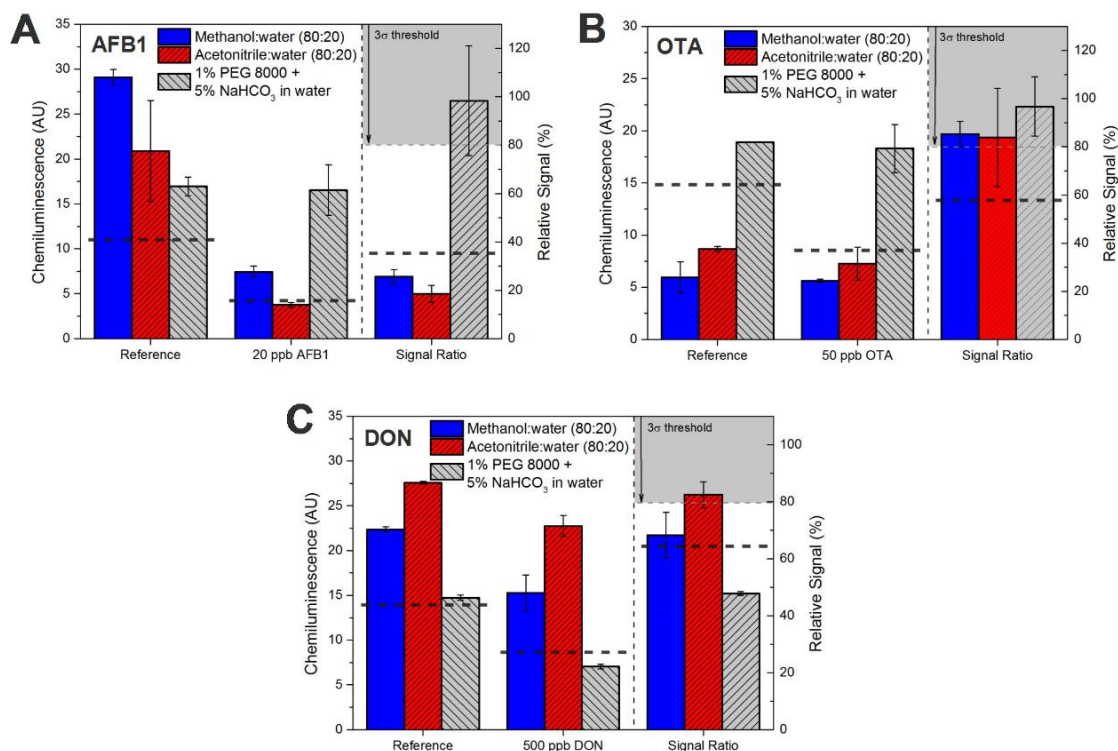


Figure 4.8 - Evaluation of standard extraction solutions for extraction and immunodetection of AFB1 (A), OTA (B) and DON (C), spiked in corn samples. The horizontal dashed lines indicate the average chemiluminescence value obtained for the optimized conditions using a PEG-phosphate ATPS. The error bars refer to $\pm\sigma$ of the signals, measured in duplicate.

4.7. Mycotoxin calibration curves using the optimized PEG-phosphate ATPS

The optimized PEG-phosphate based ATPS extraction methodology was subsequently evaluated for the maximum sensitivity it provides (limit-of-detection, LoD) when coupled to the microfluidic competitive immunoassay. This was evaluated by analyzing increasing concentrations of each toxin spiked in corn, adjusting a logarithmic regression and then computing the mycotoxin concentration which generates a relative signal equal to 3 times the standard deviation (σ) of the reference signals, measured in triplicate. The results for each calibration curve are plotted in **Figure 4.9** as the chemiluminescence signals relative to the reference sample (CL_R). The results show that the obtained LoDs are below the required minimum mycotoxin concentrations for the whole range of the EC regulatory limits for AFB1 and recommendations for OTA and DON. Assuming the concentration factors from **Figure 4.3-B**, the LoDs shown in **Figure 4.9** result in effective average concentrations of 1.1, 3.6 and 7.0 ng.mL⁻¹ in the 10-fold diluted top phase for AFB1, OTA and DON, respectively. From this observation

and considering the previously reported LoDs for each mycotoxin spiked in buffer solutions of ≈ 0.1 , 0.3 and 1 ng.mL^{-1} for AFB1, DON and OTA, respectively [42], three major conclusions can be drawn. The first conclusion is that there is a pronounced loss in sensitivity due to matrix interference of ~ 4 -fold for OTA, ~ 10 -fold for AFB1 and ~ 20 -fold for DON. A second conclusion is that, despite the considerable matrix interference, the concentration effect provided by the ATPS-based extraction effectively improves (for OTA) or equals (for AFB1) the LoDs expected for buffer in the absence of the concentration effect which would have been theoretically 0.1 ng.mL^{-1} for AFB1 and 0.7 ng.mL^{-1} for OTA. Finally, a third conclusion is that while the detection of DON shows the greatest decrease in sensitivity compared to the assays in buffer, the obtained sensitivity is still below the required limits. Overall, using the optimized extraction conditions, all the required limits for each of the three mycotoxins were met, providing a semi-quantitative sensing range approaching 2 orders of magnitude. The semi-quantitative nature of this assay is justified by the limits-of-quantification (LoQ, typically defined by a 10σ threshold) being above a large fraction of the required target mycotoxin concentrations in feeds, calculated here as $> 50 \text{ ng.g}^{-1}$ for AFB1, $> 200 \text{ ng.g}^{-1}$ for OTA and $669 \text{ ng.g}^{-1} \pm 41\%$ (CV) for DON.

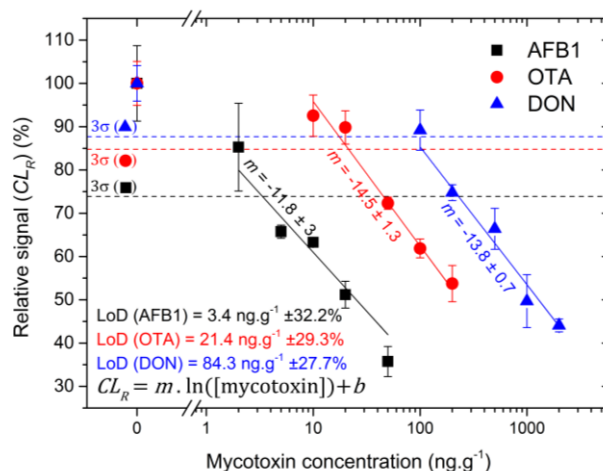


Figure 4.9 - Calibration curves for increasing concentrations of AFB1, OTA and DON within relevant recommended limits for feeds in the EU. Each of the mycotoxin concentrations was spiked in corn and extracted using the previously optimized PEG-phosphate conditions (PEG 8,000, 15% salt and a top phase dilution of $10\times$). The relative signal values (CL_R) are the percentage of absolute chemiluminescence signal obtained for a SUA relative to the average signal obtained for the references (0 ng.g^{-1}). The horizontal dashed lines mark the 3σ threshold for each of the mycotoxins after analyzing each of the reference samples in triplicate. The LoD values refer to the limit-of-detection for each toxin, calculated as the concentration that results in a CL_R equal to 3σ using the fitted logarithmic regression. The error of the LoD values is calculated as the coefficient of variation (CV). All error bars, except for the references, refer to $\pm\sigma$ of each analysis performed in duplicate.

4.8. Mycotoxin calibration curves using a biodegradable PEG-sodium citrate ATPS

After optimizing a PEG-phosphate ATPS for the single-step extraction and subsequent immunodetection of the target mycotoxins, a study was made to prove that the methodology can be generalized to other ATPS systems by exploring how the extraction and concentration performance respond to a change in salt composition. In this study, citrate was tested as a greener alternative, since phosphate salts are a significant cause of nutrient pollution in effluents, resulting in the hypertrophication of bodies of water [304, 305]. As an alternative to phosphate salts, organic, non-toxic and biodegradable trisodium citrate salt was selected for further studies for the following reasons: (1) there is a high similarity between phase diagrams when compared to those of sodium/potassium phosphate when combined with PEG 8,000 [306]; (2) while a pH of 7 is not within the buffering range of citrate solutions, the pH of pure 15% w/w sodium citrate solutions was measured to be approximately within a physiological range ($\text{pH} = 7.48 \pm 0.01$), being optimum for antibodies [307], (3) sodium citrate salt is relatively low cost, within the same range as phosphate salts; and (4) its production at large scale uses mostly fermentative processes [308], which are generally simpler, greener and more energy efficient relative to chemical synthesis. To evaluate this alternative ATPS composition, the first approach was to measure the concentration factors using the same methodology as discussed in **Section 4.3**. The measured values were $4.62 \pm 0.61 \times (\pm\sigma)$ for AFB1, $3.26 \pm 0.18 \times (\pm\sigma)$ for OTA and $1.62 \pm 0.34 \times (\pm\sigma)$ for DON, approximately half of those obtained for the PEG-phosphate systems, highlighting a less pronounced driving force for mycotoxin partition towards the top phase. This observation can be justified by the citrate anions being weaker kosmotropes relative to phosphate anions according to the Hoffmeister series [309], which implies a relatively lower solubility of hydrophobic molecules (i.e. mycotoxins) in phosphate salt solutions relative to citrate salt solutions, thus generating a stronger exclusion effect towards the more hydrophobic top phase in the former. This hypothesis is also supported by the most hydrophobic mycotoxin, AFB1, having the most pronounced drop in concentration factor, a 2.25-fold difference between $10.4 \pm 1.04 \times$ in the system with phosphate buffer and $4.62 \pm 0.61 \times (\pm\sigma)$ in the system with the sodium citrate. Subsequently, the performance of the PEG-citrate systems was evaluated by extracting and detecting increasing concentrations of each mycotoxin using the same conditions optimized for the

PEG-phosphate systems, in an analogous way as previously reported for **Figure 4.9**. The relative signal results obtained for each mycotoxin are shown in **Figure 4.10-A** and the completed extraction procedure can be visualized in the photograph in **Figure 4.10-B**, together with bright field microscopy images of the absolute chemiluminescence signals acquired with the microscope. The average LoDs obtained with the PEG-citrate system were not significantly different ($p > 0.1$) from those previously obtained using PEG-phosphate, based on a Welch's t-test for unequal variances with a two-tailed distribution. Considering this result, it is important to highlight that despite the lower concentration factors for each mycotoxin, the extraction using PEG-citrate achieved a similar performance relative to PEG-phosphate. This result indicates that while there is a lower concentration of mycotoxins in the top phase after extraction, any co-extracted hydrophobic interfering compounds in solution are also excluded from this phase, thus resulting in the same final effective immunoassay sensitivity.

Finally, after determining the sensitivity of the PEG-citrate system, the method was applied to naturally contaminated corn samples. The results obtained after extracting and analyzing a corn sample naturally contaminated with 1.76 ng.g^{-1} AFB1, 8.63 ng.g^{-1} OTA and $1,066 \text{ ng.g}^{-1}$ DON (quantified by HPLC-MS in a certified laboratory), are shown as stars in **Figure 4.10-A**. The results show that the signals for AFB1 and OTA were below the detection limit, not providing significantly different chemiluminescence signals relative to the reference corn feed. On the other hand, the average relative signal of $53.2\% \pm 5.3\%$ obtained for DON indicated a concentration of $1,214 \text{ ng.g}^{-1}$ calculated from the logarithmic fit, resulting in a recovery of 113%, meaning an overestimation of 13% compared to the certified quantification.

4.9. PEG-sodium citrate ATPS for processing multiple types of feed matrices

Furthermore, to demonstrate that the optimized PEG-citrate ATPS-based extraction conditions are a robust, general and versatile sample processing methodology for subsequent immunodetection, the system was tested for 4 additional types of feeds, without further optimization for each type of feed: (1) a chickpea-based preparation; (2) a sunflower-based preparation; (3) a soy based preparation; and (4) complete salmon feed supplemented with astaxanthin. To allow comparison with previous results, the same mycotoxin concentrations of 20 ng.g^{-1} AFB1, 50 ng.g^{-1} OTA and 500 ng.g^{-1} DON were

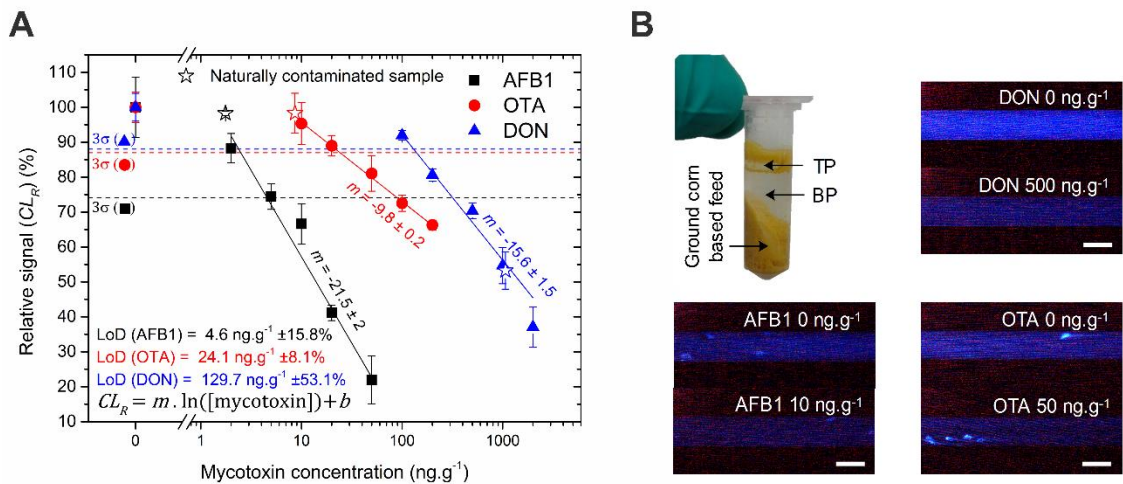


Figure 4.10 - A – Calibration curves for increasing concentrations of AFB1, OTA and DON within relevant recommended limits for feeds in the EU. Each of the mycotoxin concentrations was spiked in corn and extracted using a PEG-citrate system with the same conditions optimized for the PEG-phosphate system (PEG 8,000, 15% salt and a top phase dilution of 10 \times). The relative signal values (CL_R) are the percentage of absolute chemiluminescence signal obtained for a SUA relative to the average signal obtained for the references (0 ng.g^{-1} mycotoxin). The horizontal dashed lines mark the 3σ threshold for each of the mycotoxins after analyzing the reference samples for each toxin in triplicate. The LoD values refer to the limit-of-detection for each toxin, calculated as the concentration that results in a CL_R equal to 3σ using the fitted logarithmic regression. The error of the LoD values is calculated as the CV. All error bars, except for the references, refer to $\pm\sigma$ of each analysis performed in duplicate. The star shaped points refer to the analysis of a naturally contaminated corn sample using the same procedure, analyzed also in duplicate. **B** – Photograph of the PEG-citrate ATPS extraction procedure after phase separation (TP- top phase, BP- bottom phase) and microscopy bright field images of the obtained chemiluminescence signals for particular mycotoxin concentrations. The images were acquired in the dark with an exposure time of 20 s and contrast enhanced for visualization purposes. The scale bar indicates a size of 200 μm .

spiked in each feed and analyzed relative to the references. The results are shown in **Figure 4.11**, together with photographs of the complete extraction procedure after centrifugation. The results highlight a pronounced variability in the measured absolute signals among feeds for all mycotoxins. This implies, as expected, that each feed induces a variable degree of matrix interference, hindering the binding of the anti-mycotoxin antibodies to the immobilized mycotoxin-BSA conjugates to a variable extent. This interference effect was observed to be particularly pronounced in the sunflower-based feed, which provided a very dark brown top phase, highlighting the high concentration of hydrophobic compounds such as polyphenols and oils. Nevertheless, despite the variability in assay interference, the average chemiluminescence values measured for the contaminated samples were below the 3σ threshold of the references, i.e., they were below the LoD for all feeds. This highlights the aspect that the optimized PEG-citrate ATPS extraction conditions are a versatile and fit-for-purpose sample processing methodology

for multiple dried complex matrices, even without tailoring the extraction conditions to each feed to normalize possible interferences.

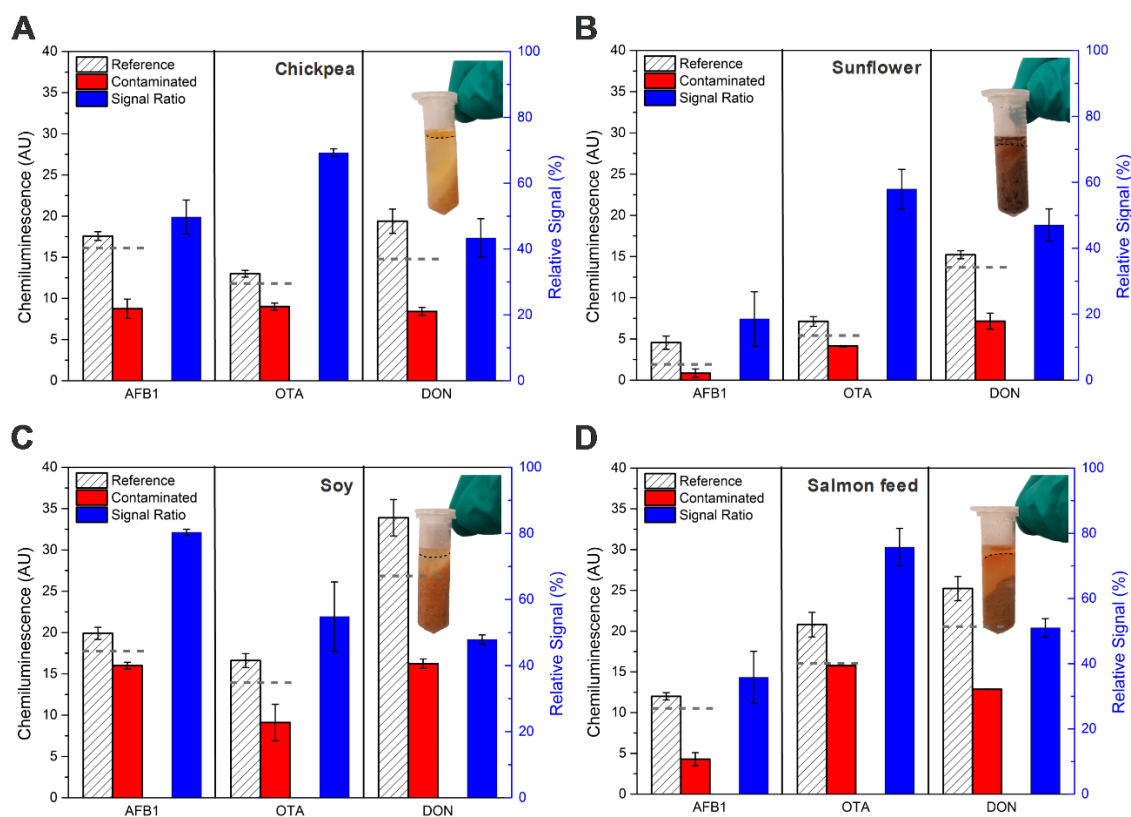


Figure 4.11 - Absolute and relative chemiluminescence measurements for the extraction and analysis of a (A) chickpea-based feed, (B) sunflower based feed, (C) soy-based feed and (D) complete salmon feed supplemented with astaxanthin under reference or contaminated (20 ng.g^{-1} AFB1, 50 ng.g^{-1} OTA and 500 ng.g^{-1} DON) conditions. The extraction procedure was performed with the PEG-citrate ATPS using the previously optimized conditions (PEG 8,000, 15% salt and a top phase dilution of $10\times$). The inset photographs, with the interface highlighted as a dashed line, show the respective feed after extraction and subsequent centrifugation. All measurements were performed in duplicate and the error bars indicate $\pm\sigma$. The horizontal dashed lines indicate the 3σ threshold for each set of reference measurements.

4.10. Chapter conclusions

A novel sample preparation methodology utilizing the concept of aqueous two-phase separation to simultaneously extract and concentrate three target mycotoxins, AFB1, OTA and DON, from a variety of complex solid feed matrices within less than 20 min was described. The ATPS was composed of PEG and sodium citrate, a protocol that is green, biodegradable, safe to handle and inexpensive. With the aim of developing an extraction method suitable for point-of-need applications, the methodology was coupled with a miniaturized multi-mycotoxin competitive immunoassay and was successfully optimized in terms of tie-line-length (15% sodium citrate and $75 \mu\text{L}$ PEG

8,000 50% w/w) and top PEG-rich phase dilution (10-fold) to achieve a fit-for-purpose sensitivity below the required regulatory and recommended limits in the EU. In conclusion, this procedure serves as a versatile approach to process samples on the field, coupled to point-of-need compatible immunosensors which can then be further integrated with photosensors [21] or multiplexing strategies [42], as previously reported by our group, towards a fully integrated analysis platform.

Chapter 5

Rapid and Regenerable Microfluidic Immunoassay with Integrated Optical Signal Transduction

This chapter reports the optimization of the microfluidic immunoassay for OTA discussed in **Chapter 3** to achieve (1) microchannel and immobilized antigen reusability and (2) ultrarapid analysis times. The optimized immunoassay was further integrated with a portable optical signal transduction platform. A novel ultra-rapid, sensitive (limit-of-detection (LoD) < 0.5 ng/mL) and simple physisorption-based microfluidic competitive immunoassay for OTA detection was developed with integrated photosensing and optimized to provide quantitative results in less than 5 minutes. Furthermore, a regeneration protocol was developed to effectively reuse the same PDMS microchannel and immobilized antigen molecules at least 8 times without a significant drop in sensitivity (LoD < 2 ng/mL). The optimized assay could also effectively detect OTA in red wine extracts at the regulatory limit (2 ng/mL). Thus, this biosensing device showed promise for further automation and reduction in assays times for a true point-of-need mycotoxin quantification tool. This work was developed within the scope of the European project DEMOTOX (FP7-SME-2013- 604752) in collaboration with Lumisense Lda. The experiments were performed at the facilities of INESC MN and laboratory of Lumisense Lda in Tec Labs (campus of the Faculty of Science from the University of Lisbon). At the end of the chapter, the final OTA biosensor prototype (main deliverable of DEMOTOX) co-developed with Lumisense Lda. is also presented and discussed. The contents of this chapter are reproduced with appropriate adaptations from one original research article [21] co-authored (equal contribution) with Dr. Diogo Ramadas (at the time PhD student at Lumisense Lda).

5.1. Materials and experimental methods

5.1.1. Chemicals and biologicals

Anti-OTA-HRP affinity purified rabbit polyclonal antibodies were purchased from Immunechem (Burnaby, Canada) as a 250 $\mu\text{g}/\text{mL}$ solution. OTA-bovine serum albumin (BSA), glycine, phosphate buffered saline, BSA, OTA from *Petromyces albertensis*, $\geq 98\%$, sodium phosphate monobasic, potassium phosphate dibasic and Polyethylene glycol with an average MW of 20 kDa were purchased from Sigma-Aldrich. Luminol and hydrogen peroxide, Super-Signal[®] West Femto Substrate Trial Kit 34094, were used as purchased from Thermo Scientific. Red wine for spiking with OTA was purchased from a local supermarket.

5.1.2. Microfluidic immunoassay

Prior to performing the immunoassays, Tygon[®] tubing with an internal diameter of 0.19 mm (VWR), coupled to an Ismatech (Wertheim, Germany) ism597d peristaltic pump was adapted to a 1-200 μL pipette tip and connected to the outlets of the microchannels. A pipette tip inserted at the inlets serves as a reservoir for the solutions that will flow inside the channel via the negative pressure created by the pump. To functionalize the channels with OTA-BSA molecules, an OTA-BSA solution was first flowed inside the channels. The best functionalization condition such as OTA-BSA concentration, flow rate and total time was optimized. Then, a solution of BSA at a concentration of 4% (w/v) is subsequently flowed at 3.11 $\mu\text{L}/\text{min}$ for 5 min to ensure a full coverage of the PDMS surface, avoiding non-specific physisorption of the anti-OTA-HRP antibody. After functionalizing the channel, the sample under analysis (SUA) containing anti-OTA-HRP antibodies at a certain concentration is flowed into the channels at an optimized flow rate and total time. All optimization assays were performed simultaneously in the same PDMS structure for each condition, to ensure maximum comparability with a single experiment per condition. The luminol measurements were performed sequentially by aligning each channel with a photodiode as described below.

5.1.3. Chemiluminescent signal acquisition

To quantify the surface concentration of antibodies, each microchannel was first aligned with a Si photodiode (S6428-01, Hamamatsu Photonics, Tokyo, Japan) by sliding the structure through an in-house designed and 3D printed (Kossel home-built delta printer) polylactic acid (PLA) support. The Si photodiode was connected to an in-house

designed PCB connected through USB to a laptop and programmed in C with an Arduino™ interface. The luminol solution was flowed at 10 $\mu\text{L}/\text{min}$ in the dark. The chemiluminescence reaction, catalyzed by the enzyme HRP covalently attached to the anti-OTA antibodies, produces light at an approximate maximum wavelength of 445 nm. The measurement of the current generated by the photodiode at 0 V bias in response to the CL emission is carried out by means of a very high gain current-to-voltage converter in which a 1 nA photodiode current generates a voltage of 1 V. A LMC6482 low power opamp (Texas Instruments) was used in a current to voltage converter with a low frequency compensation pole for stability. This circuit had an output swing of ± 4.90 V giving a wide measuring range. Further signal amplification or attenuation is used depending on the light intensities to adapt the measuring range to the ADC used in the main processor.

5.1.4. Red wine sample processing

The red wine samples were processed according to the method optimized in **Chapter 3**. Briefly, 175 mg sodium phosphate monobasic, 75 mg potassium phosphate dibasic and 40 mg of polyethylene glycol with an average MW of 20 kDa were first weighed in a tube to a final concentration of 12.5% phosphate salt, 2% PEG and a pH of 7 after the subsequent addition of 1,881 μL of raw red wine plus 19 μL of a PBS solution (for reference) or a solution of 200 ng/mL OTA prepared in PBS. Then, the solution was mixed vigorously for about 60 s and centrifuged at 2,000 g for 15 min in a Labnet Spectrafuge™ mini-centrifuge. A total of 10 μL of small top PEG-rich phase was subsequently collected and mixed with 23.3 μL of an anti-OTA-HRP solution to the final optimized concentration.

5.2. Immunoassay design and photosensor integration

The first step to develop a microfluidic immunoassay for OTA quantification is to select the appropriate architecture of the assay, meaning the type of immunoassay and selection of the appropriate surface chemistry. All the selected features intrinsic to the immunoassay are schematized in **Figure 5.1**. A direct competitive immunoassay, where the antigen is immobilized on the solid phase rather than the antibody, was selected. The chemical principle behind this assay is that higher concentrations of OTA in solution compete with the OTA immobilized on the walls for binding with the free anti-OTA-HRP in solution. Thus, the higher the concentration of OTA in solution, the lower the resulting

surface concentration of anti-OTA-HRP molecules. The rationale behind choosing the immobilization of the antigen as opposed to antibodies is due to the lack of a precise spatial orientation during the immobilization of antibodies, which poses a well-known challenge [168, 169]. Besides, BSA molecules have a very high affinity to the hydrophobic PDMS channel surface, previously reported to provide a virtually irreversible interaction [310, 311]. In this case, since the aim is to integrate the assay in a point-of-need type of device, the speed of detection is a critical issue, thus, the primary antibody used is directly labeled with HRP, not requiring an extra secondary antibody to provide a signal, namely a chemiluminescence-based signal using a luminol substrate in this case. Assuming that the surface preparation steps, comprising the adsorption of OTA-BSA and blocking with BSA, are performed beforehand, the assay itself can be performed in a single step reaction, followed by detection with luminol. Furthermore, it would also be advantageous to regenerate the channel and perform multiple immunoassays using the same OTA-BSA molecules adsorbed on the surface. This was achieved using a glycine solution at a highly acidic pH (pH = 2), which can selectively disrupt the affinity-based antibody-antigen interactions without significantly compromising the adsorbed OTA-BSA based on the reproducibility of the absolute luminescence signal obtained by repeating the immunoassay after each regeneration cycle. This regeneration step will be further discussed ahead in this chapter.

The use of a serpentine like microchannel design (200 x 100 μm , width x height), instead of a straight channel, serves a dual purpose. The first is that maintaining an aspect ratio closer to 1, in contrast to a wider microchannel (i.e. 1 mm) with the same height, ensures a more homogenous flow through the channel, without preferential wetting certain areas due to inhomogeneity in the corona treatment before sealing. The second purpose relates to the importance of having a microchannel wide enough to provide a reasonable margin of error when positioning the device relative to the signal acquisition apparatus, while simultaneously directing more photons towards the sensing area. Nevertheless, it was also taken in consideration that the channel could not be excessively long to avoid any possible molecular depletion along the channel, both during the assay and the luminol flow steps.

The next step was to design and engineer a structure to allow a reproducible and simple alignment of the microchannels with the photodiode. The structure, as shown in **Figure 5.2**, was designed in a CAD software, 3D printed, and holes were drilled for wiring to the microcontroller board and placement of the photodiode. The photodiode has

a light sensing area of 2.4×2.8 ($L \times W$) mm^2 , which provides a comfortable alignment margin with the 1 mm wide serpentine at half the total length and width of the channel. Although the serpentine channel is narrower than the total width of the photodiode (2.8 mm), the excess area of the photodiode (0.9 mm on each side) is still useful to collect the light that is isotropically emitted from the microchannel located 500 μm above the sensor. The measurements were performed with the structure contained inside a Faraday-cage-like closed metallic box to prevent electronic interference. An example of a typical measurement is shown in **Figure 5.2**, where the voltage signal rises after flowing luminol in both the reference and the 2 ng/mL microchannels and achieves a steady plateau for as long as fresh luminol solution is pumped at a constant flow rate through the channel. It can also be clearly seen that the photodiode signal plateau measured in the reference channel reaches a considerably higher level (approximately twice) of that obtained for the 2 ng/mL microchannel. This is due to the higher surface concentration of anti-OTA-HRP molecules bound to the adsorbed OTA-BSA molecules, which convert the luminol substrate to light emission at a higher rate.

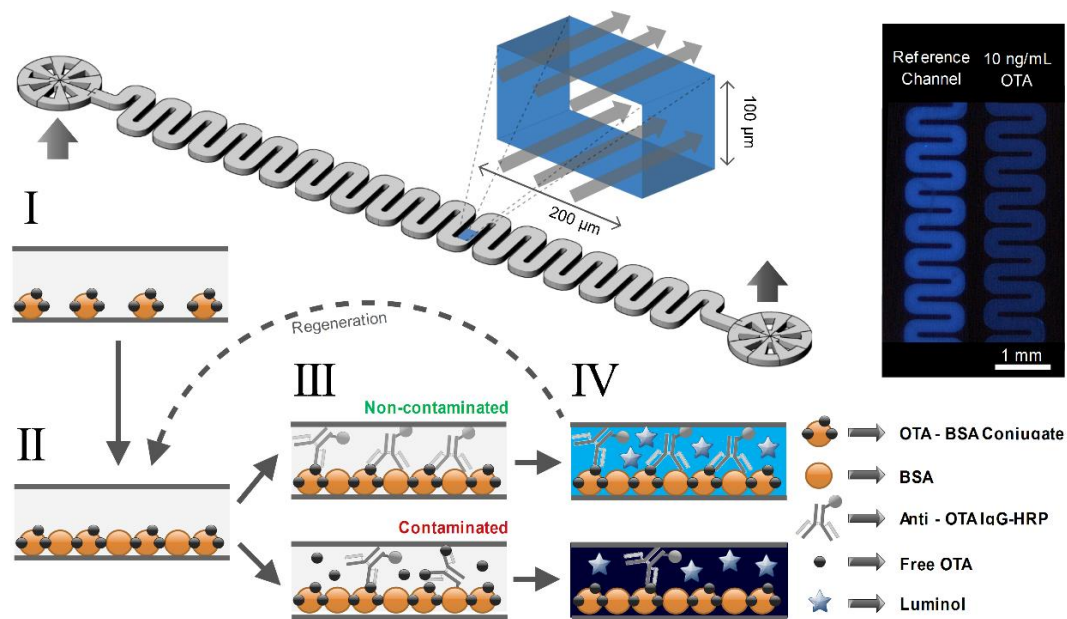


Figure 5.1 - Schematics of the microfluidic competitive immunoassay design used for OTA quantification. The serpentine channel structure has a total width of 1 mm and a length of 1 cm. The total length of the channel is 3.5 cm. The grey arrows represent the inlet and outlet for each of the solutions. I- Adsorption of OTA-BSA molecules in the surface of the microchannel. II- Blocking of the free space between the OTA-BSA molecules with BSA. III- Flow of the sample-under-analysis (SUA) containing a target concentration of OTA and anti-OTA antibodies conjugated with HRP. IV- Flow of a luminol solution containing hydrogen peroxide. The density of emitted photons is inversely proportional to the concentration of OTA in the SUA. The regeneration step, performed using glycine buffer (pH=2) followed by a BSA 4% (w/v) solution, reverting the channel surface back to step II by selectively removing all the specifically immobilized anti-OTA antibodies. The images on the right were acquired under the microscope, in the dark, with an exposure of 10s and a gain of 10 \times .

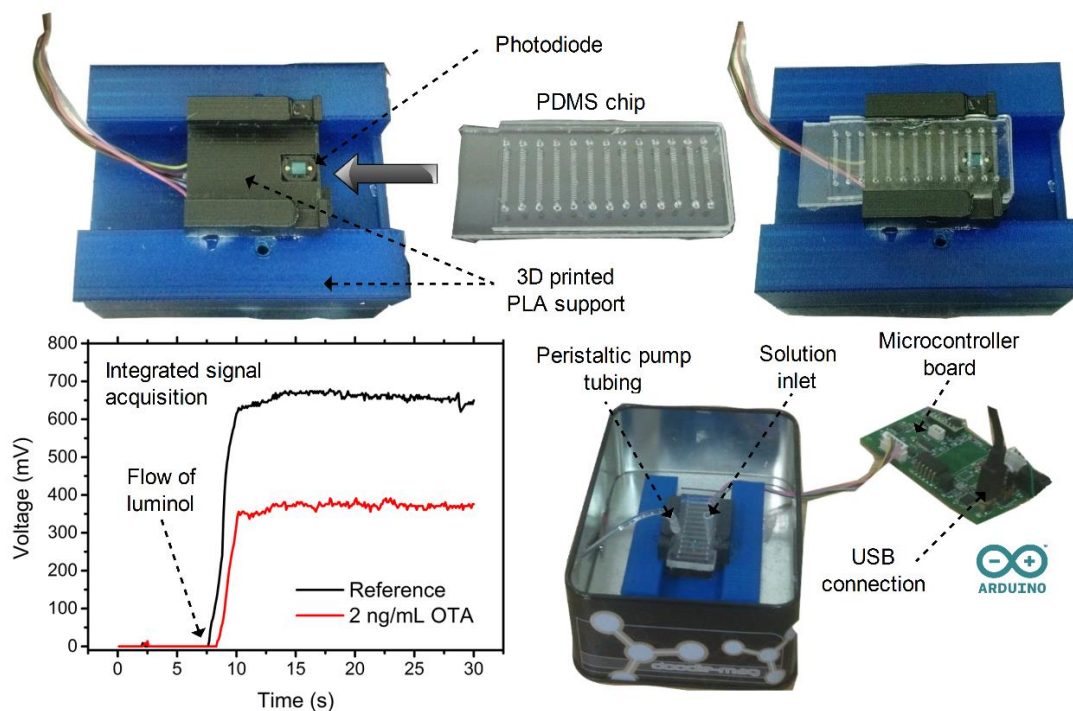


Figure 5.2 - Schematics of the measurement setup used to acquire the photoluminescent signal emitted from the microchannel. The target microchannel is aligned with a photodiode by sliding a PDMS chip containing 13 channels through the 3D printed support with an embedded photodiode connected to a microcontroller board. The board is connected to a computer and programmed using an Arduino™ application to output the voltage measurements (refresh rate of 0.1 s). The results plotted on the left were measured by flowing luminol at 10 $\mu\text{L}/\text{min}$ after performing two immunoassays using either a solution containing 0 ng/mL of OTA (reference) or 2 ng/mL OTA spiked in PBS buffer. These immunoassays were performed using the optimized conditions described ahead in this chapter.

5.3. Systematic optimization of the immunoassay

To optimize the immunoassay performance for rapid detection with the highest reagent economy, without compromising the sensitivity of the assay, each of the OTA-BSA adsorption and SUA incubation steps were systematically analyzed. For each of these steps the most critical variables are the molecular concentration, the incubation time (the time during which the solutions are continuously pumped through the microchannel) and the flow rate (how quickly the solution is replenished with new molecules). The optimization was performed in such way that both the assay time and reagent consumption were minimized, without compromising the achievement of a simultaneously low value for the ratio between the 10 ng/mL OTA and reference samples. A concentration of 10 ng/mL OTA was chosen to perform the optimization based on previous observations by our group that this value provides a significant drop in signal without saturating the competitive assay [10]. Furthermore, this ratio must be obtained

from voltage measurements appreciably above the noise threshold. For each condition, each reference and 10 ng/mL assays were performed simultaneously in two independent microchannels, and then the acquisition of the chemiluminescence signal in each microchannel was performed one at a time over the same photosensor.

The optimization of the above-mentioned parameters for the OTA-BSA step are summarized in **Figure 5.3**. The initial conditions of flow rate and incubation time (3.11 $\mu\text{L}/\text{min}$ and 5 min, respectively) to optimize the OTA-BSA concentration were chosen empirically to provide a good photocurrent signal above the noise threshold with reasonable economy of assay time and reagents. In **Figure 5.3-A** increasing concentrations of OTA-BSA in solution provide an increasing surface coverage, based on the chemiluminescence intensities obtained for the reference channel, in which a plateau is reached at about 50 $\mu\text{g}/\text{mL}$, suggesting a full surface coverage. The same behavior is observed for the 10 ng/mL OTA channel. This is the preferable working condition since the system becomes less sensitive to slight variations in surface coverage. Thus, based on this observation and the tendency observed for the signal ratios, reaching a minimum at the same value of 50 $\mu\text{g}/\text{mL}$, this condition was kept for further experiments. Interestingly, in **Figure 5.3-B**, it seems that in the range of 1-9 min incubation time, the obtained surface coverage is virtually constant, indicating that the physisorption of OTA-BSA molecules on the hydrophobic PDMS surface is a relatively fast process and equilibrium is reached in under 1 min. This observation is in agreement with the high affinity of BSA to PDMS surfaces as previously reported in the literature [24]. Thus, an incubation time of 1 min was fixed for further experiments to avoid incomplete coverage at shorter incubation times. Finally, the results obtained for increasing flow rates plotted in **Figure 5.3-C**, ranging from static conditions (0 $\mu\text{L}/\text{min}$) up to 20 $\mu\text{L}/\text{min}$, corresponding to a residence time of 2.1 s, show that a plateau in the reference signal, indicating full surface coverage, is reached in 1 min of incubation time using a flow rate of 10 $\mu\text{L}/\text{min}$. In summary, the optimal conditions, as highlighted in **Figure 5.3** were a concentration of OTA-BSA of 50 $\mu\text{g}/\text{mL}$, 1 min of incubation time and a 10 $\mu\text{L}/\text{min}$ flow rate.

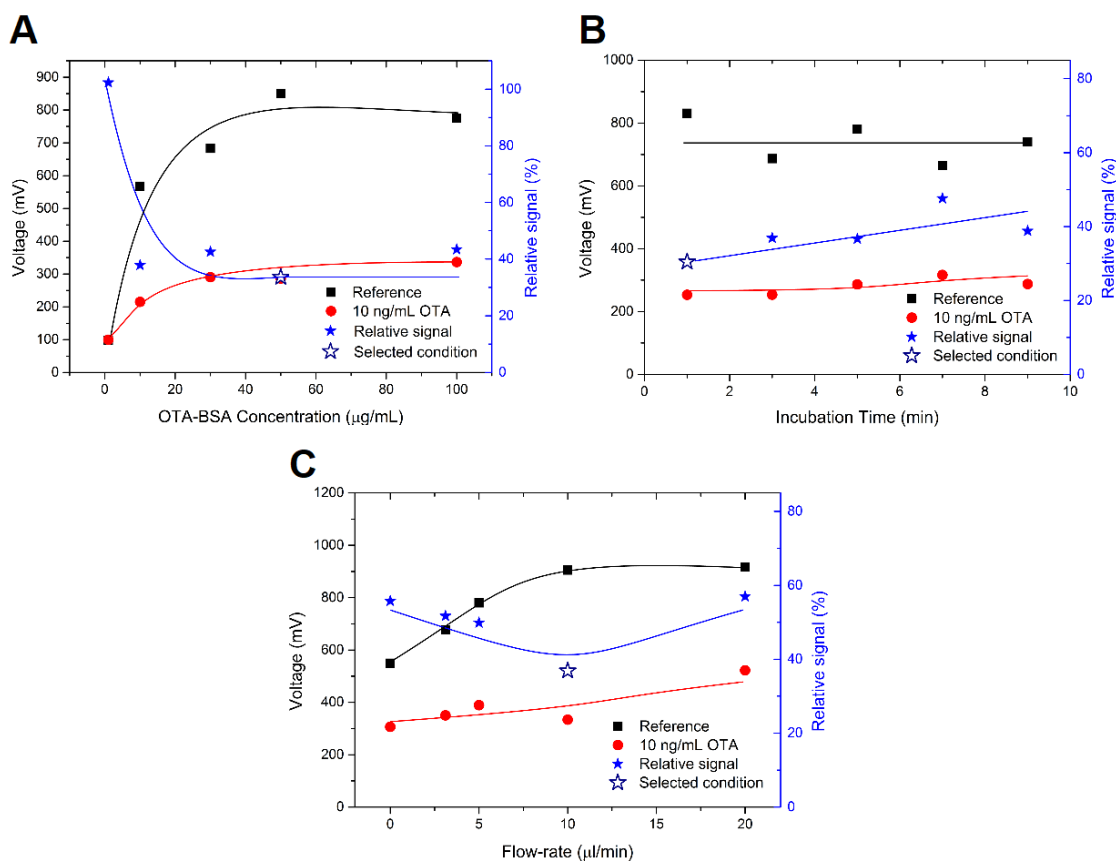


Figure 5.3 - Optimization of the OTA-BSA concentration (A), total incubation time (B) used to immobilize the antigen (OTA-BSA) on the walls of the microchannel via physisorption (B) and flow rate of the solution through the microchannel (C). The relative signal values are calculated by dividing the absolute voltage obtained in the 10 ng/mL OTA channel by the absolute voltage obtained in the reference channel. The flow rate and incubation time in A were fixed at 3.11 $\mu\text{L}/\text{min}$ and 5 min, respectively. The OTA-BSA concentration and flow rate in B were fixed at 50 $\mu\text{g}/\text{mL}$ and 3.11 $\mu\text{L}/\text{min}$, respectively. The OTA-BSA concentration and incubation time in C were fixed at 50 $\mu\text{g}/\text{mL}$ and 1 min, respectively. The final optimized conditions, highlighted in each plot with an empty star, were 50 $\mu\text{g}/\text{mL}$ for the concentration, 10 $\mu\text{L}/\text{min}$ for the flow rate and 1 min for the incubation time.

A similar optimization procedure was followed for the anti-OTA-HRP antibody. This molecule is spiked in the SUA containing a certain target concentration of OTA and flowed through the microchannel after a blocking step using 4% (w/v) BSA. The overall optimization process is summarized in **Figure 5.4**. First, to optimize the concentration of antibody in the SUA, two different approaches of analyzing the data were selected, plotted in **Figure 5.4-A** and **B** respectively. The first approach was to test the effect of the antibody concentration on the detection sensitivity of OTA. This was achieved by measuring calibration curves using increasing antibody concentrations, each mixed with a sample of increasing OTA concentrations spiked in a PBS buffer solution ranging from 0.5 to 100 ng/mL. These concentration range contains most regulatory limits for multiple foods and feeds according to the European Commission regulation 1881/2006. To

accurately evaluate the sensitivity of each condition, a threshold of 3 times the standard deviation of 12 independent reference measurements (using 2 $\mu\text{g/mL}$ anti-OTA-HRP) was plotted to define the overall LoD of the measurements and the intrinsic variability of the assay. This implies that at each antibody concentration, the smallest detectable concentration of OTA is defined by the abscissa of the intersection point between the 3σ threshold and each of the curves. It can be observed in **Figure 5.4-A** that while the decreasing trend of the curves remains approximately constant, the LoD tends to decrease with a decrease in antibody concentration, reaching sensitivities below 0.1 ng/mL OTA with the lowest tested concentration of 0.5 $\mu\text{g/mL}$ of anti-OTA-HRP. It can be noted that the trends for the 0.5 and 4 $\mu\text{g/mL}$ seem slightly different from the remaining curves, however, this observation results solely from the intrinsic variability of the assay, here plotted from single experiments. The main observation that the sensitivity tends to decrease as the concentration of antibody increases is expected in a competitive assay and has previously been reported in the literature [24, 312] since for a fixed concentration of OTA, the higher the concentration of antibody in solution, the lower the molar fraction of anti-OTA-HRP occupied with free OTA in equilibrium, implying a simultaneously lower relative change in the reference signal. However, the concentration of antibody that provides the highest sensitivity is not necessarily the optimal condition, since a higher sensitivity simultaneously compromises the absolute voltage signals obtained. This can be observed in **Figure 5.4-B**. The signals for both the reference and the 10 ng/mL samples increase with an increase in antibody concentration, translating the same effect to the signal ratios. Therefore, to simultaneously provide sufficient sensitivity, meaning a significant difference between the contaminated and the reference samples, and linear range (around 3 orders of magnitude), a concentration of 2 $\mu\text{g/mL}$ was selected.

The incubation time and the flow rate were subsequently optimized within the same range as previously performed for OTA-BSA. Interestingly, it can be observed in **Figure 5.4-C** that the signals obtained for both the reference and 10 ng/mL channels have a clear linear dependence with the tested range of incubation times. Two conclusions can be drawn from this observation. First, a fine control of the incubation time for the primary antibody is critical for accuracy and reproducibility. Second, since a conservative margin from the noise threshold was given when selecting the optimal antibody concentration, it allowed a further reduction in assay time from 5 down to only 3 min. This also highlights the potential of having even faster analysis times with the same assay sensitivity by increasing the antibody concentration. However, due to practical constraints of

maintaining reproducible incubation times it was not reduced further. Finally, the optimized flow rate was fixed at 5 $\mu\text{L}/\text{min}$ since, according to the observations plotted in **Figure 5.4-D**, while the signal from the contaminated sample does not change appreciably with an increase in flow rate, the signal from the reference reaches a maximum at 5 $\mu\text{L}/\text{min}$. The existence of this maximum value, similarly to what was observed for OTA-BSA, can be related with a maximum surface coverage. Differently, in this case, the maximum signal is a peak rather than a plateau and progressively decreases at higher flow rates possibly due to an increased erosion of the immobilized antibodies. This may be simultaneously due to a higher shear stress and the larger size of the OTA-BSA-antibody-HRP complexes as compared to OTA-BSA only.

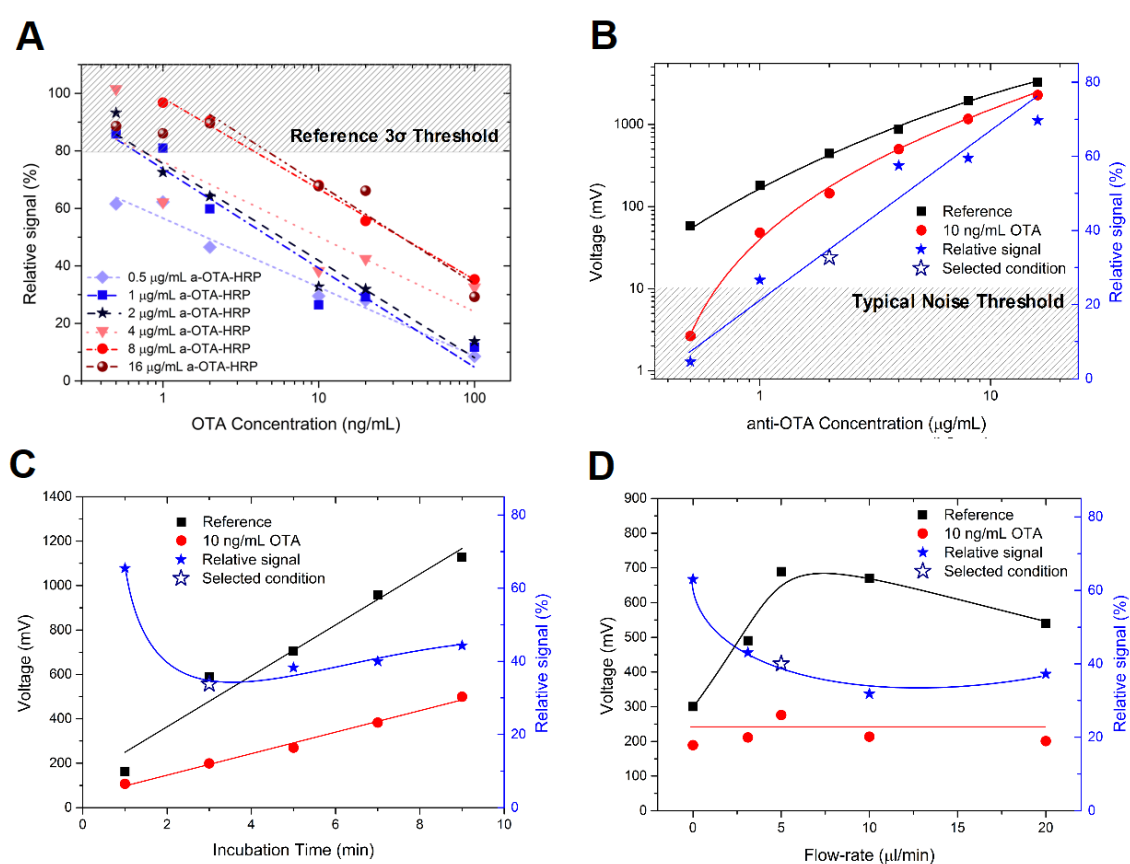


Figure 5.4 - Optimization of anti-OTA-HRP (a-OTA-HRP) concentration in the SUA (**A** and **B**), total incubation time (**C**) and flow rate of the solution through the microchannel (**D**). All the experiments were performed using the OTA-BSA conditions previously optimized in **Figure 5.3**. In **A** the intersection of the 3 σ threshold line with each of the curves defines the minimum OTA concentration that can provide a signal drop equal to three times the standard deviation of 12 reference measurements (performed with a concentration of 2 $\mu\text{g}/\text{mL}$ only). Relative signals are calculated by dividing the absolute voltage obtained for a given OTA concentration by the absolute value obtained for the reference. The flow rate and incubation time in **A** and **B** were fixed at 3.11 $\mu\text{L}/\text{min}$ and 5 min, respectively. The anti-OTA-HRP concentration and flow rate in **C** were fixed at 2 $\mu\text{g}/\text{mL}$ and 3.11 $\mu\text{L}/\text{min}$, respectively. The anti-OTA-HRP concentration and incubation time in **D** were fixed at 2 $\mu\text{g}/\text{mL}$ and 3 min, respectively. The final optimized conditions, highlighted in each plot with a non-filled star, were 2 $\mu\text{g}/\text{mL}$ for the concentration, 5 $\mu\text{L}/\text{min}$ for the flow rate and 3 min for the incubation time.

5.4. OTA calibration curve and assay regeneration

After optimizing each of the major variables for the OTA-BSA immobilization and primary antibody incubation steps, a calibration curve for increasing concentrations of OTA (0.5-100 ng/mL) was measured using the optimal conditions. The results are shown in **Figure 5.5-A**. The inset plot shows the absolute voltage values obtained for 12 independent reference measurements compared to the average value (526 mV), plotted as a straight line. The standard deviation (σ) of these measurements was used to calculate the LoD (concentration corresponding to a signal of 79%) here defined as 3σ and plotted as a straight dashed line. It can be observed that the entire curve is below the LoD threshold, thus, the optimized setup can detect at least 0.5 ng/mL OTA in solution, within the range required to meet the regulatory limits in most foods and feeds. The fitting of the curve was performed with a simple logarithmic fit according to **Equation 3.1**.

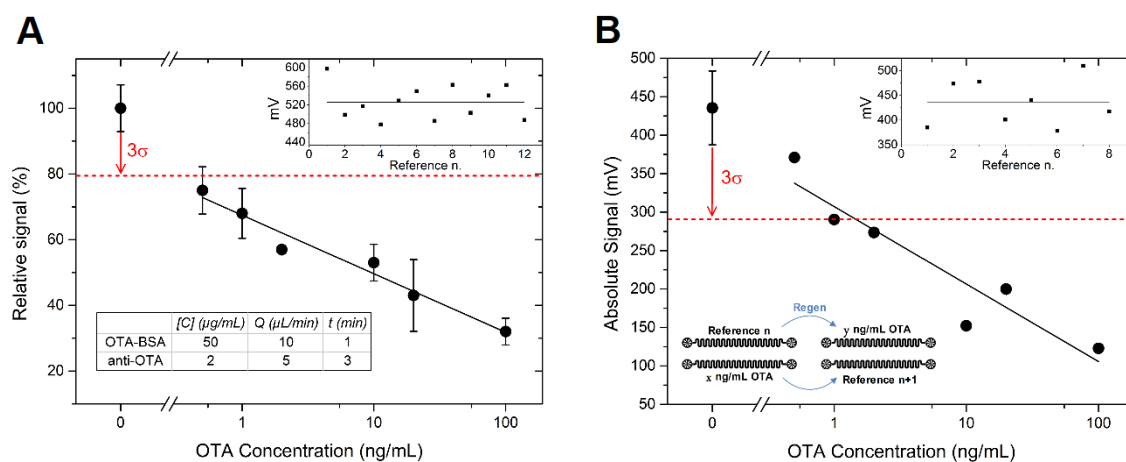


Figure 5.5 - Calibration curves of relative voltage signals obtained for increasing OTA concentrations using the optimized conditions described in the inset table without (**A**) and with regeneration (**B**). (**A**) The inset plot shows the results obtained for all the 12 independently prepared references, relative to the average value plotted as a straight line. The value of the standard deviation for this average value multiplied by 3 corresponds to the red dashed line in the main plot. The intersection of the red dashed line with the calibration curve corresponds to LoD, here < 0.5 ng/mL OTA according to the 3σ definition. (**B**) All the assays were performed in the same pair of channels, in which each pair of experiments was intercalated with a glycine buffer + BSA 4% regeneration step. As described in the inset schematics, each pair of experiments (reference and x ng/mL of OTA) were swapped after each measurement to confirm a complete and reproducible recovery of the signal for the references. The inset plot shows the results obtained for all the 8 independently prepared references, relative to the average value plotted as a straight line. The value of the standard deviation for this average value multiplied by 3 corresponds to the red dashed line in the main plot. The intersection of the red dashed line with the calibration curve corresponds to LoD, here between 1 and 2 ng/mL OTA according to the 3σ definition.

After evaluating the performance of the assay performed in independent channels for each reference and target concentration of OTA, the same optimized immunoassay protocol was tested within the same pair of channels for 8 consecutive measurements.

The results are shown in **Figure 5.5-B**. For this, each experiment (reference channel plus a target concentration of OTA) was intercalated with a regeneration step. The regeneration protocol comprises a first step of removal of the affinity bound anti-OTA-HRP antibodies by flowing a solution at a low pH (pH = 2), a standard condition known to break affinity interactions [307]. Then, a subsequent blocking step with BSA was performed to ensure that any BSA molecules removed from the surface during the previous stringent step are effectively replaced to prevent a subsequent increase in non-specific binding. In total, this regeneration process takes less than 5 min. To ensure that the signal drop from the SUA channel was not due to a loss of OTA-BSA concentration on the surface, each of the 2 channels were swapped after each experiment as schematized in **Figure 5.5-B**, meaning, that the channel where the reference was performed in one experiment was used as a SUA channel in the subsequent experiment. From the 8 references shown in the inset plot in **Figure 5.5-B** it can be concluded that the loss of OTA-BSA from the surface of the channel is negligible during the 8 subsequent assays. It can be observed that using the same channels the LoD was slightly increased in comparison to the previous case when new channels were always used, from 0.5 up to 1-2 ng/mL. This increase comes from a higher variability in the reference measurements with a 3σ of 67%, as compared to the previous 79%, which may arise from conformational changes in the OTA-BSA layer adsorbed on the surface. This variability can be reduced in future work by performing a systematic optimization of the regeneration solution towards the specific targeting of the antibody-antigen interactions. Nevertheless, the sensitivity obtained from this assay still covers most of the required regulatory spectrum with the increased advantage that the same OTA-BSA functionalized surface can be used for several consecutive measurements, reducing the overall cost per assay.

5.5. Detection of OTA in red wine at the regulatory limits

Finally, an experiment was performed to evaluate if the optimized assay can be used to quantify OTA at the regulatory limits (2 ng/mL) in red wine extracts. This matrix was selected since it provides pronounced matrix interference effects [19, 24, 293, 313] and requires a highly sensitive detection to cope with the particularly low regulatory limits, thus providing a worst case scenario. The full processing steps are described in detail in **Section 5.1.4** and, in summary, comprises the artificial spiking of three raw red wine samples with 2 ng/mL OTA which were then subjected to an ATPS processing step.

Then, the diluted PEG-rich phase was used directly as the SUA for the analysis. The references were prepared in the same way using non-spiked red wine. The results from the voltage readings over time are shown in **Figure 5.6** and the absolute values obtained from averaging the plateau (from 15 to 25 s) are shown in the inset plot. The measurements were performed in 6 independent channels without a regeneration step. The signal ratios obtained were 77, 67% and 79% for each of the first, second and third replicates respectively, averaging a signal reduction of $74.3 \pm 6.4\%$, just below the LoD threshold of 79%. Thus, it can be concluded that the optimized assay can effectively detect the presence of OTA in red wines at the regulatory limits within a total assay time of less than 25 min, including sample preparation. **Table 5.1** aims at comparing the reported assay with others previously discussed in the introductory **Chapter 1**. Based on the collected data, it can be concluded that this assay serves as a potential tool towards point-of-need mycotoxin screening among the state-of-the-art, being simple to prepare, rapid, regenerable and portable, while still providing sufficient sensitivity.

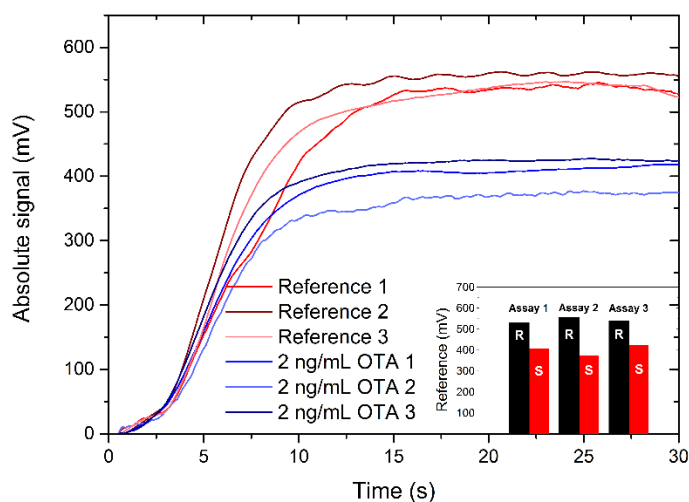


Figure 5.6 - Plot of voltage measurements (moving average values of 3 s) for three independent references and three wine samples spiked with 2 ng/mL OTA while flowing luminol through the microchannel at $10 \mu\text{L}/\text{min}$. Both references and spiked samples were prepared in raw red wine and subsequently processed according to the method developed by Soares and co-workers [19]. The inset plot shows the average absolute voltage obtained for the reference (labeled as “R”) and contaminated sample (labeled as “S”) in each of the three independent assays. The inter-assay variability in terms of oscillations observed during the plateau arise from electromagnetic interference.

Table 5.1 - Summary of recent OTA biosensing strategies published between 2014 and 2015. (1) Preparation time refers to the reported time required to prepare the sensing surface prior to the OTA biosensing step. (2) and (3) The portability and regenerability aspects refer only to what is reported by the authors, although it may be possible that all the methods can be engineered to have these characteristics.

Assay	Sensing surface	Prep. time ⁽¹⁾	Signal acquisition	LoD (ng/mL)	Assay time (min)	Portable ⁽²⁾	Regenerable ⁽³⁾	Ref.
This work	PDMS	< 10 min	Photodiode	< 1	5	Yes	Yes	-
Xie <i>et al</i>	Gold	> 18 h	Electrochemical cell	≈ 0.00012	> 60	No	No	[314]
Yao <i>et al</i>	Magnetic nanoparticle	> 4 h	Spectrofluorimeter	≈ 0.00013	80	No	No	[174]
Yang <i>et al</i>	Gold	> 4h	Electrochemical Analyzer	≈ 0.0003	35	No	No	[315]
Park <i>et al</i>	Gold	> 12 h	96-well plate reader	≈ 0.4	20	No	Yes	[155]
Wang R. <i>et al</i>	Silica	> 24 h	Photodiode	≈ 1.2	20	No	Yes	[316]
Wang C. <i>et al</i>	Magnetic beads	> 2 h	Spectrofluorimeter	0.0054	60	No	No	[317]
Reveal Q+ (Neogen)	Hydrophilic polymer	n.s.	AccuScan Pro Reader	2 (ppb)	9	Yes	No	-
ROSA ® (Charm)	Hydrophilic polymer	n.s.	Charm ROSA-M Reader	< 2 (ppb)	10	Yes	No	-
Ochra-V (Vicam)	Hydrophilic polymer	n.s.	Vertu Lateral Flow Reader	2.5 (ppb)	7	Yes	No	-

5.6. Integration of the immunoassay in a portable biosensor prototype

The immunoassay described in this chapter was further integrated in a prototype device co-developed with Lumisense Lda. within the context of the EU project DEMOTOX (FP7-SME-2013- 604752). The prototype box, illustrated in **Figure 5.7**, contained all the instrumentation required to perform the immunoassay, namely (1) a commercial c-Si photodiode, (2) a peristaltic pump to drive the liquid through the microchannels, (3) a microcontroller board to control the pump and acquire the current from the photodiode, pre-amplified by a 180 dB gain transimpedance circuit, (4) a Bluetooth® communication module and (5) a simple setup to align the PDMS device (schematized in **Figure 5.8**) above the photosensor, allowing continuous liquid flow with negligible light contamination.

Overall, this device provided the same analytical performance obtained using the setup described in **Figure 5.2**, while requiring significantly fewer manual operations. The user is only required to add 3 solutions, namely the SUA, PBS buffer and luminol substrate, in sequence, as requested by the software in the laptop computer. Since the prototype was designed with a single pumping port coupled to the PDMS device, the full analysis takes approximately 10 min, since the reference and the sample must be quantified in sequence.

Considering that the main objective of the DEMOTOX project was the detection of OTA in red wines and grape juice, the prototype was demonstrated to wine producers in Monção, Viana do Castelo, Portugal, to obtain feedback on the device performance for

routine screening of OTA contamination in grapes. The negative feedback given by the producers was extremely important to guide further developments, focusing on two major flaws, namely (1) 10 min for the time of analysis was not suitable for the fast-paced wine industry, particularly when raw materials are received from multiple vineyards and (2) the requirement of three steps to perform the analysis, with intervals of a few minutes, not only forces the user to be close to the equipment throughout the entire duration of the assay, but also hinders the parallelization of multiple analysis, often required to adequately screen a large lot of grapes. Potential solutions to these design flaws are addressed in this thesis, discussed below after **Chapter 8**. The subsequent **Chapters 6 and 7** address first the multiplexed analysis of multiple samples and mycotoxins and the simplification of the liquid flow mechanism and signal acquisition, which are also potential limitations of this prototype, depending on the target application.

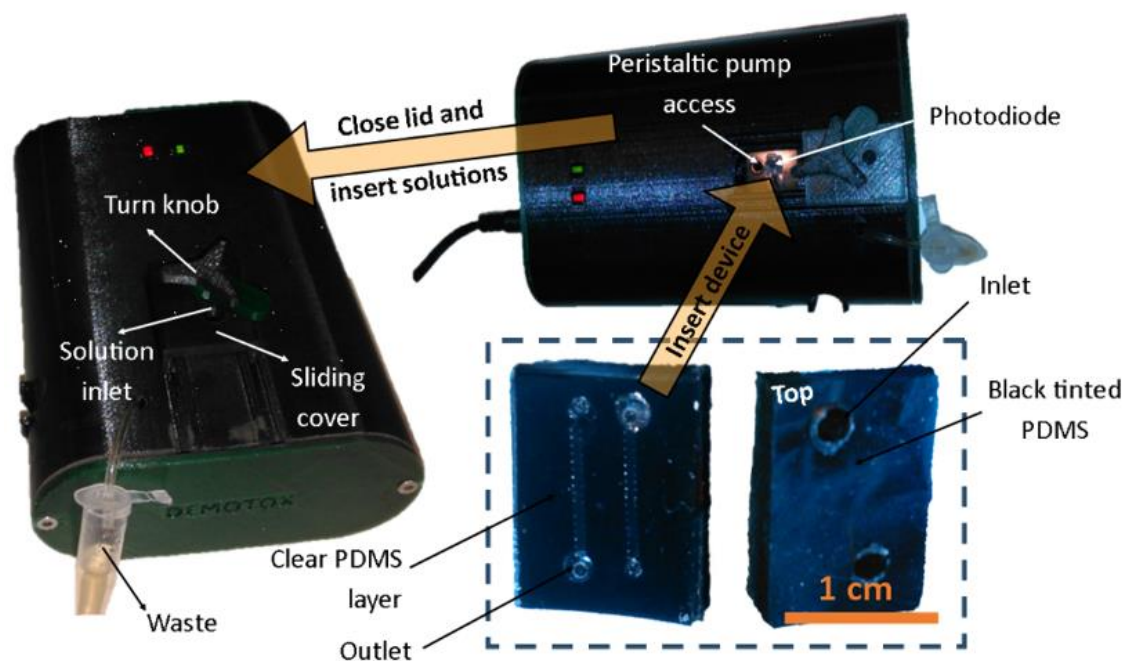


Figure 5.7 – Photographs of the integrated biosensor prototype co-developed in collaboration with Lumisense Lda. within the context of the EU project DEMOTOX (FP7-SME-2013- 604752). The body of the box was 3D printed with black PLA filament to minimize room and/or sunlight interference. The inside of the box was sprayed with a conductive ink to serve as a ground for the circuitry. The previously described amplification circuit and microcontroller board were contained inside the box and connected to the photodiode and a miniaturized peristaltic pump to drive the solutions through the PDMS devices. To allow true portability, the box used a standard 5 V power pack as power supply and integrated a Bluetooth® wireless module, allowing communication with a tablet computer. The disposable PDMS device to perform the immunoassay is described in **Figure 5.8**. The PDMS device fits into the pocket of the box and is automatically aligned with the c-Si photodiode and an access hole to the peristaltic pump. The sliding cover is coupled with a manual turn knob to press down the device, ensuring an air-tight seal against the pump access. The solutions are added through a hole in the sliding cover as instructed by a software in the tablet computer, which also controls the peristaltic pump.

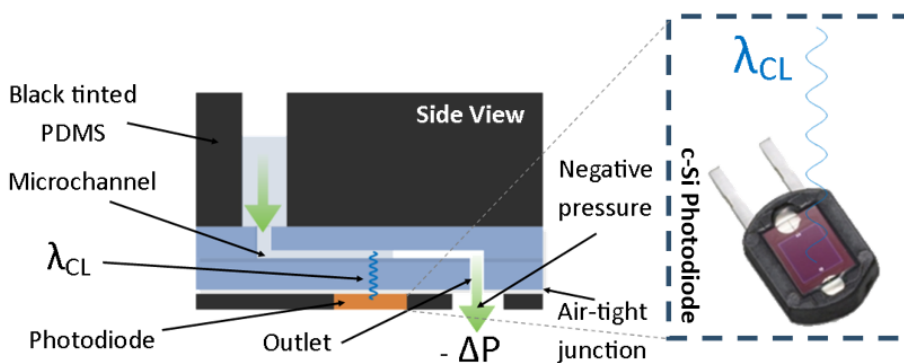


Figure 5.8 – Schematics of the PDMS device coupled with the integrated prototype described in **Figure 5.7**. The top side of the device (pressing against the sliding cover) was tinted with black ink to prevent light contamination. The solution is added to the top well and is driven into the microchannels by the negative pressure exerted by the peristaltic pump. The microchannel PDMS layer and sealing layer are both optically transparent in the visible range, allowing the chemiluminescent light to reach the photodiode below. λ_{CL} refers to the emitted chemiluminescent light and ΔP to the difference in pressure (negative) generated by the peristaltic pump.

5.7. Chapter conclusions

This chapter described a novel OTA biosensing strategy based on a direct competitive chemiluminescent immunoassay performed in a microfluidic channel. By integrating a photosensing setup, ultrarapid measurements were provided below the regulatory limits for all regulated foods in the European union (< 0.5 ng/mL), in less than 5 min. Furthermore, the assay could be easily regenerated for at least 8 times without a significant loss in sensitivity. The optimized immunoassay was also validated for the quantification of OTA at the regulatory limit of 2 ng/mL in spiked samples of red-wine previously subjected to an extraction process with a polyethylene glycol (PEG)-salt ATPS. These results highlight the potential of this type of assay to compete with the current state-of-the-art in point-of-need mycotoxin detection after subsequent improvements in assay automation, as is the case of the prototype device discussed in **Section 5.6**. Furthermore, the same design can be easily extended to other highly relevant mycotoxins such as aflatoxins, deoxynivalenol, fumonisins or zearalenone and also further improved using novel engineered biorecognition molecules such as nanobodies fused with enzymes [318], providing increased affinity, stability and resistance to matrix interference.

Chapter 6

Immunoassay Multiplexing Coupled with a Microarray of Photoconductors

Considering the common co-contamination of foods and feeds with multiple types of mycotoxins, often associated with synergistic toxic effects, this chapter reports the extension of the microfluidic immunoassay to multiplex the detection of three mycotoxins in three samples simultaneously. In this context, a novel, simple, negative pressure-driven device with manually operated magnetic valves was developed and the simultaneous immunodetection of these three mycotoxins was demonstrated via the laminar flow patterning of probes in an area of $\approx 0.12 \text{ mm}^2$ and subsequent chemiluminescence generation via HRP-labelled antibodies. The three mycotoxins were detected in less than 20 min at concentrations of 100 ng/mL for OTA and DON and 3 ng/mL for AFB1, spiked in a sample under analysis and simultaneously compared to a toxin-free reference and a standard contaminated with critical target concentrations. The on-chip optical detection was performed in a single acquisition step by integrating a microfabricated array of $25 \times 25 \text{ }\mu\text{m}$ hydrogenated amorphous silicon (a-Si:H) photosensors below the microfluidic chip. The device presented in this chapter is also a simple and effective approach for point-of-need multiplexing of immunoassays in general. The contents of this chapter are reproduced with appropriate adaptations from one original research article [42] co-authored with Denis R. Santos, PhD student at INESC MN, who performed the photosensor fabrication, optimization and characterization.

6.1. Materials and experimental methods

6.1.1. Preparation of PDMS devices with embedded NdFeB magnets

The polydimethylsiloxane (PDMS) devices with embedded N48 Ni-plated NdFeB rod shaped magnets with 3 mm diameter and 6 mm height (Supermagnete, Gottmadingen, Germany), were fabricated as follows. First, PDMS pre-polymer was mixed at a ratio of 1:10 curing agent to PDMS oligomers ratio, degassed and spin coated on top of the SU-8 mold for an average final thickness of 200 μm . The mold was then baked at 70 °C in a convection oven for 30 min. After this baking step, the magnets were manually

aligned on top of the PDMS layer and fully immersed in a second thicker layer of uncured PDMS. The device was subsequently baked for an additional 75 min under the same conditions and peeled off from the mold. The remaining processing steps was performed as described in detail in **Chapter 2**.

6.1.2. Operation of the multiplexed microfluidic device

A schematic illustration of the structure of the device is shown in **Figure 6.1** and the operation steps are described in detail and shown in **Figure 6.2**. The operation was performed as follows. Liquids were introduced in the microchannels via a 20 ga metal adapter coupled to polyethylene capillary tubing inserted into one of the two available outlet ports, identified with radial features (A). The polyethylene tubing was connected to a syringe pump and PBS buffer solution (PBS tablets from Sigma-Aldrich) was introduced in the microchannels at a flow rate of 43 $\mu\text{L}/\text{min}$ by applying a positive pressure until liquid was observed to flow out of the device through every inlet port (B). Then, the pump was stopped and two NeFeB magnets were used to seal the channel perpendicular to the one being pumped by the syringe pump. Next, without removing the metal adapter from the outlet, pipette tips containing spacer solutions and capturers were inserted in the respective inlets and carefully released from the pipette. All the spacer solutions are prepared by dissolving polyethylene glycol (PEG) with an average MW of 8 kDa (Sigma-Aldrich) at a concentration of 11% (w/w) in water. It is essential that during this step no air bubbles are trapped between the solutions and the buffer inside the device. After inserting the pipette tips, the following steps were performed: (C) PBS was inserted inside the device at 43 $\mu\text{L}/\text{min}$ for 10 s by applying a positive pressure with the syringe pump; (D) after 10 s, the direction of pumping was reversed to pulling without stopping the syringe pump, while maintaining the flow rate at 43 $\mu\text{L}/\text{min}$ for an additional 15 s; (E) finally, the flow rate was reduced to 3 $\mu\text{L}/\text{min}$. After 10 min of flowing the capturer streams, the pump was stopped, the metal adapter was removed, washed by purging out buffer solution, inserted back in the same outlet and PBS was flowed inside at 10 $\mu\text{L}/\text{min}$ for 30 s to remove any weakly bound or dispersed capturer molecules (F). After the laminar flow-based patterning the capturer molecules, the magnets were removed and shifted by 90° and the metal adapter was inserted in the second outlet. Before the subsequent insertion of the pipette tips containing spacer and target solutions, PBS is flowed at 10 $\mu\text{L}/\text{min}$ to assure the removal of any air bubbles trapped in the inlet holes or microchannel network (G). Afterwards, the pipette tips were inserted and steps (H) to (J)

were performed in the same way as previously described for (C) to (E), followed by 5 min of flowing the target streams and washing with PBS for 1 min at 10 $\mu\text{L}/\text{min}$ (K). Before and after flowing the target molecules, the region of interest (ROI) was rinsed with PBS at 10 $\mu\text{L}/\text{min}$ for 1 min.

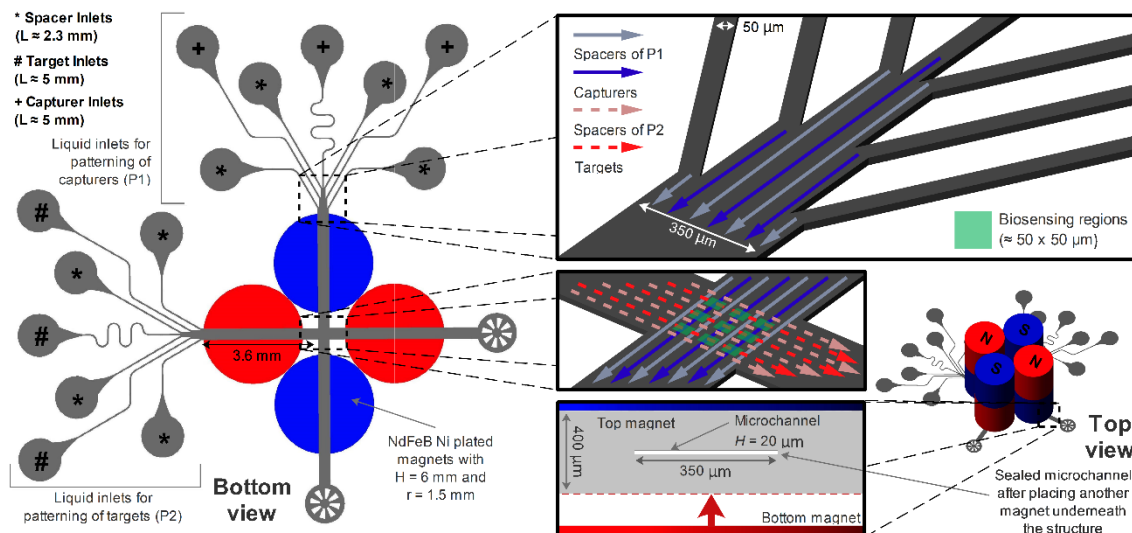


Figure 6.1 - Schematics of the microfluidic structure used for multiplexing of immunoassays. Both intersecting channels are identical in terms of features and dimensions. The term “capturers” refers to the molecules intended to be immobilized on the microchannel surface. The term “target” refers to the molecules intended to be selectively captured by the capturers previously immobilized on the microchannel surface. The term “spacer” refers to a solution which serves the function of preventing cross diffusion between each of the different capturer and target streams.

6.1.3. Operation of the multiplexed microfluidic device

Detailed schematics of the operation of the device for multiplexed toxin immunoassays are described in detail in **Figure 6.3**. The device was operated using the conditions described in **Section 6.1.2**. with two additional steps: (1) flowing a 4% (w/v) BSA solution and (2) flowing luminol or 3,3',5,5'-Tetramethylbenzidine (TMB) solutions containing hydrogen peroxide. The first step (1) was performed immediately after patterning the capturers (BSA-toxin conjugates) by flowing a solution of BSA 4% (w/v) prepared in PBS through the outlet at 5 $\mu\text{L}/\text{min}$ for 30 s and 0.5 $\mu\text{L}/\text{min}$ for 5 min. This step was followed by a PBS washing step at 10 $\mu\text{L}/\text{min}$ for 30 s. The second step (2) was performed after washing the weakly bound targets (anti-toxin antibodies) by continuously flowing a luminol (SuperSignal® West Femto Maximum Sensitivity Substrate, Thermo-Scientific) or TMB (ready to use 1-Step™ Ultra TMB-Blotting, Thermo-Scientific) solutions at 10 $\mu\text{L}/\text{min}$ through the outlet by applying a constant positive pressure. OTA-BSA, AFB1-BSA, BSA, ochratoxin A, aflatoxin B1 and deoxynivalenol were purchased from Sigma-Aldrich. Anti-OTA-HRP polyclonal antibodies were purchased from

Immunechem Pharmaceuticals (Burnaby, Canada). Anti-AFB1 mouse monoclonal antibodies (AFA-1) were purchased from Abcam (Cambridge, UK). Anti-DON mouse monoclonal antibodies were purchased from Biotez (Berlin, Germany). All solutions and reactions were prepared or carried out in ultrapure water obtained from a MilliQ water purification system (EMD Millipore, Billerica, MA, USA).

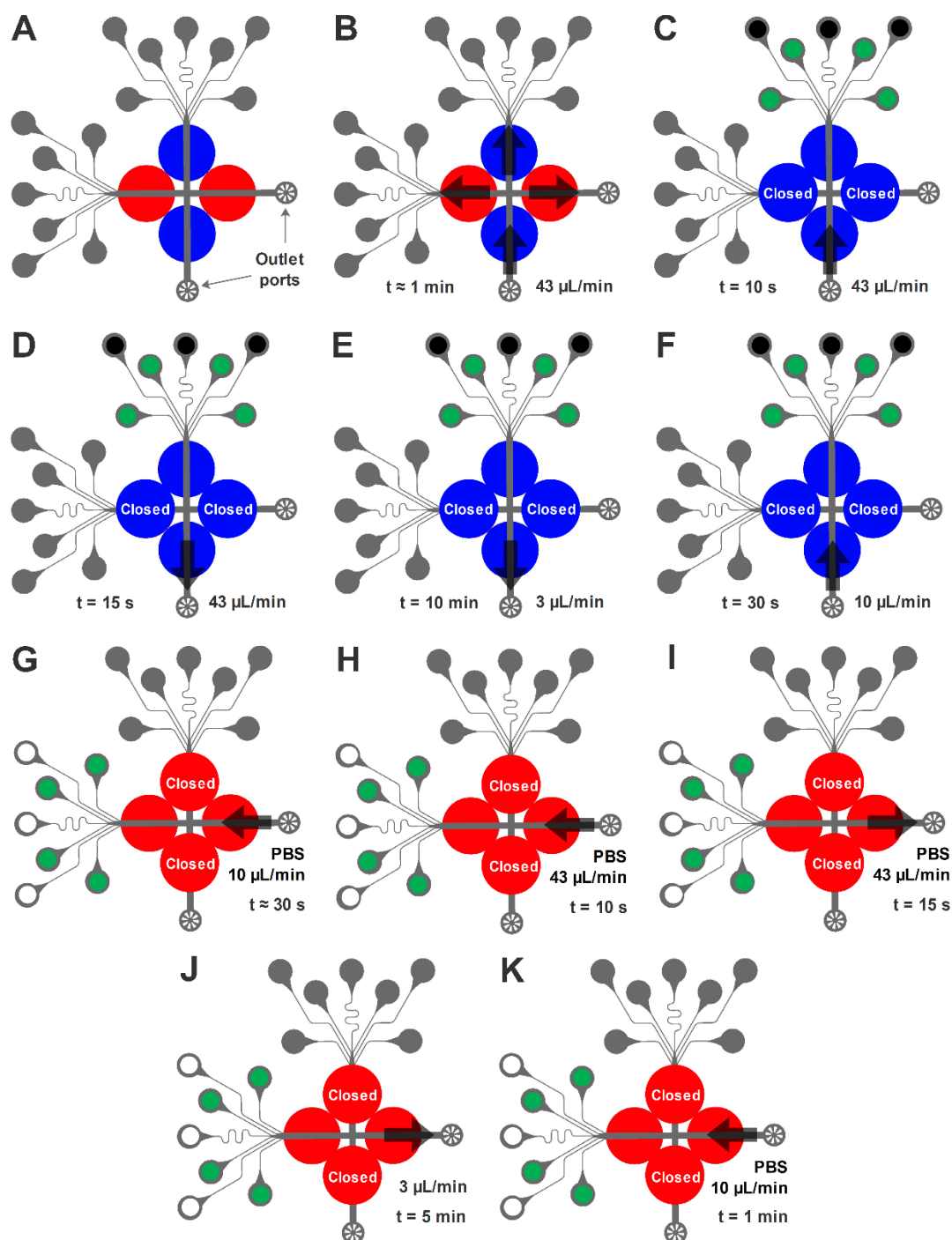


Figure 6.2 - General operation schematics of the multiplexing device. The black arrows indicate the access points where a negative or positive pressure is applied and the direction of the liquid flow. The black, green and white circles indicate the inlets for the capturers, spacers and targets, respectively.

6.1.4. Preparation of DON-BSA, anti-AFB1 IgG-HRP and anti-DON IgG-HRP

The DON-BSA conjugates were prepared using 1,1'-carbonyldiimidazole (CDI) chemistry with a protocol adapted from Maragos and McCormick [113]. Briefly, 5 mg of CDI (Sigma-Aldrich) were added to 1 mg of DON in an amber glass vial and subsequently dissolved in 100 μ L of anhydrous HPLC grade acetone (Sigma-Aldrich) to activate the DON molecules with CDI. The mixture was then incubated for 30 min in the dark under constant stirring. Without ceasing the stirring motion, 1 mL of a 10 mg/mL BSA solution prepared in 100 mM sodium bicarbonate was quickly added to the reactive DON solution. The mixture was kept for 2 more hours in the dark under constant stirring. To remove the acetone and bicarbonate salts, the DON-BSA conjugate solution was washed 5 times with phosphate buffered saline (PBS) buffer at pH 7.4 in 10 kDa Amicon ultra 0.5 mL centrifugal devices (Merck Millipore) by centrifugation at $14,000 \times g$ for 7 min. The solution was then diluted with PBS for a final concentration of 1 mg/mL. The anti-DON and anti-AFB1 IgG-HRP conjugates were prepared using an HRP conjugation Kit (ab102890) purchased from Abcam. Briefly, 10 μ L of proprietary modifier agent were added to a 100 μ L solution of antibody with a concentration of 1 mg/mL and the mixture was used to re-suspend the lyophilized HRP. After complete dissolution the mixture was left for 3 hours in the dark at room temperature and, subsequently, 10 μ L of proprietary quencher solution was added. The conjugates were used without further purification.

6.1.5. Measurements using the photoconductor array

The addressing of the 9 photosensors during the chemiluminescence acquisition was performed using two multiplexer integrated circuits of 8 input channels to 1 output each (MAX 338, Maxim Integrated) located on a PCB which contains 2 coaxial BNC connectors to interface with a Keithley 237 picoammeter. Details of photosensor characterization can be seen in **Figure 6.4**. A Samtec edge card socket (part # MB1-120-01-F-S-02-SL) soldered to the bottom of the PCB of the multiplexer is used to insert and connect the photosensor array PCB. An Arduino Uno Rev3 microcontroller is connected with pin connections to the multiplexer circuits for channel selection and for power and is programmed using the Arduino IDE via serial communication through USB connection. A Graphical User Interface (GUI) programmed with Python and PyQT4 is used to read General Protocol Interface Bus (GPIB) and process the data from the picoammeter.

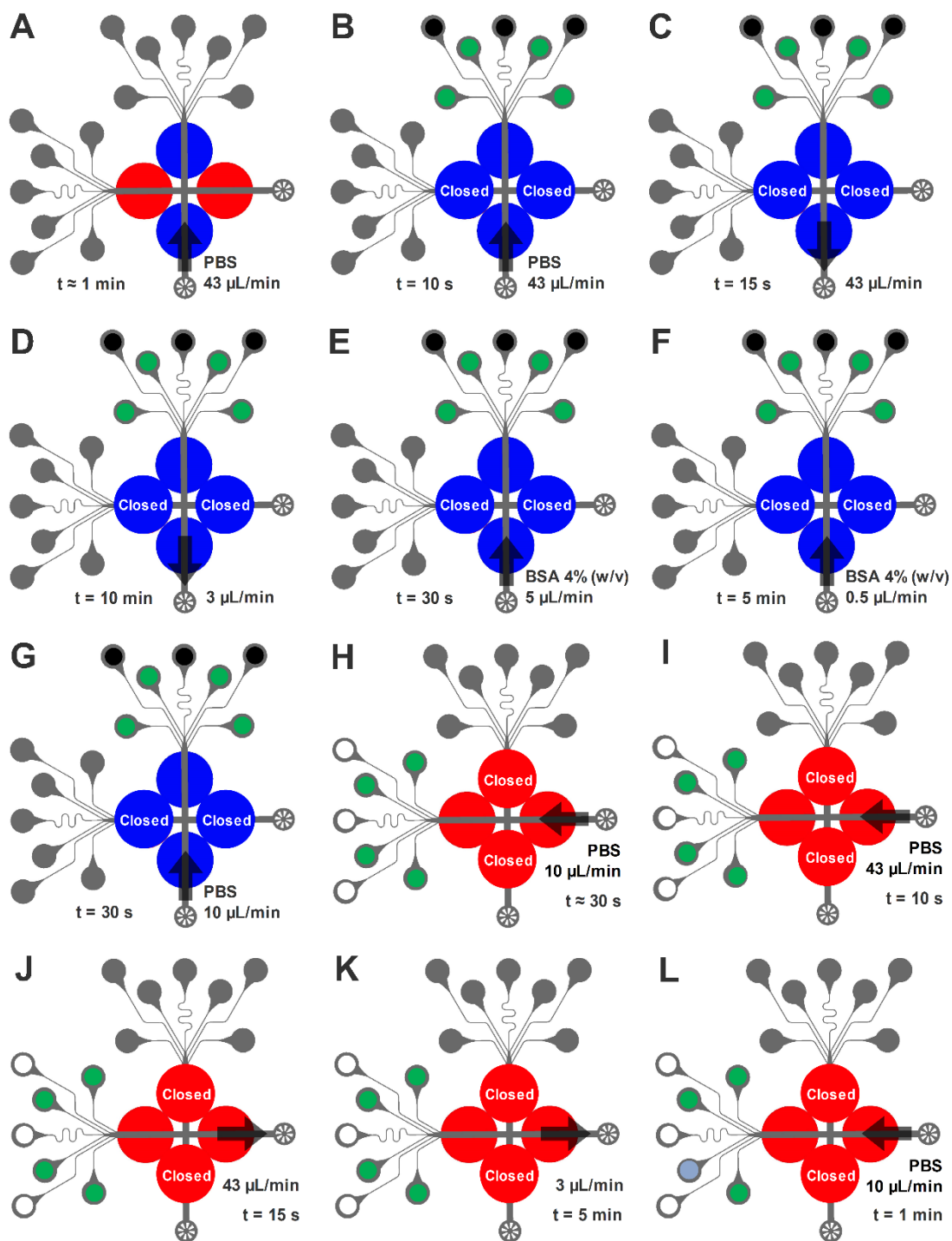


Figure 6.3 - Detailed operation schematics for the multiplexed assays. The black arrows indicate the access points where a negative or positive pressure is applied and the direction of the liquid flow. The black, green and white circles indicate the inlets for the BSA-toxin conjugates, PEG 8,000 11% (w/w) solutions and anti-toxin antibodies plus SUA, respectively. After the step schematized in L, a solution of luminol or TMB is flowed along the same direction also at 10 $\mu\text{L}/\text{min}$, without opening the respective closed magnetic valves.

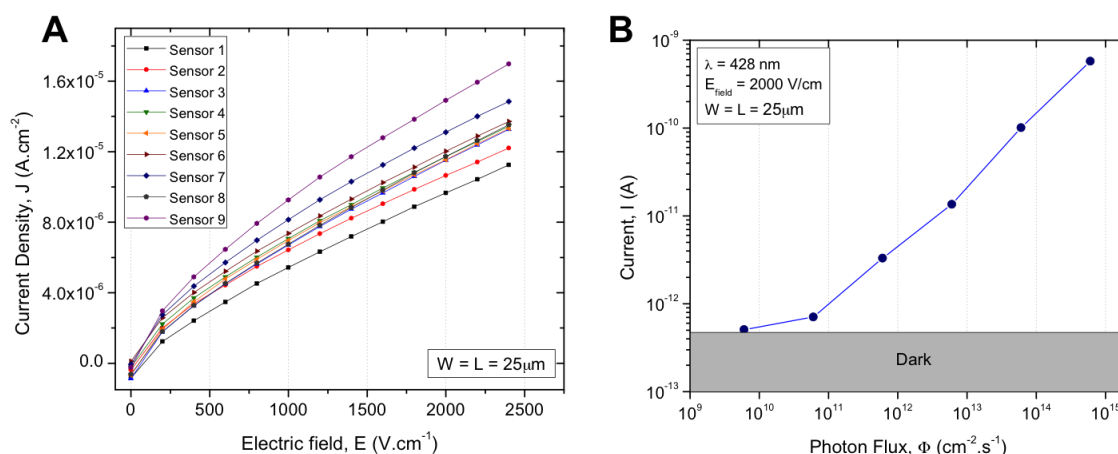


Figure 6.4 - The photosensors were characterized individually in the dark and using light from a tungsten-halogen lamp (250W) coupled to a monochromator (Oriol Model 77250) for wavelength selection. The current-voltage (I - V) in the dark and the current-photon flux (I - Φ) photoresponse curves at 428 nm (wavelength corresponding to the immunoassay chemiluminescence emission) were measured using a picoammeter. The incident photon flux was determined using a calibrated silicon photodetector (S1226-5BQ, Hamamatsu Photonics K. K.). The current signals generated by the photosensors array during the immunoassay were acquired with the picoammeter 237. **A**- Current density (J) of all 9 photoconductors as a function of the applied electric field (E). The J - E characteristics were measured at room temperature and in dark conditions. The photoconductor array exhibits a dark conductivity of $\sigma_{\text{dark}} = 5.1 \times 10^{-9} \pm 5.0 \times 10^{-10} \text{ S}\cdot\text{cm}^{-1}$. **B**- The sensor photoresponse at chemiluminescence emission wavelength ($\lambda_{\text{em}} = 428 \text{ nm}$) was also measured showing a linear photocurrent dependence with the incident photon flux Φ in the range of $\Phi \sim 6 \times 10^{10} \text{ cm}^{-2}\cdot\text{s}^{-1}$ to $\Phi \sim 6 \times 10^{14} \text{ cm}^{-2}\cdot\text{s}^{-1}$.

6.2. Multiplexing concept and microchannel design

The microfluidic structure is shown schematically in **Figure 6.1**. The short travel distances and laminar flow obtained under these flow conditions ($Re < 1$) allow the molecules to flow in parallel with no convection and negligible diffusion. To further reduce any possible cross contamination, a highly viscous spacer solution flows between each of the capturer and target molecule streams. By first flowing three streams containing BSA-toxin conjugates, acting as capturers, in one channel, and then flowing three streams containing anti-toxin-HRP antibodies, acting as targets, in the perpendicular channel, a matrix of 9 independent biosensing regions is obtained, allowing the simultaneous detection of three different analytes in three different samples. The region containing the biosensing areas will henceforth be referred to as region of interest (ROI). To flow the liquids individually in each direction, a magnetic valve system was integrated in the device, comprising permanent NdFeB magnets at a fixed $200 \mu\text{m}$ distance above the microchannels, each generating a magnetic field of 1.37-1.42 T. These valves are normally open and can be closed by placing a magnet with the opposite polarity facing

the embedded magnet. The force exerted between the magnets is sufficient to compress the PDMS and close the microchannel. When closed, this valve system can sustain pressures of up to at least 300 kPa, limited by delamination of the sealing membrane. After removing the magnet, the valve opens in less than 1 s. To further simplify the system, the flow of the liquids was controlled by applying negative pressure at the outlet with the inlets designed to allow the spacer solutions to flow simultaneously inside the channel before the flow of the capturers and targets, thus creating 3 discrete flow streams, separated by spacer streams, and preventing adsorption in the regions in-between the streams. This was done by increasing the distance of the capturer/target inlets from the main channel (≈ 5.5 mm) as compared to the spacer inlets (≈ 2.3 mm).

6.3. Spatially resolved adsorption of BSA fluorescent conjugates

To first evaluate the resolution of the physisorption-based molecular patterns of the multiplexing device previously discussed (shown and described in **Figure 6.5-A**), solutions of green fluorescent BSA-FITC conjugates and red fluorescent BSA-Alexa 555 conjugates were used along the two perpendicular directions of the device. **Figure 6.5-B** shows the results, imaged using a fluorescence microscope. It was observed that the interface positions between each of the solutions, as shown in **Figure 6.5-C**, were very stable, with virtually no discernible flow oscillations for at least 10 min. The PEG based spacer solution thus provides (1) a stable flow of the solutions via the application of a negative pressure, (2) an inert medium for primary channel wetting preventing cross-solution contamination from one capturer/target solution wetting the channel before the other, (3) improved contrast for monitoring of the process under the microscope due to refractive index differences between the spacer solution and capturer/target solutions and (4) minimal lateral diffusion between solutions of interest up to the ROI. Regarding point (4), it is relevant to highlight that assuming Brownian motion and a diffusion coefficient of $3.35 \times 10^{-12} \text{ m}^2 \cdot \text{s}^{-1}$ for the BSA molecules [319] in the PEG solution used ($\eta \approx 10 \text{ mPa} \cdot \text{s}$), the molecules of BSA will only experience a lateral diffusion of around $1.8 \text{ }\mu\text{m}$ before reaching the ROI, which represents approximately 0.5% of the total channel width. On the other hand, had pure water been used as the spacer solution, the expected lateral diffusion would have been $8.2 \text{ }\mu\text{m}$, comparable to the width of each stream, considering that diffusion occurs on both sides of the spacer. The fluorescence microscopy image in

Figure 6.5-C also highlights both the good patterning resolution and the nine points of intersection between each of the adsorbed BSA-conjugate streams.

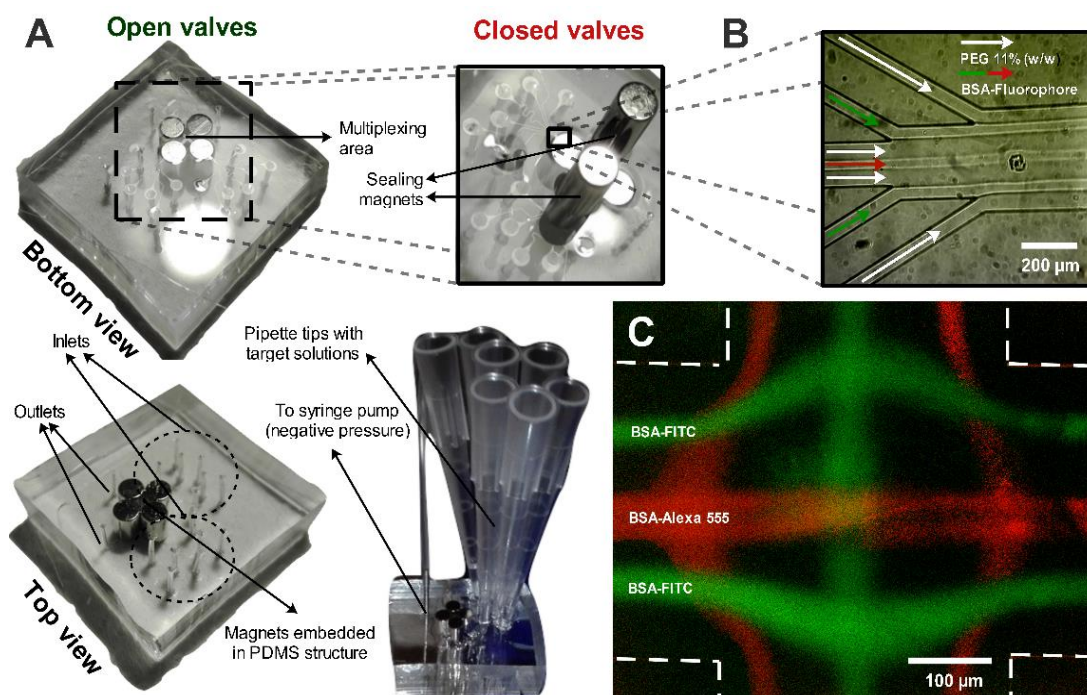


Figure 6.5 - **A**- Photographs and schematic operation of the microfluidic device. **B**- The interface of the spacer solutions is visible under the bright field microscope due to a higher refraction index of the highly concentrated PEG spacer solutions. **C**- Composite of the green and red channels of two images acquired under the fluorescence microscope using blue or green excitation lights, respectively. Both fluorescence images were acquired after flowing the BSA-fluorophore solutions and spacers in both directions, first from left to right, and washing the channel with PBS for 1 min.

6.4. Simultaneous calibration and immunodetection of the mycotoxins OTA, AFB1 and DON

After optimizing the operating conditions to provide nine discrete biosensing points, the multiplexing device was subsequently tested for the simultaneous detection of three different mycotoxins, OTA, AFB1 and DON, using the direct competitive immunoassay strategy described in **Figure 6.6**. With the purpose of blocking the channel surface after patterning the capturers, a solution of 4% (w/v) BSA was used, with the blocked region showing a decrease in non-specific signal of about one order of magnitude, compared to the non-blocked region as can be seen in **Figure 6.7**. After flowing the targets, a solution of luminol and hydrogen peroxide is flowed through the ROI to generate a stable plateau of chemiluminescence as described previously [21]. This signal is proportional to the surface density of antibody-HRP molecules on each spot and inversely proportional to the target toxin concentration. Prior to performing the

multiplexed detection of multiple mycotoxins, it was important to evaluate any cross-reactivity between the antibodies and target mycotoxins. The results in **Figure 6.6-A** and **B** clearly show that, based on the optical microscopy images and the 3D intensity plots there is negligible cross-reactivity. In **Figure 6.6-B**, the use of an antibody mixture results in all 9 spots showing significant chemiluminescence intensity whereas when using the individual antibodies, as in **Figure 6.6-A**, only the region where the respective target toxin-BSA conjugate is patterned has a measurable signal, resulting in the observed diagonal spot profile. It is also important to highlight that this laminar-flow patterning-based methodology can be further scaled-up to detect more analytes and samples in a single run.

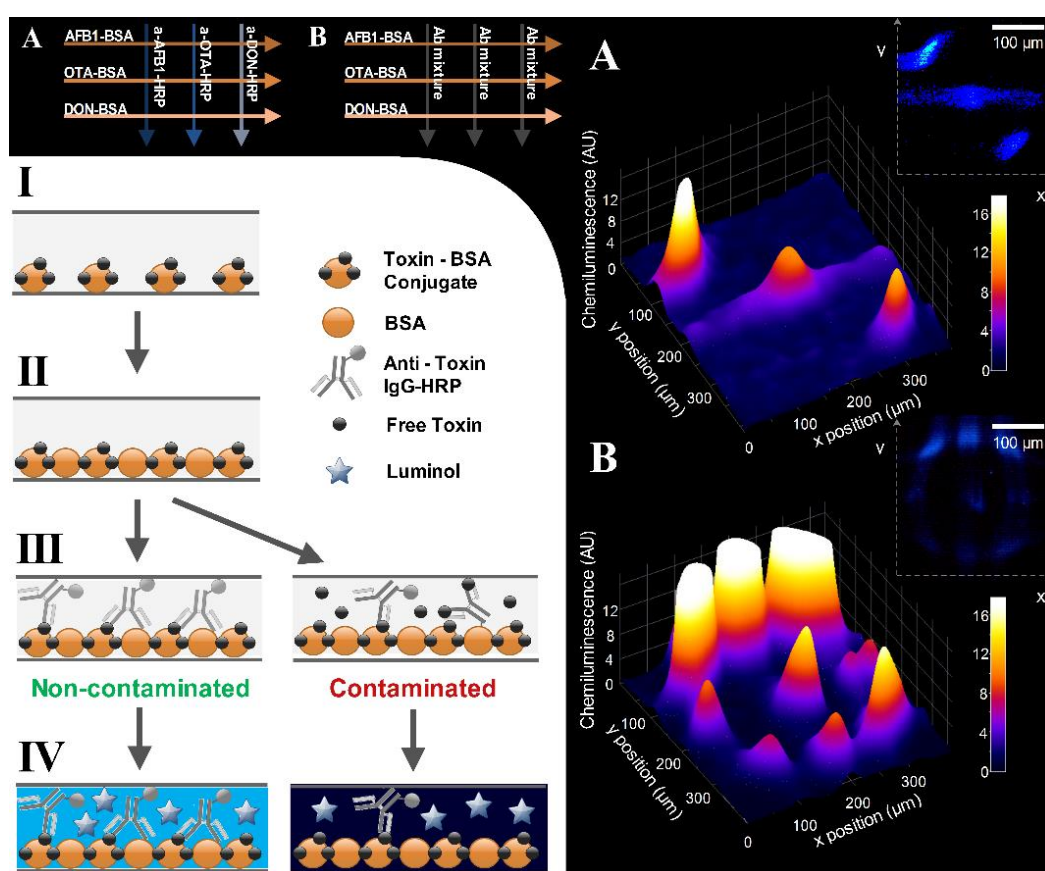


Figure 6.6 - Schematics of the direct competitive immunoassays and results of the cross-reactivity tests. I- Adsorption of toxin-BSA conjugates. II- Blocking with unconjugated BSA molecules. III- Flow of solutions-under-analysis (SUA) containing horseradish peroxidase (HRP) conjugated anti-toxin antibodies. IV- Flow of a luminol solution to generate light proportional to the surface concentration of HRP. A and B - Intensity profile, microscope image and schematics of the ROI of the experiment used to test cross reactivity of anti-toxin antibodies to non-specific toxins. The horizontal arrows in the schematics of the experiments refer to the capturers flowed long the x axis while the vertical arrows refer to the targets flowed along the y axis. Ab mixture refers to a solution containing all the three anti-toxin antibodies (a-AFB1-HRP, a-OTA-HRP and a-DON-HRP). The microscopy images were contrast-enhanced for visualization purposes.

Prior to the multiplexed assays, calibration curves for each toxin were measured by performing the immunoassays in independent $20 \times 200 \times 5000 \mu\text{m}$ ($H \times W \times L$) straight PDMS microchannels in a singleplex mode based on the same methodology described in detail in **Chapter 4**. The results obtained for the assay calibrations in single channels are shown in **Figure 6.8-A** where it can be observed that limits of detection (LoD) of at least 0.1, 0.3 and 1 ng/mL were obtained for AFB1, DON and OTA, respectively, according to the 3σ criterion. This result thus validates the architecture of the competitive assays and chemiluminescence based detection per se, prior to testing the detection in the multiplexing device, with the obtained sensitivities complying with most of the regulatory limits in foods and feeds for both OTA and AFB1 and all regulatory limits for DON (in European Commission regulation 1881/2006 and European Commission recommendation 2006/576/EC). The multiplexing tests were designed to include simultaneous measurements of both a reference and a standard along with the sample under analysis (SUA). The compositions of these solutions and each of the SUAs are described in **Figure 6.8-B**. The function of the reference solution is to establish the maximum signal obtained for each of the anti-toxin-HRP antibodies in the absence of the specific toxin, while the standard contains a target concentration (i.e. at a certain critical regulatory limit for a feed under analysis) of each toxin, for example, 3 ng/mL AFB1, 100 ng/mL OTA and 100 ng/mL DON, which are values within the regulatory ranges and chosen as hypothetical critical concentrations for a certain target food or feed. Thus, by comparing the signal obtained for both the SUA and standard relative to the reference solution, it is possible to evaluate whether the SUA is contaminated or not with the target toxins under analysis. The contrast-enhanced bright field images of light emission from the ROI and the respective 3D intensity plots for each of the SUAs are shown in **Figure 6.8-C**. One can clearly see that the SUA signal drops to intensity levels comparable to those of the standard solution if the specific toxin is present, i.e., if only DON is present at the target level, only the signal from DON biosensing region will drop. **Figure 6.8-D** shows the absolute average chemiluminescence intensity of the reference, standard and sample under analysis (SUA). It can be observed that the signals obtained for non-contaminated and contaminated SUAs are within the SD (from 3 independent experiments) of the reference or standard spots, respectively. These results show that the multiplexed immunoassay can simultaneously detect DON, OTA and AFB1 spiked in a buffer solution, where contaminated solutions had average relative chemiluminescence signals of $62.6 \pm 1.6\%$, $64.6 \pm 4\%$ and $66 \pm 2.1\%$ (average \pm SD), while non-contaminated

solutions had signals of 92%, 98% and 105% for DON, OTA and AFB1, respectively, relative to the signal obtained for the respective references. However, it can be noted that compared to the singleplex assays in straight channels (**Figure 6.8-A**) there is a slight decrease in sensitivity since the ratio of contaminated to non-contaminated chemiluminescence values obtained in the multiplexing experiments is higher than those obtained in the single channels, for the same toxin concentrations. This relative decrease in sensitivity can be attributed to the higher concentrations of anti-toxin-HRP antibodies used in the multiplex chip to compensate for a decrease in absolute signals. This decrease in signal can possibly be due to (1) an increased erosion of surface adsorbed proteins, namely BSA-toxin conjugates by the concentrated PEG solution, due to the high affinity of hydrophobic PEG molecules to the methyl groups on the PDMS surface; or to (2) the formation of a thin PEG solution film in contact with the PDMS surface, which envelops the capturer or target streams, hindering the diffusion of molecules towards the surface. We have previously reported this phenomenon [24]. Nevertheless, the relative decrease in sensitivity can be easily counteracted by using antibodies with higher affinities to the target compound or by using more sensitive signal acquisition and/or signal amplification techniques, allowing the use of lower anti-toxin antibody concentrations.

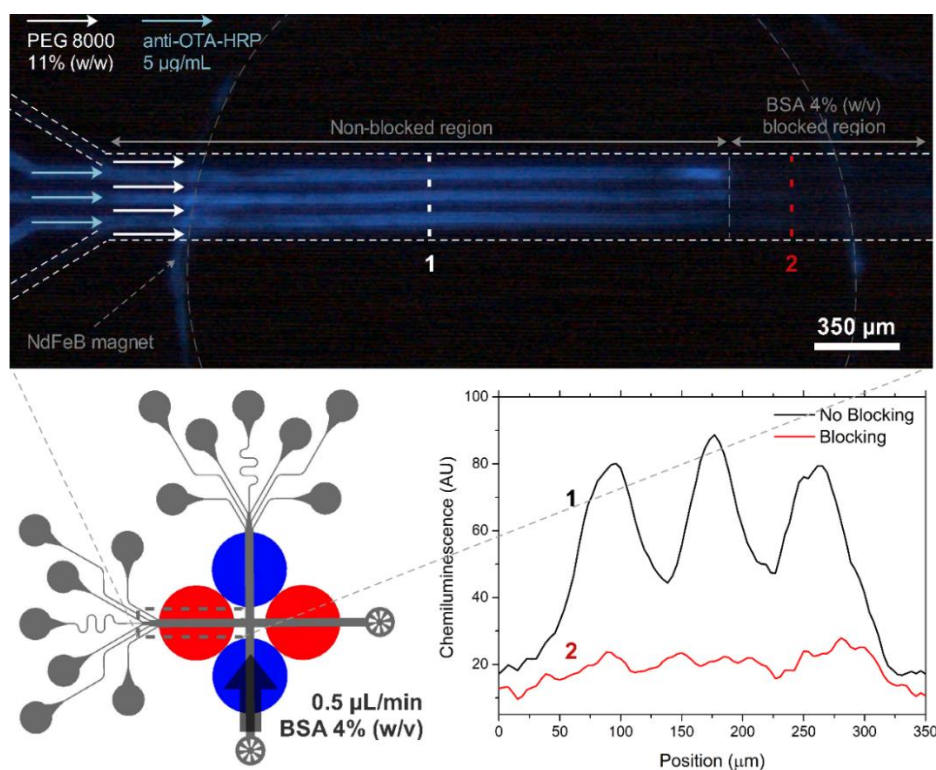


Figure 6.7 - Optical microscopy image (total magnification of 40 \times) acquired in the dark (10 s exposure, 10 \times gain) while flowing a luminol plus hydrogen peroxide solution at 10 $\mu\text{L}/\text{min}$ from right to left, relative to the image. The BSA blocking was performed prior to acquisition by flowing a solution of BSA 4% (w/v) at 0.5 $\mu\text{L}/\text{min}$ for 5 min as schematized with the red magnet valves closed.

6.5. Simultaneous detection of OTA, AFB1 and DON using a multiplexed array of a-Si:H photoconductors

After establishing the proof-of-concept of the multiplexed immunoassays using a chemiluminescence-based approach coupled to fluorescence microscopy, a 3×3 photoconductor array was designed to allow integrated on-chip detection of the light generated by the 9 spots in the ROI (**Figure 6.9-A, B, C**). Each of the 9 sensors was addressed sequentially for 4 s at a sampling rate of 500 ms, resulting in an acquisition of 8 data points per sensor passage. The data acquisition began in dark conditions and with the syringe pump stopped. This step is crucial to determine the dark current (i_d) of the sensors that constitute the signal baseline of the assay. The dark current measured during the experiments for all sensors was $i_d = 5.47 \times 10^{-13} \pm 4.30 \times 10^{-14}$ A. The signals, which correspond to the photocurrent, i_{ph} , measured in the presence of chemiluminescence minus the dark current, i_d , depend on the quantity of HRP enzymes at each ROI spot and are of the order of hundreds of fA. After two full addressing iterations of the sensor array in the dark, the syringe pump is turned on while the current from each sensor is continuously acquired. The chemiluminescence emitted by the discrete spots in the ROI generated a photocurrent in the sensors (i_{ph}). Cross-talk generated by the chemiluminescent spot on sensors at a neighboring spot (minimum distance between adjacent photosensors is 100 μm) was assessed. For that purpose, reference immunoassays for only one toxin (DON), were used to optimize the uniform and discrete chemiluminescence signals generated in the ROI as can be seen in **Figure 6.10**. By selectively immobilizing HRP-labeled antibodies on only 3 spots, light cross-contamination between sensors was observed not to impair the detection of mycotoxins at the concentrations tested in the previously described (**Section 6.4**) standard sample. This is justified by the signals measured between sensors (**Figure 6.10-C**) having statistically significant differences above 95% certainty with p-values of 0.03 for a distance of at least 100 μm between the dark sensor and the sensor exactly below the chemiluminescence light source (top row against middle row) or 0.01 for a distance of at least 200 μm (top row against bottom row).

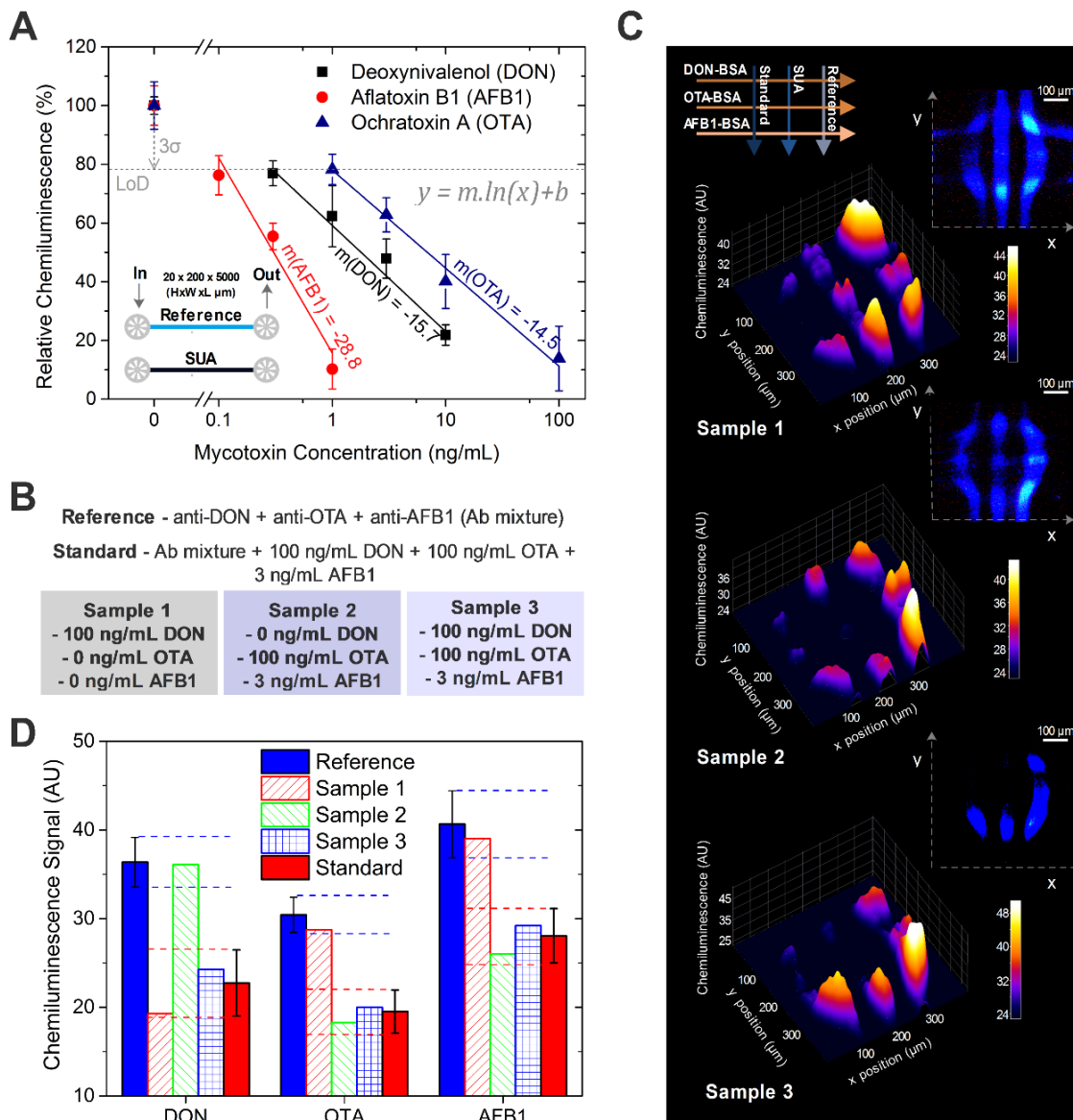


Figure 6.8 - **A**- Calibration curves for each target mycotoxin measured in singleplex mode, carried out in individual straight channels. Relative chemiluminescence values were calculated by the dividing the absolute chemiluminescence obtained by the SUA at a certain toxin concentration by the chemiluminescence signal obtained for the reference (0 ng/mL toxin). Each point was measured in triplicate and error bars correspond to \pm SD. The limit of detection (LoD) threshold was calculated as the relative chemiluminescence value corresponding to 3 times the standard deviation of the reference measurement with the higher variability. **B**- Mycotoxin concentrations tested in the multiplexed assays. **C**- Microscope images and 3D intensity plots of the ROI for each of the samples 1, 2 and 3 according to the schematics presented on the top. **D**- Absolute chemiluminescence signals obtained for each spot from the 3 analyses. The error bars of the reference and standard samples refer to \pm SD of the 3 experiments.

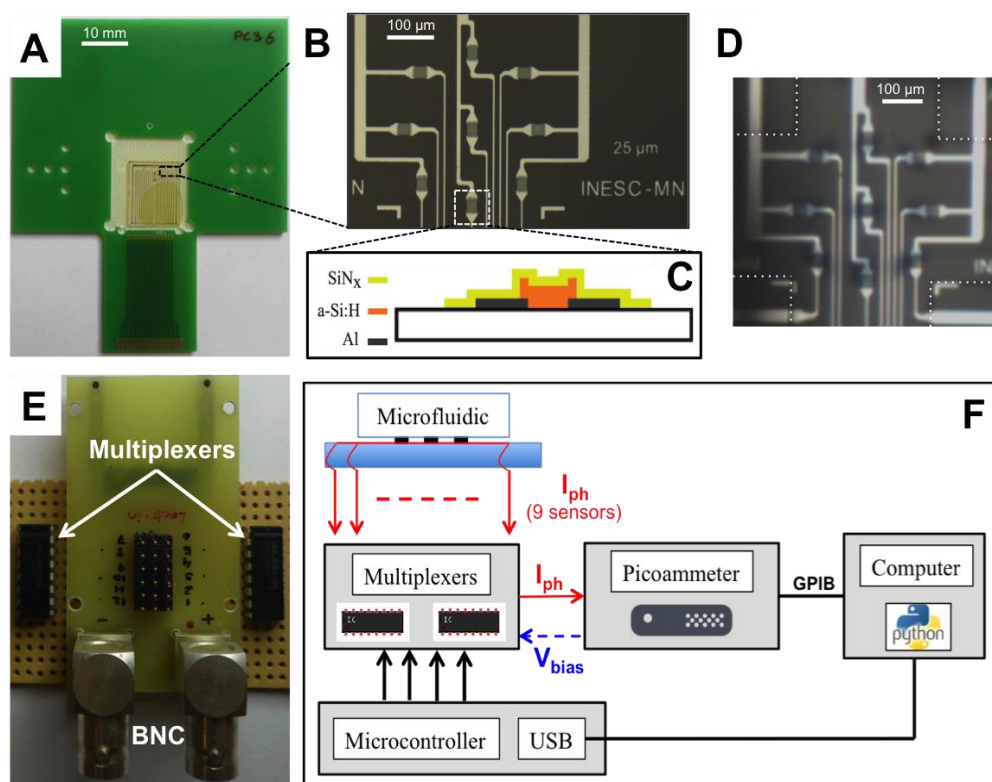


Figure 6.9 - A- Photoconductor array chip wire-bonded to a PCB. B- Optical microscopy image of the 9-sensor array designed to match the relative position of the 9 spots in the ROI. C- Photoconductor cross section schematics. D- Optical microscopy image of the 9 sensors array aligned with the microfluidic chip. The 9 blue spots in the ROI were obtained by flowing a blotting TMB solution. All spots correspond to a conjugate of anti-DON-HRP bound to adsorbed DON-BSA molecules (reference). Dotted white corners indicate microfluidic channel walls which are aligned with the “L shaped” alignment marks. E- Top view of the interface PCB. F- Schematics of the multiplexing circuit setup.

To measure the chemiluminescent signal generated by each spot, the microfluidic structure was aligned with the photoconductors using the corners of the ROI cross and the patterned “L”-shaped alignment marks (**Figure 6.9-D**). It is important to highlight that after measuring the light emission using the photosensors, a blotting solution of TMB flows to the ROI to produce a colorimetric reaction that allows a visual assessment of the position of the spots and to have an indication of the quality of the measurements. In analogy with the luminol solution, the intensity of the spot (i.e. the absorbance) is inversely proportional to the concentration of toxin. The multiplexing results obtained with the integrated photosensors are shown in **Figure 6.11** for two different SUAs. It is possible to observe that the signals for SUA 1 are within the 3σ threshold of the reference signal. On the other hand, for SUA 2, the spots corresponding to OTA and DON are significantly lower and within $\pm SD$ of the signal from the standard sample, highlighting the statistical significance in distinguishing contaminated solutions of all three toxins. These results are consistent with the results from optical microscopy presented in

Section 6.4 and validate the use of integrated photosensors as an effective way of acquiring data from multiplexed immunoassays in real time and with compatibility to point-of-need applications.

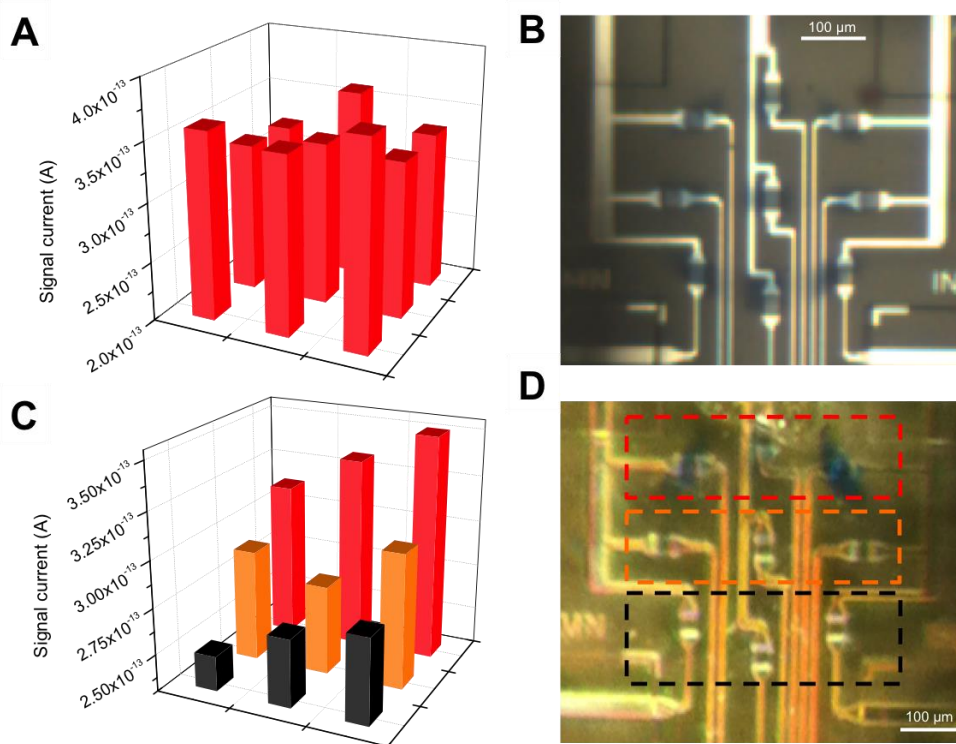


Figure 6.10 - Microfluidic immunoassay signal currents of the 9 integrated photosensors for the detection of 9 discrete spots. All spots correspond to a molecular recognition event between adsorbed DON-BSA and anti-DON-HRP, in the absence of DON. The absence of a spot is generated by flowing a plain PBS solution instead of an anti-DON-HRP solution in the respective position. **A** and **C**- 3D intensity plot of the 9 ROI generated current by an immunoassay designed to produce chemiluminescence signal either in all 9 spots (**A**) or only the top row of spots (**C**). It can be seen (orange columns in **C**) that light cross-contamination exists for adjacent spots, with a p-value of 0.03, comparing the averages of the 3 red and orange columns, respectively (distance $\geq 100 \mu\text{m}$). At greater distance ($\geq 200 \mu\text{m}$) this cross-contamination is negligible, with a p-value of 0.01, comparing the average of the 3 red and black columns, respectively. The p-values were calculated based on the average signal of each row of spots and a t-student distribution with 2 degrees of freedom. **B** and **D**- Microscope image of the integrated microfluidic chip with the photoconductor array after the flow of a TMB solution, highlighting the alignment between the spots and the respective photoconductors.

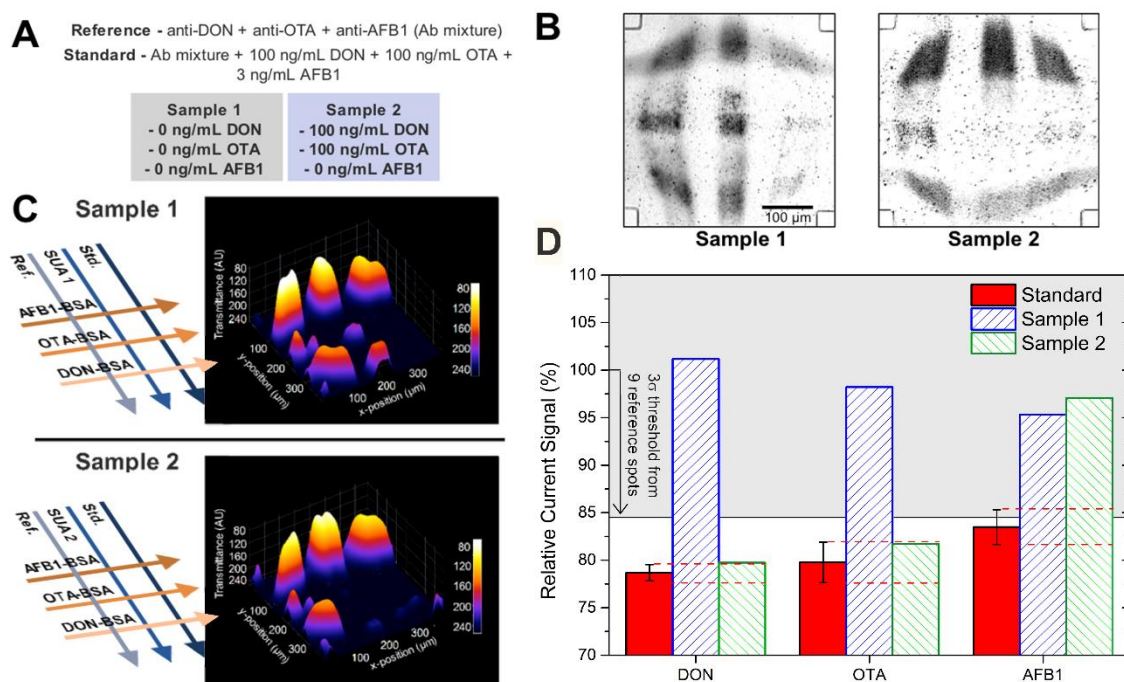


Figure 6.11 - Multiplexed chemiluminescence detection of mycotoxins with integrated calibration using the thin film amorphous photoconductors array. **A**- Mycotoxin concentrations tested in the multiplexed assays. **B**- Enhanced colorimetry images of both mycotoxins immunoassays using optical microscopy. The spots were obtained by flowing a blotting TMB commercial solution at 10 $\mu\text{L}/\text{min}$ for 2 min after the chemiluminescence acquisition with the photosensors. **C**- 3D transmittance plots of the ROI from replicate experiments using the same samples after flowing TMB for each of the samples 1 and 2, according to the schematics presented on the left side. **D**- Average relative signals obtained using the integrated photoconductors for the standard and SUA solutions, calculated by dividing the absolute chemiluminescence signal obtained for the SUA and standard at a certain toxin concentration by the chemiluminescence signal obtained for the respective reference. The error bars from the standards are the average from two independent experiments. The 3σ threshold is obtained from the average of 9 reference spots for the same toxin. These results are detailed in **Figure 6.10**.

6.6. Chapter conclusions

A simple methodology for microfluidic multiplexed biosensing was demonstrated using a device comprising active permanent magnet valves coupled with a single negative pressure source. The valves allowed the selective patterning of three different capturers in one direction and the molecular recognition of three different targets solutions in a perpendicular direction, resulting in the generation of a nine-point matrix in an area of $350 \times 350 \mu\text{m}^2$. This device was successfully used to simultaneously detect three different mycotoxins, namely DON, OTA and AFB1 in three independent samples using a direct competitive immunoassay, where two of the samples were used as a reference and a standard, respectively. The detection of 100 ng/mL of OTA and DON and 3 ng/mL for AFB1 was demonstrated in under 20 min of total analysis time by acquiring the

chemiluminescence signal with an optical microscope. Comparable results were obtained by acquiring the signal using an array of $25 \times 25 \mu\text{m}$ photodetectors aligned to the microfluidics, which demonstrates a relatively low-cost and integrated platform that is compatible with point-of-need applications. Additionally, the absence of contact between the biomolecular recognition site in the disposable microfluidic structure and the sensor makes the photosensor chip reusable. In conclusion, this device could potentially be the basis of a simple and scalable multiplexing module for point-of-need applications, easily amenable to integration either with appropriate and fit-for-purpose external sample preparation methodologies or with integrated sample preparation and/or sample pre-concentration modules, as previously reported by our group using a similar assay architecture [21, 24], and to automation for further simplification of the operating procedure.

Chapter 7

Capillary Microfluidic Immunoassays for Mycotoxin Detection Coupled with Smartphone Signal Acquisition

This chapter discusses the integration of the multiplexed immunoassay reported in **Chapter 6** in an autonomous capillary-driven microfluidic chip. The use of capillarity as a means of fluidic manipulation in lab-on-a-chip systems can potentially reduce the complexity of the instrumentation and allow the development of user-friendly devices for point-of-need analyses. In this work, a PDMS microchannel-based, colorimetric, autonomous capillary chip provides a multiplexed and semi-quantitative immunodetection assay. Results are acquired using a standard smartphone camera and analyzed with a simple gray scale quantification procedure. The performance of this device was tested for the simultaneous detection of the mycotoxins OTA, AFB1 and DON. The multiplexed assay was performed approximately within 10 minutes and the achieved sensitivities of < 40, 0.1-0.2 and < 10 ng/mL for OTA, AFB1 and DON, respectively, fall within the majority of currently enforced regulatory and/or recommended limits. Furthermore, to assess the potential of the device to analyze real samples, the immunoassay was successfully validated for these 3 mycotoxins in a corn-based feed sample after a simple sample preparation procedure. The contents of this chapter are reproduced with appropriate adaptations from one original research article [154], co-authored with a MSc student (Jessica M. D. Machado) in biotechnology at Instituto Superior Técnico (University of Lisbon). I was responsible for the co-supervision of the student in the lab, troubleshooting, planning of experiments and thorough revision of the published paper.

7.1. Materials and experimental methods

7.1.1. Chemicals and biologicals

Polyethylene glycol (PEG) with a molecular mass of 8 kDa, phosphate buffered saline (PBS) tablets (137 mM NaCl, 2.7 mM KCl, 10 mM phosphate, pH 7),

1,1'-Carbonyldiimidazole (CDI), acetone (99%), anhydrous ethanol, anhydrous methanol, bovine serum albumin (BSA), ochratoxin A (OTA), aflatoxin B1 (AFB1), deoxynivalenol (DON), Anti-Mouse IgG (whole molecule), OTA-BSA conjugates and AFB1-BSA conjugates were purchased from Sigma-Aldrich. DON-BSA conjugates were prepared in-house using CDI chemistry according to the same procedure previously described in detail [42]. The stock solutions of mycotoxins were prepared as follows: OTA was dissolved in a 1:2 parts methanol and water solution (100 µg/mL), AFB1 was dissolved in anhydrous ethanol (200 µg/mL) and DON was dissolved in anhydrous methanol (1 mg/mL). Affinity purified anti-OTA polyclonal antibodies conjugated with horseradish peroxidase (HRP) were purchased from Immunechem Pharmaceuticals (Burnaby, Canada), anti-AFB1 mouse monoclonal antibodies (AFA-1) were purchased from Abcam (Cambridge, UK) and anti-DON mouse monoclonal antibodies were purchased from Biotex (Berlin, Germany). The anti-AFB1 and anti-DON antibodies were conjugated with HRP using an HRP labelling kit, purchased also from Abcam. TMB was purchased from Thermo Scientific as a ready to use 1-Step™ Ultra TMB-Blotting Solution. All solutions were prepared using ultrapure water obtained from a MilliQ system from EMD Millipore. All feeds under study were kindly supplied by a major feed producer.

7.1.2. Capillary-driven immunoassay

Each of the four chambers (1.5×1.5 mm $W \times L$) was spotted with 0.4 µL of α -mouse with a concentration of 0.1 mg/mL in chamber 1 (used as an internal control and henceforth referred to as reference chamber) and with a concentration of 1 mg/mL of the three respective toxin-BSA conjugates in chambers 2-4. 5-10 min after reversible sealing the PDMS device to a hydrophilic glass slide (treated with an oxygen plasma according with **Chapter 2**), 4 µL of BSA 4% were flowed through the chambers to block the surface and avoid nonspecific adsorption. In the case of a single-inlet microfluidic structure, after flowing the entire volume of BSA solution, 2 µL of a mixture containing 5 µg/mL of α -OTA-HRP, 5 µg/mL of α -AFB1-HRP and 10 µg/mL α -DON-HRP antibodies mixed with defined concentrations of the free toxins was introduced at the structure inlet. Finally, after exhausting the previous solution, 4-6 µL of TMB plus hydrogen peroxide were introduced at the inlet to generate a colorimetric signal in each of the chambers. **Figure 7.1** shows a schematic of the assay steps. This single inlet structure was used to perform all assays in this paper except for the analysis of a pre-processed corn sample. In this case,

after inserting the solution in the first inlet, the solutions corresponding to the second and third inlets were added sequentially, and the immunoassays were autonomously performed with solutions flowing in sequence. Details about the autonomous sequential liquid insertion structure are discussed in **Section 7.2.1**.

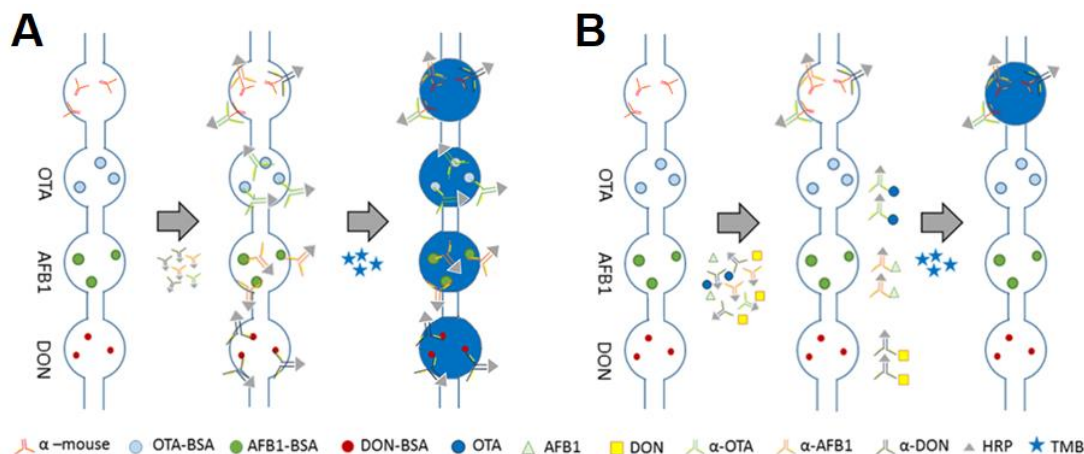


Figure 7.1 - Schematic representation of the direct competitive ELISA (dcELISA), using a non-contaminated sample (**A**) and a sample contaminated with a certain concentration of OTA, AFB1 and DON (**B**). The chamber highlighted in blue in the final step represents the light-absorbing precipitates accumulated in the chamber due to the enzymatic processing of the TMB, which is proportional to the surface concentration of anti-toxin-HRP molecules immobilized on the surface via affinity interactions with the adsorbed mycotoxin-BSA molecules. The top chamber contains an internal reference.

7.1.3. Signal acquisition and data analysis

The colorimetric signal was acquired using a smartphone camera (Samsung Galaxy Grand Prime Value Edition SM-G531F, 8 MP, 3264 x 2448 pixels) in ambient artificial lighting. Pictures were taken manually at a focal distance of approximately 30 cm. Subsequently, the photos were analyzed using ImageJ software. A square area of 600 pixels² centered at the colorimetric spot was defined, which included the total area of the spot. The measured signal in terms of gray scale (32-bit) is proportional to the transmittance after computing the difference between minimum (center of the spot) and maximum (background) gray scale intensity values according to **Equation 7.1**, where S is the signal for a given spot, T_{\max} is the maximum of transmittance in AU and T_{\min} is the minimum of transmittance in AU. To normalize the signal, the S value was divided by the signal provided by the internal control containing spotted anti-mouse antibodies (**Equation 7.2**, in which R_S is the relative signal, S_{SUA} is the signal from the sample-under-analysis and S_{REF} is the signal from the reference spot). A visual representation of the quantification process is shown in **Figure 7.2**.

$$S = T_{max} - T_{min} \quad (7.1)$$

$$R_S = \frac{S_{SUA}}{S_{REF}} \quad (7.2)$$

It is important to highlight that due to the relatively low resolution of the smartphone camera relative to microscopy equipment (**Figure 7.3**) at this specific amplification, any non-uniformities of the spots are averaged in the image, allowing for the approach of using the maximum pixel intensity in the spot. The effectiveness of the spot. The effectiveness of the normalization process was further validated under different light conditions to infer about the sensitivity of the assay performance to significant differences in lighting, ranging from a poorly illuminated room to direct sunlight impinging on the device (**Figure 7.4**).

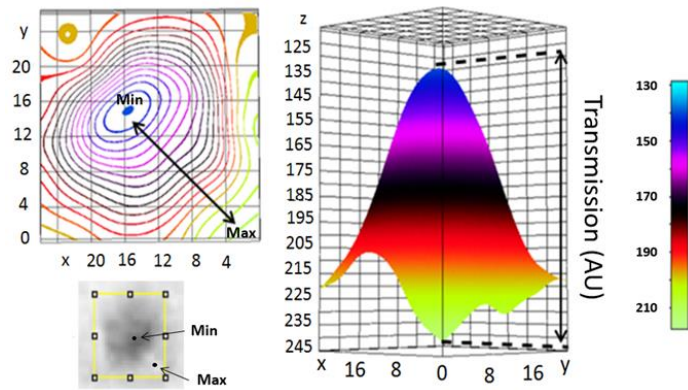


Figure 7.2 - Selection of 600 pixel² centered in the colorimetric spot and the analysis performed in ImageJ. The values on the y- and x-axis refer to the number of pixels.

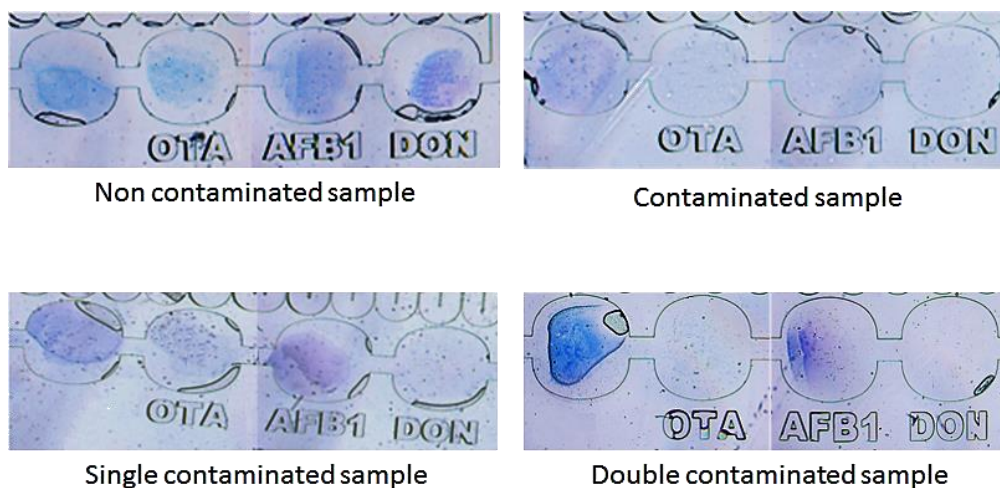


Figure 7.3 - Colorimetric signal acquired with an optical microscope after testing a non-contaminated sample (0 ng/mL OTA, AFB1 and DON), a single contaminated sample (100 ng/mL DON), a double contaminated sample (100 ng/mL OTA and DON) and a sample contaminated with all 3 toxins (100 ng/mL OTA, 1 ng/mL AFB1 and 100 ng/mL DON).

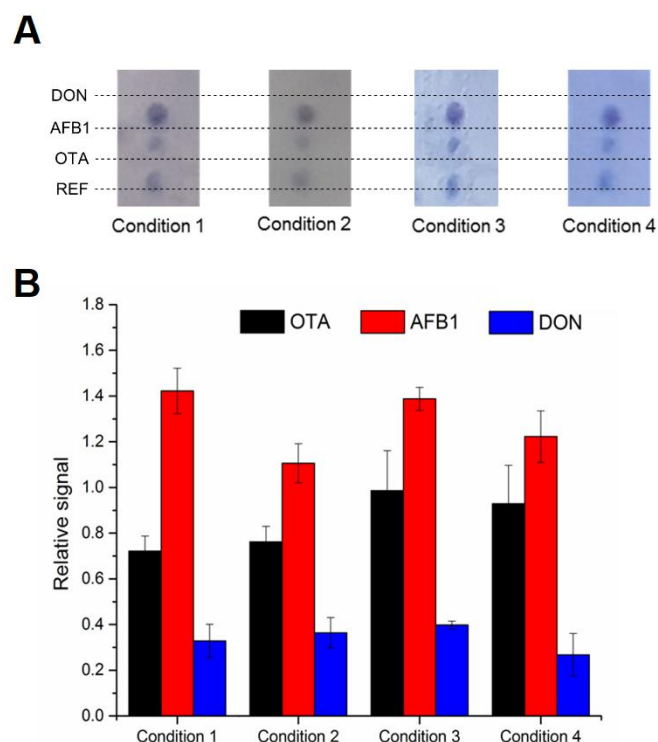


Figure 7.4 - Data acquired with smartphone camera using different lighting conditions (**A**) and respective quantification (**B**). The sample under analysis was spiked with 500 ng/mL of DON. Condition 1 refers to a room with an artificial light source only, condition 2 to a room illuminated by sunlight. Conditions 3 and 4 were acquired outside under direct sunlight or under a shade, respectively. The results in B are the average of 3 replicates and error bars refer to \pm SD. The relative signals are the signals from each toxin normalized to the reference.

7.1.4. Sample preparation of corn samples

The sample preparation of corn samples was performed as optimized in **Chapter 4**. Briefly, a total mass of 400 mg corn feed was spiked with 1 μ L of a toxin mixture prepared in absolute ethanol (20 μ g/mL OTA, 8 μ g/mL AFB1 and 0.2 mg/mL DON) to obtain final concentrations of 50 ppb OTA, 20 ppb AFB1 and 500 ppb DON. The tube with the contaminated feed was vortexed and left open for 5 min to allow the ethanol to evaporate. Subsequently, 75 μ L of PEG 8,000 50% (w/w) and 1.2 mL of phosphate 15% (w/w) (final pH of 7) were added to the spiked feed and a continuous vortex mixing (2,400 rpm) was performed for 3 min to extract the mycotoxins. To separate the immiscible phases and sediment any suspended feed debris, a centrifugation step was performed for 15 min at 2,000 g. Finally, 40 μ L of supernatant were collected, submitted to a second centrifugation step for 5 min and 1 μ L of clean supernatant was mixed with 14 μ L of a solution containing α -toxin antibodies (α -OTA: 2.50 μ g/mL, α -AFB1: 5 μ g/mL, α -DON: 5 μ g/mL) and subsequently used as the SUA.

7.2. Multiplexed competitive immunoassay design

The design of the simple dual-step competitive immunoassay used to detect multiple mycotoxins in solution is shown schematically in **Figure 7.1**. Considering the competitive nature of the assay, the antigens are immobilized on the PDMS by physisorption after manually spotting the BSA-mycotoxin conjugates prepared in PBS in each detection chamber. Then, if a certain concentration of a given toxin is present in solution, the free toxins compete with the toxins immobilized on the PDMS surface for occupancy of the specific α -mycotoxin IgG-HRP binding sites. Hence, a large concentration of a given free toxin will result in a low density of α -mycotoxin IgG-HRP captured by the BSA-mycotoxin conjugates immobilized on the surface. After flowing a TMB plus hydrogen peroxide blotting solution through the chambers, a colorimetric signal that is inversely proportional to the concentration of free toxins is generated. To have an internal standard in each assay, a fourth chamber with an immobilized anti-mouse Ab is used to capture the anti-toxin-HRP antibodies regardless of their affinity. This chamber, working as a negative control (maximum signal), provides a signal to normalize the variability in flow rate and total time of TMB flow through the chambers, thus allowing a reduction of the inter-assay variability due to small differences in flow rate and reaction time, derived from the TMB substrate conversion kinetics (**Figure 7.5**). Furthermore, to simplify the signal acquisition, the color intensity in each spot was quantified after acquiring a photograph using a mid-range smartphone camera at a fixed focal distance and room lighting conditions. The spots were subsequently analyzed using the software ImageJ as shown in **Figure 7.2** and described in **Section 7.1.3**.

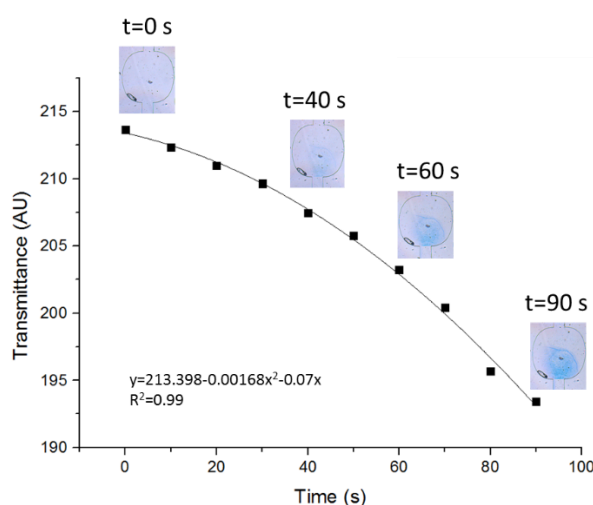


Figure 7.5 - TMB conversion kinetics measured in an optical microscope over time as the mean intensity (gray scale) of the spot.

7.2.1. Microfluidic structure design: autonomous and sequential liquid delivery

The microfluidic structure design (**Figure 7.6**) can be divided in three main sections according to their purpose: autonomous fluid delivery; reaction chamber; and capillary pumps for control of the liquid flow rate. In order to develop an autonomous and more user-friendly device, a sequential fluid insertion module (**Figure 7.6-A**), previously developed and described in detail [34, 37] was integrated in the microfluidic structure. This design allows the user to place all three solutions at the beginning of the assay while the sequence of liquid flow and specific flow time for a given liquid are controlled autonomously by the volume of solutions and architecture of the pump network, as will be discussed in the next section.

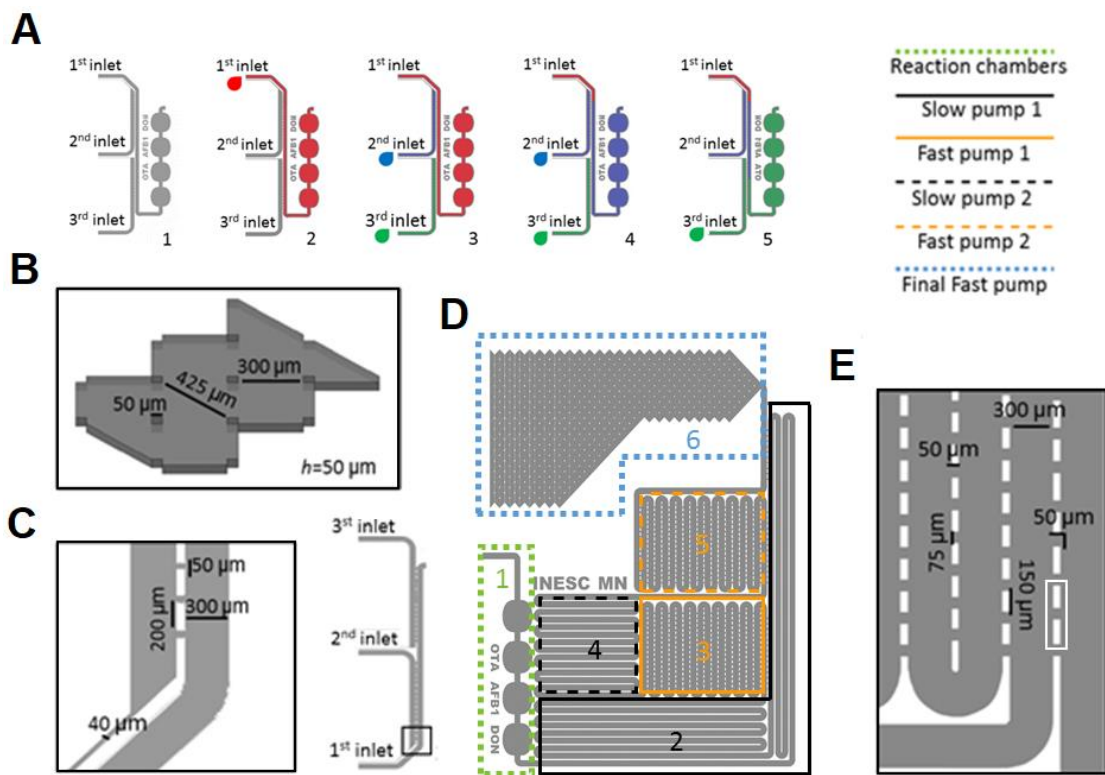


Figure 7.6 - Detailed schematics of the capillary device, including the liquid insertion (**A** and **C**) and pumping (**B**, **D** and **E**) modules. (**A1**) Empty inlets open to air; (**A2**) first solution placed at the 1st inlet, (**A3**) the first solution flows to the common microchannel while the remaining second and third solutions are blocked by a positive pressure; (**A4**) when the first solution is finished, the second solution is allowed to flow into the common microchannel, since the small 40 μm channel from the 1st inlet is now open to the air; (**A5**) when the second solution is finished, the third solution flows to the common microchannel according to the same mechanism as in **A4**. Detailed dimensions of the final fast pump (**B**), sequential module (**C**) and fast pump (**E**). Top view of the structure of the capillary chip without the liquid insertion module (**D**) and the sequence of progression of the liquids along the device (1 to 6).

7.2.2. Microfluidic structure design: control of liquid velocity profile

After the autonomous liquid delivery section, the remainder of the microfluidic chip (**Figure 7.6-D**) continues with the 4 reaction chambers for the internal control (α -mouse IgG) and each of the OTA, AFB1 and DON-BSA conjugates (**Figure 7.6-D**, green dotted box). Downstream from the reaction chambers, two different types of channels were designed in series, referred to as slow pumps (**Figure 7.6-D**, black full and dotted boxes) and fast pumps (**Figure 7.6-D**, orange full and dotted boxes), based on the previous work by Novo and co-workers [34, 37]. The slow capillary pumps correspond to standard 300 μm wide rectangular channels. This type of capillary pump accumulates hydraulic resistance over time, resulting in a progressive decrease in flow rate through the detection chambers. Slow pumps thus provide relatively lower flow rates on average and are used in blocking and adsorption steps of the immunoassay, where case longer residence times are needed. The slow pump communicates with the fast pumps through 50 \times 50 μm^2 passageways separated by 200 μm intervals (**Figure 7.6-E**, white box). These passageways provide a reduced total fluidic resistance by bypassing entire sections of the structure already wetted by the flowing solution. The fast capillary pump is formed by a 300 μm wide channel comprising 50 \times 75 μm^2 passageways separated by 150 μm barriers. These passageways allow the liquid to bypass the channel walls as it proceeds around each turn, which dramatically reduces the accumulated hydraulic resistance along the microchannels [34]. In this way, the flow rates achieved with these pumps are higher and more stable over the total length of the pump, which is critical to rapidly and fully replacing the solutions inside the detection chambers in between each of the immunoassay steps and to achieve a stringent washing step. The final pump of the device (blue dotted line in Figure 2D and zoom-in in **Figure 7.6-B**), henceforth referred to as final fast pump, is based on a design by Delamarche and co-workers [320]. This capillary pump comprises a wide-open area supported by an array of square posts and can be considered an ultra-fast pump since it can provide higher flow rates ($\approx 3 \mu\text{L}/\text{min}$, approximately 3-fold higher than the flow rate reached with the fast pumps described above). In addition, this final pump can also accommodate a higher volume of TMB substrate solutions, which is critical to achieve rapid assays by providing a reaction-limited instead of a substrate-limited regime when flowing the TMB substrate. The dimension of this pump was empirically optimized considering the flow rate obtained by [320] and the required time to provide an easily measurable maximum colorimetric signal for the reference assays. The overall liquid flow rate profile along the capillary chip is shown in **Figure 7.7**,

together with the conditions used for the immunoassay, namely the flow rates along the different capillary pumps and the volume of solution delivered in each step of the assay. The architecture and conditions tailored to the assay were based on previously optimized assays by Soares and co-workers [21, 42]. During the development of the immunoassay, the assays were performed using the microfluidic device without the sequential fluid insertion module, unless stated otherwise. In this case the solutions were manually pipetted to the device inlet sequentially after the previous solution was fully depleted.

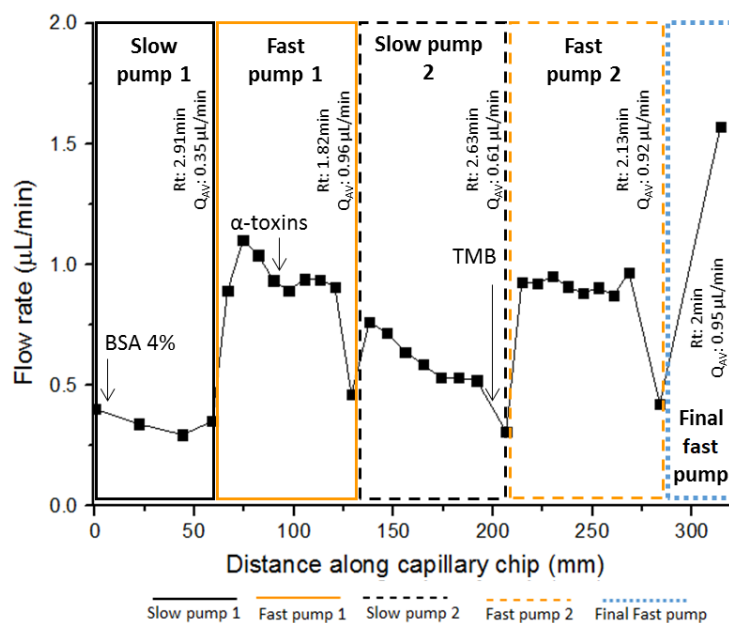


Figure 7.7 - Characteristic flow rate profile in the capillary device during the immunoassay and corresponding average residence times. The measurements shown here were performed without the sequential fluid insertion module.

7.3. Evaluation of cross-reactivity

Prior to evaluating the sensitivity of the assay in detecting each of the target mycotoxins, it is essential to validate the multiplexed assay in terms of cross-reactivity. The presence of non-specific mycotoxins in solution should not interfere with the binding of the specific antibodies with its target mycotoxin. The cross-reactivity was evaluated by analyzing SUAs spiked with one (single contamination) or two different mycotoxins (double contamination). By observing the results in the plots A and B in **Figure 7.8** it can be concluded that the signal from each toxin is not significantly affected by the presence of the other two toxins, which is in agreement with previous reported findings by our group [42].

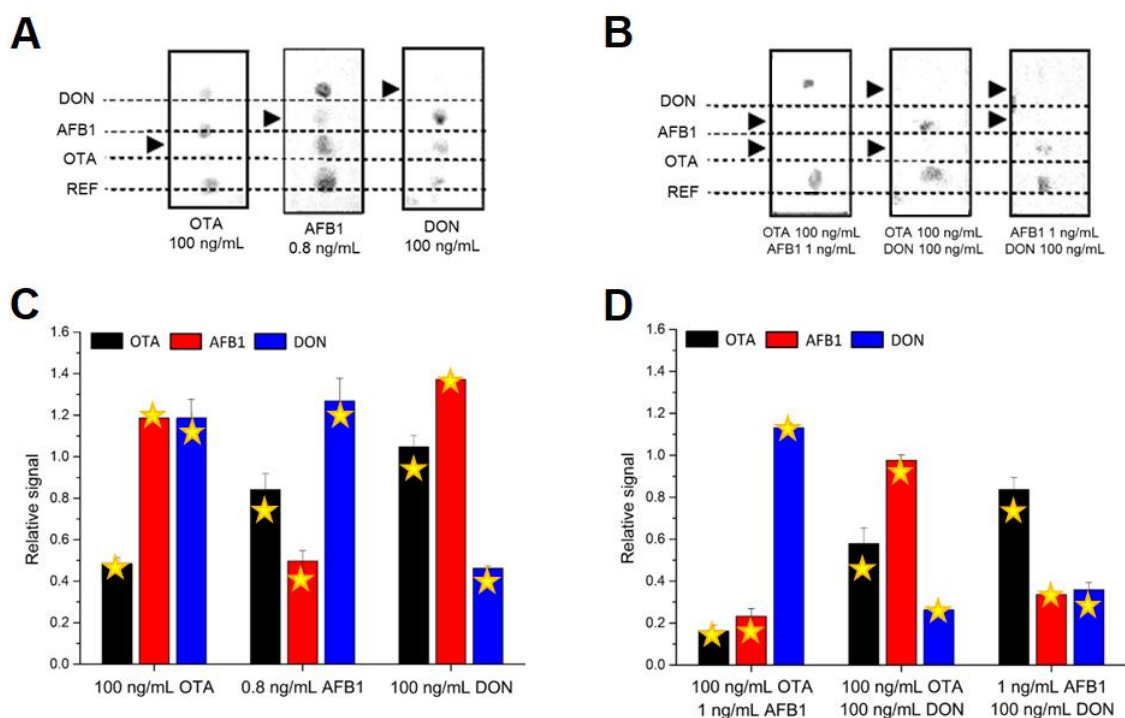


Figure 7.8 - Data acquired with smartphone camera from a sample contaminated with one (A) or two mycotoxins (B) and respective quantification (C and D, respectively). The results in C and D are the average of 3 replicates and error bars refer to \pm SD. The relative signals are the signals from each toxin normalized to the reference. All photos (in A and B) were contrast-enhanced for visualization purposes. The stars represent the specific relative signal of the replicate displayed above the graphs.

7.4. Calibration curves for OTA, AFB1 and DON

After confirming the absence of cross-reactivity in this assay, calibration curves for each mycotoxin were measured using the capillary device by spiking a buffer solution with increasing concentrations of all mycotoxins under study, ranging from 0 ng/mL to 100 ng/mL for OTA and DON and 0 ng/mL to 1 ng/mL for AFB1 (Figure 7.9). For each toxin a regression curve was adjusted to the data and a logarithmic response was obtained for all toxins. Considering the fit-for-purpose semi-quantitative nature of the assay, the limits of detection (LoDs), calculated from a 3σ threshold for the variability of the reference assay (0 ng/mL mycotoxins), were within the ranges of < 40 , 0.1-0.2 and < 10 ng/mL for OTA, AFB1 and DON, respectively. In accordance to previous reports using the same anti-toxin antibodies, the highest sensitivity was obtained for AFB1 detection [19, 42], which is possibly due to a relatively higher affinity of the anti-AFB1 antibody to the free AFB1 antigen relative to the immobilized BSA-AFB1 antigen, compared to the other antibodies for their respective toxins. On the other hand, comparing the performance of this assay with results obtained using a similar pressure driven flow

immunoassay [42] it is possible to observe a significant decrease in sensitivity. This decrease in sensitivity does not seem to be derived from a reduced response to the increase in toxin concentration (i.e. mass transport limitations), since the measured slopes are comparable in both cases, but instead to the intrinsically higher inter-assay variability in the capillary devices, resulting in relatively less precise assays (i.e., with higher standard deviations). However, despite the lower precision, possibly resulting from small differences in surface hydrophobicity between microfluidic structures, the obtained limits of detection for all mycotoxins comply with most regulatory and recommended limits for animal feeds (**Table 1.3** and **Table 1.4**) and, for DON in particular, also with all limits imposed for human consumption (**Table 1.2**). Furthermore, the performance of the assay is well suited for a semi-quantitative analysis, in which the internal control dramatically reduces the inter-assay variability associated with variations in flow velocities and times during the TMB flowing step and with variable lighting conditions during signal acquisition. It can also be noted that, depending on the application, this assay can also be used as a qualitative tool by visually analyzing the spots relative to the respective internal reference, in analogy with lateral flow immunoassay devices currently being commercialized by companies such as Vicam.

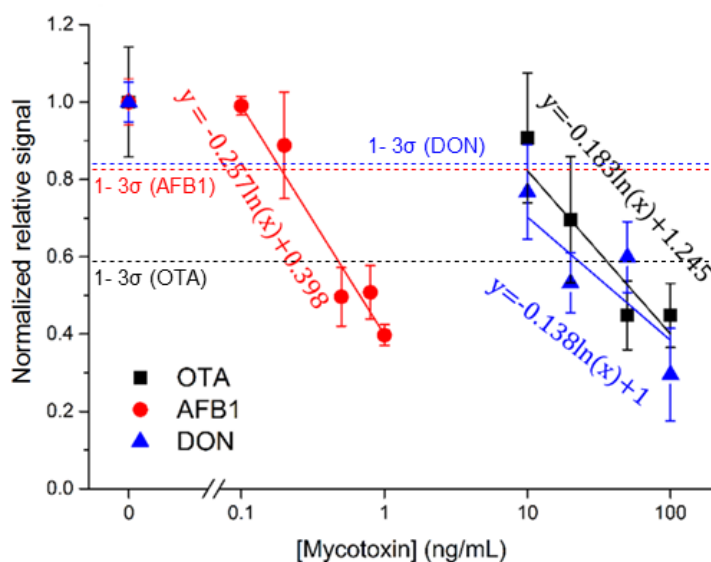


Figure 7.9 - Calibration curves obtained for OTA (black squares), AFB1 (red circles) and DON (blue triangles). The black, red and blue dashed lines represent the 3σ threshold from the average signal of reference samples measured in triplicate for each toxin.

7.5. Detection of mycotoxins in spiked corn feed samples

Finally, one critical aspect of mycotoxin quantification in food safety applications is that the sample under analysis is very commonly a complex matrix, and when the analysis is transferred from a buffer to a real matrix this often results in a pronounced loss of sensitivity [19, 160, 321, 322]. In this case, a sample processing method comprising an aqueous-two-phase extraction composed of PEG and phosphate salts was used, as previously optimized [180]. To evaluate the compatibility of the capillary device with toxin quantification in complex matrices using the above-mentioned sample preparation strategy, corn-based samples used for fish feed production were spiked with all targets at relevant concentrations considering regulatory limits in animal feeds and subsequently analyzed. This analysis was performed with the sequential liquid insertion module and the flow pattern obtained in this case was similar to the one obtained without this structure (**Figure 7.10**). Two different conditions in which the sample was spiked simultaneously with two toxins (50 ppb of OTA and 20 ppb of AFB1) or three toxins (50 ppb of OTA, 20 ppb of AFB1 and 500 ppb of DON) were evaluated. These concentrations spiked in the solid feed are estimated to result in approximately 4.4, 5.6 and 25.2 ng/mL AFB1, OTA and DON, respectively, in the sample under analysis tested in the device according with the results obtained in **Chapters 3 and 4**. The results of the analysis are shown in **Figure 7.11**. Interestingly, comparing the measured normalized relative signals to those obtained in **Figure 7.9**, while the results for AFB1 and DON were comparable to those measured in spiked buffer solutions, there was an apparent increase in sensitivity for OTA. This unexpected result can be justified by a pronounced decrease in absolute signal obtained for the reference and respective OTA spots, thus enhancing any small differences in intensity at the cost of a reduced linear range. On the other hand, considering that the absolute signal for DON was still comparable to the assays performed in buffer, it is reasonable to assume that the decrease in signal obtained for the other spots is due to specific matrix interferences rather than possible mass transport limitations arising from a higher solution viscosity. Nevertheless, despite the relatively low absolute intensity obtained for the OTA, AFB1 and REF spots, the signals obtained for the reference spots were still measurable and the normalized relative signals for the contaminated samples were well below the standard deviation of the signals obtained for the non-contaminated samples for all mycotoxins.

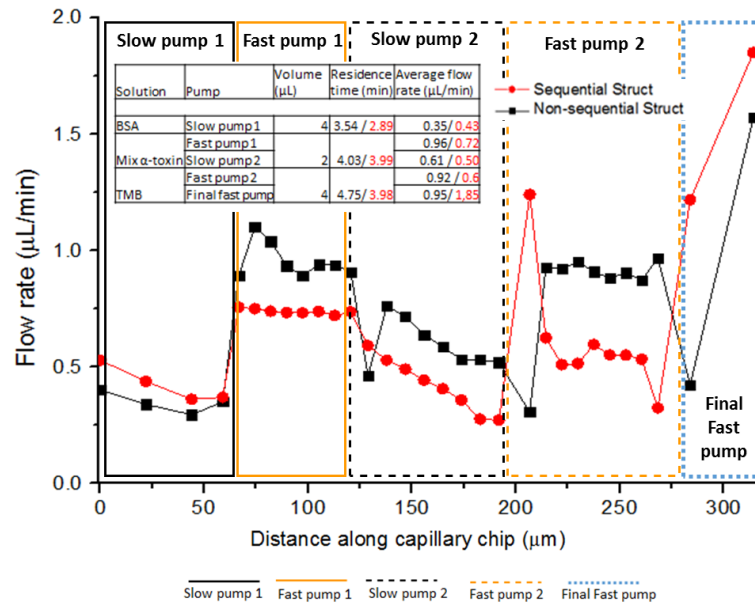


Figure 7.10 - Comparison of velocity profiles measured with the autonomous sequential structure or by inserting the solutions manually in a single common inlet (non-sequential structure). The differences in the magnitude of the flow rate arise from different hydrophilization degrees, being unrelated to the behavior of the sequential pump.

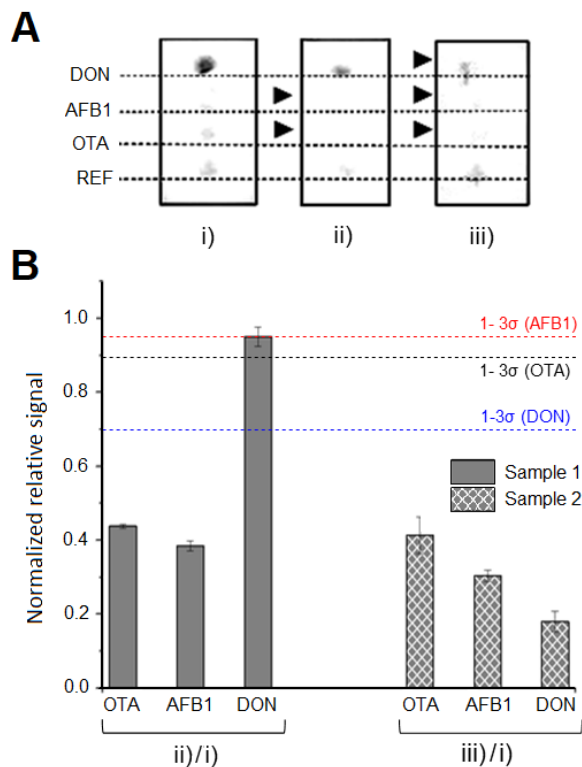


Figure 7.11 - Photos (A) and respective quantification (B) for the analysis of a corn-based feed either i) non-contaminated; ii) spiked with 50 ppb of OTA and 20 ppb of AFB1 (sample 1); or iii) contaminated with 50 ppb of OTA, 20 ppb of AFB1 and 500 ppb of DON (sample 2). The error bars correspond to \pm SD. The black, red and blue dashed lines represent the standard deviation from the average signal of reference samples measured in duplicate for each toxin. Analysis performed with sequential liquid insertion structure. All photos were contrast-enhanced for visualization purposes. The signals obtained for samples 1 and 2 were normalized in respect to the signal obtained for the reference sample (i).

7.6. Chapter conclusions

A microfluidic capillary chip with smartphone acquisition of colorimetric signal capable of performing a multiplexed semi-quantitative direct competitive ELISA in around 10 min was described. As a proof of concept, three important mycotoxins (OTA, AFB1 and DON) were detected in spiked buffer samples after optimizing the appropriate molecular recognition assay and microfluidic structure design, where detection limits of < 40 , $0.1-0.2$ and < 10 ng/mL were obtained for OTA, AFB1 and DON respectively. Furthermore, corn-based feed samples spiked with all three toxins were successfully analyzed after a simple sample preparation procedure comprising a single-step liquid-liquid separation. Comparing this device to other recently reported strategies in the literature (**Table 7.1**), considering that all devices are sufficiently selective and able to reach, at least, the majority of relevant mycotoxin limits for a variety of foods, the following advantages can be highlighted: (1) the device is easily portable and the signal acquisition requires only a ubiquitous mid-range smartphone, (2) the internal control dramatically reduces inter-assay variability both in terms of lighting conditions and signal development time, (3) the full multiplexed analysis can be performed in less than 10 min, being among the fastest assays recently reported in the literature and (4) the sensing surface is relatively simple and rapid to prepare.

Overall, this device is demonstrated to be compatible with point-of-need applications with a relatively low cost and simple operation, its application is extendable to other analytes and target samples and it does not require complex or expensive instrumentation to perform the colorimetric signal transduction, which can be either performed visually or resorting to a smartphone camera for a more precise semi-quantitative analysis. Further improvements to the assay should focus on enhanced simplicity of operation and robustness. It is desirable to reduce the number of user-intervention steps such as pipetting, and, in this direction, it is possible to conceive the incorporation of enclosed loading regions at the inlets, such as blister-type structures, where the reagent solutions can be stored until the beginning of the experiments without evaporation or contamination, requiring only manual pressing for actuation. Furthermore, to allow a rapid and user-independent smartphone mediated quantification, the development of a software application to perform advanced spot analysis that can handle, for example, different lighting conditions and camera-to-device distances, is required.

Overall, these further developments hold great promise in the development of point-of-need, user-friendly, rapid and low-cost means of biosensing.

Table 7.1 - Summary of OTA, AFB1 and DON biosensing strategies published between 2015 and 2017. (1) Preparation time refers to the total time required to prepare the sensing surface prior to the handling of the sample under analysis. (2, 3) The portability and multiplexing characteristics are solely based on what is reported by the authors, although it may be possible that all the methods can be engineered to have these characteristics. NC, CM and CL refer to nitrocellulose, colorimetry and chemiluminescence, respectively.

Assay	Sensing surface	Prep. time (min) ⁽¹⁾	Signal	Multiplexed ⁽²⁾	Assay time (min)	Portable ⁽³⁾	Required external equipment	Internal control
This work	PDMS	< 10	CM	Yes	10	Yes	Smartphone (optional)	Yes
Luan <i>et al</i> [323]	n.a.	n.a.	CM	No	10	No	Spectrophotometer	No
Soares <i>et al</i> [21]	PDMS	< 10	CL	No	5	Yes	Syringe pump and c-Si photodiode	No
Luan <i>et al</i> [324]	AuNPs	>20	CM	No	30	No	Spectrophotometer	No
Zangheri <i>et al</i> [136]	NC	~125	CL	Yes	30	Yes	CCD scanner	Yes
Xiong <i>et al</i> [325]	96-well plates	> 600	CM	No	150	No	Spectrophotometer (optional)	n.a.
Kong <i>et al</i> [326]	NC	~270	CM	Yes	20	Yes	Handheld strip scan reader (optional)	Yes
Zhou <i>et al</i> [300]	NC	~120	CM	No	15	Yes	None	Yes

Chapter 8

Bead-Based Microfluidic Immunoassays to Improve Assay Speed and Sensitivity

After developing and optimizing several microfluidic immunosensing strategies for mycotoxin detection (**Chapters 3 to 7**), it became clear that it would not be reasonable to decrease the assay time below 5 min and the total number of steps performed by the user below two (i.e. flowing the sample plus enzyme substrate for chemiluminescence and colorimetry and sample plus a wash step for fluorescence). Using a planar PDMS channel in reaction-limited conditions, a significant time is required to accumulate a measurable signal on the surface, particularly considering that in competitive assays the signal generating molecule (e.g. labeled antibody) should be used at low concentrations, comparable to those of the antigen in the range of ng/mL to low $\mu\text{g/mL}$. Such limitations are impeditive of an adequate implementation of these biosensors for point-of-need mycotoxin screening, particularly in fast-paced raw material/food trade operations. Therefore, aiming at achieving ultrarapid detection times and single-step biosensing towards simple and in-field mycotoxin detection, bead-based assays integrated in microfluidic channels were considered. This chapter reports the first approach to this concept, which was explored and applied in several sensing applications and coupled also with integrated thin-film photosensors. The contents are reproduced with appropriate adaptations from two original research articles [18, 327], co-authored with the PhD students Inês F. Pinto, Denis R. Santos and Catarina R. F. Caneira. I. F. Pinto introduced the concept of integrating microbeads in microchannels to screen chromatography ligands, Denis R. Santos developed and optimized the integrated optical sensors and C. R. F. Caneira focused on DNA biosensing applications. I focused on the quantitative analysis of molecular recognition and mycotoxin biosensing applications.

8.1. Materials and experimental methods

8.1.1. Packing of beads in microfluidic devices

Commercially available beads were provided as a slurry in a storage buffer (ethanol 20%). The first step was to homogenize the bead stock using a pipette, ensuring

thorough mixing. Then, a certain volume of stock solution was added to a polyethylene glycol (PEG) 8000 20% (w/w) solution, to obtain a final solution with 1-2% (v/v) bead volume. The use of a viscous solution allowed the beads to remain suspended and homogeneously dispersed without significant settling, thus avoiding problems of clogging when flowing the beads inside the micro-columns. The beads were packed using a negative pressure and it was important that the syringe and capillary tubing always remained free of air gaps which could potentially hinder the rapid decrease in pressure. After the first liquid flowing step, it was critical to remove the metal adapter connected to the syringe pump before removing the pipette tip, otherwise, any accumulated negative pressure could quickly trap air bubbles at the interface between the liquid column in the inlet hole and the subsequent solution. Subsequently, the PEG solution was washed from the micro-columns using an appropriate buffer solution and the specific sequence of steps comprising the assay were performed.

8.1.2. DNA hybridization assay

The sequences of DNA oligonucleotides modified with biotin or Atto 430LS ($\lambda_{\text{ex}} = 433 \text{ nm}$, $\lambda_{\text{em}} = 545 \text{ nm}$) were stored in 100 μL aliquots prepared in Tris-EDTA buffer. The sequences of 3'-biotin modified-probe and 3'-Atto 430LS-labeled-targets used were as follows: ssDNA probe, 5'-CAGGTCAAAGGGTCCTTAGGGA-(Biotin- triethylene glycol (TEG))-3'; ssDNA complementary target, 5'-TCCCTAAGGACCCTTTTGACCTG-(Atto 430LS)-3' and ssDNA non-complementary target, 5'-CGTGTCGTTACATCTGTCCGT-(Atto 430LS)-3'. All ssDNA molecules were purchased from Stab Vida (Caparica, Portugal). For each experiment two separated channels were tested simultaneously, one for the complementary target and another for the non-complementary target (control). The ssDNA probe solution consisted of a mixture of streptavidin (1.64 μM) and ssDNA probe (6.56 μM) at a molar ratio of 1:4, prepared and pre-incubated (10 min) before insertion into the microchannel. The ssDNA target solutions were diluted using filtered PBS. Sodium polyacrylate (PAA) 8,000 45% w/w. was diluted to a working solution of 5% w/w in PBS. Q-Sepharose Fast Flow beads were first packed in a microchannel. All subsequent washing steps were performed at a flow rate of 5 $\mu\text{L}/\text{min}$ for 1 min. ssDNA probe solution was flowed through the packed beads at 1 $\mu\text{L}/\text{min}$ for 10 min, followed by a PBS washing step. Next, a solution of PAA 8000 (5% w/w), aimed at preventing non-specific interactions of the target DNA with the beads, was flowed inside the channel at 5 $\mu\text{L}/\text{min}$ for 2 min and subsequently washed. The acquisition of

fluorescence images was done separately for the two channels where non-complementary or complementary ssDNA target Atto 430LS were flowed for 10 min at 1 $\mu\text{L}/\text{min}$, followed by image acquisition at $t = 0$ min and $t = 10$ min.

8.1.3. AFB1 biosensing assay

The commercial BSA-AFB1 conjugates (Sigma-Aldrich) at an initial concentration of 1 mg/mL and a total volume of 500 μL were first concentrated to about 20 mg/mL using Amicon Ultra-0.5 centrifugal filter units with a MWCO of 10 kDa (Merck Millipore), centrifuged at 14000 g for 10 min, after a wash using 400 μL of 100 mM sodium bicarbonate at pH 9.2, required to perform the subsequent conjugation reaction. The BSA-AFB1 was then conjugated to the amine-reactive dye Alexa Fluor[®] (A430) NHS ester (Thermo Scientific) by mixing 24 μL of the concentrated solution with 6 μL of reactive dye solution. The reaction was incubated in the dark with mild agitation for 1 h at room temperature. The final solution was washed with PBS in a series of 10 diafiltration steps using Amicon Ultra-0.5 centrifugal filter units (MWCO of 10 kDa) to remove the non-conjugated free dye. The anti-AFB1 antibodies were first incubated in the presence of the Protein A beads at a concentration of 25 $\mu\text{g}/\text{mL}$ for 15 min in PBS before packing. Before flowing the sample under analysis (SUA), the beads were rinsed with phosphate buffered saline (PBS) at 15 $\mu\text{L}/\text{min}$ for 2 min. A continuous flow of the SUA solution containing either only 2 $\mu\text{g}/\text{mL}$ AFB1-BSA-Alexa 430 (reference) or also 0.1 ng/mL of free AFB1 (contaminated) was introduced in the microchannel at a flow rate of 15 $\mu\text{L}/\text{min}$.

8.1.4. Free prostate specific antigen (f-PSA) biosensing assay

The micro-column was packed with agarose beads functionalized with recombinant Protein A (MabSelect SuRe), purchased from GE Healthcare. A volume of 10 μL of anti-PSA IgG solution was obtained by diluting the stock of capture antibody in PBS to a final concentration of 100 $\mu\text{g}/\text{mL}$. An initial flow rate of 5 $\mu\text{L}/\text{min}$ was set and after the liquid started to enter the channel (observed from the liquid meniscus moving on the pipette tip), the flow rate was reduced to 1 $\mu\text{L}/\text{min}$, referred to henceforth as a ramp down to 1 $\mu\text{L}/\text{min}$. Unless stated otherwise, after each assay step the micro-column was washed with PBS at a flow rate of 5 $\mu\text{L}/\text{min}$ for approximately 3 min. To prevent non-specific interactions between the biotin labeled detector antibody and free Protein A binding sites, the beads were blocked using a mixture of human immunoglobulins

(Gammanorm[®], purchased from Octapharma) for 5 min at a concentration of 165 $\mu\text{g/mL}$, ramping down the flow to 1 $\mu\text{L/min}$, as previously described. Subsequently, 10 μL of a specific target concentration of PSA (0, 10 or 100 ng/mL), spiked either in buffer or in unprocessed human serum, was inserted after a ramp down to 1 $\mu\text{L/min}$. The same procedure was followed for the detector anti-PSA-biotin and streptavidin-HRP conjugates, both flowed at a concentration of 100 $\mu\text{g/mL}$. Finally, to quantify the concentration of capture antibody bound to the beads, a 5 $\mu\text{L/min}$ flow of luminol solution was introduced into the channel.

8.1.5. Antibody labelling with Alexa 430 and HRP

The immunoglobulin G (IgG) molecules were a mixture of human antibodies (Gammanorm[®]) at a concentration of 165 mg/mL . For the fluorescence measurements, the antibodies were labeled with a fluorophore using an Alexa Fluor[®] 430 (A430) succinimidyl ester amine-reactive dye (Life Technologies). To perform the conjugation, the IgG was diluted to 5 mg/mL in 0.1 M sodium bicarbonate buffer and processed as described for BSA-AFB1 in **Section 8.1.3**. The degree of labeling (DOL) was calculated as 3.26 dyes/IgG molecule using a previously reported method [18]. For the chemiluminescence and colorimetric measurements, the conjugation was performed using a commercial horseradish peroxidase (HRP) conjugation kit (Abcam). The IgG was diluted to a concentration of 1 mg/mL in PBS and the conjugation was performed as instructed by the supplier. Briefly, 10 μL of modifier reagent were added to 100 μL of IgG solution. The mixture was subsequently incubated in the dark for three hours at room temperature. Finally, 10 μL of quencher were added to the solution.

8.1.6. Photodiode optical signal acquisition setup and instrumentation

The die with the photodiode array was mounted and wirebonded on a PCB. The photodiodes were operated at 0 V and their current was measured using a Keithley 237 picoammeter (Keithley Instruments, Inc., USA) connected to the PCB via low noise coaxial and triaxial connections. The measurements from the picoammeter were acquired through GPIB by a computer graphical user interface (GUI) programmed in Python and PyQt4 which reads, processes, stores and plots the data. For the fluorescence measurements, the microfluidic devices were first aligned with the photodiodes and the excitation laser beam $\lambda_{\text{exc}} = 405 \text{ nm}$ was focused on the end of the section of the microchannel containing the packed beads. The laser excitation light passed through a 1.0

neutral density (ND) filter before reaching the microfluidic device at a photon flux $\Phi_{(405\text{nm})}$ of $1.04 \times 10^{16} \text{ cm}^{-2} \cdot \text{s}^{-1}$. The IgG-A430 molecules were flowed inside the channel at $1 \mu\text{L}/\text{min}$, by applying a positive pressure in the inlet of the channel. To measure chemiluminescence, after flowing $10 \mu\text{L}$ of IgG-HRP conjugate at $1 \mu\text{L}/\text{min}$, the microchannels were aligned with the photodiodes and the dark current was acquired. Then, the luminol substrate solution was flowed inside the channel at $10 \mu\text{L}/\text{min}$ by applying a positive pressure for 2 min, while continuously acquiring the current. For the colorimetric measurements, TMB-hydrogen peroxide (H_2O_2) (Thermo-Scientific) substrate was subsequently flowed inside the channel at the same flow rate after focusing a 658 nm diode laser at the end of the section of the microchannel. The laser light was passed through a 4.0 ND filter to reduce the light intensity and avoid light flooding and photodiode saturation. The current was continuously monitored while the TMB solution was flowed inside the channel for 3 min.

8.2. Microfluidic bead-based biosensing strategies to detect mycotoxins, proteins and oligonucleotides

A typical rectangular microchannel, with $100 \mu\text{m}$ width and $20 \mu\text{m}$ height, has a surface-to-volume ratio of $\sim 10^5 \text{ m}^2/\text{m}^3$. In this scenario, the degree of interaction of the molecules in solution with the surface can be evaluated by the Péclet number (Pe , **Equation 1.1**). In this case, considering a flow rate of $0.5 \mu\text{L}/\text{min}$ (U of the order of $10^{-3} \text{ m}/\text{s}$), the characteristic Péclet number is about 10^5 for a typical antibody (D of approximately $10^{-12} \text{ m}^2/\text{s}$ [12]). This means that the molecules at the center of the channel have a very limited interaction with the microchannel walls and any immobilized probe molecules on their surface.

Therefore, in microchannels there is a compromise between a high rate of molecular capture and a high efficiency of capture. This implies that if one requires a rapid supply of molecules to the reactions occurring at the surface of the channel (high flow rates), a large fraction of molecules (>90%) will be lost [9]. On the other hand, the insertion of nanoporous microbeads in a microchannel leads to a pronounced enhancement of the surface-to-volume ratio by a factor of 50 (from 10^5 to $5 \times 10^6 \text{ m}^2/\text{m}^3$ [328] considering 4% cross-linked agarose beads), a subject that has been increasingly explored and validated in recent years [329]. The short analyte transport length, reduced to the distance between adjacent beads and average bead matrix pore sizes, results in a

simultaneous enhancement in both the rate and the efficiency of capture of analyte biomolecules [330, 331]. Furthermore, commercial microbeads are widely available with a variety of robust and dense surface functionalization, which are relatively simple to handle in microfluidic systems. Hence, a microbead-based microfluidic platform is a potential development in miniaturized biosensing and biotechnology assays.

To explore the versatility of bead-based assays performed in microfluidic channels, the microfluidic device shown in **Figure 8.1-A** was fabricated, as a general approach to perform a multitude of bioassays schematized in **Figure 8.1-B** to **D**. These were aimed at detecting (1) ssDNA using a hybridization assay, (2) mycotoxins using a fluorescence-based competitive immunoassay or (3) protein disease biomarkers using a sandwich immunoassay transduced using chemiluminescence. The results obtained using each of the bioassays are compiled in **Figure 8.2**.

8.2.1. Mycotoxin detection assay

In accordance to previous results (**Chapters 3 to 7**) performing a competitive assay at the surface of a planar microfluidic channel [21], the results obtained for the toxin screening assay clearly showed that the binding kinetics of the AFB1-BSA-Alexa 430 conjugate to the anti-AFB1 antibody immobilized on the beads are highly dependent on the presence of free AFB1 in solution. This further highlights the high capture efficiency of the beads that rapidly generated a measurable signal while flowing a target compound (AFB1-BSA-Alexa 430 conjugate) at a relatively low concentration of 1 $\mu\text{g/mL}$. This competitive effect thus serves as a powerful real-time AFB1 sensing strategy. It was observed that even a very low toxin concentration of 0.1 ng/mL significantly changes the effective binding kinetics by competition with the AFB1-BSA-Alexa 430 conjugate for occupancy of the protein A binding sites, thus resulting in a decrease in the measured fluorescence intensity by $24.9\% \pm 5.4\%$, after 3 min of flowing the fluorescent conjugate at 15 $\mu\text{L/min}$ (**Figure 8.2-A**). This high sensitivity, considering a 4-order of magnitude difference in concentration between the conjugate and the competing free mycotoxin, can be justified by a higher affinity of the antibodies against the free toxin as compared to the conjugated version, which may have associated stereochemical hindrance effects. The achieved sensitivity is, thus, below or equals previous recent reports by our group using multi-step immunoassays [21, 42]. Furthermore, considering the binding kinetic profiles obtained and shown in duplicate in the inset to **Figure 8.2-A**, the assay is highly reproducible and can potentially be performed in even shorter times to detect toxins at higher

concentrations. Overall, this assay architecture showed great promise for the development of ultrarapid and single-step mycotoxin immunosensors and will be further explored in the subsequent **Chapters 9 and 10**.

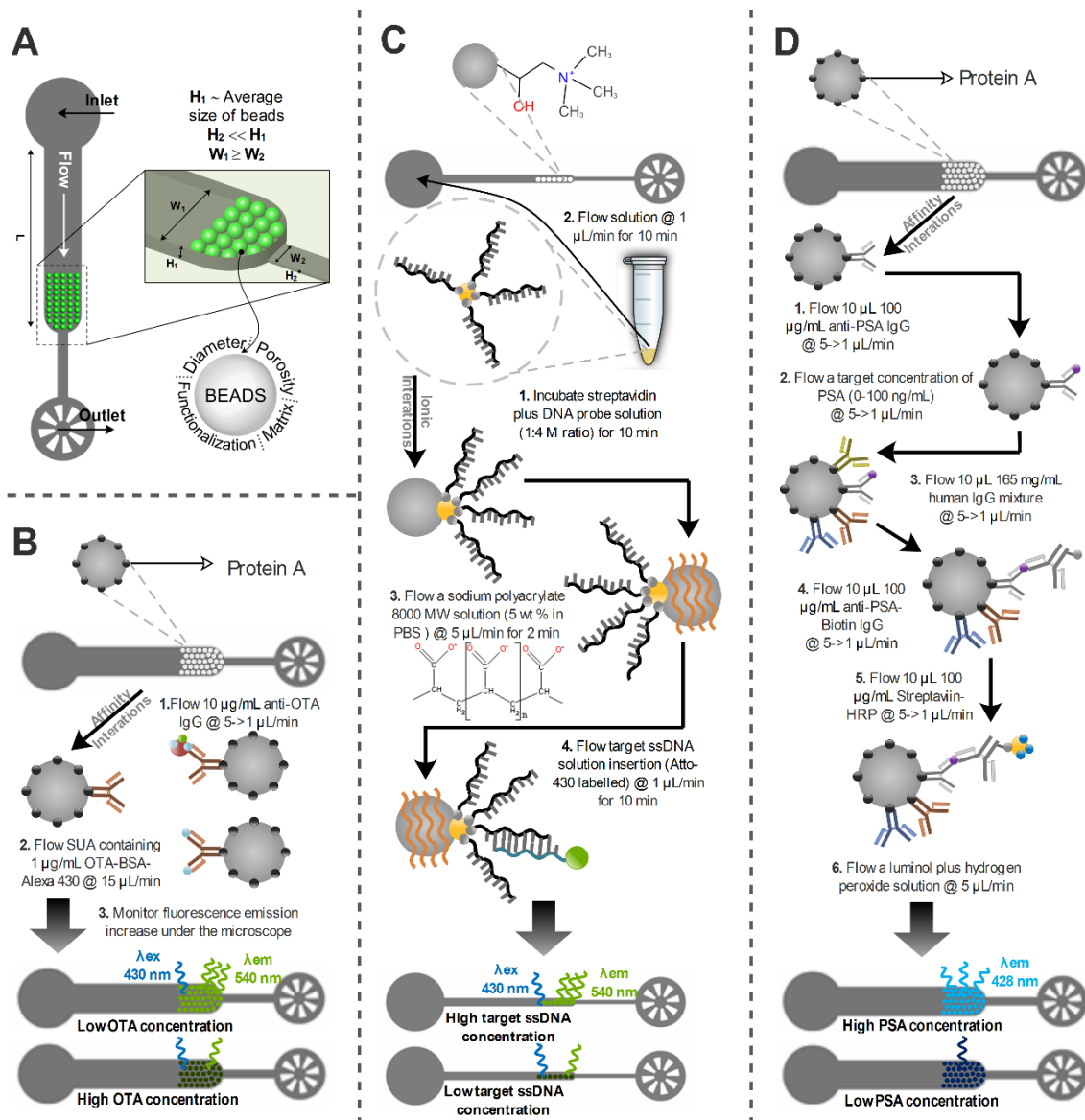


Figure 8.1 - Schematics of the microchannel designed for trapping beads (**A**) and individual steps/ timeline of different assays resorting to beads inside a microchannel, namely for (**B**) toxin detection; (**C**) ssDNA hybridization and; (**D**) free prostate specific antigen (f-PSA) detection. In (**A**) the beads are inserted in a tall channel (H_1) by applying a negative pressure at the outlet and remain blocked by a shallower channel (H_2). H_1/W_1 and H_2/W_2 correspond to the heights/widths of the tall and shallow channel, respectively. L is the length of the larger channel, where a packed bed is created at the interface region. In all assays, after each step, a wash was performed using a PBS solution at 5 $\mu\text{L/min}$.

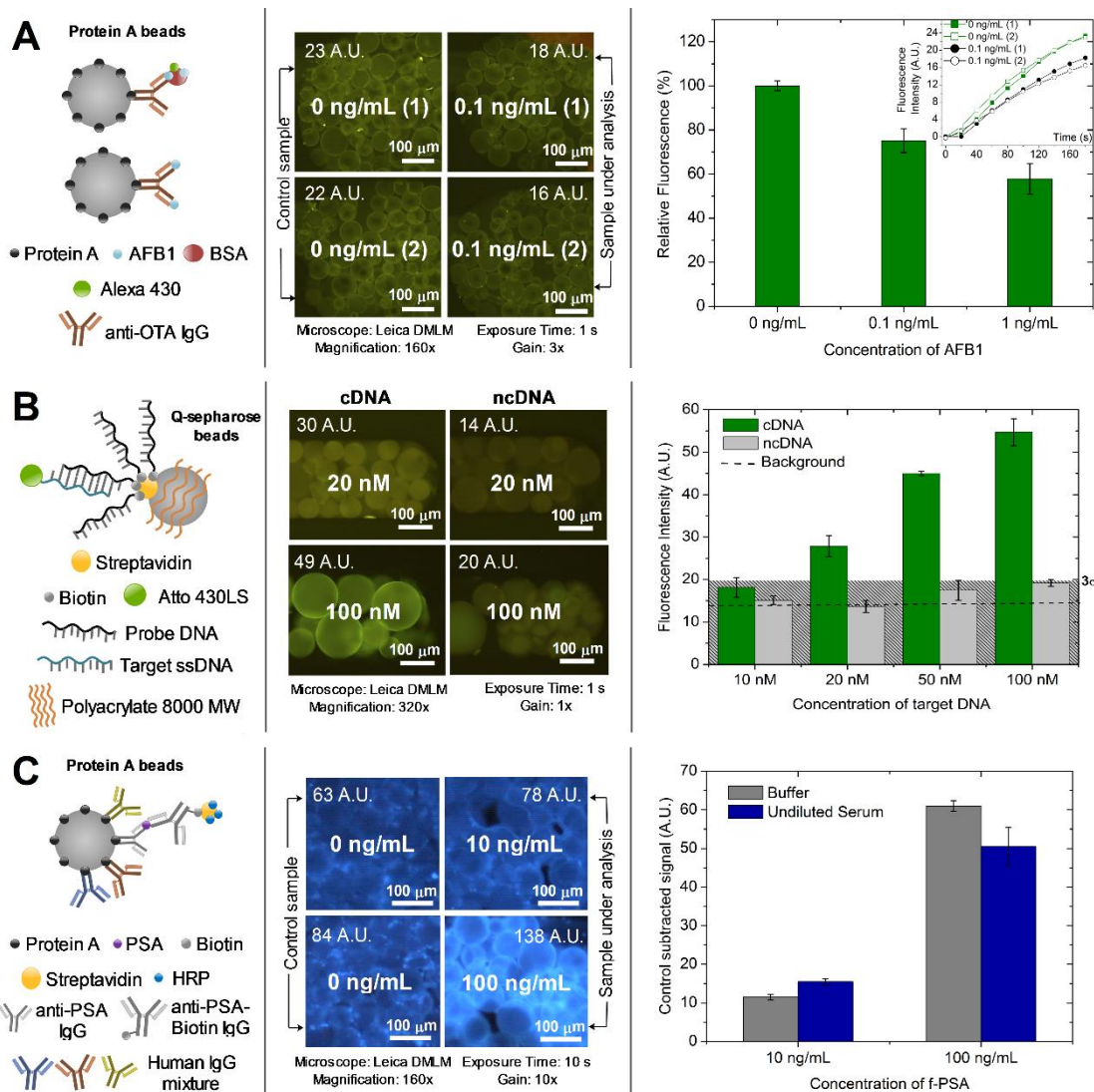


Figure 8.2 - Summary of novel bead-based screening and biosensing strategies using the previously discussed bead-trapping structure, highlighting the versatility of this design for (A) biosensing of mycotoxins, (B) ssDNA and (C) clinically relevant protein biomarkers directly in undiluted serum.

8.2.2. DNA hybridization assay

In this assay four concentrations of ssDNA target were tested (10, 20, 50, and 100 nM). The results presented in **Figure 8.2-B** show that for the ssDNA complementary target (cDNA) it is possible to detect concentrations of 20, 50 and 100 nM of target ssDNA above the nonspecific signal background. In all the four target concentrations, the data also indicates that the ssDNA non-complementary target (ncDNA) always falls below the nonspecific signal background, indicating the high selectivity of the assay. Performing a non-linear fit to the data, the LoD was found to be $11.4 \text{ nM} \pm 1.1 \text{ nM}$ ($\sim 10^{-8} \text{ M}$). A similar system was previously reported with a LoD of 10^{-10} M [332], in which beads covalently functionalized with streptavidin were used for immobilizing ssDNA. On the other hand, the system described here is based on an electrostatic

interaction between streptavidin (negatively charged) and the bead surface (positively charged). This approach, while less specific, is more versatile and inexpensive since it allows for a simpler and easier regeneration of the beads (using for example a solution with high salt concentration). Thus, the same micro-column can be reused to immobilize and detect different ssDNA targets. In this context, further work is being conducted to decrease the LoD and improve sensitivity, to reach clinically relevant concentrations in the pM range.

8.2.3. f-PSA detection assay

Also using protein A functionalized beads, PSA was captured and detected in spiked buffer solutions or undiluted human serum. In this case, since a secondary detector antibody is also included in the assay protocol, the unoccupied Protein A binding sites of the beads were blocked with a mixture of human IgG at a high concentration of 165 mg/mL. The results clearly show that there is still a considerable amount of non-specific signal in the absence of target f-PSA, even with the current blocking strategy, despite a significant specific signal obtained for both 100 and 10 ng/mL PSA, already within the clinically relevant range (4-10 ng/mL [333]), for both buffer and serum conditions (**Figure 8.2-C**). It is also worth noting that the chemiluminescence intensities in undiluted serum were very similar to those obtained in pure buffer (after subtraction of non-specific signal), which suggests that this detection strategy is highly resistant to matrix interference. Considering that the maximum CVs obtained for the buffer and serum experiments were 2.16% and 9.23%, respectively, the 3σ values for each of the 10 ng/mL PSA samples is above zero after calculating the difference between the PSA concentration under analysis and the negative control. Therefore, the limit of detection of this experiment is at least 10 ng/mL PSA. Overall, this was the first report of f-PSA detection in undiluted human serum sample by our group, within the clinically relevant range.

8.3. Integration of *p-i-n* a-Si:H photodiodes in bead-based microfluidics to transduce fluorescence, chemiluminescence and colorimetry

The optical-to-electrical signal transduction of molecular capture events under different chemical-to-optical modes of transduction (fluorescence, chemiluminescence, colorimetry) was performed by integration of *p-i-n* amorphous silicon (a-Si:H) thin film

photodiodes with the microfluidic device. **Figure 8.3-A** shows the schematics of the measurement setup after aligning the section of the microchannel with the packed beads on top of the photodiode. For the fluorescence measurements (**Figure 8.3-A (i)**), the photodiode was fabricated with an integrated a-SiC:H layer (1.8 μm thick) deposited on top of the SiN_x passivation layer, which works as a long pass absorption filter to cut the excitation light ($\lambda_{ex, laser} = 405 \text{ nm}$) while allowing the peak of the emission of the Alexa 430 fluorophore ($\lambda_{em, Alexa} = 539 \text{ nm}$) reach the photodiode through the Indium Tin Oxide (ITO) transparent contact. The detailed spectral characteristics of the filter are reported elsewhere [327]. The fluorescence generates a current in the photodiode that is proportional to the fluorescence intensity being emitted by the immobilized IgG-Alexa 430 conjugates on the beads, if the signal is above the photodiode background (or dark) signal. The chemiluminescence measurements were performed using photodiodes without the absorption filter (**Figure 8.3-A (ii)**). The photodiodes were aligned below the section of the microchannel where the beads are packed. The reaction of IgG-HRP conjugates immobilized on the beads with a luminol substrate solution flowing through the microchannel produces light at 428 nm that generates a current in the photodiodes that is proportional to the number of IgG-HRP conjugates present on the beads. The colorimetry experiments were performed by measuring the transmission of a red laser ($\lambda_{in} = 650 \text{ nm}$) through the packed beads (**Figure 8.3-A (iii)**) where the IgG-HRP conjugates were previously immobilized while a solution of TMB is flowing inside the channel. The HRP catalyzes the oxidation of the TMB substrate to form a dark-blue precipitate, which accumulates inside the channel over time and absorbs the laser light. Thus, the transmission of light measured by the photodiode will be inversely proportional to the concentration IgG-HRP conjugates on the beads.

The results in **Figure 8.3-A** to **C** are representative of the response of the *p-i-n* photodiodes at 0 V bias as a function of the assay time for the different stages of operation involved in the detection of fluorescence, chemiluminescence and colorimetry. In the fluorescence measurements (**Figure 8.3-A**), the dark current of the photodiode is initially measured and allowed to stabilize. The background signal is obtained by measuring the transmission of the excitation laser ($\lambda_{ex, laser} = 405 \text{ nm}$) through the microchannel containing only the packed beads. This signal (after subtracting the dark current) corresponds to excitation light that gets through the a-SiC:H filter and constitutes the baseline for the calculation of the fluorescence signal (FL signal) in the biological assay. IgG-Alexa 430 solutions at different concentrations were then flowed into the

microchannel for 10 min, after which the excitation laser was turned on and the resultant photodiode response due to fluorescence was measured. The signal due to fluorescence is obtained by taking the difference between the photodiode response under excitation light before and after IgG-Alexa 430 immobilization. In this case, a wash step using PBS buffer was not required prior to acquiring the fluorescence signal since it was observed that both the free and non-specifically bound IgG-Alexa 430 molecules in the channel contribute less than 1% of the total measured signal [327]. The chemiluminescence signal acquisition (**Figure 8.3-B**) using the photodiodes is simpler than the fluorescence assay, as in this case the IgG-HRP conjugates were previously immobilized on the protein A beads and the sharp increase in current above the dark current, when flowing a luminol solution, corresponds directly to the chemiluminescence signal. The measurements of the colorimetry assay (**Figure 8.3-C**) are based on measuring the transmission of light from a red laser ($\lambda_{in} = 658 \text{ nm}$) through the beads packed in the microchannel while flowing a solution of TMB through the channel. The photodiode response under laser illumination before starting the flow of TMB corresponds to a 100% transmittance value. As light-absorbing precipitates are produced and accumulate inside the channel upon the flow of the TMB solution, the transmission of the laser begins to decrease resulting in the decrease of the photodiode response. The colorimetric signal results from the measurement of transmission through the accumulated precipitates generated by the oxidation of TMB over a total time of 3 min and was calculated by taking the decrease in current from the maximum value obtained in conditions considered as 100% transmittance. For the chemiluminescence and colorimetry measurements, it was observed that the flow of luminol and TMB substrate solutions during 60 and 180 s, respectively, does not significantly remove ($\sim 10\%$ decrease in signal) the affinity captured IgG molecules [327]. This decrease in signal was deemed non-significant since (1) in the case of chemiluminescence, the signal was measured as the initial increase in current above the dark level in the first few seconds after starting the flow of luminol and, (2) in the case of colorimetry, the signal was integrated over 180 s and thus a decrease of 10% in measured signal over this period should result from the loss of significantly less than 10% of the IgG molecules.

Overall, after an in-depth quantitative analysis recently published by our group, all signal transduction methodologies previously explored in **Chapters 3 to 7** proved compatible with integrated photosensing in bead-based microfluidics. In particular, chemiluminescence provided the highest relative sensitivity (approx. 80-fold more

photons generated per captured target molecule) compared to colorimetry and fluorescence measurements using Alexa 430. On the other hand, fluorescence measurements require only a single step to perform, since the specific signal at bead-level can be monitored above the background of flowing molecules, having significant potential for assay simplification. Therefore, the use of fluorescence is preferable for applications which do not require the analysis at the lowest target concentrations (e.g. below 0.1-1 $\mu\text{g}/\text{mL}$ for a probe-target interaction with a K_D of $\sim 1.8 \times 10^{-7} \text{ M}$) as is the case of the competitive immunoassays for mycotoxin detection explored in this thesis.

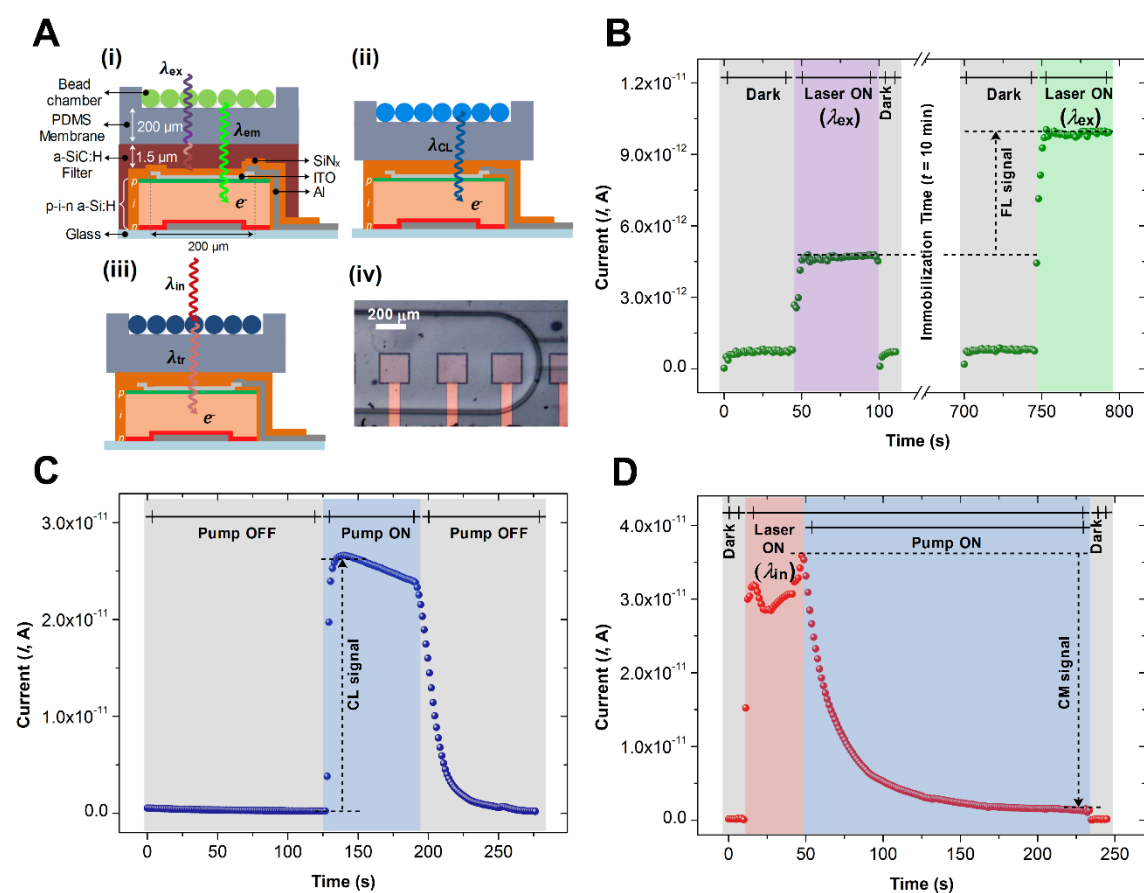


Figure 8.3 – **A** - Structural schematics of the thin-film photodiodes with and without an integrated excitation a-SiC:H filter and respective optical measurement setup after aligning the bead microchannel above the sensor. (i), (ii) and (iii) refer to measurements of FL, CL and CM, respectively. (iv) shows a microscopy photo of the microchannel without packed beads aligned with a linear array of $200 \times 200 \mu\text{m}$ ($L \times W$) a-Si:H photodiodes. **B** to **D** - Photodiode current measurements at 0 V bias for each of the optical detection modes. **(B)** Fluorescence measurement of 30 $\mu\text{g}/\text{mL}$ IgG-Alexa 430 immobilized on protein A beads. The current value measured before the immobilization of the IgG corresponds to the background excitation light leaked through the a-SiC:H filter. 1 $\mu\text{g}/\text{mL}$ IgG-HRP measured by **(C)** chemiluminescence (by flowing luminol) or **(D)** colorimetry (by flowing TMB).

8.4. Chapter conclusions

The concept of integrating highly optimized commercial microbeads in microchannels to provide (1) increased surface areas, (2) improved capture efficiencies, (3) reproducible surface chemistry, (4) high signal to-background ratios without a washing step and (5) faster binding kinetics relative to planar microchannels, proved potentially disruptive towards the development of a portable microfluidic immunosensor. Focusing on the bead-based mycotoxin immunoassay reported in this chapter (**Section 8.2.1**), highly promising results were obtained for the rapid detection of AFB1. Measuring the fluorescence intensity at bead level over time, proportional to the surface concentration of AFB1-BSA-Alexa 430 conjugate, allowed the detection of AFB1 concentrations as low as 0.1 ng/mL in less than 3 min. The measurement of the fluorescence derived from the Alexa 430 fluorophore on bead-based microfluidics was further confirmed to be compatible with the integration of *p-i-n* thin film a-Si:H photodiodes, coupled with an a-SiC:H absorption filter.

The following **Chapters 9 and 10** report (1) the development of a capillary-driven bead-based immunoassay to detect DON and a model mycotoxin and (2) an improved multiplexing strategy to detect 3 mycotoxins simultaneously in a single step. Both these assays are significant improvements over the assays discussed in **Chapter 6 and 7**, providing a simpler operation and dramatically reduced assay times.

Chapter 9

Capillary Bead-Based Microfluidic Immunoassay for Ultrarapid Mycotoxin Detection

After introducing the strategy of integrating nanoporous commercial microbeads in microfluidic channels, this concept was combined with a capillary driven flow to improve the assay previously discussed in **Chapter 7**. For microfluidic devices to achieve a practical point-of-need application, it is necessary to circumvent the often-excessive system complexity required, such as external pumps and multi-step operation to provide a rapid and simple, while still robust and fit-for-purpose device. This chapter reports a simple capillary-based microfluidic device with integrated microbeads and a no-wash, single-step mode of operation that achieves a sub-minute detection of analytes using a fluorescent competitive immunoassay. Minimum detectable limits of 1.7 ng/mL were obtained for mycotoxin detection within 70 s assay time, using 4.5 μ L of sample. Furthermore, an internal control was also included in the microfluidic device to provide additional robustness and result validation. The contents of this chapter are reproduced with appropriate adaptations from one original research article [334], co-authored with a MSc student (Roberta Epifania) in Biomedical Engineering at University of Rome “La Sapienza” in Rome, Italy, who developed her research project at the research facilities of INESC MN. I was responsible for the co-supervision of the student in the lab, troubleshooting, planning of experiments and thorough revision of the published paper.

9.1. Materials and experimental methods

9.1.1. Preparation of antibody functionalized beads

To immobilize anti-BSA and anti-deoxynivalenol (DON) IgG molecules on the beads via coupling to protein G, the commercial protein G-coated agarose beads were incubated for 15 min in solutions with (1) anti-BSA IgG at a concentration of 50 μ g/mL in a total volume of 23 μ L or (2) anti-DON IgG at a concentration of 26 μ g/mL in a total volume of 15 μ L. The stock solution of beads was composed of ~70% (v/v) bead slurry in PBS, from which 3 μ L were pipetted to the previous final volumes. To prevent the cross-binding of free antibodies between the two chambers after spotting of the beads, a

pre-washing step was required. Thus, 200 μL of PBS were added to both bead solutions, which were mixed and centrifuged to allow the beads to sediment to remove the excess liquid. This step was repeated three times to ensure sufficient dilution of any free antibodies. Protein G-coated 4% cross-linked agarose beads with an average diameter of 90 μm were purchased from GE Healthcare Life Sciences as Protein G Sepharose 4 Fast Flow. Anti-DON IgG mouse monoclonal antibodies were acquired from Biotex (Berlin, Germany) and anti-BSA IgG rabbit polyclonal antibodies were acquired from Thermo Fisher Scientific.

9.1.2. Capillary-driven competitive immunoassay for DON detection

To confine the beads within the respective microfluidic chambers, 0.1 μL of protein G beads previously incubated with anti-BSA IgG were manually pipetted on the PDMS surface of the control chamber area; the same volume of protein G beads incubated with anti-DON IgG was pipetted on the test chamber area. This manual pipetting step was observed to provide sufficiently reproducible and compact bead distributions in the respective chambers. Then, the PDMS structure was reversibly sealed against a glass substrate previously treated with a plasma cleaner (800 mTorr oxygen, 1 min at medium intensity; Harrick Plasma Expanded Plasma Cleaner, NY, USA). The same strategy was used with the single chamber structure by inserting beads with one given type antibody functionalization in the microfluidic chamber. After sealing the structure against the glass, the device was ready to be used by inserting the sample from the inlet. The sample insertion was performed 10 min after the plasma treatment, as previously optimized for providing a capillary-driven flow rate of $\sim 1 \mu\text{L}/\text{min}$ [154]. Depending on the experiment to be performed, the sample manually pipetted into the inlet at a total volume of 4.5 μL was composed of (1) increasing concentrations of DON-BSA-Alexa 430 in the case of the calibration curves or (2) a fixed concentration of 10 $\mu\text{g}/\text{mL}$ of DON-BSA-Alexa 430 mixed with different concentrations of free DON toxin for the competitive assay. All bead-packed devices were single-use, being discarded after each experiment. PBS tablets, carbonyldiimidazole (CDI), bovine serum albumin (BSA) and deoxynivalenol (DON) were purchased from Sigma-Aldrich. The DON-BSA-Alexa 430 conjugates were prepared by first conjugating BSA with DON using CDI chemistry according to the method described in **Chapter 6** and subsequently conjugating a succinimidyl ester-activated Alexa Fluor 430 dye, purchased from Thermo Fisher Scientific. The conjugation of a toxin-BSA conjugate with Alexa 430, followed by a diafiltration in

Amicon Ultra-4 centrifugal units, 10 kDa cutoff (EMD Millipore) for removal of non-conjugated dye was previously described in **Chapter 8**.

9.2. Capillary device design and operation

The design of the bead-based capillary device is shown schematically in **Figure 9.1**. Considering that the beads have an average size of 90 μm , the channel height of the device was designed to be 100 μm . The device has two main modules: the chambers where the beads are packed and the capillary pump for driving the liquid flow. Two different versions of the structure were used, which differ only in the number and dimensions of chambers in parallel relative to the direction of the liquid flow. The single chamber structure has one $3,250 \times 660 \mu\text{m}^2$ chamber, while the double chamber structure has two $1,587 \times 660 \mu\text{m}^2$ compartments, physically separated by a 75 μm wide continuous barrier. The dimensions of the chambers were designed to match the size of a 2-200 μL pipette tip to allow for a manual bead insertion. The single chamber structure was used for optimization studies, by packing beads with one type of antibody functionalization for each assay and flowing solutions with increasing concentrations of the conjugates. The double chamber structure was designed to simultaneously pack beads with the two types of antibody functionalization to have an internal control in the assay. The internal control chamber and test chamber will be henceforth referred to as CC and TC, respectively. In both structures, the chambers are delineated by $150 \times 75 \mu\text{m}^2$ pillars spaced by 50 μm gaps allowing the sample to flow into the bead chamber and subsequently follow into the capillary pump. To allow the liquid to wet the extremes of the chambers without trapping air bubbles, two air outlets were included in the device design. The microchannels leading to the air outlets have a cross-section of $40 \mu\text{m} \times 100 \mu\text{m}$ ($W \times H$) to fully prevent the liquid from flowing through this narrow passage. According to the literature [34, 37], this effect originates from the observation that the capillary-driven flow is promoted only by the plasma cleaner treated glass surface (contact angle (γ) $\approx 0^\circ$ [154]), while the untreated hydrophobic PDMS surfaces prevent the liquid flow ($\gamma > 100^\circ$ [335]). Therefore, the minimization of the glass to PDMS surface ratio is here used as a strategy to provide an air-selective barrier.

The capillary pump used to drive the liquid flow through the bead chambers is made up of two segments: the first one is a 22 mm long, 300 μm wide continuous channel. Here, the fluid accumulates hydraulic resistance allowing an effective wetting of the

entire capillary chamber. This segment is followed by a 115 mm long “fast pump”, where the channel walls are composed of $150 \times 50 \mu\text{m}$ pillars spaced by $75 \mu\text{m}$ gaps. This design, as described in detail elsewhere [34], allows the liquid front to move along the main channels while it shortens the path through the gaps at each successive turn, allowing a relatively stable flow rate over time, without a significant accumulation of hydraulic resistance as previously demonstrated [154]. The stability and magnitude of the flow rate in this case is of critical importance to minimize the duration of the assay by avoiding mass transport limitations. Nevertheless, by including an internal control chamber in the device it is possible to normalize any flow rate variations, which affect both chambers simultaneously, by measuring the relative fluorescence. It is also important to highlight that in order to ensure a stable and reproducible capillary-driven flow rate from device to device in practical applications, these should be stored in vacuum packaging to prevent adsorption of organic contaminants [336]. However, for this work, the stability of contact angle between devices was assured only by flowing the SUA at a fixed, constant time after performing the plasma treatment.

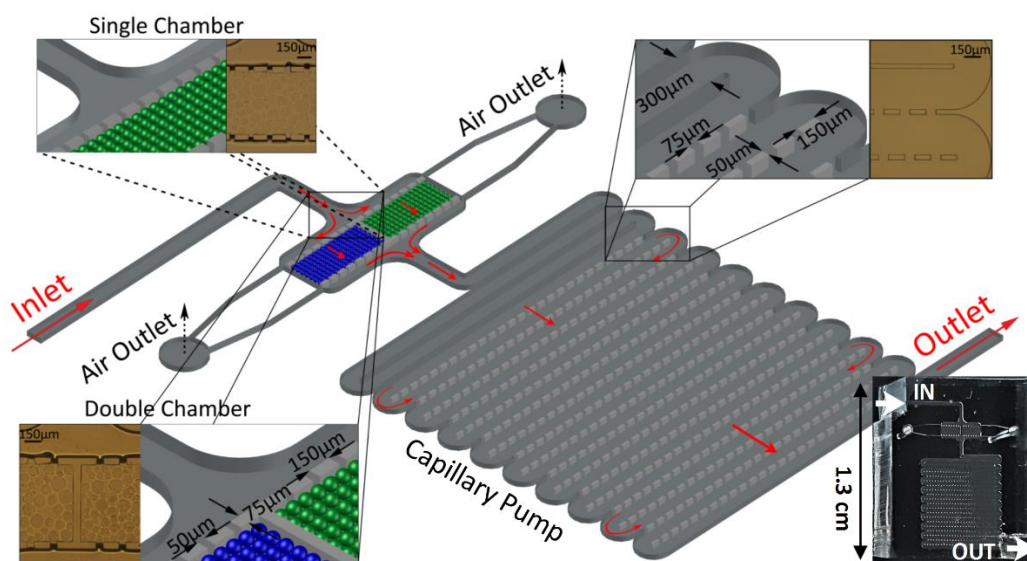


Figure 9.1 - 3D schematic visualization and microscopy photos of the capillary bead-based device showing its two main elements: the chamber where the beads are packed and the capillary pump. Two different versions of the structure were used in this paper, comprising either a single chamber or double chambers arranged in parallel. In the first structure, beads with only one type of antibody functionalization were packed to optimize the assay. In the latter, beads with two different types of antibody functionalization were packed simultaneously on each side of a continuous wall to spatially discriminate the control signal in one chamber (right, control chamber, CC) and the test signal in the other chamber (left, test chamber, TC). The air outlets prevent the trapping of bubbles at the edges of the entrance and exit of the chambers, which would impair the homogeneity of the signal. For both devices, the sample flowed via a capillary pump, designed to provide a specific and constant flow rate over time. A photograph of the device containing the double chamber is shown in the bottom right corner, sealed against a glass slide.

9.3. Optimization of a competitive immunoassay for deoxynivalenol (DON) quantification and an anti-BSA internal control

To perform a competitive mycotoxin immunoassay where the internal control and the test signal are simultaneously measured, calibration curves of DON-BSA-Alexa 430 captured on beads incubated with either anti-DON IgG or anti-BSA IgG are first required. Solutions with four different concentrations of DON-BSA-Alexa 430 (10 $\mu\text{g/mL}$, 20 $\mu\text{g/mL}$, 40 $\mu\text{g/mL}$ and 80 $\mu\text{g/mL}$) were flowed through the structure after packing the beads. The fluorescence emission was measured as an average of three independent measurements under the same experimental conditions and normalized relative to the background signal before flowing the solutions. In **Figure 9.2-A** and **B** the calibration curves for the capture of the conjugate by the anti-BSA IgG and anti-DON IgG molecules immobilized on the beads are shown, highlighting a linear correlation in the tested range of concentrations. The microscopy images included on each plot were acquired when the DON-BSA-Alexa 430 solution reached the outlet. It is possible to observe that at a concentration of 10 $\mu\text{g/mL}$ the fluorescence signal measured on each type of functionalized beads (16.3 ± 4.1 AU ($\pm\text{SD}$) for anti-BSA and 14.4 ± 1.7 AU ($\pm\text{SD}$) for anti-DON) is not significantly different. Therefore, this concentration of DON-BSA-Alexa 430 was selected for further experiments to perform a competitive immunoassay for DON detection, considering that the signal generated on the anti-DON beads in the absence of free DON in solution is comparable to the anti-BSA control. According to the competitive immunoassay presented in previous work [143], the presence of free DON in solution, mixed with the DON-BSA-Alexa 430 conjugates, induces a decrease in the fluorescence emission measured on the beads with anti-DON IgG in a concentration dependent manner. As shown in **Figure 9.2-C**, the higher the concentration of free DON in solution, the lower the signal measured on the beads. This competitive assay provided a minimum detectable concentration (L_D) of 1.7 ng/mL DON, calculated as the concentration of DON that provides a signal decrease equal to 3.29 times the standard deviation of the blank measurements, using the adjusted logarithmic regression ($y = -2.16 \ln(x) + 25.2$, $R^2 = 0.97$). This value is considerably below all regulatory and recommended limits for DON in food and feed enforced in the European Union [79, 84] where the strictest concentration limit is set at 20 ng/g in cereal and maize-based products for consumption by young children. Furthermore, this value is comparable to the minimum detection limits achieved using commercial lateral-flow devices while achieving significantly shorter

times of analysis [1] owing to the shorter diffusion distances provided by the nanoporous beads and a rapid/stable linear liquid velocity provided by the precise and reproducible mold replication process. This excess in minimum detectable limit potentially allows a significant degree of sample dilution after extraction and sample preparation using previously developed and validated methodologies [180], in order to minimize matrix interference effects and background non-specific fluorescence while monitoring the DON-BSA-Alexa 430 conjugate being captured on the beads. To evaluate the binding kinetics of the optimized concentration of DON-BSA-Alexa 430 conjugates to each of the beads, the fluorescence intensity was measured over time in 10 s intervals. In **Figure 9.2-D** it is possible to observe that the liquid takes about 70 s to reach the end of the capillary pump. Furthermore, the final absolute fluorescence intensity is achieved between 40 and 50 s of flowing the sample, highlighting potential to achieve detection in sub-minute assay times in conditions where the signal is continuously monitored.

9.4. Ultrarapid detection of DON using the double-chamber device

After the previous optimization, it was possible to use the double chamber structure shown in **Figure 9.1** to design a standalone assay to detect DON contamination. The bar chart in **Figure 9.3** shows the quantification of the fluorescence emission of the DON competitive immunoassay as an average of two independent experiments at increasing concentrations of free DON. The microscopy images in **Figure 9.3** show the wall interface in each condition. It is possible to observe that the signal of the control chamber (above the wall in each image) remains the same despite the presence of the free toxin in solution, while the signal measured in the test chamber (below the wall in each image) decreases significantly below that of the control chamber. Therefore, the competitive immunoassay performed in the double chamber structure provides a response in a single step considering the background ($\approx 16.6 \pm 1.8$ AU) normalized fluorescence ratio between the TC and CC, varying from $88\% \pm 8\%$ (\pm SD) at 0 ng/mL DON down to $59\% \pm 5\%$ (\pm SD) and $22\% \pm 1\%$ (\pm SD) for 10 and 100 ng/mL DON spiked in solution, respectively. Nevertheless, comparing the absolute values with those measured in **Figure 9.2**, a slight decrease in sensitivity can be noticed, possibly from cross-chamber light contamination, hindering the decrease in signal of the test chamber due to the high signal in the control chamber. Furthermore, the relatively high variability in the measurements is mostly derived from the image analysis considering (1) the variable

dispersion in bead packing and (2) non-uniform molecular distribution within each bead due to diffusion limitations. The use of smaller and more monodisperse beads, as well as a better control of pore size are expected to reduce variability.

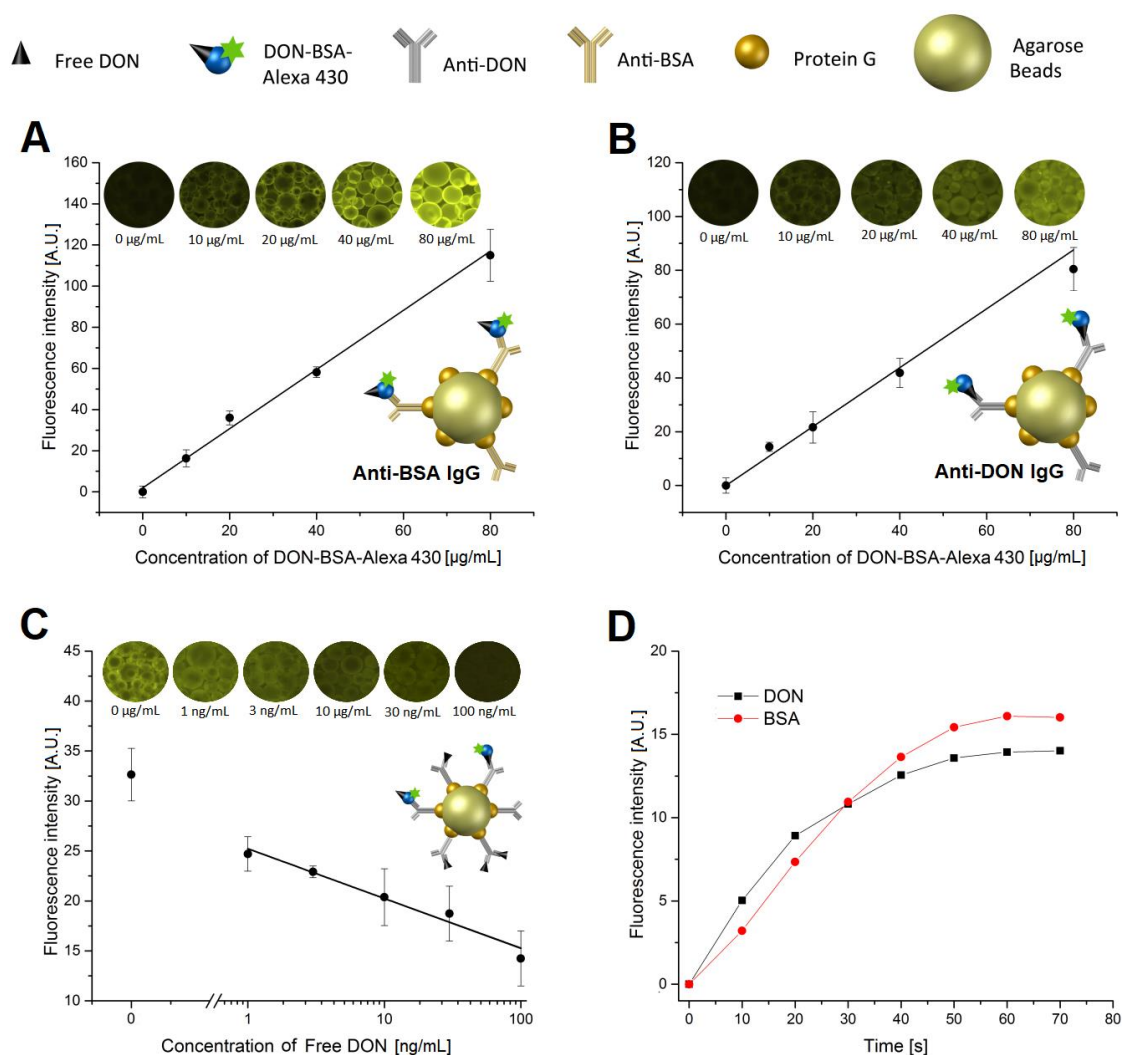


Figure 9.2 - Calibration curves measured after flowing a solution with increasing concentrations of DON-BSA-Alexa 430 and measuring the average fluorescence of the protein G beads incubated with (A) anti-BSA IgG at a concentration of 50 µg/mL or (B) anti-DON IgG at a concentration of 26 µg/mL. The point at a concentration of zero corresponds to the fluorescence emission of the beads before flowing the solution (background fluorescence intensity, $\sim 16.6 \pm 1.8$ AU). This value was subtracted from all points in the plots (A) and (B). (C) Calibration curve for the DON competitive immunoassay at increasing concentrations of free DON in solution, mixed with a fixed concentration of 10 µg/mL DON-BSA-Alexa 430. In the plots (A) to (C) the fluorescence intensities for each concentration were measured as three independent experiments (\pm SD) using three disposable microfluidic devices. (D) Background normalized fluorescence emission over time measured in a chamber packed with beads specific for DON (black squares) or to BSA (red circles) while flowing a solution containing 10 µg/mL of DON-BSA-Alexa 430. The single chamber device has been used to perform all these experiments. Error bars refer to \pm SD of three independent experiments. In (C), images were contrast enhanced for visualization purposes.

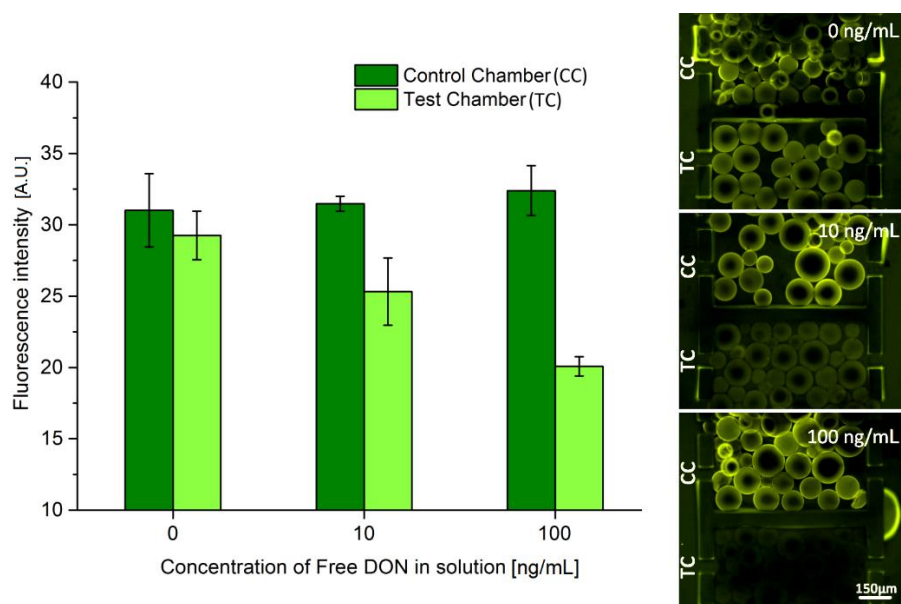


Figure 9.3 - Fluorescence emission of the DON competitive immunoassay measured in the double chamber structure with an internal maximum signal control. Increasing concentrations of free DON were mixed with a fixed concentration of 10 $\mu\text{g/mL}$ DON-BSA-Alexa 430 and flowed through the device. The protein G beads incubated with anti-BSA IgG are packed in the control chamber (CC) while the beads incubated with anti-DON are packed in the test chamber (TC). The bar chart shows the quantification of the average fluorescence signal for both chambers. Error bars refer to $\pm\text{SD}$ of two independent experiments measured using two disposable microfluidic devices. Images were contrast enhanced for visualization purposes.

9.5. Chapter conclusions

This chapter demonstrates a proof-of-concept for a novel no-wash and ultrarapid bead-based capillary assay performed in a microfluidic device. The simple mode of operation was combined with detection limits comparable to those achieved using state of the art lateral flow assays, particularly for a competitive immunoassay, detecting as low as 1.7 ng/mL of the mycotoxin DON in 60 s assay time. These features were further enhanced by the addition of an internal control to provide a robust response from the single-step competitive assay. These results highlight this device as a potentially multiplexable and general approach to perform rapid analyses of multiple analytes at the point-of-need, using minimal sample volumes. However, to realize a fully portable device, it will be necessary to integrate fluorescent detection with the microfluidic device, which can be achieved, for example, by integrating thin-film photodetectors aligned below the bead chambers, as previously demonstrated for the continuous monitoring of on-bead fluorescence in the presence of a complex matrix [51]. Furthermore, it is also critical to optimize and automate the packaging of the beads in microfluidic device for increased robustness and repeatability.

Chapter 10

Multiplexed Microfluidic Immunoassay Addressed by a Photodetector Array for Point-of- Need and Sub-Minute Detection of Mycotoxins

This chapter reports a dramatic improvement over the multiplexed device discussed in **Chapter 6** by integrating discrete bead chambers against different mycotoxins, integrated in series relative to the sample flow. To achieve ultrarapid detection of mycotoxins, namely aflatoxin B1, ochratoxin A and deoxynivalenol, at the point-of-need, a novel multiplexed bead-based microfluidic competitive immunosensor, coupled with an array of a-Si:H thin-film photodiodes for integrated fluorescence signal acquisition, was developed. Simultaneously measuring the initial binding rate for each analyte of the sample under analysis against an internal reference, this device provided limits of detection below 1 ng/mL for all mycotoxins in a single-step assay and within 1 minute after mixing the sample under analysis with a fluorescent conjugate. The compatibility of the device with the analysis of mycotoxins spiked in corn samples was further demonstrated after performing a sample preparation procedure based on aqueous two-phase extraction. The short times of analysis and sensitivities in the low ng/mL range make these devices potentially competitive with the lateral flow devices that are currently the standard for this application. Furthermore, this device architecture can be easily expanded to other analytes in food safety, biomedical and other applications. The contents of this chapter are reproduced with appropriate adaptations from one original research article [49] co-authored with Denis R. Santos and Inês F. Pinto, PhD students at INESC MN. D. R. Santos performed the (1) photosensor fabrication, optimization and characterization and (2) optimized the integrated circuit and software used for signal acquisition after a proof-of-concept version I prepared within the scope of a course on sensors and instrumentation (Appendix A). I. F. Pinto conceptualized the bead-based microfluidic device for multiplexed analytics and participated in discussions and troubleshooting.

10.1. Materials and experimental methods

10.1.1. Functionalization and packing of beads in microchannels

To functionalize the agarose beads with antibodies against each of the target mycotoxins, commercial protein G conjugated beads were first incubated in anti-mycotoxin IgG solutions for 15 min in PBS buffer using a rotator mixer (20 revolutions per min) to avoid settling. For the incubation, 3 μL of a bead solution in PBS (~ 50% v/v bead resin) were transferred to 12 μL anti-AFB1, 12 μL anti-DON or 0.5 μL anti-OTA IgG solutions, prepared also in PBS to a final IgG concentration of 50 $\mu\text{g}/\text{mL}$, except for the anti-OTA IgG where the final concentration was 41.7 $\mu\text{g}/\text{mL}$. To pack the beads in the single microchannels, 110 μL of a solution of 1 mg/mL BSA in PBS was added to each set of beads. Then, after suspending the beads in solution, 40 μL of each bead solution were pipetted and the pipette tip subsequently released after being fitted to the inlet hole of the microchannels. Afterwards, a syringe pump was immediately used to exert a negative pressure at the outlet of the microchannel at a flow rate of 15 $\mu\text{L}/\text{min}$. The microchannels with the packed beads were stored at 4 °C until further use.

10.1.2. Immunoassay optimization in individual bead microchannels

To facilitate the optimization of the immunoassay, single channels coupled with fluorescence microscopy for signal acquisition were first used. The bead microchannel devices used for optimizing the immunoassay were the same as previously discussed in **Chapter 8**. To perform the immunoassays, a PBS solution containing a certain concentration of spiked mycotoxin plus mycotoxin-bovine serum albumin (BSA)-Alexa 430 conjugates (prepared as described in detail in **Chapter 8**), at concentrations of 8 $\mu\text{g}/\text{mL}$ AFB1-BSA-Alexa 430, 8 $\mu\text{g}/\text{mL}$ DON-BSA-Alexa 430 or 10 $\mu\text{g}/\text{mL}$ OTA-BSA-Alexa 430, was flowed through the microchannels at 17.5 $\mu\text{L}/\text{min}$, by applying a negative pressure at the outlet using a syringe pump. The signal acquisition was performed by acquiring images of the beads on a fluorescence microscope (Leica DMLM equipped with a DFC300FX camera and a 100 W short arc mercury lamp as excitation light source, coupled to a I3 filter cube) in 15 s intervals (1 s exposure) starting from the moment the pump was turned ON. The quantification of the signal after acquiring the images was performed using the grey scale of the entire bead, processed using the software ImageJ (National Institutes of Health, MD, USA). The protein G functionalized beads (Protein G Sepharose 4 Fast Flow) were purchased from GE Healthcare. The anti-

AFB1 IgG (AFA-1 mouse monoclonal) was purchased from Abcam, anti-DON IgG (mouse monoclonal) was purchased from Biotez (Berlin, Germany) and anti-OTA IgG (rabbit polyclonal) was purchased from Immunechem (Burnaby, British Columbia, Canada).

10.1.3. Multiplexed immunoassays

The multiplexed immunoassays were performed using the microfluidic structure shown schematically in **Figure 10.1-A**. Each set of protein-G beads for each of the four chambers was first incubated with the respective anti-mycotoxin or anti-BSA IgG solutions. The incubation was performed exactly as described in **Section 10.1.1** for the anti-mycotoxin IgG molecules and, for the anti-BSA IgG, 3 μL of beads were added to 19 μL of anti-BSA IgG at a concentration of 50 $\mu\text{g}/\text{mL}$. After 15 min of incubating each of the 4 sets of beads, 110 μL of polyethylene glycol (PEG) 20% (w/w) in PBS were added to each solution. To insert the beads in each of the 4 chambers, the microfluidic structure was first filled with PBS buffer and pipette tips containing 40 μL of each bead solution were inserted in the respective chamber inlets, followed by the application of a negative pressure at 10 $\mu\text{L}/\text{min}$. Subsequently, each bead chamber was sealed using 20 ga metal plugs. To minimize non-specific interactions with the microchannel PDMS surface and with the agarose beads, a solution of 1% purified casein (w/v) was flowed via the sample under analysis (SUA) inlet (**Figure 10.1-A**) at 17.5 $\mu\text{L}/\text{min}$ for 1 min, after first washing the channel and beads by flowing plain PBS buffer at 17.5 $\mu\text{L}/\text{min}$ for 2 min. The SUA spiked with a certain concentration of each mycotoxin plus 4 $\mu\text{g}/\text{mL}$ AFB1-BSA-Alexa 430, 6 $\mu\text{g}/\text{mL}$ DON-BSA-Alexa 430 and 10 $\mu\text{g}/\text{mL}$ OTA-BSA-Alexa 430 was then flowed through the device at 17.5 $\mu\text{L}/\text{min}$ according to **Figure 10.1-A**. Anti-BSA IgG (rabbit polyclonal) and casein (1% w/v) blocking solution were purchased from Thermo-Fisher Scientific and PEG (MW = 8,000 g/mol) was purchased from Sigma-Aldrich.

10.1.4. Instrumentation, signal acquisition and processing

The acquisition and analog processing of the current signals generated by the photodiodes was performed using a transimpedance amplifier (TIA) circuit. A stable 2.5 V output generated by a low-noise and very low-drift precision voltage reference (ADR4525, Analog Devices, Norwood, Massachusetts, US) coupled to an operational amplifier in voltage follower configuration, is used as a virtual ground (VGND). The operational amplifier used in the TIA was a LMC6482 CMOS dual rail-to-rail operational

amplifier from Texas Instruments. The TIA amplification stage is set by a 1 G Ω resistor (for a 180 dB gain), in parallel with a 100 pF ceramic capacitor for stabilization of the circuit. Further amplification of the TIA voltage output is performed using a voltage difference amplifier and resistors of 1 k Ω and 100 k Ω were selected to achieve a gain of 40 dB (for a total of 220 dB) and therefore reach a voltage magnitude quantifiable by the Teensy 3.2 microcontroller ADC (PJRC, Sherwood, Oregon, US) set to 14-bit resolution. The amplification circuit and the Teensy 3.2 microcontroller were mounted on a circuit board which connects to the photodiode PCB through a 5-wire shielded cable. The circuit board includes a Bluetooth HC-05 module that can be used for wireless communication when the board is powered by an external power supply or battery for true portability. A MATLAB graphical user interface (GUI) script was developed to communicate, through USB or Bluetooth, with the microcontroller during the measurements to receive, store and plot the data in real time. To illuminate all sensors and chambers simultaneously and homogeneously, a 405 nm diode laser was focused with a beam diameter of approximately 2 mm. The laser was first attenuated by a neutral density (ND) 1.0 filter in order to reduce the illumination photon flux to $\Phi_{exc} \sim 1.0 \times 10^{16} \text{ cm}^{-2} \cdot \text{s}^{-1}$, providing a compromise between high fluorescence emission and minimal photobleaching effects through the duration of the assay.

10.2. Design of the microbead-based microfluidic device for immunoassay multiplexing with an internal reference

The main goals of this work were to (1) design and develop a multiplexed microfluidic immunoassay for detecting mycotoxins at the relevant regulatory limits and (2) minimize the required number of steps and assay time relative to the state-of-the art on biosensors for mycotoxin detection (**Table 1.6**). Previously reported microfluidic approaches for mycotoxin detection are mostly based on competitive immunoassays performed on the inner surfaces of a microchannel, utilizing fluorophores [24] or enzymes [21] to generate an optical signal. In general, the competitive immunoassay is based on first immobilizing the (1) mycotoxin antigen (free or bound to a protein carrier such as BSA) or an anti-mycotoxin antibody (probe) on the microchannel walls and then (2) flowing the sample containing free toxin (target) plus a labelled target complementary to the probe, which may be an antibody or the target toxin. The specific signal from the label, which is inversely proportional to the concentration of free toxin in the sample, can

thus be used to correlate the titers of free toxin, having as a control a blank sample that provides the maximum signal. This signal intensity for both the blank and contaminated samples increases over time while labelled target molecules are being captured by the probes according to **Equation 1.4**, which assumes Langmuir kinetics. Here, the presence of free toxin reduces the concentration of effective probes (b_m), thus reducing the rate $\delta b/\delta t$ for the labelled molecule. The signal acquisition is thus typically performed after a certain amount of time after washing the sensing area to minimize non-specific interactions. This amount of time can be either (i) a constant time to provide a sufficient and measurable signal for the blank, resulting in a transient, i.e. time dependent, probe concentration (shorter assay, $b(t)$, **Equation 1.5**) or (ii) a sufficient amount of time to reach an equilibrium probe concentration, providing a relatively more stable signal (longer assay, b_{eq} **Equation 1.6**).

Based on the previous discussion, the continuous measurement of the rate $\delta b/\delta t$ would provide the fastest method to perform the competitive immunoassay. To employ such strategy, the rate must be measured while the sample is under flow, requiring a single-step methodology. To achieve this, commercial pre-functionalized microbeads were integrated in the microfluidic device to provide (1) shorter diffusion distances, (2) increased surface to volume ratios and (3) higher probe surface densities and reproducible surface chemistries [18]. These properties, combined with the use of fluorescence as the signal transduction mode, allow $\delta b/\delta t$ to be measured continuously on the beads.

The developed bead-based microfluidic structure is shown schematically in **Figure 10.1-A**. Each of the first three chambers, in series with the liquid flow direction, contains antibodies against the 3 different toxins, namely OTA, AFB1 and DON, immobilized on commercial protein-G functionalized agarose beads. The competitive immunoassay, which is summarized in **Figure 10.1-B**, is based on mycotoxin-BSA-Alexa 430 (TBA) conjugates spiked in the sample-under-analysis (SUA) which compete for binding to the anti-mycotoxin antibodies. Therefore, the higher the specific mycotoxin concentration in solution, the lower the increases in fluorescence signal over time in each bead chamber. The fourth chamber contains anti-BSA antibodies and works as an internal negative control, providing the maximum signal level. This internal control is required to normalize and validate the assay in terms of liquid flow velocity and overall antibody stability.

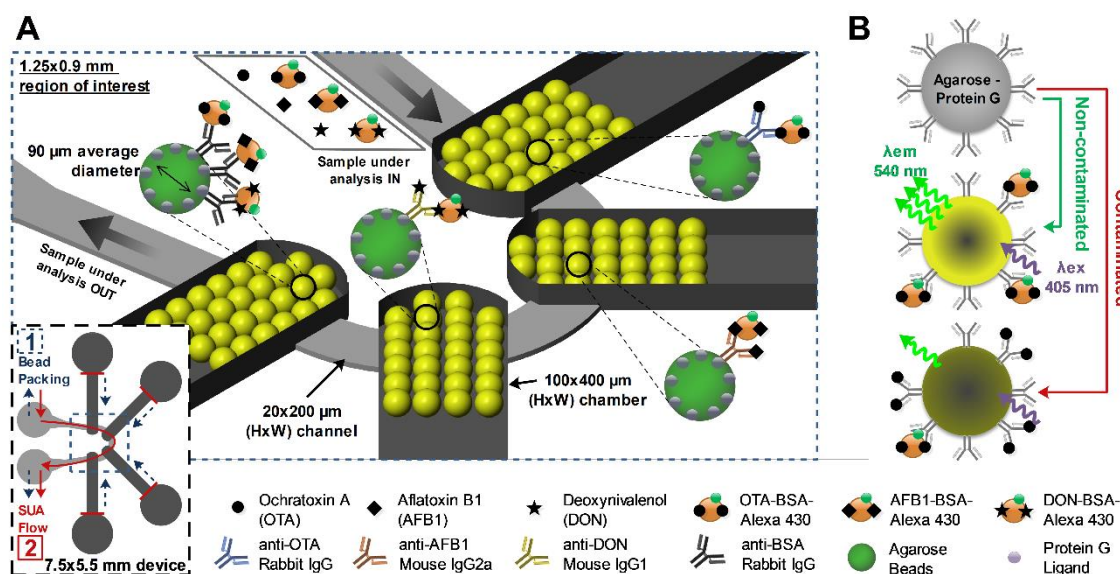


Figure 10.1 - A- Schematics of the bead-based multiplexed microfluidic device with an internal reference for immunodetection of OTA, AFB1 and DON. The bottom left diagram illustrating the top view of the device describes the two steps for (1) bead packing and (2) subsequent flow of the sample-under-analysis (SUA). B- Schematics of the competitive fluorescence immunoassay.

10.3. Development and optimization of a competitive immunoassay for sub-minute mycotoxin quantification in model solutions

Before testing the performance of the multiplexed assay using 4 chambers in series, each mycotoxin immunoassay was tested individually in single chambers using a simplified microchannel design as previously introduced in **Chapter 8**. An optimization procedure for the anti-mycotoxin IgG concentration used for bead functionalization and concentration of TBA conjugates spiked in the SUA (**Figure 10.2**) was first performed for DON detection. This optimization procedure was performed for a single toxin since it was previously observed that for the antibodies being used, comparable signal intensities are generated at equal assay conditions [42]. It was concluded that in the tested range of concentrations similar sensitivities were obtained, thus, the concentrations reported in **Section 10.1.2**. were chosen to provide a signal significantly above the background for the blank (0 ng/mL DON). The time-dependence of the relative fluorescence signals measured on the beads, at increasing mycotoxin concentrations, are shown in **Figure 10.3**. In **Figure 10.3-A, B and C** it can be observed that an increase in mycotoxin concentration significantly reduces the rate increase of fluorescence over time, which is directly proportional to $\delta[TBA]/\delta t$, where [TBA] is the surface concentration of TBA conjugates on the beads. These kinetic profiles for each mycotoxin can then be used to

calculate calibration curves of the initial TBA binding rate ($\delta[TBA]/\delta t$), measured in the first 60 s of the assay (left of the vertical dashed line) in the presence of increasing mycotoxin concentrations, as shown in **Figure 10.3-D**. Based on the curves, minimum detectable limits (L_D) below 1 ng/mL were obtained for all mycotoxins, calculated as the concentration of mycotoxin necessary to reduce the initial TBA binding rate below 3.29 times the standard deviation of the blank measurements (black stars in **Figure 10.3-A, B** and **C**, 0 ng/mL mycotoxin). These results are comparable to those previously obtained using 5-30 fold lengthier and multi-step microfluidic assays using chemiluminescence or fluorescence [21, 24, 42], while potentially providing adequate sensitivities to meet the wide majority of current EU regulatory and recommended limits for AFB1, DON and OTA in foods [79] and feeds [82, 84]. Furthermore, by continuously computing $\delta[TBA]/\delta t$, the detection times can be reduced below the 60 s threshold, where fluorescence signals can be measured significantly above the noise threshold.

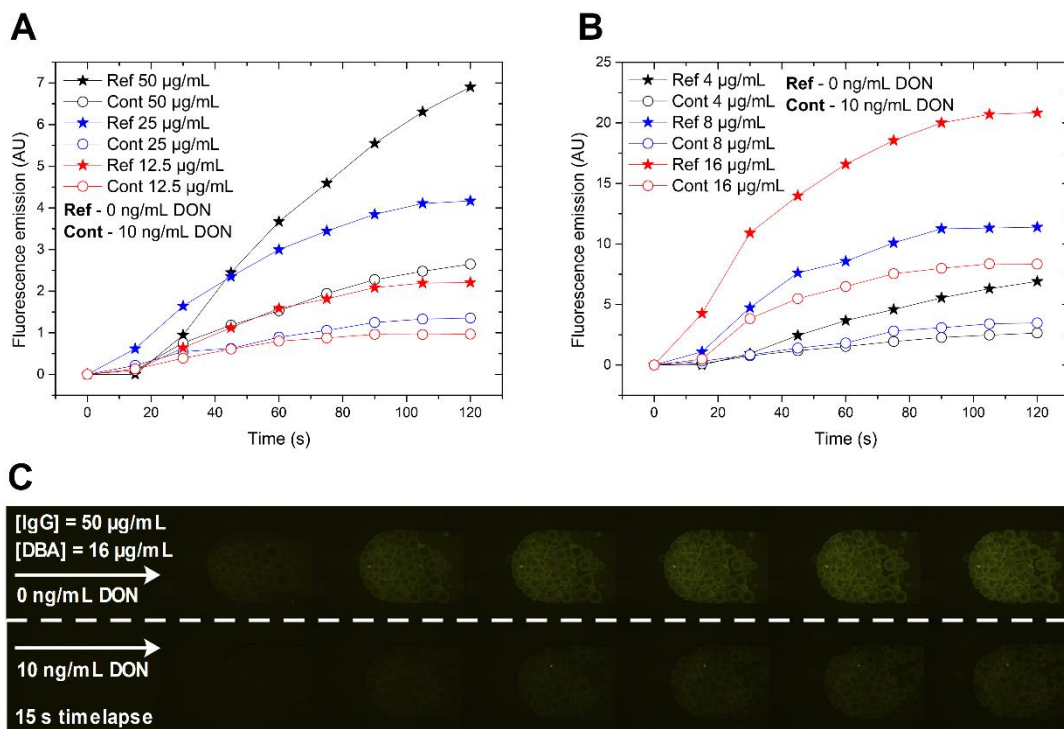


Figure 10.2 - A- Optimization of anti-DON concentration to functionalize the agarose protein-G beads. **B-** Optimization of the concentration of DON-BSA-Alexa 430 spiked in the SUA solution. **C-** Time-lapse of the packed beads measured under the fluorescence microscope while flowing the SUA at 17.5 µL/min in the presence or absence of 10 ng/mL of DON. The raw microscopy photos shown were acquired every 15 s using an exposure time of 1 s.

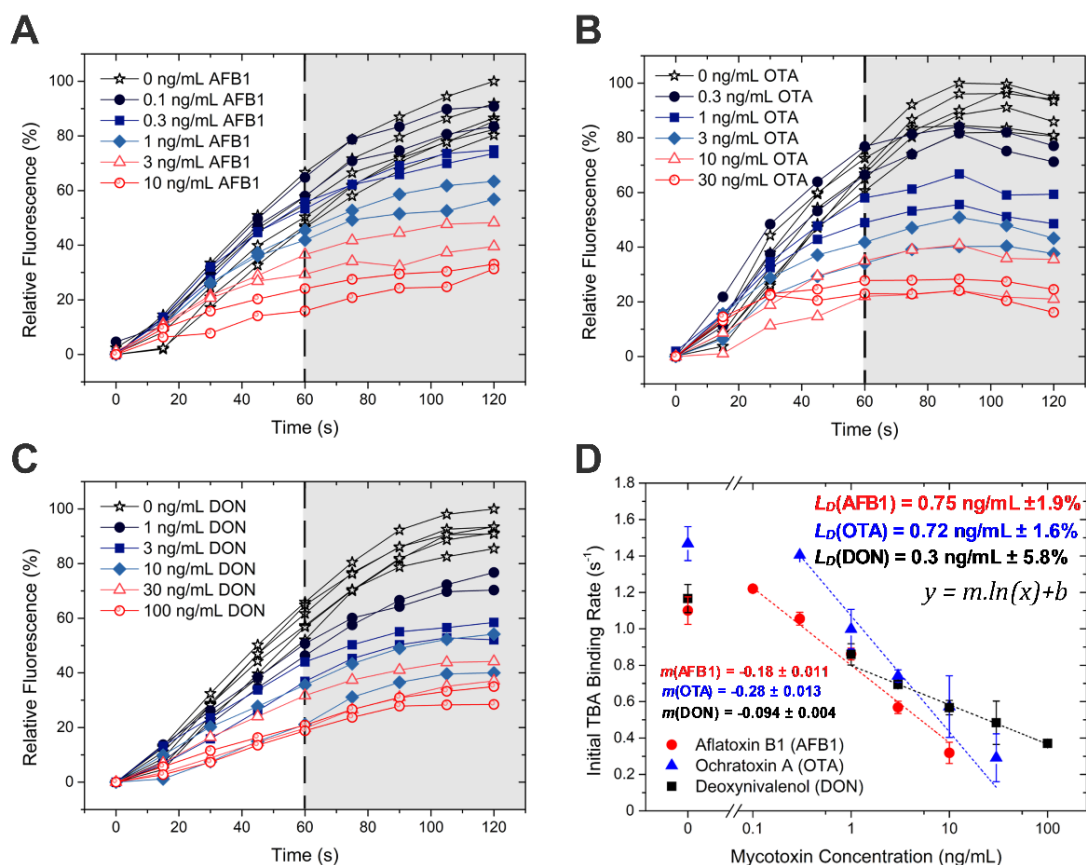


Figure 10.3 - Binding kinetics of each of the TBA conjugates to the respective anti-mycotoxin IgG molecules i.e. (A) AFB1, (B) OTA and (C) DON, immobilized on the beads in the presence or absence of free mycotoxins in solution. The kinetics were measured in reference conditions (0 ng/mL of free toxins) as 6 independent experiments and 2 independent experiments for each of the increasing free toxin concentrations. The relative fluorescence intensity values are calculated relative to the maximum absolute fluorescence measured in the absence of free toxins. The fluorescence intensities were measured under the fluorescence microscope in 15 s intervals. **D**- Calibration curves of increasing free mycotoxin concentrations measured as the initial TBA binding rate in the first 60 s (non-shaded region in plots A, B and C). The TBA binding rate values are calculated as the maximum 3-point linear slope from regressions between 0-30 s, 15-45 s and 30-60 s. These experiments were performed using single microchannels as described in detail in **Chapter 8**.

10.4. Simultaneous detection of AFB1, OTA and DON using the multiplexed device

After optimizing anti-mycotoxin immobilization and TBA concentration for the immunoassay for each mycotoxin, the multiplexed immunoassay using 4 bead chambers in series was tested. It was previously shown that the antibodies used in this assay had negligible cross-reactivity effects for the toxins being tested [42]. The implementation of a standalone and single-step multiplexed assay requires an internal control to normalize the fluorescence signal measured in each anti-mycotoxin chamber. The use of an anti-BSA chamber as internal control provides a fluorescence signal that is independent

of the concentration of free mycotoxins in solution, but dependent on all other assay parameters such as flow rate, matrix interference or any photobleaching effects. Therefore, it allows the normalization of the slope measured on the anti-mycotoxin chambers for comparison between independent experiments.

However, in contrast to the single microfluidic column experiments in **Section 10.3**, the use of an anti-BSA internal control required two additional conditions: (1) the blocking agent used for bead packing and stabilization prior to flowing the SUA cannot be based on a concentrated BSA solution, which would result on the blocking of the specific binding sites of the anti-BSA antibodies and; (2) the fluorescence intensity measured over time in the internal control chamber should be comparable to the anti-mycotoxin chambers (which should also have comparable fluorescence intensities between them). The first condition was achieved using purified casein molecules instead of BSA for the blocking, proving equally effective within the tested experimental conditions in terms of minimizing signal background, which was below the intrinsic fluorescence of the flowing TBA solution in both cases. However, in this case, the packing procedure was performed in a concentrated PEG solution as discussed in **Chapter 8**, prior to the blocking procedure by flowing a casein solution, since the rapid settling times would often induce clogging at the entrance of the microfluidic channels. Regarding the second condition, the signal provided by the anti-BSA control chamber was first tested at increasing anti-BSA concentrations (**Figure 10.4**) while flowing a TBA mixture containing the previously optimized concentrations. Then, by performing reference multiplexed immunoassays, using the previously optimized TBA concentrations in **Section 10.3** for the singleplex assays, (1) the concentrations of each conjugate were adjusted to provide fluorescence signals which are between 70-130% of the signal obtained for the internal reference chamber and (2) the total concentration of BSA-Alexa 430 in the TBA pool was minimized to reduce the fluorescence background from the solution. The optimized concentrations of each conjugate to spike in the SUA were 4 $\mu\text{g/mL}$, 6 $\mu\text{g/mL}$ and 10 $\mu\text{g/mL}$ for AFB1-, DON- and OTA-BSA-Alexa 430, respectively. It is important to highlight that this optimization is specific to a given set of anti-mycotoxin antibodies, which may vary significantly in their intrinsic dissociation constants (K_d) for the respective target mycotoxins. Using the optimized packing, blocking and TBA concentrations, the microscopy image of the bead-packed device and fluorescence microscopy images of a blank and contaminated samples are shown in **Figure 10.5-A**.

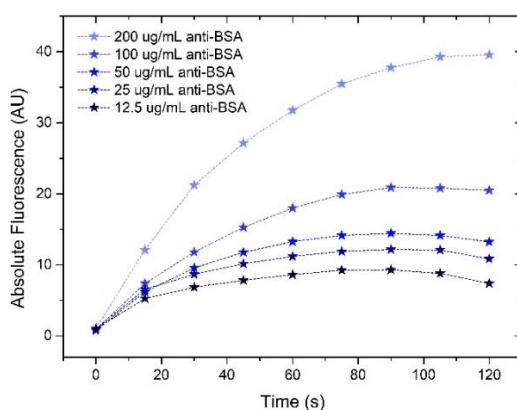


Figure 10.4 - Optimization of anti-BSA concentration used to functionalize the agarose protein-G beads. The curves were measured while flowing a blank SUA (0 ng/mL mycotoxins) containing 8 $\mu\text{g/mL}$ AFB1-BSA-Alexa 430, 8 $\mu\text{g/mL}$ DON-BSA-Alexa 430 and 10 $\mu\text{g/mL}$ OTA-BSA Alexa 430.

After the initial optimization procedure, the results of the multiplexed assay obtained at increasing concentrations of free mycotoxins are shown in **Figure 10.5-B** to **D**. Initial concentrations of 10, 1 and 3 ng/mL for DON, AFB1 and OTA, respectively (**Figure 10.5-C**), were tested since these are simultaneously relevant within the current regulatory limits and provide a significant decrease in TBA binding rate of $49\% \pm 5\%$ ($\pm\sigma$), $71\% \pm 4\%$ ($\pm\sigma$) and $50\% \pm 4\%$ ($\pm\sigma$) for DON, AFB1 and OTA relative to the non-contaminated assay (**Figure 10.5-B**), respectively, which is in accordance with the results shown in **Figure 10.3-D**. It is also possible to observe that an increase in free mycotoxin concentration clearly reduces the TBA binding kinetics relative to the anti-BSA internal control. This decrease is also clearly measurable in the first 60 s of flowing the SUA (left of the vertical dashed line). To normalize the response of the device at each anti-mycotoxin chamber relative to the anti-BSA internal control, the calculated slope of the fluorescence signal (proportional to the initial TBA binding rate) for each anti-mycotoxin chamber was divided by the slope measured for the control chamber in the same time interval. Thus, the maximum value of the slope ratio (i.e. normalized kinetics) measured in the first 60 s is calculated as the assay response, which is inversely proportional to the mycotoxin concentration in solution. **Figure 10.5-E** shows the results for the average normalized kinetics of two independent assays at increasing mycotoxin concentrations. It is possible to observe that at the lowest mycotoxin concentrations tested, the response of the device falls already within the detection capability of the assay (response $< 3.29 \sigma$ of the blank). Furthermore, the response provided in a single step assay using the internal control is not significantly different from the ratio of the initial TBA binding rates obtained using the calibration curves shown in **Figure 10.3-D**, relative to the respective blank assays (0 ng/mL mycotoxin).

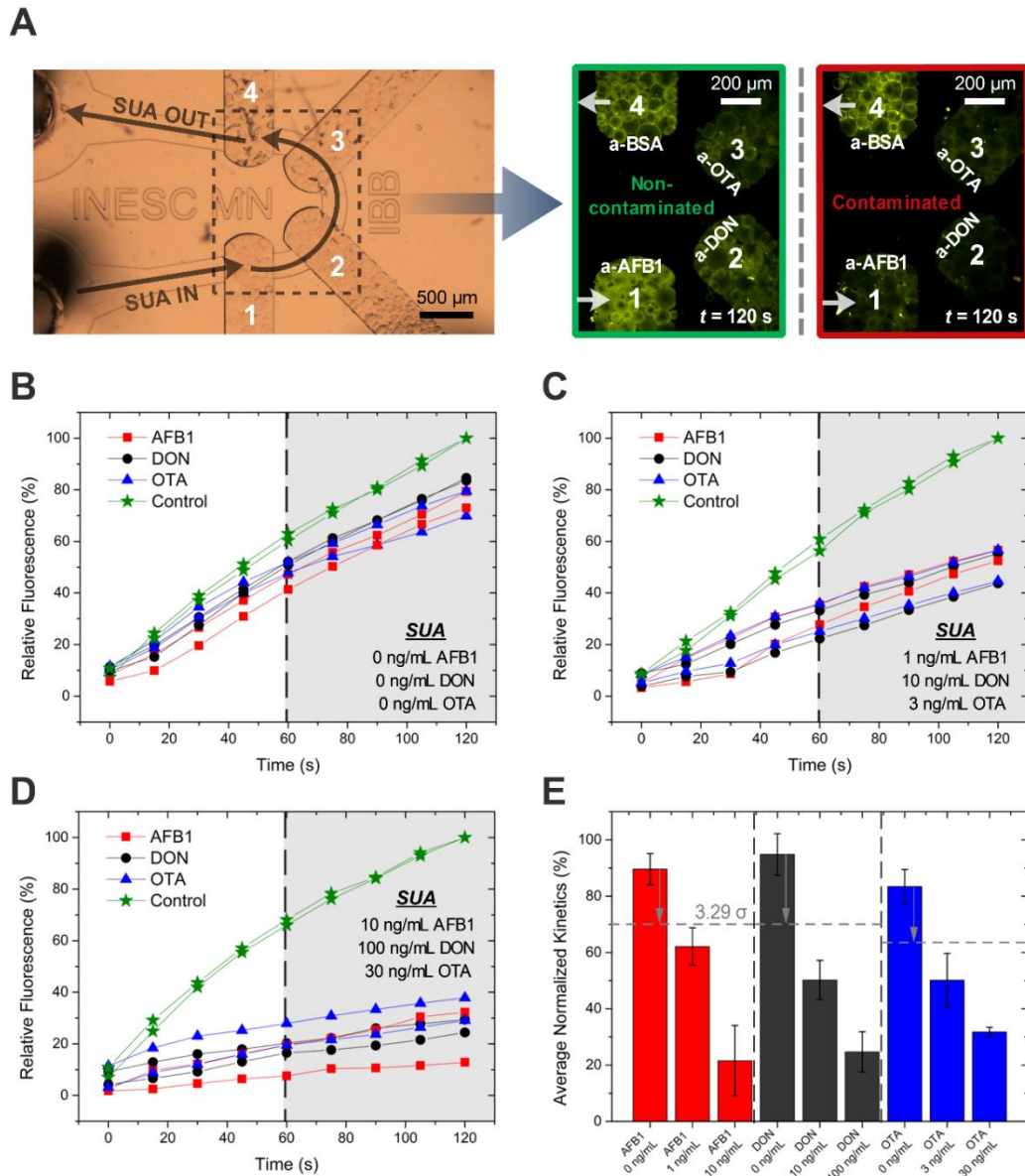


Figure 10.5 - **A**- Bright field microscopy image of the multiplexing device with the anti-mycotoxins and anti-BSA microbeads packed in the respective chambers. On the right, the fluorescence microscopy photos were acquired after flowing either a non-contaminated sample under analysis (SUA) containing only the TBA mixture or the same solution spiked (contaminated) with 1 ng/mL AFB1, 10 ng/mL DON and 3 ng/mL OTA. These images were contrast-enhanced for visualization purposes. **B-D**- Binding kinetics as relative fluorescence over time measured in the chambers for each respective mycotoxin and internal control (anti-BSA) for increasing concentrations of mycotoxins in solution. Each four chambers of each device were measured as two independent experiments for each mycotoxin concentrations. The relative fluorescence values were calculated in relation to the signal of the reference chamber in each device after 120 s. **E**- Average normalized kinetics from two independent experiments for increasing concentrations of each mycotoxin. The values of the normalized kinetics were calculated as the rate of increase in absolute fluorescence for each anti-toxin chamber relative the same rate measured for the respective reference chamber in the first 60 s of the assay. The rates of increase for each chamber were computed as the maximum 3-point linear slope between 0-30 s, 15-45 s and 30-60 s. The horizontal dashed lines represent the device response value equal to 3.29 times the standard deviation (σ) of the blank (0 ng/mL mycotoxin).

10.5. Point-of-need compatible fluorescence signal acquisition with an integrated photodiode array

The integrated fluorescence signal acquisition setup developed to address each of the bead chambers is shown in **Figure 10.6-A**. An array of four $200 \times 200 \mu\text{m}$ a-Si:H photodiodes was designed and fabricated so that each sensor was centered under each respective bead chamber. Prior to further experiments, I - V curves in the dark, photoresponse (I - Φ) and external quantum efficiency (EQE) in the visible spectrum (**Figure 10.7**) of each of the photosensors in the array was measured. To minimize and enhance the reproducibility of the distance between the microfluidic bead chambers and the sensor (i.e. rigid sealing surface providing a constant distance between the chamber and the sensor), the $500 \mu\text{m}$ thick PDMS membrane used to seal the devices when measuring using the fluorescence microscope was replaced by a $100 \mu\text{m}$ thick glass slide. The sealed device was then aligned directly on top of the sensor die.

The acquisition and analog processing of the current generated by the photodiodes, which is linearly proportional to the photon flux, is usually achieved in compact instruments using current-to-voltage converters such as transimpedance amplifier (TIA) circuits. Microscale thin-film photodiodes designed for integrated detection in microfluidic environments, such as the ones shown here, typically generate low currents which require high gain transimpedance amplification. For stability and linearity this amplification was developed in a two-level amplification configuration where most of the current-to-voltage gain is achieved in the first stage, according to the schematics in **Figure 10.6-B**. Therefore, the current of the photodiode was first converted into voltage by a low input bias current (i_{BIAS}) high gain TIA (180 dB) followed by a differential amplifier (40 dB), providing a total gain of 10^{11} V/A (220 dB), i.e. an input current of 1 pA is amplified to a 100 mV voltage at the TIA output. The photocurrents generated by the fluorescence emission impinging on the photodiode array, in the pA range, are quasi-stationary and can, therefore, be represented as DC signals. For that reason and to maximize the signal-to-noise ratio, the photodiodes were operated at zero voltage bias. Moreover, in portable devices a stable virtual ground, provided by a voltage reference circuit with an output of 2.5 V (**Figure 10.6-B**), must be used as reference for all the circuitry as no earth grounding is available. Furthermore, towards improved portability, a Bluetooth transmission module was integrated in the circuit allowing the acquired signals to be wirelessly transmitted in real-time to a personal computing device.

An example of the raw data measured and processed in real time using MATLAB is shown in **Figure 10.8**.

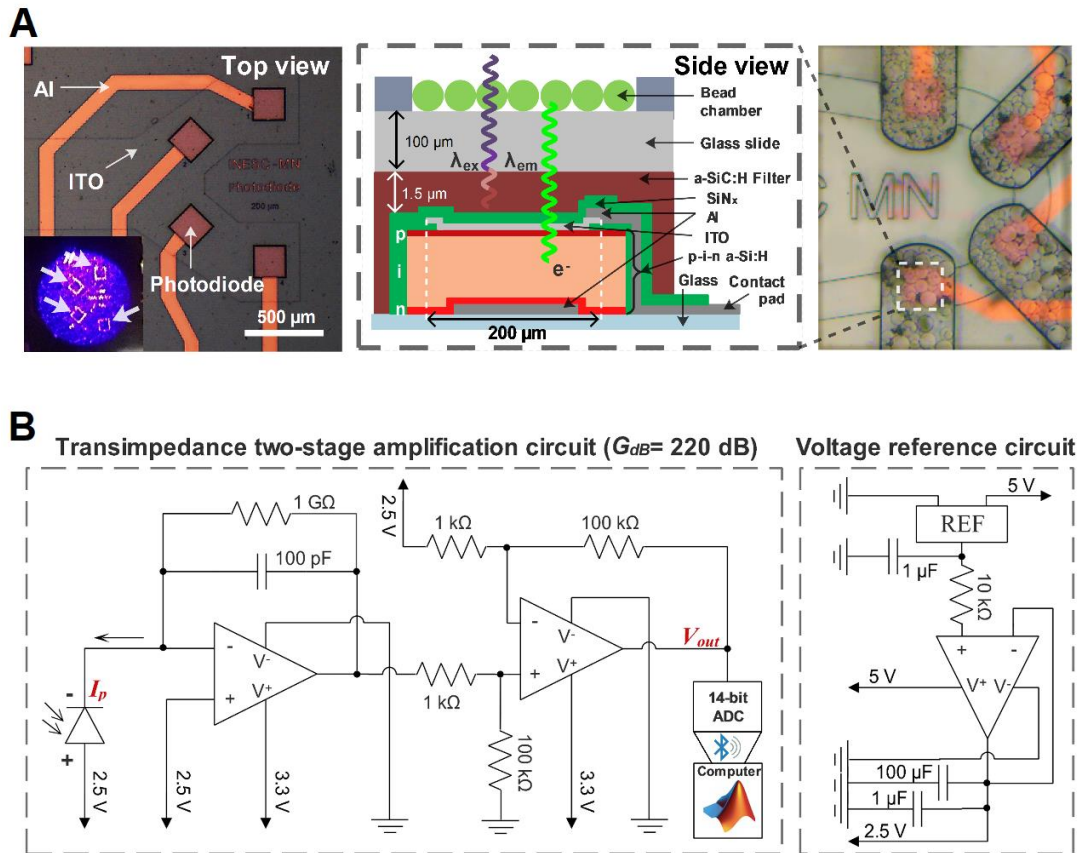


Figure 10.6 - **A**- Schematics of the thin-film a-Si:H photodiode array for performing a continuous fluorescence signal transduction. The inset image on the left shows the laser focal point ($\varnothing \approx 2$ mm) illuminating all 4 photodiodes simultaneously, highlighted by the white arrows. The ITO top contact connects all photodiodes to a common voltage reference (2.5 V). The microscopy photo on the right shows the microfluidic device aligned directly on top of the photodiode array. The side view schematics are not to scale. **B**- Schematics of the transimpedance amplification circuit used to address the current generated by the photodiodes (I_p) at 0 V bias. The voltage output was acquired by a microcontroller board with a 14-bit analog to digital converter (ADC) and the raw signals, transmitted wirelessly via Bluetooth, were acquired and plotted in real time (0.4 s acquisition rate) using a MATLAB program.

The results obtained using the integrated photodiode array and TIA circuit are shown in **Figure 10.9**. The measured photocurrent in each chamber is amplified and converted to a voltage as described above and continuously plotted in the GUI (**Figure 10.8**). After 30 s of measurement, the slope values were continuously calculated as a linear regression of the previous 75 points. These slope values can be used to calculate the response parameter (R), calculated as the ratio of the maximum slope of the respective mycotoxin chamber, divided by the maximum slope of the reference chamber. According to the results of **Sections 10.3 and 10.4** it is expected that R decreases as the concentration of respective mycotoxin increases. Firstly, it was important to evaluate (i) the reproducibility of the internal control measurements; (ii) the possibility of signal cross-

contamination between sensors, i.e. if the signal emitted from one chamber induces a significant increase in current in the sensors aligned with adjacent chambers, and (iii) the minimum signal measured in each chamber arising from non-specific TBA interactions. These points were evaluated by a measurement where all 4 chambers contain anti-BSA IgG, i.e. the internal control (**Figure 10.9-A**) and a measurement where only a single chamber contains immobilized anti-BSA antibodies, while the others contain the protein A conjugated agarose beads alone (**Figure 10.9-B**). From these two measurements it was possible to conclude that (i) the measurements of multiple ($n = 4$) reference chambers are reproducible, providing maximum slopes having a coefficient of variation (CV) of 16%; (ii) it was observed that there is no significant cross-contamination of fluorescence signal to the nearest sensor, considering that in **Figure 10.9-B** sensors 2 (closest) and 4 (furthest) did not provide significantly different slopes ($1.07 \pm 0.09 \text{ mV}\cdot\text{s}^{-1}$ and $0.90 \pm 0.09 \text{ mV}\cdot\text{s}^{-1}$, respectively); and (iii) considering the existence of a residual non-specific signal in the

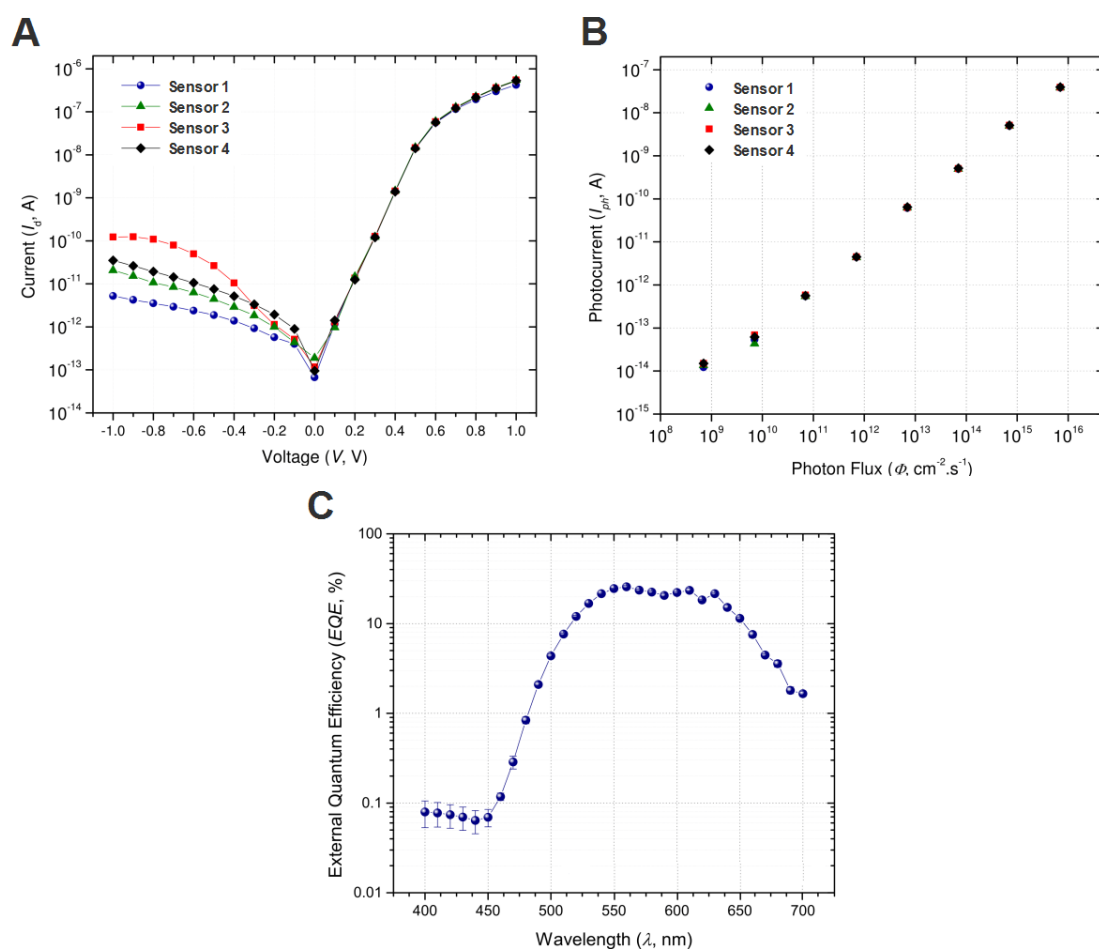


Figure 10.7 - Photosensor characterization plots for each sensor in the array. The photosensors 1 to 4 correspond to those used to measure the anti-AFB1, anti-OTA, anti-DON and anti-BSA chambers, respectively. **A**- I - V curves measured in dark conditions; **B**- Photoresponse (I - Φ) at 540 nm and; **C**- Average external quantum efficiency measured for the 4 sensors (\pm SD).

absence of specific antibodies bound to the protein A beads, it is expected that the minimum R does not fall below $25 \pm 7\%$ for the optimized TBA concentrations.

After the previous analysis, the device and signal transduction platform were tested for the detection of relevant concentrations of mycotoxins, namely 1, 3 and 10 ng/mL of AFB1, OTA and DON, respectively. The results of the measurement of non-contaminated and contaminated samples, i.e. PBS buffer artificially spiked with mycotoxins, are shown in **Figure 10.9-C** and D. The results agree with the previous measurements using a fluorescence microscope (**Section 10.4**), showing that a decrease in TBA capture rate in the presence of free mycotoxins could be detected in less than 1 min total assay time using the integrated photodiodes. The R values measured for the contaminated sample were below the L_D for all mycotoxins, considering a threshold of 3.29σ relative to the measurements performed with a non-contaminated sample.

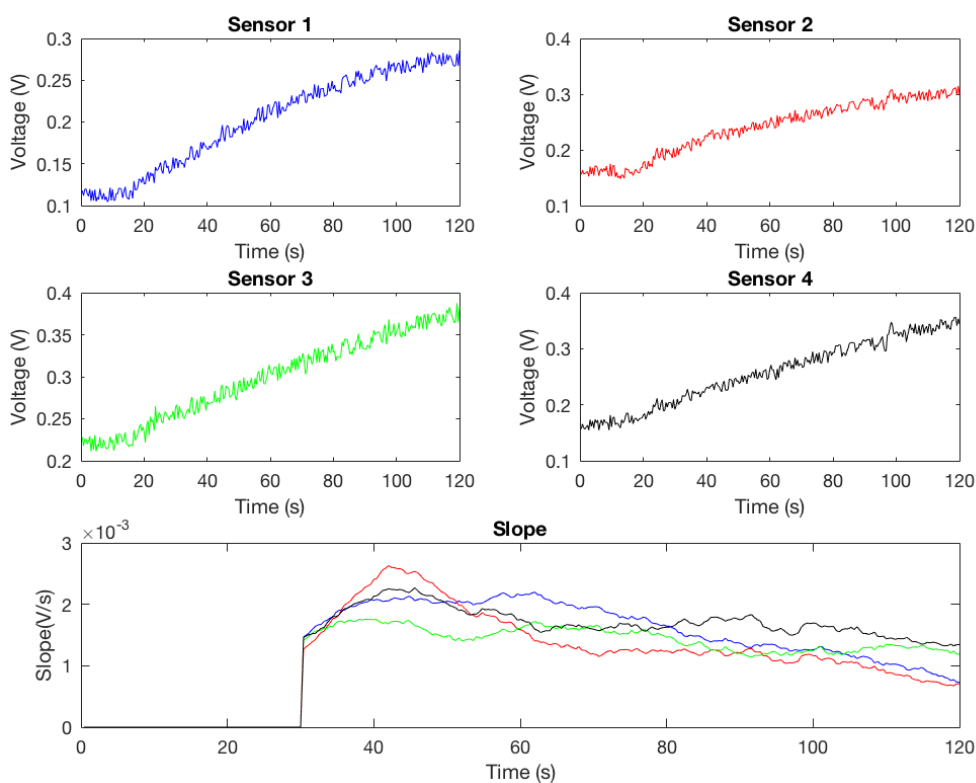


Figure 10.8 - Example of the raw voltage measurements acquired in real-time (2.5 points per second) for each photosensor and respective 30 s linear slopes, plotted after the first 30 s. The figure corresponds to a screenshot of the data as acquired and processed using the MATLAB program. The results in the figure were acquired by flowing a non-contaminated sample (syringe pump turned-on at $t = 10$ s) in a device with anti-BSA antibodies immobilized in all chambers (same assay as plotted in **Figure 10.9-A**).

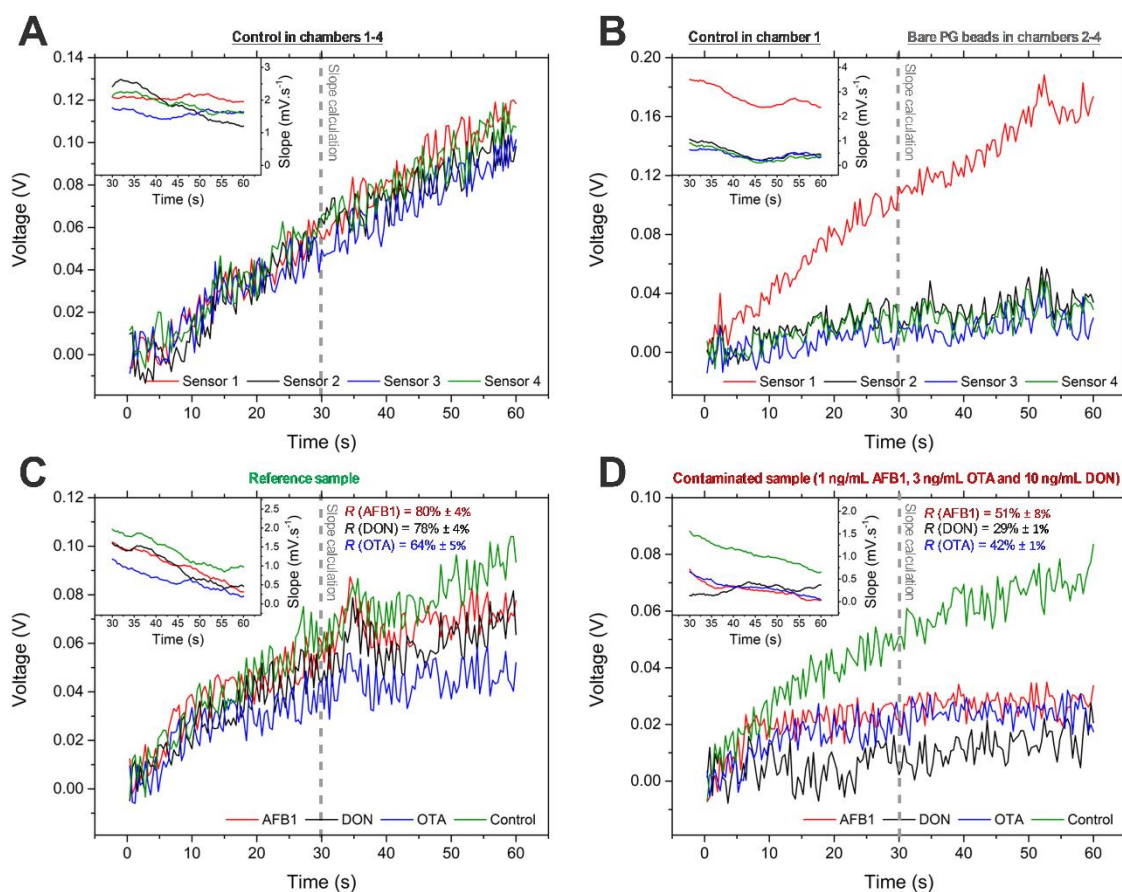


Figure 10.9 - **A**- Validation of the device performance in terms of photoresponse uniformity and assay reproducibility. The 4 bead chambers were prepared under the same conditions, all having anti-BSA IgG immobilized on protein G. **B**- Assessment of cross-signal contamination between photodiodes in the same array and signal from non-specific adsorption. Only the chamber 1, aligned with sensor 1 had anti-BSA immobilized on protein G, while chambers 2-4, aligned with the respective sensors 2-4 contained beads with protein G only. **C**- Measurement of a reference sample without spiked mycotoxins. **D**- Measurement of a contaminated sample spiked with 1 ng/mL AFB1, 3 ng/mL OTA and 10 ng/mL DON. For the measurements shown in **C** and **D**, sensors 1-4 were aligned with the anti-AFB1, anti-DON, anti-OTA and anti-BSA (control) chambers respectively. All plotted voltage values are the raw data acquired in real time (2.5 Hz acquisition rate) and normalized to the respective background voltage induced by the excitation light, typically ranging between 0.1-0.2 V. The slope measurements were calculated also in real-time after the first 30 s, corresponding to the slope of the linear regression of the previous 75 data points (30 s). The inset R values (\pm SD, $n = 2$) for each mycotoxin were calculated as the percent ratio of the maximum slope of the respective mycotoxin chamber, divided by the slope of the reference chamber.

10.6. Multiplexed detection of mycotoxins in corn extracts as a model food matrix

To establish a proof-of-concept regarding the compatibility of the developed device with the analysis of mycotoxins in complex matrices as is the case of food and feed samples, the multiplexed detection of AFB1, OTA and DON was applied to corn samples as a model complex matrix. The PEG-citrate salt-based extraction system

optimized in **Chapter 4** was used to perform the off-chip extraction of the mycotoxins from artificially spiked corn samples, at concentrations of 20 ng/g AFB1, 50 ng/g OTA and 500 ng/g DON. These values are within relevant target regulatory and recommended concentration ranges for mycotoxins in animal feeds (**Table 1.3** and **Table 1.4**). In this case, to perform the immunoassay, 4 μ L of the top PEG-rich phase were collected and mixed with 36 μ L of TBA conjugate solution in PBS to the final concentrations described in **Section 10.1.3**. The results obtained for the analysis of a reference (non-contaminated) and contaminated corn extracts are shown in **Figure 10.10**. Unlike the measurements performed in buffer solutions, both the control and anti-mycotoxin chambers were observed to provide comparable binding kinetics during the first 50 s of the assay for the reference and contaminated samples. However, after this time, the binding kinetics of the contaminated sample showed a significant deviation from the control. This can be clearly observed in **Figure 10.10-A** and **B** by comparing the slope values measured over time normalized to the internal control, which are significantly lower for the contaminated sample in the shaded region. Therefore, despite the 20 s delay in the total assay time, by calculating the response parameter R between 60 and 80 s, the obtained results for the reference sample are comparable to those reported in **Figure 10.9-C** for the analysis performed in PBS buffer. Furthermore, the R values of the contaminated sample, computed in the same time interval, were below the L_D (3.29σ threshold) for all mycotoxins at the tested concentrations. These results demonstrate the feasibility of using the developed integrated device to detect mycotoxins in complex food matrices after coupling an appropriate extraction methodology tailored to the target matrix.

The observed measurement of two different kinetic profiles when testing the corn samples was further explored using fluorescence microscopy. Interestingly, it could be observed that using the mercury lamp of the microscope as excitation source, a significant non-specific signal could be measured when flowing a reference corn-extract through protein G conjugated beads (without mycotoxin specific antibodies), which was comparable with the signal obtained in the presence of mycotoxin specific antibodies (**Figure 10.11**). This observation implies that intrinsically fluorescent organic contaminants in corn, as is the case of polyphenols, are contributing to the overall fluorescence emission by non-specific adsorption to the beads. On the other hand, using the 405 nm laser as excitation source, a two-fold increase in specific signal was obtained (**Figure 10.11**). Thus, exciting the fluorophore using the narrow wavelength of the laser, closer to the absorption maximum of Alexa 430, provided superior selectivity compared

to a broad excitation band ranging between 450 and 490 nm of the fluorescence microscope. Overall, these observations highlight the importance of tailoring appropriate fluorophores and excitation sources to a specific target SUA, to minimize non-specific signal background.

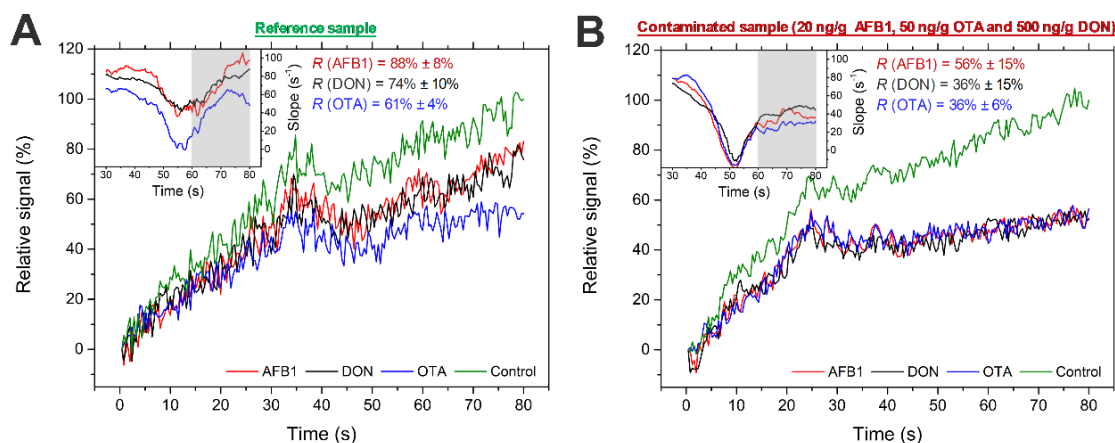


Figure 10.10 - Multiplexed detection of mycotoxins spiked in corn. **A**- Reference corn sample without mycotoxins ($\ll 1$ ng/g). **B**- Corn sample spiked with 20 ng/g AFB1, 50 ng/g OTA and 500 ng/g DON. The plotted relative signal values are the raw voltage data acquired in real time, relative to the highest voltage signal measured for the control chamber during 80 s of measurement (2.5 Hz acquisition rate), calculated after normalization to the respective background voltage induced by the excitation light. The slope measurements at each time point (relative slope) were calculated as the ratio of the slope of the linear regression of the previous 75 data points (30 s) for a specific mycotoxin chamber, relative to the slope calculated for the control chamber. The inset R values (\pm SD, $n = 2$, two independent measurements of the same corn extract) for each mycotoxin were calculated as the percent ratio of the maximum slope ($V \cdot s^{-1}$) of the respective mycotoxin chamber, divided by the slope ($V \cdot s^{-1}$) of the reference chamber, between 60 and 80 s assay time (shaded area in inset plots).

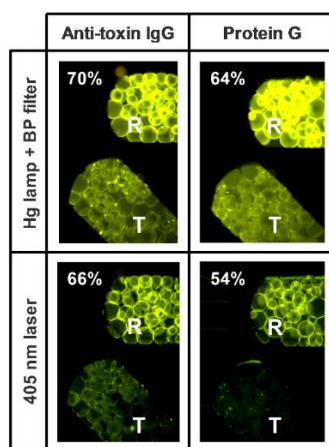


Figure 10.11 - Fluorescence microscopy photos of the reference (R) and test (T) chambers of the multiplexing device, after flowing a non-contaminated corn extract spiked with the optimized TBA mixture. The device was imaged having either anti-DON immobilized on the test chamber (left) or plain protein G beads (right). The light excitation source used to measure the fluorescence emission was either the 100 W Hg vapor lamp of the Leica DMLM microscope coupled with a blue excitation filter (450-490 nm band pass, model I3) or the 405 nm laser. The percentage values were calculated as the fluorescence signal of the T chamber relative to the R chamber in each case. All images were contrast enhanced for visualization purposes.

10.7. Chapter conclusions

The development of a simple and ultrafast bead-based microfluidic competitive immunoassay for mycotoxin screening was discussed. This system offers a multiplexed operation and point-of-need fluorescence signal transduction. By performing the analysis in PBS buffer solutions, minimum detectable limits below 1 ng/mL were achieved for AFB1, OTA and DON in less than 60 s total assay time using a fluorescence microscope for continuous signal acquisition. This time of analysis is among the fastest reported in recent literature for immunosensors and aptasensors (**Table 1.6**), requiring only a single step after adding the mycotoxin conjugate to the sample. After extending the assay to a multiplexed setup and integrating an appropriate internal reference, a comparable performance was achieved, allowing the sub-minute simultaneous detection of 1 ng/mL AFB1, 3 ng/mL OTA and 10 ng/mL DON, thus showing promise to achieve the strictest regulatory limits currently enforced in European Union. A comparable performance could be achieved with a system integrating an array of a-Si:H photodiodes aligned $\sim 100\ \mu\text{m}$ below each of the mycotoxin-specific bead chambers and addressing the photosensors with a simple transimpedance amplification circuit coupled with a microcontroller board, successfully extending the assay for point-of-need applications. Finally, the application of the developed device to a multiplexed analysis of mycotoxins spiked in corn was demonstrated, highlighting the need for adequate extraction procedures and selection of fluorophores to minimize matrix interference. Both considerations are critical to allow the extension of the assay to other food and feed matrices.

Furthermore, since the developed device provides a versatile operation and rapid detection times, other highly relevant fields relying significantly on immunoassays could greatly benefit from such features for point-of-care applications, such as the screening of environmental contaminants or monitoring disease biomarkers.

Chapter 11

Conclusions and Outlook

This chapter provides a global overview of the achievements reported in this thesis focusing on (1) improvements to the state-of-the-art on rapid mycotoxin screening and main novelty factors contributed to the current literature, (2) proposing further research directions towards the commercial implementation of a fully portable and sample-to-answer analytical device and (3) the extension of the analytical methodology to the pre-emptive detection of mycotoxigenic fungi in foods and feeds.

11.1. Novelty and main improvements to the state-of-the-art

Considering the highly interdisciplinary challenge of optimizing a fully integrated and portable microfluidic biosensor for mycotoxin detection, the work developed in this thesis focused on developing discrete modules of the device. In general, these modules comprised (1) sample preparation and pre-concentration for liquid and solid samples, (2) miniaturized multiplexed immunoassay, (3) integrated thin-film photosensors to transduce the optical signal into an electrical signal and (4) coupling appropriate miniaturized electronics to address the photodetectors.

11.1.1. Module 1 - sample preparation and pre-concentration

Regarding the development of the first module, the main breakthroughs were the (1) novel application of aqueous two-phase extraction to perform a simultaneous extraction, matrix neutralization and analyte preconcentration coupled to immunoassays and (2) the first report of a liquid-liquid separation process integrated in-line with an immunoassay in a single microfluidic device. In both configurations, minimum detection limits as low as those achieved in plain buffer conditions were achieved for wine samples. On the other hand, the method also proved compatible with dramatically different solid matrices without a significant signal suppression or enhancement. These developments highlight the potential of aqueous two-phase separation to serve as a general single-step sample preparation procedure within and beyond the scope of mycotoxin immunodetection. A relevant example of applications beyond the scope of mycotoxin

detection lies within the biomedical field, considering that ATPE has already been explored for the isolation of several biomolecules such as oligonucleotides and immunoglobulins, as discussed in **Section 1.4.2**. These, differently from food safety applications, where most relevant samples are in a solid state, would also benefit greatly from an integrated microfluidic sample preparation, since target samples are typically raw blood, plasma or serum. Considering the emerging body of research focusing on alternative two-phase forming components beyond standard polymer-polymer and polymer-salt systems, combined with the development of high-throughput screening and robotic tools to optimize ATPE [201, 202, 337], it is thus expected that upon an appropriate optimization, this approach may serve as a new and potentially disruptive tool within the context of sample preparation.

11.1.2. Module 2 - miniaturized multiplexed immunoassay

Regarding the second module, the immunoassay developed in collaboration with Lumisense Lda. within the scope of the EU project DEMOTOX (FP7-SME-2013-604752), achieved detection times of 5 min and comprising three detection steps, being among the fastest and simplest mycotoxin immunoassays. This immunoassay was further combined with a fully integrated prototype biosensor to provide a response in approximately 10 min after six manual steps performed by the user (three steps for the reference and SUA tested in sequence). The same immunoassay architecture was further multiplexed to detect three different mycotoxins, while simultaneously integrating an internal control to provide a semi-quantitative response in a single analysis. This multiplexing procedure was performed using either (1) an innovative micromosaic-based immunoassay using permanent magnet valves to actuate the liquid flow, allowing the simultaneous imaging of at least nine discrete immunoassay reactions or (2) an autonomous capillary-driven flow device comprising four individual chambers in series with the liquid flow. In both cases, the minimum detection limits achieved were compatible with those currently enforced by EU regulations for most foods and feeds. All these developments in miniaturized sensing strategies contributed significantly to the simplification, speed of analysis and throughput using competitive immunoassays in general. The integrated biosensor prototype co-developed with Lumisense Lda. and the autonomous capillary-driven device combined with a smartphone-based signal acquisition already demonstrated possible routes towards commercial microfluidic-based immunosensors, upon appropriate optimization of (1) reagent stability, (2) surface

stability, (3) cost-effectiveness of materials and (4) analytical performance according to appropriate ISO guidelines.

Despite the relative success and relevance of the previous assays compared to the state-of-the-art, there is an increasing demand by food producers to further decrease detection times and assay simplicity, allowing a rapid screening of raw materials with minimal operating time and user intervention. These requirements were not achievable using the immunoassay architecture employed in **Chapters 3 to 7**. Thus, such demand motivated the further improvement of the microfluidic immunoassay by integrating nanoporous beads, allowing the development of sub-minute and single-step multiplexed immunoassays, among the fastest and simplest reported in the literature. This degree of assay simplicity, short detection times, scalable design to n target mycotoxins, coupled to a small footprint, paves the way for a direct competition with currently standard lateral-flow assays and state-of-the-art microfluidic immunoassays. Furthermore, this technical innovation described here for mycotoxin detection (**Chapters 9 and 10**), has been also demonstrating significant promise in the development of highly sensitive and rapid assays to detect DNA and protein biomarkers within the biomedical arena [18, 327].

11.1.3. Module 3 – integrated photosensing

Regarding the third module, several photodetection setups and designs were used to acquire chemiluminescent or fluorescent signals generated by each of the developed microfluidic immunoassays. These included the integration of mm-scale commercial c-Si $p-n$ photodiodes and arrays of in-house fabricated $p-i-n$ a-Si:H photoconductors and photodiodes with dimensions ranging from 50 to 200 μm . The latter proved highly promising for miniaturization, providing an excellent optical coupling with the microchannels by direct alignment of the sealed device on top of the photosensor array. These a-Si:H based thin-film sensors have been previously combined with several model analytical and biological systems at INESC MN [34, 338-342]. However, their integration in analytical devices aiming at achieving strict regulatory concentrations in the short amount of time demanded for mycotoxin detection was the main novelty factor. Comparing all setups explored in this thesis, the integration of photodiodes for fluorescence detection can be highlighted since they allow a continuous signal monitoring without the need of flowing secondary reagents after the SUA for signal development, as is the case of enzymatic substrates. On the other hand, the requirement for fluorophores

with an adequate Stokes shift and an excitation light source may limit its range of applications.

Alternatively, an approach based on detecting colorimetric signals using a smartphone camera was also addressed, coupled with the capillary-driven device. This approach, particularly when coupled with an autonomous liquid flow mechanism and on-chip stored reagents to minimize handling complexity, can be particularly promising to reduce the cost of analysis, which is particularly relevant for mycotoxin screening applications.

11.1.4. Module 4 – miniaturized electronics to address the sensors

Finally, regarding the fourth module, the ultimate goal was to develop cost effective and portable electronics coupled to a personal computing device to address the photodetectors. This objective was accomplished in collaboration with Lumisense Lda. (as reported in **Chapter 5** using a commercial photosensor) during the development of the fully integrated prototype and also in collaboration with PhD student Denis Santos at INESC MN for the integrated array of photodiodes (as reported in **Chapter 10**).

11.2. Future research towards a fully integrated and portable mycotoxin screening device

This section discusses future research directions to achieve the full integration of the developed modules towards a sample-to-answer device to rapidly screen mycotoxin contamination on the field.

To develop a portable analytical device to screen mycotoxins directly on the field, it is important to consider that most target samples are in a solid state and that the mycotoxin contamination is not homogeneously distributed in the bulk of sample. As such, integrated microfluidic processing and pre-concentration strategies as those developed in **Chapter 3** are only compatible with a shortlisted number of sample groups, as is the case of alcoholic beverages and fruit juices. Therefore, any screening device aiming at rapidly quantifying mycotoxins on multiple small solid samples, also requires an integrated means of collecting a certain mass of sample, performing a grinding procedure and efficiently dose the grinded sample for subsequent mixture with the extraction solution. This extra module (henceforth referred as “module zero”) is thus required upstream of the sample extraction and preparation. Such developments were not

addressed in this thesis, since they fall outside the academic research scope within the topic of biotechnology and biosciences. Nevertheless, having the appropriate collaborations with mechanical engineering experts or industrial partners, such developments are critical to conceive a fully functional prototype.

Regarding the remaining modules one to four, it became clear that the ATPS-based strategy was highly promising to combine mycotoxin extraction, matrix neutralization and pre-concentration, despite being currently the limiting step in terms of assay speed (~ 20 min), which is common to all state-of-the-art sample preparation methods. On the other hand, the analytical assay based on multiple bead-chambers in series, as discussed in **Chapter 10**, provides the simplest and fastest means of quantitatively detecting multiple mycotoxins simultaneously. Therefore, based on the results obtained in this thesis, the best performing integrated device would comprise the abovementioned “module zero” proceeded by the following modules: (1) ATPS-based extraction integrated with a μL -mL scale mixer and/or grinder plus miniaturized centrifugation (e.g. lab-on-disk based) and micromixing, to efficiently isolate the mycotoxin-rich phase and add the immunoassay reactants; (2) Direct the isolated and diluted PEG-rich phase into a microbead-based device to perform the fluorescence-based competitive immunoassay (via capillary-, pressure- or centrifugation-driven flow), (3) Acquire the fluorescence signal in real-time using miniaturized photodetectors aligned beneath the packed beads (a laser or LED can be used as excitation light sources) and (4) address the sensors with a simple transimpedance amplification circuit coupled to a microcontroller board with wireless signal transmission capabilities. From an industrial and commercial perspective, it is important to highlight that while each of the separate modules was previously shown to potentially meet the detection performance with minimal risk of failure, the full integration of all modules is a high-risk challenge that would still require at least 2-3 years of dedicated research and development. Therefore, a second round of an EU funded project as was the case of DEMOTOX (FP7-SME-2013-604752) from 2013 to 2015, would be a potentially fruitful opportunity to gather industrial partners and funding to further translate the acquired knowledge in the past 3 years into an improved prototype and towards a commercial device.

11.3. Extension of the analytical device for the pre-emptive detection of mycotoxigenic fungi in foods and feeds

An emerging complementary approach to the direct screening of mycotoxins at the point-of-need is the pre-emptive detection of mycotoxigenic fungi infecting crops on the field [343]. This would allow the mitigation of losses due to misclassification of samples contaminated with mycotoxigenic fungi as safe, by inadvertently disregarding the potential for mycotoxin production during transport and storage. Examples of mycotoxigenic fungi commonly found in foods are the AFB1 producers *Aspergillus flavus* and *A. parasiticus*; the OTA producers *A. carbonarius*, *A. ochraceus*, *A. niger* and *Penicillium verrucosum* and; the DON producer *Fusarium graminearum* [343]. In this context, there are several barriers to overcome in order to develop a point-on-need device to screen mycotoxigenic fungi as is subsequently discussed.

11.3.1. Standard procedures to identify fungal contaminations

To identify the presence of mycotoxigenic fungi in a sample based on their taxonomy, there are in general two major approaches which are based either on (1) morphology of the colony using suitable growth media (e.g. color, size, texture and tridimensional features) and microscopic features of the organism (e.g. shape of conidia, conidiophore or spores, presence of metulae and phialides, cell size and branching of hyphae), or (2) molecular methods based on detecting the presence of specific gene sequences or profiling the transcriptome [343, 344]. On the other hand, having mycotoxigenic fungi as target microorganisms in the context of food safety, the second approach may not be focused on the characterization of the fungus taxonomy but instead on the presence of genes involved in mycotoxin synthesis [344]. Nevertheless, it is clear that to develop a point-of-need screening tool, the approach based on fungal inoculation is unsuitable, considering its labor-intensive and time-consuming operation, environment dependency, unfeasible standardization and significant expertise required to perform an adequate visual inspection and identification based on morphology alone [344].

Focusing on DNA-based molecular methods, there are several major challenges that must be overcome to adequately predict the mycotoxin contamination potential of a given sample. In brief, these are (1) the misidentification of the fungal species using single gene sequences alone (e.g. structural conserved genes), since closely related species within the same genera may produce a different array of mycotoxins or no mycotoxins at

all; (2) the fungi being correctly identified but having the mycotoxin biosynthesis genes silenced due to epigenetic factors and thus not producing mycotoxins and; (3) the number of quantified sequences not being correlated directly to the number of spores/conidia due to each having a variable number of nuclei and some genes (i.e. mitochondrial) having multiple number of copies in each cell [344, 345]. These challenges have been approached by several research groups as will be subsequently discussed.

11.3.2. Strategies to identify mycotoxigenic fungi in food and feed samples

To find fit-for-purpose gene sequences to unambiguously identify the genus and species of a particular fungi, there has been a focus on (1) the ribosomal gene family (i.e. 18S, 5.8S, 28S, ITS1, ITS2 and intergenic spacer), allowing also a higher sensitivity considering their multi-copy feature; (2) the calmodulin coding gene; (3) the α and β -tubulin coding genes and; (4) genes coding for elongation factors such as TEF1- α or TEF2 [344]. In particular, for the *Fusarium* genus, the internal transcribed spacer (ITS) region does not allow a full taxonomic discrimination, allowing discrimination between similar species while the TEF1- α gene seems to be the most discriminating gene available [344]. On the other hand, for *Aspergillus* fungi, the ITS region was used successfully to discriminate mycotoxigenic species present in soil samples with high sensitivity [346]. Several authors have also successfully targeted key genes (among at least 25 structural genes) from the aflatoxin biosynthesis pathway to discriminate mycotoxigenic fungi in artificially inoculated grains [344]. In the same context, Yang and co-workers reported the use of multiplexed PCR to detect three aflatoxin biosynthesis genes and ITS as an internal control [347], where two important conclusions were achieved namely: (1) some non-mycotoxigenic fungi lacked only some of the three tested genes, highlighting the importance of multiplexing for a correct identification and (2) non-aflatoxigenic *A. flavus* fungi were found, meaning that analysis based on taxonomy alone is clearly insufficient. Furthermore, as reported by Degola and co-workers [348], within the same *A. flavus* species containing the same aflatoxin biosynthesis genetic profile differed significantly in the speed of synthesis, which may result in under or over-estimations of aflatoxin contamination risk under environmental conditions. The same approach based on mycotoxin biosynthesis genes have also been successfully applied for DON and OTA producers [344], despite the biosynthetic pathway of OTA still not being clearly elucidated [344]. Based on the previous discussion, it becomes clear that the multiplexing of multiple gene sequences is critical for an unambiguous evaluation of the

mycotoxigenic potential. As examples, Godet and Munaut reported a multi-step strategy focusing simultaneously on aflatoxigenic genes, ITS genes and digestion protocols in order to identify specific *A. flavus* strains [349]. On the other hand, the multiplexing protocols can be instead directed to obtaining information only about the mycotoxin-risk instead of the exact species [344]. Alternatively, specifically designed protocols have been used to discriminate the presence of the most important mycotoxigenic species within the genera *Aspergillus*, *Fusarium* and *Penicillium* in agricultural commodities, using a single set of primers and 4 different Taqman probes [350]. More recently, Sadhasivam and co-workers used several primers to develop a rapid protocol for identification of multiple mycotoxigenic fungi in wheat grains, combined with subsequent mycotoxin profiling to validate a correlation between the presence of mycotoxigenic fungi and mycotoxin contamination [351].

11.3.3. Research directions to integrate a mycotoxigenic fungi identification module in a portable analytical device

Considering that the key target molecule for fungal identification is the genomic DNA, the miniaturized analytical platform should contain a (1) DNA extraction module, (2) a DNA amplification module and (3) a DNA detection module. The DNA extraction module should be optimized to ideally comprise only the mixing of a lysis solution with the sample potentially containing the target fungus, followed by sedimentation or centrifugation if required. On the other hand, the amplification module should ideally be based on an isothermal DNA amplification technique such as nucleic acid sequence-based amplification (NASBA), strand displacement amplification (SDA), loop-mediated isothermal amplification (LAMP) and rolling circle amplification (RCA). These procedures contrast with standard polymerase chain reaction PCR which, although highly efficient at amplifying specific and individual genes, has the practical inconvenience of requiring precise and successive heating and cooling cycles, significantly increasing the cost and complexity of integrated devices. Finally, regarding the DNA detection module, it is expected that a DNA hybridization technology resorting to bead-based microfluidics [18] can easily and effectively be integrated with a significant part of the multiplexing [49] and photosensor integration technologies [327] discussed in this thesis. Overall, the development of an integrated and portable device to monitor the contamination of foods and feeds with mycotoxigenic fungi would be extremely challenging, particularly considering the cost effectiveness and assay speed required for this type of application.

On the other hand, such application has not only a significant disruptive potential in the food safety landscape, but miniaturized DNA detection technologies in general have also a rapidly growing relevance and demand for critical biomedical applications as is the case of disease diagnostics and monitoring of antibiotic resistant bacterial strains. Therefore, this broad range of relevant applications relying on the same fundamental detection principles, contributes greatly to the mitigation of the risk involved in this project.

Bibliography

- [1] R.R.G. Soares, A. Ricelli, C. Fanelli, D. Caputo, G. de Cesare, V. Chu, et al., Advances, challenges and opportunities for point-of-need screening of mycotoxins in foods and feeds, *Analyst*, 143(2018) 1015-35.
- [2] R.R.G. Soares, D.F.C. Silva, P. Fernandes, A.M. Azevedo, V. Chu, J.P. Conde, et al., Miniaturization of aqueous two-phase extraction for biological applications: From microtubes to microchannels, *Biotechnol J*, 11(2016) 1498-512.
- [3] G.M. Whitesides, The origins and the future of microfluidics, *Nature*, 442(2006) 368-73.
- [4] Y. Xia, G.M. Whitesides, Soft Lithography, *Angew Chem Int Ed*, 37(1998) 550-75.
- [5] C.-C. Lee, G. Sui, A. Elizarov, C.J. Shu, Y.-S. Shin, A.N. Dooley, et al., Multistep Synthesis of a Radiolabeled Imaging Probe Using Integrated Microfluidics, *Science*, 310(2005) 1793-6.
- [6] B. Kuswandi, Nuriman, J. Huskens, W. Verboom, Optical sensing systems for microfluidic devices: A review, *Anal Chim Acta*, 601(2007) 141-55.
- [7] A.A. K., H. Wilson, H.L. F., F. Albert, 3D-Printed Microfluidics, *Angew Chem Int Ed*, 55(2016) 3862-81.
- [8] D.J. Guckenberger, T.E. de Groot, A.M.D. Wan, D.J. Beebe, E.W.K. Young, Micromilling: a method for ultra-rapid prototyping of plastic microfluidic devices, *Lab Chip*, 15(2015) 2364-78.
- [9] T.M. Squires, R.J. Messinger, S.R. Manalis, Making it stick: convection, reaction and diffusion in surface-based biosensors, *Nat Biotechnol*, 26(2008) 417-26.
- [10] M. Zimmermann, E. Delamarche, M. Wolf, P. Hunziker, Modeling and Optimization of High-Sensitivity, Low-Volume Microfluidic-Based Surface Immunoassays, *Biomed Microdevices*, 7(2005) 99-110.
- [11] H. Parsa, C.D. Chin, P. Mongkolwisetwara, B.W. Lee, J.J. Wang, S.K. Sia, Effect of volume- and time-based constraints on capture of analytes in microfluidic heterogeneous immunoassays, *Lab Chip*, 8(2008) 2062-70.
- [12] N. Madaboosi, R.R.G. Soares, V. Chu, J.P. Conde, A microfluidic immunoassay platform for the detection of free prostate specific antigen: a systematic and quantitative approach, *Analyst*, 140(2015) 4423-33.
- [13] M. Ren, H. Xu, X. Huang, M. Kuang, Y. Xiong, H. Xu, et al., Immunochromatographic assay for ultrasensitive detection of aflatoxin B(1) in maize by highly luminescent quantum dot beads, *ACS Appl Mater Interfaces*, 6(2014) 14215-22.
- [14] B.V. Chikkaveeraiah, V. Mani, V. Patel, J.S. Gutkind, J.F. Rusling, Microfluidic electrochemical immunoarray for ultrasensitive detection of two cancer biomarker proteins in serum, *Biosens Bioelectron*, 26(2011) 4477-83.

- [15] D. Tang, R. Yuan, Y. Chai, Ultrasensitive Electrochemical Immunosensor for Clinical Immunoassay Using Thionine-Doped Magnetic Gold Nanospheres as Labels and Horseradish Peroxidase as Enhancer, *Anal Chem*, 80(2008) 1582-8.
- [16] B. Giri, B. Pandey, B. Neupane, F.S. Ligler, Signal amplification strategies for microfluidic immunoassays, *TrAC, Trends Anal Chem*, 79(2016) 326-34.
- [17] E. Fu, K.E. Nelson, S.A. Ramsey, J.O. Foley, K. Helton, P. Yager, Modeling of a Competitive Microfluidic Heterogeneous Immunoassay: Sensitivity of the Assay Response to Varying System Parameters, *Anal Chem*, 81(2009) 3407-13.
- [18] I.F. Pinto, C.R.F. Caneira, R.R.G. Soares, N. Madaboosi, M.R. Aires-Barros, J.P. Conde, et al., The application of microbeads to microfluidic systems for enhanced detection and purification of biomolecules, *Methods*, 116(2017) 112-24.
- [19] R.R. Soares, P. Novo, A.M. Azevedo, P. Fernandes, V. Chu, J.P. Conde, et al., Aqueous two-phase systems for enhancing immunoassay sensitivity: simultaneous concentration of mycotoxins and neutralization of matrix interference, *J Chromatogr A*, 1361(2014) 67-76.
- [20] A.G. Crevillén, M. Hervás, M.A. López, M.C. González, A. Escarpa, Real sample analysis on microfluidic devices, *Talanta*, 74(2007) 342-57.
- [21] R.R.G. Soares, D. Ramadas, V. Chu, M.R. Aires-Barros, J.P. Conde, A.S. Viana, et al., An ultrarapid and regenerable microfluidic immunoassay coupled with integrated photosensors for point-of-use detection of ochratoxin A, *Sens Actuators, B*, 235(2016) 554-62.
- [22] V.N. Morozov, S. Groves, M.J. Turell, C. Bailey, Three Minutes-Long Electrophoretically Assisted Zeptomolar Microfluidic Immunoassay with Magnetic-Beads Detection, *J Am Chem Soc*, 129(2007) 12628-9.
- [23] J. Park, V. Sunkara, T.H. Kim, H. Hwang, Y.K. Cho, Lab-on-a-disc for fully integrated multiplex immunoassays, *Anal Chem*, 84(2012) 2133-40.
- [24] R.R. Soares, P. Novo, A.M. Azevedo, P. Fernandes, M.R. Aires-Barros, V. Chu, et al., On-chip sample preparation and analyte quantification using a microfluidic aqueous two-phase extraction coupled with an immunoassay, *Lab Chip*, 14(2014) 4284-94.
- [25] L. Lafleur, D. Stevens, K. McKenzie, S. Ramachandran, P. Spicar-Mihalic, M. Singhal, et al., Progress toward multiplexed sample-to-result detection in low resource settings using microfluidic immunoassay cards, *Lab Chip*, 12(2012) 1119-27.
- [26] A. Bernard, B. Michel, E. Delamarche, Micromosaic Immunoassays, *Anal Chem*, 73(2001) 8-12.
- [27] H. Zhang, L. Liu, X. Fu, Z. Zhu, Microfluidic beads-based immunosensor for sensitive detection of cancer biomarker proteins using multienzyme-nanoparticle amplification and quantum dots labels, *Biosens Bioelectron*, 42(2013) 23-30.

- [28] M. Herrmann, E. Roy, T. Veres, M. Tabrizian, Microfluidic ELISA on non-passivated PDMS chip using magnetic bead transfer inside dual networks of channels, *Lab Chip*, 7(2007) 1546-52.
- [29] Y. Yang, S.W. Nam, N.Y. Lee, Y.S. Kim, S. Park, Superporous agarose beads as a solid support for microfluidic immunoassay, *Ultramicroscopy*, 108(2008) 1384-9.
- [30] X. Yu, Y. Xia, Y. Tang, W.L. Zhang, Y.T. Yeh, H. Lu, et al., A Nanostructured Microfluidic Immunoassay Platform for Highly Sensitive Infectious Pathogen Detection, *Small*, 13(2017).
- [31] D. Yang, X. Niu, Y. Liu, Y. Wang, X. Gu, L. Song, et al., Electrospun Nanofibrous Membranes: A Novel Solid Substrate for Microfluidic Immunoassays for HIV, *Adv Mater*, 20(2008) 4770-5.
- [32] J.V. Jokerst, J. Chou, J.P. Camp, J. Wong, A. Lennart, A.A. Pollard, et al., Location of Biomarkers and Reagents within Agarose Beads of a Programmable Bio-nano-chip, *Small*, 7(2011) 613-24.
- [33] L. Gervais, M. Hitzbleck, E. Delamarche, Capillary-driven multiparametric microfluidic chips for one-step immunoassays, *Biosens Bioelectron*, 27(2011) 64-70.
- [34] P. Novo, V. Chu, J.P. Conde, Integrated optical detection of autonomous capillary microfluidic immunoassays: a hand-held point-of-care prototype, *Biosens Bioelectron*, 57(2014) 284-91.
- [35] Y. Zhao, G. Czilwik, V. Klein, K. Mitsakakis, R. Zengerle, N. Paust, C-reactive protein and interleukin 6 microfluidic immunoassays with on-chip pre-stored reagents and centrifugo-pneumatic liquid control, *Lab Chip*, 17(2017) 1666-77.
- [36] H. Ramachandraiah, M. Amasia, J. Cole, P. Sheard, S. Pickhaver, C. Walker, et al., Lab-on-DVD: standard DVD drives as a novel laser scanning microscope for image based point of care diagnostics, *Lab Chip*, 13(2013) 1578-85.
- [37] P. Novo, F. Volpetti, V. Chu, J.P. Conde, Control of sequential fluid delivery in a fully autonomous capillary microfluidic device, *Lab Chip*, 13(2013) 641-5.
- [38] L. Gervais, E. Delamarche, Toward one-step point-of-care immunodiagnostics using capillary-driven microfluidics and PDMS substrates, *Lab Chip*, 9(2009) 3330-7.
- [39] J.-u. Shim, R.T. Ranasinghe, C.A. Smith, S.M. Ibrahim, F. Hollfelder, W.T.S. Huck, et al., Ultrarapid Generation of Femtoliter Microfluidic Droplets for Single-Molecule-Counting Immunoassays, *ACS Nano*, 7(2013) 5955-64.
- [40] B. Hadwen, G.R. Broder, D. Morganti, A. Jacobs, C. Brown, J.R. Hector, et al., Programmable large area digital microfluidic array with integrated droplet sensing for bioassays, *Lab Chip*, 12(2012) 3305-13.
- [41] A.E. Kirby, N.M. Lafreniere, B. Seale, P.I. Hendricks, R.G. Cooks, A.R. Wheeler, Analysis on the go: quantitation of drugs of abuse in dried urine with digital microfluidics and miniature mass spectrometry, *Anal Chem*, 86(2014) 6121-9.

- [42] R.R.G. Soares, D.R. Santos, V. Chu, A.M. Azevedo, M.R. Aires-Barros, J.P. Conde, A point-of-use microfluidic device with integrated photodetector array for immunoassay multiplexing: Detection of a panel of mycotoxins in multiple samples, *Biosens Bioelectron*, 87(2017) 823-31.
- [43] S.H. Kim, J.W. Shim, S.M. Yang, Microfluidic multicolor encoding of microspheres with nanoscopic surface complexity for multiplex immunoassays, *Angew Chem Int Ed Engl*, 50(2011) 1171-4.
- [44] M. Han, X. Gao, J.Z. Su, S. Nie, Quantum-dot-tagged microbeads for multiplexed optical coding of biomolecules, *Nat Biotechnol*, 19(2001) 631.
- [45] G. Deng, K. Xu, Y. Sun, Y. Chen, T. Zheng, J. Li, High sensitive immunoassay for multiplex mycotoxin detection with photonic crystal microsphere suspension array, *Anal Chem*, 85(2013) 2833-40.
- [46] K.N. Han, C.A. Li, G.H. Seong, Microfluidic chips for immunoassays, *Annu Rev Anal Chem (Palo Alto Calif)*, 6(2013) 119-41.
- [47] D.R. Santos, R.R.G. Soares, V. Chu, J.P. Conde, Performance of Hydrogenated Amorphous Silicon Thin Film Photosensors at Ultra-Low Light Levels: Towards Attomole Sensitivities in Lab-on-Chip Biosensing Applications, *IEEE Sens J*, 17(2017) 6895-903.
- [48] Y. Date, S. Terakado, K. Sasaki, A. Aota, N. Matsumoto, H. Shiku, et al., Microfluidic heavy metal immunoassay based on absorbance measurement, *Biosens Bioelectron*, 33(2012) 106-12.
- [49] R.R.G. Soares, D.R. Santos, I.F. Pinto, A.M. Azevedo, M.R. Aires-Barros, V. Chu, et al., Multiplexed microfluidic fluorescence immunoassay with photodiode array signal acquisition for sub-minute and point-of-need detection of mycotoxins, *Lab Chip*, 18(2018) 1569-80.
- [50] B. Hu, J. Li, L. Mou, Y. Liu, J. Deng, W. Qian, et al., An automated and portable microfluidic chemiluminescence immunoassay for quantitative detection of biomarkers, *Lab Chip*, 17(2017) 2225-34.
- [51] I.F. Pinto, D.R. Santos, R.R.G. Soares, M.R. Aires-Barros, V. Chu, A.M. Azevedo, et al., A regenerable microfluidic device with integrated valves and thin-film photodiodes for rapid optimization of chromatography conditions, *Sens Actuators, B*, 255(2018) 3636-46.
- [52] A. Kling, C. Chatelle, L. Armbrecht, E. Qelibari, J. Kieninger, C. Dincer, et al., Multianalyte Antibiotic Detection on an Electrochemical Microfluidic Platform, *Anal Chem*, 88(2016) 10036-43.
- [53] S. Numthuan, T. Kakegawa, T. Anada, A. Khademhosseini, H. Suzuki, J. Fukuda, Synergistic effects of micro/nano modifications on electrodes for microfluidic electrochemical ELISA, *Sens Actuators, B*, 156(2011) 637-44.
- [54] M.D.M. Dryden, A.R. Wheeler, DStat: A Versatile, Open-Source Potentiostat for Electroanalysis and Integration, *PloS one*, 10(2015) e0140349.

- [55] C.K. Tang, A. Vaze, M. Shen, J.F. Rusling, High-Throughput Electrochemical Microfluidic Immunoarray for Multiplexed Detection of Cancer Biomarker Proteins, *ACS sensors*, 1(2016) 1036-43.
- [56] Y. Xie, X. Zhi, H. Su, K. Wang, Z. Yan, N. He, et al., A Novel Electrochemical Microfluidic Chip Combined with Multiple Biomarkers for Early Diagnosis of Gastric Cancer, *Nanoscale Res Lett*, 10(2015) 477.
- [57] Z. Olcer, E. Esen, T. Muhammad, A. Ersoy, S. Budak, Y. Uludag, Fast and sensitive detection of mycotoxins in wheat using microfluidics based Real-time Electrochemical Profiling, *Biosens Bioelectron*, 62(2014) 163-9.
- [58] J.A. Goode, J.V.H. Rushworth, P.A. Millner, Biosensor Regeneration: A Review of Common Techniques and Outcomes, *Langmuir*, 31(2015) 6267-76.
- [59] R.A.G. de Oliveira, E.M. Materon, M.E. Melendez, A.L. Carvalho, R.C. Faria, Disposable Microfluidic Immunoarray Device for Sensitive Breast Cancer Biomarker Detection, *ACS Appl Mater Interfaces*, 9(2017) 27433-40.
- [60] X. Luo, J.J. Davis, Electrical biosensors and the label free detection of protein disease biomarkers, *Chem Soc Rev*, 42(2013) 5944-62.
- [61] A.C. Sabuncu, J. Zhuang, J.F. Kolb, A. Beskok, Microfluidic impedance spectroscopy as a tool for quantitative biology and biotechnology, *Biomicrofluidics*, 6(2012) 034103.
- [62] J. Mok, M.N. Mindrinos, R.W. Davis, M. Javanmard, Digital microfluidic assay for protein detection, *Proc Natl Acad Sci*, 111(2014) 2110-5.
- [63] C.E. Nwankire, A. Venkatanarayanan, T. Glennon, T.E. Keyes, R.J. Forster, J. Ducree, Label-free impedance detection of cancer cells from whole blood on an integrated centrifugal microfluidic platform, *Biosens Bioelectron*, 68(2015) 382-9.
- [64] P.S. Katsamba, I. Navratilova, M. Calderon-Cacia, L. Fan, K. Thornton, M. Zhu, et al., Kinetic analysis of a high-affinity antibody/antigen interaction performed by multiple Biacore users, *Anal Biochem*, 352(2006) 208-21.
- [65] D.S. Wang, S.K. Fan, Microfluidic Surface Plasmon Resonance Sensors: From Principles to Point-of-Care Applications, *Sensors (Basel)*, 16(2016).
- [66] H. Guner, E. Ozgur, G. Kokturk, M. Celik, E. Esen, A.E. Topal, et al., A smartphone based surface plasmon resonance imaging (SPRi) platform for on-site biodetection, *Sens Actuators, B*, 239(2017) 571-7.
- [67] L. Anfossi, C. Baggiani, C. Giovannoli, G. D'Arco, G. Giraudi, Lateral-flow immunoassays for mycotoxins and phycotoxins: a review, *Anal Bioanal Chem*, 405(2013) 467-80.
- [68] E. O'Brien, D.R. Dietrich, Ochratoxin A: the continuing enigma, *Crit Rev Toxicol*, 35(2005) 33-60.

- [69] X. Li, P. Li, Q. Zhang, Y. Li, W. Zhang, X. Ding, Molecular Characterization of Monoclonal Antibodies against Aflatoxins: A Possible Explanation for the Highest Sensitivity, *Anal Chem*, 84(2012) 5229-35.
- [70] J.H. Williams, T.D. Phillips, P.E. Jolly, J.K. Stiles, C.M. Jolly, D. Aggarwal, Human aflatoxicosis in developing countries: a review of toxicology, exposure, potential health consequences, and interventions, *Am J Clin Nutr*, 80(2004) 1106-22.
- [71] Some traditional herbal medicines, some mycotoxins, naphthalene and styrene, IARC monographs on the evaluation of carcinogenic risks to humans, 82(2002) 1-556.
- [72] A. el Khoury, A. Atoui, Ochratoxin a: general overview and actual molecular status, *Toxins*, 2(2010) 461-93.
- [73] J.J. Pestka, Deoxynivalenol: Toxicity, mechanisms and animal health risks, *Anim Feed Sci Tech*, 137(2007) 283-98.
- [74] D.L. Sudakin, Trichothecenes in the environment: relevance to human health, *Toxicol Lett*, 143(2003) 97-107.
- [75] A. Zinedine, J.M. Soriano, J.C. Molto, J. Manes, Review on the toxicity, occurrence, metabolism, detoxification, regulations and intake of zearalenone: an oestrogenic mycotoxin, *Food Chem Toxicol*, 45(2007) 1-18.
- [76] J.M. Soriano, L. González, A.I. Catalá, Mechanism of action of sphingolipids and their metabolites in the toxicity of fumonisin B1, *Prog Lipid Res*, 44(2005) 345-56.
- [77] O. Puel, P. Galtier, P.I. Oswald, Biosynthesis and Toxicological Effects of Patulin, *Toxins*, 2(2010).
- [78] Commission Regulation (EU) No 165/2010 of 26 February 2010 amending Regulation (EC) No 1881/2006 setting maximum levels for certain contaminants in foodstuffs as regards aflatoxins (Text with EEA relevance), in: E.C. Regulation (Ed.), Official Journal of European Union, 2010.
- [79] Setting Maximum Levels for certain Contaminants in Foodstuffs, in: E.C.R. (EC) (Ed.) 1881/2006, Official Journal of European Union, 2006, pp. L364/15-16.
- [80] Commission Regulation (EC) No 1126/2007 of 28 September 2007 amending Regulation (EC) No 1881/2006 setting maximum levels for certain contaminants in foodstuffs as regards Fusarium toxins in maize and maize products (Text with EEA relevance), in: E.C. Regulation (Ed.), Official Journal of European Union, 2007.
- [81] S.C. Duarte, C.M. Lino, A. Pena, Ochratoxin A in feed of food-producing animals: An undesirable mycotoxin with health and performance effects, *Veterinary Microbiology*, 154(2011) 1-13.
- [82] Commission Regulation (EU) No 574/2011 of 16 June 2011 amending Annex I to Directive 2002/32/EC of the European Parliament and of the Council as regards maximum levels for nitrite, melamine, *Ambrosia* spp. and carry-over of certain coccidiostats and histomonostats and consolidating Annexes I and II thereto Text with EEA relevance, in: E.C. Regulation (Ed.), Official Journal of European Union, 2011.

- [83] Directive of the European Parliament and of the Council of 7 May 2002 on undesirable substances in animal feed, in: E.C. Directive (Ed.) 2002/32/EC, Official Journal of European Union, 2002, p. L0032/11.
- [84] Commission Recommendation on the presence of deoxynivalenol, zearalenone, ochratoxin A, T-2 and HT-2 and fumonisins in products intended for animal feeding, in: E.C. Recommendation (Ed.) 2006/576/EC, Official Journal of European Union, 2006, pp. L 229/7-9.
- [85] M. Reverberi, A. Ricelli, S. Zjalic, A.A. Fabbri, C. Fanelli, Natural functions of mycotoxins and control of their biosynthesis in fungi, *Appl Microbiol Biotechnol*, 87(2010) 899-911.
- [86] N. Magan, A. Medina, D. Aldred, Possible climate-change effects on mycotoxin contamination of food crops pre- and postharvest, *Plant Pathol*, 60(2011) 150-63.
- [87] P. Battilani, P. Toscano, H.J. Van der Fels-Klerx, A. Moretti, M. Camardo Leggieri, C. Brera, et al., Aflatoxin B1 contamination in maize in Europe increases due to climate change, *Sci Rep*, 6(2016) 24328.
- [88] R.R. Paterson, N. Lima, Thermophilic Fungi to Dominate Aflatoxigenic/Mycotoxigenic Fungi on Food under Global Warming, *Int J Environ Res Public Health*, 14(2017).
- [89] F.a.A.O.o.t.U.N. (FAO), Climate-related transboundary pests and diseases, Technical background document from the expert consultation held on 25 to 27 February 2008, Rome, Italy, 2008.
- [90] L.-A. Jaykus, M. Woolridge, J.M. Frank, M. Miraglia, A. McQuatters-Gollop, C. Tirado, et al., Climate Change: Implications for Food Safety, Food and Agriculture Organization of the United Nations (FAO), Rome, Italy, 2008.
- [91] P.J. Gregory, S.N. Johnson, A.C. Newton, J.S.I. Ingram, Integrating pests and pathogens into the climate change/food security debate, *J Exp Bot*, 60(2009) 2827-38.
- [92] J.W. Madgwick, J.S. West, R.P. White, M.A. Semenov, J.A. Townsend, J.A. Turner, et al., Impacts of climate change on wheat anthesis and fusarium ear blight in the UK, *Eur J Plant Pathol*, 130(2011) 117-31.
- [93] K. Seeling, S. Dänicke, Relevance of the Fusarium toxins deoxynivalenol and zearalenone in ruminant nutrition. A review., *Journal of Animal and Feed Sciences*, 14(2005) 3-40.
- [94] M.E. Flores-Flores, E. Lizarraga, A. López de Cerain, E. González-Peñas, Presence of mycotoxins in animal milk: A review, *Food Control*, 53(2015) 163-76.
- [95] W.L. Bryden, Food and feed, mycotoxins and the perpetual pentagram in a changing animal production environment, *Animal Prod Sci*, 52(2012) 383-97.
- [96] F. Wu, Mycotoxin Risk Assessment for the Purpose of Setting International Regulatory Standards, *Environ Sci Technol*, 38(2004) 4049-55.

- [97] T.B. Whitaker, Sampling Foods for Mycotoxins, *Food Addit Contam*, 23(2006) 50-61.
- [98] T.B. Whitaker, J.W. Dickens, R.J. Monroe, Variability of aflatoxin test results, *J Am Oil Chem Soc*, 51(1974) 214-8.
- [99] N. Magan, M. Olsen, *Mycotoxins in Food: Detection and Control*: Woodhead Pub.; 2004.
- [100] A.F. Cucullu, L.S. Lee, R.Y. Mayne, L.A. Goldblatt, Determination of aflatoxins in individual peanuts and peanut sections, *J Am Oil Chem Soc*, 43(1966) 89-92.
- [101] A.S. Johansson, T.B. Whitaker, W.M. Hagler, F.G. Giesbrecht, J.H. Young, D.T. Bowman, Testing Shelled Corn for Aflatoxin, Part I: Estimation of Variance Components, *J AOAC Int*, 83(2000) 1264-9.
- [102] A.S. Johansson, T.B. Whitaker, F.G. Giesbrecht, W.M. Hagler, J.H. Young, Testing Shelled Corn for Aflatoxin, Part II: Modeling the Observed Distribution of Aflatoxin Test Results, *J AOAC Int*, 83(2000) 1270-8.
- [103] J.B. Fenn, M. Mann, C.K. Meng, S.F. Wong, C.M. Whitehouse, Electrospray ionization for mass spectrometry of large biomolecules, *Science*, 246(1989) 64-71.
- [104] R.B. Geerdink, W.M.A. Niessen, U.A.T. Brinkman, Mass spectrometric confirmation criterion for product-ion spectra generated in flow-injection analysis: Environmental application, *J Chromatogr A*, 910(2001) 291-300.
- [105] M. Careri, F. Bianchi, C. Corradini, Recent advances in the application of mass spectrometry in food-related analysis, *J Chromatogr A*, 970(2002) 3-64.
- [106] E.C. Horning, M.G. Horning, D.I. Carroll, I. Dzidic, R.N. Stillwell, New picogram detection system based on a mass spectrometer with an external ionization source at atmospheric pressure, *Anal Chem*, 45(1973) 936-43.
- [107] 2002/657/EC: Commission Decision of 12 August 2002 implementing Council Directive 96/23/EC concerning the performance of analytical methods and the interpretation of results (Text with EEA relevance) (notified under document number C(2002) 3044), in: E. Commission (Ed.), *Official Journal of European Union* 2002.
- [108] L. Rivier, Criteria for the identification of compounds by liquid chromatography–mass spectrometry and liquid chromatography–multiple mass spectrometry in forensic toxicology and doping analysis, *Anal Chim Acta*, 492(2003) 69-82.
- [109] P. Zöllner, B. Mayer-Helm, Trace mycotoxin analysis in complex biological and food matrices by liquid chromatography–atmospheric pressure ionisation mass spectrometry, *J Chromatogr A*, 1136(2006) 123-69.
- [110] A.E. Urusov, A.V. Zherdev, B.B. Dzantiev, Immunochemical methods of mycotoxin analysis (review), *Appl Biochem Microbiol*, 46(2010) 253-66.
- [111] N.W. Turner, S. Subrahmanyam, S.A. Piletsky, Analytical methods for determination of mycotoxins: A review, *Anal Chim Acta*, 632(2009) 168-80.

- [112] F.S. Chu, F.C. Chang, R.D. Hinsdill, Production of antibody against ochratoxin A, *Applied and Environmental Microbiology*, 31(1976) 831-5.
- [113] C.M. Maragos, S.P. McCormick, Monoclonal Antibodies for the Mycotoxins Deoxynivalenol and 3-Acetyl-Deoxynivalenol, *Food Agric Immunol*, 12(2000) 181-92.
- [114] F.S. Chu, I. Ueno, Production of antibody against aflatoxin B1, *Applied and Environmental Microbiology*, 33(1977) 1125-8.
- [115] M. Sajid, A.-N. Kawde, M. Daud, Designs, formats and applications of lateral flow assay: A literature review, *J Saudi Chem Soc*, 19(2015) 689-705.
- [116] X. Lin, X. Guo, Advances in Biosensors, Chemosensors and Assays for the Determination of Fusarium Mycotoxins, *Toxins*, 8(2016).
- [117] L.A. Currie, Nomenclature in evaluation of analytical methods including detection and quantification capabilities | Adapted from the International Union of Pure and Applied Chemistry (IUPAC) document "Nomenclature in Evaluation of Analytical Methods including Detection and Quantification Capabilities", which originally appeared in *Pure and Applied Chemistry*, 67 1699–1723 (1995) © 1995 IUPAC. Republication permission granted by IUPAC.1, *Anal Chim Acta*, 391(1999) 105-26.
- [118] L.A. Currie, Detection and quantification limits: origins and historical overview | Adapted from the Proceedings of the 1996 Joint Statistical Meetings (American Statistical Association, 1997). Original title: "Foundations and future of detection and quantification limits". Contribution of the National Institute of Standards and Technology; not subject to copyright.1, *Anal Chim Acta*, 391(1999) 127-34.
- [119] R. Macarthur, C. von Holst, A protocol for the validation of qualitative methods of detection, *Anal Methods*, 4(2012) 2744.
- [120] Neogen Reveal® Q+ MAX, <http://foodsafety.neogen.com/en/reveal-q-plus-max>, September 2017
- [121] Charm Sciences Inc. Mycotoxin Test Kits, <https://www.charm.com/products/mycotoxins>, September 2017
- [122] Romer Labs® - Fast and Reliable Test Kits for Mycotoxin Detection, <https://www.romerlabs.com/en/products/test-kits/mycotoxin-test-kits/>, September 2017
- [123] Neogen Veratox®, <http://foodsafety.neogen.com/en/veratox#mycotoxins>, September 2017
- [124] M. Joo, S.H. Baek, S.A. Cheon, H.S. Chun, S.W. Choi, T.J. Park, Development of aflatoxin B1 aptasensor based on wide-range fluorescence detection using graphene oxide quencher, *Colloids Surf B Biointerfaces*, 154(2017) 27-32.
- [125] L. Chen, F. Wen, M. Li, X. Guo, S. Li, N. Zheng, et al., A simple aptamer-based fluorescent assay for the detection of Aflatoxin B1 in infant rice cereal, *Food Chem*, 215(2017) 377-82.

- [126] Z. Lu, X. Chen, W. Hu, A fluorescence aptasensor based on semiconductor quantum dots and MoS₂ nanosheets for ochratoxin A detection, *Sens Actuators, B*, 246(2017) 61-7.
- [127] L. Lv, D. Li, R. Liu, C. Cui, Z. Guo, Label-free aptasensor for ochratoxin A detection using SYBR Gold as a probe, *Sens Actuators, B*, 246(2017) 647-52.
- [128] Z. Liu, Y. Zhang, S. Xu, H. Zhang, Y. Tan, C. Ma, et al., A 3D printed smartphone optosensing platform for point-of-need food safety inspection, *Anal Chim Acta*, 966(2017) 81-9.
- [129] T. Li, J.Y. Byun, B.B. Kim, Y.B. Shin, M.G. Kim, Label-free homogeneous FRET immunoassay for the detection of mycotoxins that utilizes quenching of the intrinsic fluorescence of antibodies, *Biosens Bioelectron*, 42(2013) 403-8.
- [130] W. Zhang, Y. Han, X. Chen, X. Luo, J. Wang, T. Yue, et al., Surface molecularly imprinted polymer capped Mn-doped ZnS quantum dots as a phosphorescent nanosensor for detecting patulin in apple juice, *Food Chem*, 232(2017) 145-54.
- [131] Z. Hu, W.P. Lustig, J. Zhang, C. Zheng, H. Wang, S.J. Teat, et al., Effective Detection of Mycotoxins by a Highly Luminescent Metal-Organic Framework, *J Am Chem Soc*, 137(2015) 16209-15.
- [132] D. Bueno Hernández, R.K. Mishra, R. Muñoz, J.L. Marty, Low cost optical device for detection of fluorescence from Ochratoxin A using a CMOS sensor, *Sens Actuators, B*, 246(2017) 606-14.
- [133] F. Arduini, D. Neagu, V. Pagliarini, V. Scognamiglio, M.A. Leonardis, E. Gatto, et al., Rapid and label-free detection of ochratoxin A and aflatoxin B1 using an optical portable instrument, *Talanta*, 150(2016) 440-8.
- [134] F. Di Nardo, C. Baggiani, C. Giovannoli, G. Spano, L. Anfossi, Multicolor immunochromatographic strip test based on gold nanoparticles for the determination of aflatoxin B1 and fumonisins, *Microchim Acta*, 184(2017) 1295-304.
- [135] A. Foubert, N.V. Beloglazova, S. De Saeger, Comparative study of colloidal gold and quantum dots as labels for multiplex screening tests for multi-mycotoxin detection, *Anal Chim Acta*, 955(2017) 48-57.
- [136] M. Zangheri, F. Di Nardo, L. Anfossi, C. Giovannoli, C. Baggiani, A. Roda, et al., A multiplex chemiluminescent biosensor for type B-fumonisins and aflatoxin B1 quantitative detection in maize flour, *Analyst*, 140(2015) 358-65.
- [137] Y. Lin, Q. Zhou, D. Tang, R. Niessner, D. Knopp, Signal-On Photoelectrochemical Immunoassay for Aflatoxin B1 Based on Enzymatic Product-Etching MnO₂ Nanosheets for Dissociation of Carbon Dots, *Anal Chem*, 89(2017) 5637-45.
- [138] V. Pagkali, P.S. Petrou, A. Salapatras, E. Makarona, J. Peters, W. Haasnoot, et al., Detection of ochratoxin A in beer samples with a label-free monolithically integrated optoelectronic biosensor, *J Hazard Mater*, 323(2017) 75-83.

- [139] Y. Uludag, E. Esen, G. Kokturk, H. Ozer, T. Muhammad, Z. Olcer, et al., Lab-on-a-chip based biosensor for the real-time detection of aflatoxin, *Talanta*, 160(2016) 381-8.
- [140] X. Zhou, S. Wu, H. Liu, X. Wu, Q. Zhang, Nanomechanical label-free detection of aflatoxin B1 using a microcantilever, *Sens Actuators, B*, 226(2016) 24-9.
- [141] L.H. Liu, X.H. Zhou, H.C. Shi, Portable optical aptasensor for rapid detection of mycotoxin with a reversible ligand-grafted biosensing surface, *Biosens Bioelectron*, 72(2015) 300-5.
- [142] X. Li, F. Yang, J.X.H. Wong, H.-Z. Yu, Integrated smartphone-app-chip system for on-site ppb-level colorimetric quantitation of aflatoxins, *Anal Chem*, (2017).
- [143] R.R.G. Soares, D.R. Santos, I.F. Pinto, A.M. Azevedo, V. Chu, M.R. Aires-Barros, et al., Point-of-use Ultrafast Single-step Detection of Food Contaminants: A Novel Microfluidic Fluorescence-based Immunoassay with Integrated Photodetection, *Procedia Engineering*, 168(2016) 329-32.
- [144] F. Costantini, C. Sberna, G. Petrucci, M. Reverberi, F. Domenici, C. Fanelli, et al., Aptamer-based sandwich assay for on chip detection of Ochratoxin A by an array of amorphous silicon photosensors, *Sens Actuators, B*, 230(2016) 31-9.
- [145] N. Liu, D. Nie, Y. Tan, Z. Zhao, Y. Liao, H. Wang, et al., An ultrasensitive amperometric immunosensor for zearalenones based on oriented antibody immobilization on a glassy carbon electrode modified with MWCNTs and AuPt nanoparticles, *Microchim Acta*, 184(2016) 147-53.
- [146] L. Chen, J. Jiang, G. Shen, R. Yu, A label-free electrochemical impedance immunosensor for the sensitive detection of aflatoxin B1, *Anal Methods*, 7(2015) 2354-9.
- [147] K. Abnous, N.M. Danesh, M. Alibolandi, M. Ramezani, S.M. Taghdisi, Amperometric aptasensor for ochratoxin A based on the use of a gold electrode modified with aptamer, complementary DNA, SWCNTs and the redox marker Methylene Blue, *Microchim Acta*, 184(2017) 1151-9.
- [148] Y. Qing, X. Li, S. Chen, X. Zhou, M. Luo, X. Xu, et al., Differential pulse voltammetric ochratoxin A assay based on the use of an aptamer and hybridization chain reaction, *Microchim Acta*, 184(2017) 863-70.
- [149] L. Rivas, C.C. Mayorga-Martinez, D. Quesada-Gonzalez, A. Zamora-Galvez, A. de la Escosura-Muniz, A. Merkoci, Label-free impedimetric aptasensor for ochratoxin-A detection using iridium oxide nanoparticles, *Anal Chem*, 87(2015) 5167-72.
- [150] C. Ren, H. Li, X. Lu, J. Qian, M. Zhu, W. Chen, et al., A disposable aptasensing device for label-free detection of fumonisin B1 by integrating PDMS film-based micro-cell and screen-printed carbon electrode, *Sens Actuators, B*, 251(2017) 192-9.
- [151] C. Zhang, J. Tang, L. Huang, Y. Li, D. Tang, In-situ amplified voltammetric immunoassay for ochratoxin A by coupling a platinum nanocatalyst based enhancement to a redox cycling process promoted by an enzyme mimic *Microchim Acta*, 184(2017) 2445-53.

- [152] N. Liu, S. Chen, Y. Li, H. Dai, Y. Lin, Self-enhanced photocathodic matrix based on poly-dopamine sensitized TiO₂ mesocrystals for mycotoxin detection assisted by a dual amplificatory nanotag, *New J Chem*, 41(2017) 3380-6.
- [153] Y. Ma, Y. Mao, D. Huang, Z. He, J. Yan, T. Tian, et al., Portable visual quantitative detection of aflatoxin B1 using a target-responsive hydrogel and a distance-readout microfluidic chip, *Lab Chip*, 16(2016) 3097-104.
- [154] J.M.D. Machado, R.R.G. Soares, V. Chu, J.P. Conde, Multiplexed capillary microfluidic immunoassay with smartphone data acquisition for parallel mycotoxin detection, *Biosens Bioelectron*, 99(2018) 40-6.
- [155] J.H. Park, J.Y. Byun, H. Mun, W.B. Shim, Y.B. Shin, T. Li, et al., A regeneratable, label-free, localized surface plasmon resonance (LSPR) aptasensor for the detection of ochratoxin A, *Biosens Bioelectron*, 59(2014) 321-7.
- [156] M. Sieger, G. Kos, M. Sulyok, M. Godejohann, R. Krska, B. Mizaikoff, Portable Infrared Laser Spectroscopy for On-site Mycotoxin Analysis, *Sci Rep*, 7(2017) 44028.
- [157] G. Posthuma-Trumpie, J. Korf, A. van Amerongen, Lateral flow (immuno)assay: its strengths, weaknesses, opportunities and threats. A literature survey, *Anal Bioanal Chem*, 393(2009) 569-82.
- [158] S. Song, N. Liu, Z. Zhao, E. Njumbe Ediage, S. Wu, C. Sun, et al., Multiplex lateral flow immunoassay for mycotoxin determination, *Anal Chem*, 86(2014) 4995-5001.
- [159] A. Foubert, N.V. Beloglazova, A. Gordienko, M.D. Tessier, E. Drijvers, Z. Hens, et al., Development of a Rainbow Lateral Flow Immunoassay for the Simultaneous Detection of Four Mycotoxins, *J Agric Food Chem*, (2016).
- [160] L. Anfossi, C. Giovannoli, G. Giraudi, F. Biagioli, C. Passini, C. Baggiani, A lateral flow immunoassay for the rapid detection of ochratoxin A in wine and grape must, *J Agric Food Chem*, 60(2012) 11491-7.
- [161] A.M. Streets, Y. Huang, Chip in a lab: Microfluidics for next generation life science research, *Biomicrofluidics*, 7(2013) 11302.
- [162] J.P. Conde, N. Madaboosi, R.R.G. Soares, J.T.S. Fernandes, P. Novo, G. Moulas, et al., Lab-on-chip systems for integrated bioanalyses, *Essays Biochem*, 60(2016) 121-31.
- [163] E.K. Sackmann, A.L. Fulton, D.J. Beebe, The present and future role of microfluidics in biomedical research, *Nature*, 507(2014) 181-9.
- [164] N. Pamme, Continuous flow separations in microfluidic devices, *Lab Chip*, 7(2007) 1644-59.
- [165] L. Gervais, N. de Rooij, E. Delamarche, Microfluidic chips for point-of-care immunodiagnosics, *Adv Mater*, 23(2011) H151-76.
- [166] D. Kim, A.E. Herr, Protein immobilization techniques for microfluidic assays, *Biomicrofluidics*, 7(2013) 41501.

- [167] R.D. Tilton, C.R. Robertson, A.P. Gast, Lateral diffusion of bovine serum albumin adsorbed at the solid-liquid interface, *J Colloid Interface Sci*, 137(1990) 192-203.
- [168] M.E. Wiseman, C.W. Frank, Antibody adsorption and orientation on hydrophobic surfaces, *Langmuir*, 28(2012) 1765-74.
- [169] A.K. Trilling, J. Beekwilder, H. Zuilhof, Antibody orientation on biosensor surfaces: a minireview, *Analyst*, 138(2013) 1619-27.
- [170] A. Tello, R. Cao, M.J. Marchant, H. Gomez, Conformational Changes of Enzymes and Aptamers Immobilized on Electrodes, *Bioconjugate Chem*, 27(2016) 2581-91.
- [171] V. Chan, S.E. McKenzie, S. Surrey, P. Fortina, D.J. Graves, Effect of Hydrophobicity and Electrostatics on Adsorption and Surface Diffusion of DNA Oligonucleotides at Liquid/Solid Interfaces, *J Colloid Interface Sci*, 203(1998) 197-207.
- [172] C.M. Maragos, L. Li, D. Chen, Production and characterization of a single chain variable fragment (scFv) against the mycotoxin deoxynivalenol, *Food Agric Immunol*, 23(2012) 51-67.
- [173] J. Chen, X. Zhang, S. Cai, D. Wu, M. Chen, S. Wang, et al., A fluorescent aptasensor based on DNA-scaffolded silver-nanocluster for ochratoxin A detection, *Biosens Bioelectron*, 57(2014) 226-31.
- [174] L. Yao, Y. Chen, J. Teng, W. Zheng, J. Wu, S.B. Adeloju, et al., Integrated platform with magnetic purification and rolling circular amplification for sensitive fluorescent detection of ochratoxin A, *Biosens Bioelectron*, 74(2015) 534-8.
- [175] C.M. Maragos, Extraction of aflatoxins B1 and G1 from maize by using aqueous sodium dodecyl sulfate, *J AOAC Int*, 91(2008) 762-7.
- [176] L. Anfossi, G. D'Arco, M. Calderara, C. Baggiani, C. Giovannoli, G. Giraudi, Development of a quantitative lateral flow immunoassay for the detection of aflatoxins in maize, *Food Adit Contam Part A*, 28(2011) 226-34.
- [177] C.F. Poole, N. Lenca, Green sample-preparation methods using room-temperature ionic liquids for the chromatographic analysis of organic compounds, *TrAC, Trends Anal Chem*, 71(2015) 144-56.
- [178] S. Garcia-Fonseca, A. Ballesteros-Gomez, S. Rubio, Restricted access supramolecular solvents for sample treatment in enzyme-linked immuno-sorbent assay of mycotoxins in food, *Anal Chim Acta*, 935(2016) 129-35.
- [179] M.-I. Leong, M.-R. Fuh, S.-D. Huang, Beyond dispersive liquid-liquid microextraction, *J Chromatogr A*, 1335(2014) 2-14.
- [180] R.R.G. Soares, A.M. Azevedo, P. Fernandes, V. Chu, J.P. Conde, M.R. Aires-Barros, A simple method for point-of-need extraction, concentration and rapid multi-mycotoxin immunodetection in feeds using aqueous two-phase systems, *J Chromatogr A*, 1511(2017) 15-24.

- [181] Vicam® Fumo-V Aqua, <http://vicam.com/fumonisin-test-kits/fumo-v-aqua>, September 2017
- [182] Vicam® Afla-V Aqua, <http://vicam.com/aflatoxin-test-kits/afla-v-aqua>, September 2017
- [183] S. Xiong, Y. Zhou, X. Huang, R. Yu, W. Lai, Y. Xiong, Ultrasensitive direct competitive FLISA using highly luminescent quantum dot beads for tuning affinity of competing antigens to antibodies, *Anal Chim Acta*, 972(2017) 94-101.
- [184] Y. Tan, T. Tang, H. Xu, C. Zhu, B.T. Cunningham, High sensitivity automated multiplexed immunoassays using photonic crystal enhanced fluorescence microfluidic system, *Biosens Bioelectron*, 73(2015) 32-40.
- [185] J. Xu, W. Li, R. Liu, Y. Yang, Q. Lin, J. Xu, et al., Ultrasensitive low-background multiplex mycotoxin chemiluminescence immunoassay by silica-hydrogel photonic crystal microsphere suspension arrays in cereal samples, *Sens Actuators, B*, 232(2016) 577-84.
- [186] A. Sharma, G. Istamboulie, A. Hayat, G. Catanante, S. Bhand, J.L. Marty, Disposable and portable aptamer functionalized impedimetric sensor for detection of kanamycin residue in milk sample, *Sens Actuators, B*, 245(2017) 507-15.
- [187] K. Yugender Goud, G. Catanante, A. Hayat, S. M, K. Vengatajalabathy Gobi, J.L. Marty, Disposable and portable electrochemical aptasensor for label free detection of aflatoxin B1 in alcoholic beverages, *Sens Actuators, B*, 235(2016) 466-73.
- [188] K.I. Ozoemena, S. Carrara, Biomedical electrochemical sensors for resource-limited countries, *Curr Opin Electrochem*, (2017).
- [189] Jules L. Hammond, N. Formisano, P. Estrela, S. Carrara, J. Tkac, Electrochemical biosensors and nanobiosensors, *Essays Biochem*, 60(2016) 69-80.
- [190] B.Y. Zaslavsky, *Aqueous two-phase partitioning : physical chemistry and bioanalytical applications*, United States of America: Marcel Dekker, INC.; 1994.
- [191] P.-A. Albertsson, *Partition of Cell Particles and Macromolecules*, 3 ed., New York: Wiley; 1986.
- [192] H.-O. Johansson, G. Karlström, F. Tjerneld, C.A. Haynes, Driving forces for phase separation and partitioning in aqueous two-phase systems, *J Chromatogr B*, 711(1998) 3-17.
- [193] S. Oelmeier, F. Dimer, J. Hubbuch, Molecular dynamics simulations on aqueous two-phase systems - Single PEG-molecules in solution, *BMC Biophys*, 5(2012) 14.
- [194] F. Dimer, S. Alexander Oelmeier, J. Hubbuch, Molecular dynamics simulations of aqueous two-phase systems: Understanding phase formation and protein partitioning, *Chem Eng Sci*, 96(2013) 142-51.

- [195] N.R. da Silva, L.A. Ferreira, L.M. Mikheeva, J.A. Teixeira, B.Y. Zaslavsky, Origin of salt additive effect on solute partitioning in aqueous polyethylene glycol-8000-sodium sulfate two-phase system, *J Chromatogr A*, 1337(2014) 3-8.
- [196] L.A. Ferreira, N.R. da Silva, S.R. Wlodarczyk, J.A. Loureiro, P.P. Madeira, J.A. Teixeira, et al., Interrelationship between partition behavior of organic compounds and proteins in aqueous dextran-polyethylene glycol and polyethylene glycol-sodium sulfate two-phase systems, *J Chromatogr A*, 1443(2016) 21-5.
- [197] D. Forciniti, C.K. Hall, M.R. Kula, Protein partitioning at the isoelectric point: Influence of polymer molecular weight and concentration and protein size, *Biotechnol Bioeng*, 38(1991) 986-94.
- [198] B. Lebreton, S.G. Walker, A. Lyddiatt, Characterization of aqueous two-phase partition systems by distribution analysis of radiolabeled analytes (DARA): Application to process definition and control in biorecovery, *Biotechnol Bioeng*, 77(2002) 329-39.
- [199] P.P. Madeira, A. Bessa, D.P. de Barros, M.A. Teixeira, L. Alvares-Ribeiro, M.R. Aires-Barros, et al., Solvatochromic relationship: prediction of distribution of ionic solutes in aqueous two-phase systems, *J Chromatogr A*, 1271(2013) 10-6.
- [200] S. Abdolrahimi, B. Nasernejad, G. Pazuki, Influence of process variables on extraction of Cefalexin in a novel biocompatible ionic liquid based-aqueous two phase system, *Phys Chem Chem Phys*, 17(2015) 655-69.
- [201] S. Amrhein, M.L. Schwab, M. Hoffmann, J. Hubbuch, Characterization of aqueous two phase systems by combining lab-on-a-chip technology with robotic liquid handling stations, *J Chromatogr A*, 1367(2014) 68-77.
- [202] M. Wiendahl, S.A. Oelmeier, F. Dismer, J. Hubbuch, High-throughput screening-based selection and scale-up of aqueous two-phase systems for pDNA purification, *J Sep Sci*, 35(2012) 3197-207.
- [203] B.Y. Zaslavsky, V.N. Uversky, A. Chait, Analytical applications of partitioning in aqueous two-phase systems: Exploring protein structural changes and protein-partner interactions in vitro and in vivo by solvent interaction analysis method, *Biochim Biophys Acta, Proteins Proteomics*, 1864(2016) 622-44.
- [204] P.A. Rosa, A.M. Azevedo, S. Sommerfeld, W. Backer, M.R. Aires-Barros, Continuous aqueous two-phase extraction of human antibodies using a packed column, *J Chromatogr B*, 880(2012) 148-56.
- [205] P.A. Rosa, A.M. Azevedo, S. Sommerfeld, M. Mutter, W. Backer, M.R. Aires-Barros, Continuous purification of antibodies from cell culture supernatant with aqueous two-phase systems: from concept to process, *Biotechnol J*, 8(2013) 352-62.
- [206] J. Muendges, A. Zalesko, A. Gorak, T. Zeiner, A. Gorak, Multistage aqueous two-phase extraction of a monoclonal antibody from cell supernatant, *Biotechnol Prog*, (2015).

- [207] E. Espitia-Saloma, P. Vázquez-Villegas, O. Aguilar, M. Rito-Palomares, Continuous aqueous two-phase systems devices for the recovery of biological products, *Food Bioprod Process*, 92(2014) 101-12.
- [208] J.F.B. Pereira, F. Vicente, V.C. Santos-Ebinuma, J.M. Araújo, A. Pessoa, M.G. Freire, et al., Extraction of tetracycline from fermentation broth using aqueous two-phase systems composed of polyethylene glycol and cholinium-based salts, *Process Biochem*, 48(2013) 716-22.
- [209] C. Kepka, J. Rhodin, R. Lemmens, F. Tjerneld, P.-E. Gustavsson, Extraction of plasmid DNA from *Escherichia coli* cell lysate in a thermoseparating aqueous two-phase system, *J Chromatogr A*, 1024(2004) 95-104.
- [210] M.J. Jacinto, R.R.G. Soares, A.M. Azevedo, V. Chu, A. Tover, J.P. Conde, et al., Optimization and miniaturization of aqueous two phase systems for the purification of recombinant human immunodeficiency virus-like particles from a CHO cell supernatant, *Sep Purif Technol*, 154(2015) 27-35.
- [211] A.F. Sousa, P.Z. Andrade, R.M. Pirzgalska, T.M. Galhoz, A.M. Azevedo, C.L. da Silva, et al., A novel method for human hematopoietic stem/progenitor cell isolation from umbilical cord blood based on immunoaffinity aqueous two-phase partitioning, *Biotechnol Lett*, 33(2011) 2373-7.
- [212] A.M. Azevedo, A.G. Gomes, P.A.J. Rosa, I.F. Ferreira, A.M.M.O. Pisco, M.R. Aires-Barros, Partitioning of human antibodies in polyethylene glycol–sodium citrate aqueous two-phase systems, *Sep Purif Technol*, 65(2009) 14-21.
- [213] E. Esmanhoto, B.V. Kilikian, ATPS applied to extraction of small molecules - polycetides - and simultaneous clarification of culture media with filamentous microorganisms, *J Chromatogr B*, 807(2004) 139-43.
- [214] C. Ladd Effio, L. Wenger, O. Otes, S.A. Oelmeier, R. Kneusel, J. Hubbuch, Downstream processing of virus-like particles: single-stage and multi-stage aqueous two-phase extraction, *J Chromatogr A*, 1383(2015) 35-46.
- [215] A. Prinz, J. Hönig, I. Schüttmann, H. Zorn, T. Zeiner, Separation and purification of laccases from two different fungi using aqueous two-phase extraction, *Process Biochem*, 49(2014) 335-46.
- [216] Q. Wu, D.Q. Lin, S.J. Yao, Evaluation of poly(ethylene glycol)/hydroxypropyl starch aqueous two-phase system for immunoglobulin G extraction, *J Chromatogr B*, 928(2013) 106-12.
- [217] J. Persson, D.C. Andersen, P.M. Lester, Evaluation of different primary recovery methods for *E. coli*-derived recombinant human growth hormone and compatibility with further down-stream purification, *Biotechnol Bioeng*, 90(2005) 442-51.
- [218] P.A. Rosa, A.M. Azevedo, I.F. Ferreira, J. de Vries, R. Korporaal, H.J. Verhoef, et al., Affinity partitioning of human antibodies in aqueous two-phase systems, *J Chromatogr A*, 1162(2007) 103-13.

- [219] H.-O. Johansson, E. Feitosa, A.P. Junior, Phase Diagrams of the Aqueous Two-Phase Systems of Poly(ethylene glycol)/Sodium Polyacrylate/Salts, *Polymers*, 3(2011) 587-601.
- [220] H.O. Johansson, T. Matos, J.S. Luz, E. Feitosa, C.C. Oliveira, A. Pessoa, Jr., et al., Plasmid DNA partitioning and separation using poly(ethylene glycol)/poly(acrylate)/salt aqueous two-phase systems, *J Chromatogr A*, 1233(2012) 30-5.
- [221] J.F.B. Pereira, V.C. Santos, H.-O. Johansson, J.A.C. Teixeira, A. Pessoa, A stable liquid-liquid extraction system for clavulanic acid using polymer-based aqueous two-phase systems, *Sep Purif Technol*, 98(2012) 441-50.
- [222] C.W. Ooi, S.L. Hii, S.M.M. Kamal, A. Ariff, T.C. Ling, Extractive fermentation using aqueous two-phase systems for integrated production and purification of extracellular lipase derived from *Burkholderia pseudomallei*, *Process Biochem*, 46(2011) 68-73.
- [223] I.M. Marrucho, M.G. Freire, Aqueous Biphasic Systems Based on Ionic Liquids for Extraction, Concentration and Purification Approaches, *Ionic Liquids for Better Separation Processes*, (2016) 91-119.
- [224] A.F.M. Claudio, M.C. Neves, K. Shimizu, J.N. Canongia Lopes, M.G. Freire, J.A.P. Coutinho, The magic of aqueous solutions of ionic liquids: ionic liquids as a powerful class of cationic hydrotrops, *Green Chem*, 17(2015) 3948-63.
- [225] J.F.B. Pereira, S.P.M. Ventura, F.A. e Silva, S. Shahriari, M.G. Freire, J.A.P. Coutinho, Aqueous biphasic systems composed of ionic liquids and polymers: A platform for the purification of biomolecules, *Sep Purif Technol*, 113(2013) 83-9.
- [226] R.L. Souza, S.P.M. Ventura, C.M.F. Soares, J.A.P. Coutinho, Á.S. Lima, Lipase purification using ionic liquids as adjuvants in aqueous two-phase systems, *Green Chem*, 17(2015) 3026-34.
- [227] A. Kumar, P. Venkatesu, Does the stability of proteins in ionic liquids obey the Hofmeister series?, *Int J Biol Macromol*, 63(2014) 244-53.
- [228] P.L. Show, C.P. Tan, M. Shamsul Anuar, A. Ariff, Y.A. Yusof, S.K. Chen, et al., Extractive fermentation for improved production and recovery of lipase derived from *Burkholderia cepacia* using a thermoseparating polymer in aqueous two-phase systems, *Bioresour Technol*, 116(2012) 226-33.
- [229] I.F. Ferreira, A.M. Azevedo, P.A. Rosa, M.R. Aires-Barros, Purification of human immunoglobulin G by thermoseparating aqueous two-phase systems, *J Chromatogr A*, 1195(2008) 94-100.
- [230] H.S. Ng, C.P. Tan, M.N. Mokhtar, S. Ibrahim, A. Ariff, C.W. Ooi, et al., Recovery of *Bacillus cereus* cyclodextrin glycosyltransferase and recycling of phase components in an aqueous two-phase system using thermo-separating polymer, *Sep Purif Technol*, 89(2012) 9-15.

- [231] W. Rao, Y. Wang, J. Han, L. Wang, T. Chen, Y. Liu, et al., Cloud Point and Liquid-Liquid Equilibrium Behavior of Thermosensitive Polymer L61 and Salt Aqueous Two-Phase System, *J Phys Chem B*, 119(2015) 8201-8.
- [232] J. Persson, H.O. Johansson, I. Galaev, B. Mattiasson, F. Tjerneld, Aqueous polymer two-phase systems formed by new thermoseparating polymers, *Bioseparation*, 9(2000) 105-16.
- [233] C.M. Maragos, M. Appell, V. Lippolis, A. Visconti, L. Catucci, M. Pascale, Use of cyclodextrins as modifiers of fluorescence in the detection of mycotoxins, *Food Addit Contam Part A Chem Anal Control Expo Risk Assess*, 25(2008) 164-71.
- [234] A.J. Van, J. Shanagar, R. Hjorth, M. Hall, N.C. Estmer, Separation method using single polymer phase systems, WO2010080062A12010.
- [235] R. Hjorth, K. Lacki, E. Macedo, G. Malmquist, J. Shanagar, A.J. Van, Separation method using polymer multi phase systems, WO2008156409A12008.
- [236] J. Muendges, I. Stark, S. Mohammad, A. Górak, T. Zeiner, Single stage aqueous two-phase extraction for monoclonal antibody purification from cell supernatant, *Fluid Phase Equilib*, 385(2015) 227-36.
- [237] Y. Shu, M. Gao, X. Wang, R. Song, J. Lu, X. Chen, Separation of curcuminoids using ionic liquid based aqueous two-phase system coupled with in situ dispersive liquid-liquid microextraction, *Talanta*, 149(2016) 6-12.
- [238] J.H. Santos, F.A. e Silva, S.P. Ventura, J.A. Coutinho, R.L. de Souza, C.M. Soares, et al., Ionic liquid-based aqueous biphasic systems as a versatile tool for the recovery of antioxidant compounds, *Biotechnol Prog*, 31(2015) 70-7.
- [239] M. Shao, X. Zhang, N. Li, J. Shi, H. Zhang, Z. Wang, et al., Ionic liquid-based aqueous two-phase system extraction of sulfonamides in milk, *J Chromatogr B*, 961(2014) 5-12.
- [240] P. Berton, R.P. Monasterio, R.G. Wuilloud, Selective extraction and determination of vitamin B12 in urine by ionic liquid-based aqueous two-phase system prior to high-performance liquid chromatography, *Talanta*, 97(2012) 521-6.
- [241] M.S. Noorashikin, S. Mohamad, M.R. Abas, Extraction and determination of parabens in water samples using an aqueous two-phase system of ionic liquid and salts with beta-cyclodextrin as the modifier coupled with high performance liquid chromatography, *Anal Methods*, 6(2014) 419-25.
- [242] M. Rezaee, Y. Yamini, M. Faraji, Evolution of dispersive liquid-liquid microextraction method, *J Chromatogr A*, 1217(2010) 2342-57.
- [243] M. Amid, M. Shuhaimi, M.Z. Islam Sarker, M.Y. Abdul Manap, Purification of serine protease from mango (*Mangifera Indica* Cv. Chokanan) peel using an alcohol/salt aqueous two phase system, *Food Chem*, 132(2012) 1382-6.
- [244] Y.X. Guo, J. Han, D.Y. Zhang, L.H. Wang, L.L. Zhou, An ammonium sulfate/ethanol aqueous two-phase system combined with ultrasonication for the

separation and purification of lithospermic acid B from *Salvia miltiorrhiza* Bunge, *Ultrason Sonochem*, 19(2012) 719-24.

[245] Y. Wu, Y. Wang, W. Zhang, J. Han, Y. Liu, Y. Hu, et al., Extraction and preliminary purification of anthocyanins from grape juice in aqueous two-phase system, *Sep Purif Technol*, 124(2014) 170-8.

[246] X.-Q. Wang, W. Wei, C.-J. Zhao, C.-Y. Li, M. Luo, W. Wang, et al., Negative-pressure cavitation coupled with aqueous two-phase extraction and enrichment of flavonoids and stilbenes from the pigeon pea leaves and the evaluation of antioxidant activities, *Sep Purif Technol*, 156(2015) 116-23.

[247] A.F.M. Cláudio, M.G. Freire, C.S.R. Freire, A.J.D. Silvestre, J.A.P. Coutinho, Extraction of vanillin using ionic-liquid-based aqueous two-phase systems, *Sep Purif Technol*, 75(2010) 39-47.

[248] J.-K. Yan, H.-L. Ma, J.-J. Pei, Z.-B. Wang, J.-Y. Wu, Facile and effective separation of polysaccharides and proteins from *Cordyceps sinensis* mycelia by ionic liquid aqueous two-phase system, *Sep Purif Technol*, 135(2014) 278-84.

[249] J. Fliieger, A. Czajkowska-Zelazko, Aqueous two phase system based on ionic liquid for isolation of quinine from human plasma sample, *Food Chem*, 166(2015) 150-7.

[250] C. He, S. Li, H. Liu, K. Li, F. Liu, Extraction of testosterone and epitestosterone in human urine using aqueous two-phase systems of ionic liquid and salt, *J Chromatogr A*, 1082(2005) 143-9.

[251] R.Y. Chiu, A.V. Thach, C.M. Wu, B.M. Wu, D.T. Kamei, An Aqueous Two-Phase System for the Concentration and Extraction of Proteins from the Interface for Detection Using the Lateral-Flow Immunoassay, *PloS one*, 10(2015) e0142654.

[252] D.Y. Pereira, R.Y. Chiu, S.C. Zhang, B.M. Wu, D.T. Kamei, Single-step, paper-based concentration and detection of a malaria biomarker, *Anal Chim Acta*, 882(2015) 83-9.

[253] F. Mashayekhi, R.Y. Chiu, A.M. Le, F.C. Chao, B.M. Wu, D.T. Kamei, Enhancing the lateral-flow immunoassay for viral detection using an aqueous two-phase micellar system, *Anal Bioanal Chem*, 398(2010) 2955-61.

[254] S. Hardt, T. Hahn, Microfluidics with aqueous two-phase systems, *Lab Chip*, 12(2012) 434-42.

[255] S.K. Sia, G.M. Whitesides, Microfluidic devices fabricated in Poly(dimethylsiloxane) for biological studies, *Electrophoresis*, 24(2003) 3563-76.

[256] D.F. Silva, A.M. Azevedo, P. Fernandes, V. Chu, J.P. Conde, M.R. Aires-Barros, Design of a microfluidic platform for monoclonal antibody extraction using an aqueous two-phase system, *J Chromatogr A*, 1249(2012) 1-7.

[257] J.A. Asenjo, B.A. Andrews, Aqueous two-phase systems for protein separation: phase separation and applications, *J Chromatogr A*, 1238(2012) 1-10.

- [258] S. Bamberger, G.V.F. Seaman, K.A. Sharp, D.E. Brooks, The effects of salts on the interfacial tension of aqueous dextran poly(ethylene glycol) phase systems, *J Colloid Interface Sci*, 99(1984) 194-200.
- [259] Y. Liu, R. Lipowsky, R. Dimova, Concentration dependence of the interfacial tension for aqueous two-phase polymer solutions of dextran and polyethylene glycol, *Langmuir*, 28(2012) 3831-9.
- [260] E. Atefi, J.A. Mann, Jr., H. Tavana, Ultralow interfacial tensions of aqueous two-phase systems measured using drop shape, *Langmuir*, 30(2014) 9691-9.
- [261] A. Gunther, K.F. Jensen, Multiphase microfluidics: from flow characteristics to chemical and materials synthesis, *Lab Chip*, 6(2006) 1487-503.
- [262] A. Aota, K. Mawatari, T. Kitamori, Parallel multiphase microflows: fundamental physics, stabilization methods and applications, *Lab Chip*, 9(2009) 2470-6.
- [263] S.O. Kasap, *Optoelectronics and Photonics: Principles and Practices*: Prentice Hall; 2001.
- [264] P. Alpuim, V. Chu, J.P. Conde, Amorphous and microcrystalline silicon films grown at low temperatures by radio-frequency and hot-wire chemical vapor deposition, *J Appl Phys*, 86(1999) 3812-21.
- [265] R.R.G. Soares, *Integrated Extraction, Concentration and Quantification of Ochratoxin A in Wines using a Microfluidic Aqueous Two Phase Extraction coupled to a Fluorescence Linked Immunosorbent Assay*: Instituto Superior Técnico; 2013.
- [266] P.A. Rosa, A.M. Azevedo, M.R. Aires-Barros, Application of central composite design to the optimisation of aqueous two-phase extraction of human antibodies, *J Chromatogr A*, 1141(2007) 50-60.
- [267] C. Li, J. Bai, W. Li, Z. Cai, F. Ouyang, Optimization of Conditions for Bacteriocin Extraction in PEG/Salt Aqueous Two-Phase Systems Using Statistical Experimental Designs, *Biotechnol Progr*, 17(2001) 366-8.
- [268] B. Mokhtarani, R. Karimzadeh, M.H. Amini, S.D. Manesh, Partitioning of Ciprofloxacin in aqueous two-phase system of poly(ethylene glycol) and sodium sulphate, *Biochem Eng J*, 38(2008) 241-7.
- [269] S. Raja, V.R. Murty, V. Thivaharan, V. Rajasekar, V. Ramesh, Aqueous Two Phase Systems for the Recovery of Biomolecules – A Review, *Sci Technology*, 1(2012) 7-16.
- [270] R.D. Rogers, H.D. Willauer, S.T. Griffin, J.G. Huddleston, Partitioning of small organic molecules in aqueous biphasic systems, *J Chromatogr B*, 711(1998) 255-63.
- [271] H.D. Willauer, J.G. Huddleston, R.D. Rogers, Solute Partitioning in Aqueous Biphasic Systems Composed of Polyethylene Glycol and Salt: The Partitioning of Small Neutral Organic Species, *Ind Eng Chem Res*, 41(2002) 1892-904.
- [272] H.D. Willauer, J.G. Huddleston, R.D. Rogers, Solvent Properties of Aqueous Biphasic Systems Composed of Polyethylene Glycol and Salt Characterized by the Free

Energy of Transfer of a Methylene Group between the Phases and by a Linear Solvation Energy Relationship, *Ind Eng Chem Res*, 41(2002) 2591-601.

[273] A.R. Katritzky, K. Tamm, M. Kuanar, D.C. Fara, A. Oliferenko, P. Oliferenko, et al., Aqueous Biphasic Systems. Partitioning of Organic Molecules: A QSPR Treatment, *J Chem Inf Comp Sci*, 44(2003) 136-42.

[274] Chemicalize.org (www.chemicalize.org) by ChemAxon (www.chemaxon.com), 12-20-2013

[275] M.M. Bora, S. Borthakur, P.C. Rao, N.N. Dutta, Aqueous two-phase partitioning of cephalosporin antibiotics: effect of solute chemical nature, *Sep Purif Technol*, 45(2005) 153-6.

[276] S. Saravanan, J.R. Rao, B.U. Nair, T. Ramasami, Aqueous two-phase poly(ethylene glycol)–poly(acrylic acid) system for protein partitioning: Influence of molecular weight, pH and temperature, *Process Biochem*, 43(2008) 905-11.

[277] F. Mashayekhi, A.M. Le, P.M. Nafisi, B.M. Wu, D.T. Kamei, Enhancing the lateral-flow immunoassay for detection of proteins using an aqueous two-phase micellar system, *Anal Bioanal Chem*, 404(2012) 2057-66.

[278] B. Sun, M.C. Leandro, V. de Freitas, M.I. Spranger, Fractionation of red wine polyphenols by solid-phase extraction and liquid chromatography, *J Chromatogr A*, 1128(2006) 27-38.

[279] P. Schofield, D.M. Mbugua, A.N. Pell, Analysis of condensed tannins: a review, *Anim Feed Sci Tech*, 91(2001) 21-40.

[280] M.M. Ngundi, L.C. Shriver-Lake, M.H. Moore, M.E. Lassman, F.S. Ligler, C.R. Taitt, Array Biosensor for Detection of Ochratoxin A in Cereals and Beverages, *Anal Chem*, 77(2004) 148-54.

[281] T.Y. Rusanova, N.V. Beloglazova, I.Y. Goryacheva, M. Lobeau, C. Van Peteghem, S. De Saeger, Non-instrumental immunochemical tests for rapid ochratoxin A detection in red wine, *Anal Chim Acta*, 653(2009) 97-102.

[282] A.M. Azevedo, P.A. Rosa, I.F. Ferreira, M.R. Aires-Barros, Optimisation of aqueous two-phase extraction of human antibodies, *J Biotechnol*, 132(2007) 209-17.

[283] P.A.J. Rosa, A.M. Azevedo, S. Sommerfeld, M. Mutter, M.R. Aires-Barros, W. Bäcker, Application of aqueous two-phase systems to antibody purification: A multi-stage approach, *J Biotechnol*, 139(2009) 306-13.

[284] S.A. Oelmeier, C. Ladd Effio, J. Hubbuch, High throughput screening based selection of phases for aqueous two-phase system-centrifugal partitioning chromatography of monoclonal antibodies, *J Chromatogr A*, 1252(2012) 104-14.

[285] D.H. Atha, K.C. Ingham, Mechanism of precipitation of proteins by polyethylene glycols. Analysis in terms of excluded volume, *J Biol Chem*, 256(1981) 12108-17.

- [286] J. Wu, Z. Wang, W. Lin, S. Chen, Investigation of the interaction between poly(ethylene glycol) and protein molecules using low field nuclear magnetic resonance, *Acta Biomater*, 9(2013) 6414-20.
- [287] H.P.S. Makkar, M. Blümmel, K. Becker, Formation of complexes between polyvinyl pyrrolidones or polyethylene glycols and tannins, and their implication in gas production and true digestibility in in vitro techniques, *Brit J Nutr*, 73(1995) 897-913.
- [288] T. Ozdal, E. Capanoglu, F. Altay, A review on protein–phenolic interactions and associated changes, *Food Res Int*, 51(2013) 954-70.
- [289] A. Bennick, Interaction of Plant Polyphenols with Salivary Proteins, *Crit Rev Oral Biol Med*, 13(2002) 184-96.
- [290] Y. Lu, Y. Xia, G. Luo, Phase separation of parallel laminar flow for aqueous two phase systems in branched microchannel, *Microfluid Nanofluidics*, 10(2010) 1079-86.
- [291] J.A. Vinson, B.A. Hontz, Phenol Antioxidant Index: Comparative Antioxidant Effectiveness of Red and White Wines, *J Agric Food Chem*, 43(1995) 401-3.
- [292] J.P. Conde, A.C. Pimentel, A.T. Pereira, A. Gouvêa, D.M.F. Prazeres, V. Chu, Detection of molecular tags with an integrated amorphous silicon photodetector for biological applications, *J Non-Cryst Solids*, 354(2008) 2594-7.
- [293] P. Novo, G. Moulas, D.M. França Prazeres, V. Chu, J.P. Conde, Detection of ochratoxin A in wine and beer by chemiluminescence-based ELISA in microfluidics with integrated photodiodes, *Sens Actuators, B*, 176(2013) 232-40.
- [294] M. Solfrizzo, G. Avantiaggiato, A. Visconti, Use of various clean-up procedures for the analysis of ochratoxin A in cereals, *J Chromatogr A*, 815(1998) 67-73.
- [295] A. Prella, D. Spadaro, A. Denca, A. Garibaldi, M.L. Gullino, Comparison of clean-up methods for ochratoxin A on wine, beer, roasted coffee and chili commercialized in Italy, *Toxins*, 5(2013) 1827-44.
- [296] N. Gulyaeva, A. Zaslavsky, P. Lechner, A. Chait, B. Zaslavsky, Relative hydrophobicity of organic compounds measured by partitioning in aqueous two-phase systems, *J Chromatogr B*, 743(2000) 187-94.
- [297] A.S. Schmidt, B.A. Andrews, J.A. Asenjo, Correlations for the partition behavior of proteins in aqueous two-phase systems: Effect of overall protein concentration, *Biotechnol Bioeng*, 50(1996) 617-26.
- [298] I.P. Trindade, M.M. Diogo, D.M.F. Prazeres, J.C. Marcos, Purification of plasmid DNA vectors by aqueous two-phase extraction and hydrophobic interaction chromatography, *J Chromatogr A*, 1082(2005) 176-84.
- [299] J. Chandrasekhar, G. Sonika, M.C. Madhusudhan, K.S.M.S. Raghavarao, Differential partitioning of betacyanins and betaxanthins employing aqueous two phase extraction, *J Food Eng*, 144(2015) 156-63.

- [300] W. Zhou, W. Kong, X. Dou, M. Zhao, Z. Ouyang, M. Yang, An aptamer based lateral flow strip for on-site rapid detection of ochratoxin A in *Astragalus membranaceus*, *J Chromatogr B*, 1022(2016) 102-8.
- [301] I. Azaiez, F. Giusti, G. Sagratini, J. Mañes, M. Fernández-Franzón, Multi-mycotoxins Analysis in Dried Fruit by LC/MS/MS and a Modified QuEChERS Procedure, *Food Anal Method*, 7(2014) 935-45.
- [302] R. Serra, C. Mendonça, L.s. Abrunhosa, A. Pietri, A. Venâncio, Determination of ochratoxin A in wine grapes: comparison of extraction procedures and method validation, *Anal Chim Acta*, 513(2004) 41-7.
- [303] M. Garcia, J.L. Blanco, G. Suarez, Aflatoxins B1 and G 1 solubility in standard solutions and stability during cold storage, *Mycotoxin Res*, 10(1994) 97-100.
- [304] J.H. Ryther, W.M. Dunstan, Nitrogen, Phosphorus, and Eutrophication in the Coastal Marine Environment, *Science*, 171(1971) 1008.
- [305] A.J.P. Smolders, E.C.H.E.T. Lucassen, R. Bobbink, J.G.M. Roelofs, L.P.M. Lamers, How nitrate leaching from agricultural lands provokes phosphate eutrophication in groundwater fed wetlands: the sulphur bridge, *Biogeochemistry*, 98(2009) 1-7.
- [306] A. Glyk, T. Scheper, S. Beutel, Influence of Different Phase-Forming Parameters on the Phase Diagram of Several PEG–Salt Aqueous Two-Phase Systems, *J Chem Eng Data*, 59(2014) 850-9.
- [307] R. Reverberi, L. Reverberi, Factors affecting the antigen-antibody reaction, *Blood Transfus*, 5(2007) 227-40.
- [308] M. Berovic, M. Legisa, Citric acid production, in: M.R. El-Gewely (Ed.) *Biotechnology Annual Review*, Elsevier2007, pp. 303-43.
- [309] A. Salis, B.W. Ninham, Models and mechanisms of Hofmeister effects in electrolyte solutions, and colloid and protein systems revisited, *Chem Soc Rev*, 43(2014) 7358-77.
- [310] B. Huang, H. Wu, S. Kim, R.N. Zare, Coating of poly(dimethylsiloxane) with n-dodecyl-[small beta]-d-maltoside to minimize nonspecific protein adsorption, *Lab Chip*, 5(2005) 1005-7.
- [311] R.D. Tilton, Mobility of biomolecules at interfaces, in: M. Malmsten (Ed.) *Biopolymers at interfaces*, Second Edition, Marcel Dekker, printed in USA, 2003.
- [312] J.R. Crowther, *The Elisa Guidebook*: Humana Press; 2001.
- [313] F. Zezza, F. Longobardi, M. Pascale, S.A. Eremin, A. Visconti, Fluorescence polarization immunoassay for rapid screening of ochratoxin A in red wine, *Anal Bioanal Chem*, 395(2009) 1317-23.
- [314] S. Xie, Y. Chai, Y. Yuan, L. Bai, R. Yuan, Development of an electrochemical method for Ochratoxin A detection based on aptamer and loop-mediated isothermal amplification, *Biosens Bioelectron*, 55(2014) 324-9.

- [315] X. Yang, J. Qian, L. Jiang, Y. Yan, K. Wang, Q. Liu, et al., Ultrasensitive electrochemical aptasensor for ochratoxin A based on two-level cascaded signal amplification strategy, *Bioelectrochemistry*, 96(2014) 7-13.
- [316] R. Wang, Y. Xiang, X. Zhou, L.H. Liu, H. Shi, A reusable aptamer-based evanescent wave all-fiber biosensor for highly sensitive detection of Ochratoxin A, *Biosens Bioelectron*, 66(2015) 11-8.
- [317] C. Wang, J. Qian, K. Wang, K. Wang, Q. Liu, X. Dong, et al., Magnetic-fluorescent-targeting multifunctional aptasensor for highly sensitive and one-step rapid detection of ochratoxin A, *Biosens Bioelectron*, 68(2015) 783-90.
- [318] X. Liu, Y. Xu, D.B. Wan, Y.H. Xiong, Z.Y. He, X.X. Wang, et al., Development of a nanobody-alkaline phosphatase fusion protein and its application in a highly sensitive direct competitive fluorescence enzyme immunoassay for detection of ochratoxin A in cereal, *Anal Chem*, 87(2015) 1387-94.
- [319] G.D.J. Phillies, Diffusion of bovine serum albumin in a neutral polymer solution, *Biopolymers*, 24(1985) 379-86.
- [320] M. Zimmermann, H. Schmid, P. Hunziker, E. Delamarche, Capillary pumps for autonomous capillary systems, *Lab Chip*, 7(2007) 119-25.
- [321] Z. Dzuman, M. Zachariasova, O. Lacina, Z. Veprikova, P. Slavikova, J. Hajslova, A rugged high-throughput analytical approach for the determination and quantification of multiple mycotoxins in complex feed matrices, *Talanta*, 121(2014) 263-72.
- [322] N. Arroyo-Manzanares, J.F. Huertas-Perez, L. Gamiz-Gracia, A.M. Garcia-Campana, Simple and efficient methodology to determine mycotoxins in cereal syrups, *Food Chem*, 177(2015) 274-9.
- [323] Y. Luan, Z. Chen, G. Xie, J. Chen, A. Lu, C. Li, et al., Rapid Visual Detection of Aflatoxin B1 by Label-Free Aptasensor Using Unmodified Gold Nanoparticles, *J Nanosci Nanotechnol*, 15(2015) 1357-61.
- [324] Y. Luan, J. Chen, C. Li, G. Xie, H. Fu, Z. Ma, et al., Highly Sensitive Colorimetric Detection of Ochratoxin A by a Label-Free Aptamer and Gold Nanoparticles, *Toxins*, 7(2015) 4883.
- [325] Y. Xiong, K. Pei, Y. Wu, Y. Xiong, Colorimetric ELISA based on glucose oxidase-regulated the color of acid-base indicator for sensitive detection of aflatoxin B 1 in corn samples, *Food Control*, 78(2017) 317-23.
- [326] D. Kong, L. Liu, S. Song, S. Suryoprabowo, A. Li, H. Kuang, et al., A gold nanoparticle-based semi-quantitative and quantitative ultrasensitive paper sensor for the detection of twenty mycotoxins, *Nanoscale*, 8(2016) 5245-53.
- [327] I.F. Pinto, D.R. Santos, C.R.F. Caneira, R.R.G. Soares, A.M. Azevedo, V. Chu, et al., Optical biosensing in microfluidics using nanoporous microbeads and amorphous silicon thin-film photodiodes: quantitative analysis of molecular recognition and signal transduction, *J Micromechanics Microengineering*, 28(2018) 094004.

- [328] F. Batista-Viera, J.-C. Janson, J. Carlsson, *Affinity Chromatography, Protein Purification*, John Wiley & Sons, Inc.2011, p. 231.
- [329] C.T. Lim, Y. Zhang, Bead-based microfluidic immunoassays: the next generation., *Biosens Bioelectron*, 22(2007) 1197-204.
- [330] J. Chou, A. Lennart, J. Wong, M.F. Ali, P.N. Floriano, N. Christodoulides, et al., Modeling analyte transport and capture in porous bead sensors., *Anal Chem*, 84(2012) 2569-75.
- [331] J.A. Thompson, H.H. Bau, Porous bead-based microfluidic assay: theory and confocal microscope imaging., *Microfluid Nanofluid*, 12(2011) 625-37.
- [332] J. Kim, J. Heo, R.M. Crooks, Hybridization of DNA to bead-immobilized probes confined within a microfluidic channel., *Langmuir*, 22(2006) 10130-4.
- [333] W.J. Catalona, A.W. Partin, K.M. Slawin, et al., Use of the percentage of free prostate-specific antigen to enhance differentiation of prostate cancer from benign prostatic disease: A prospective multicenter clinical trial, *JAMA*, 279(1998) 1542-7.
- [334] R. Epifania, R.R.G. Soares, I.F. Pinto, V. Chu, J.P. Conde, Capillary-driven microfluidic device with integrated nanoporous microbeads for ultrarapid biosensing assays, *Sens Actuators, B*, 265(2018) 452-8.
- [335] K. Ren, Y. Zhao, J. Su, D. Ryan, H. Wu, Convenient Method for Modifying Poly(dimethylsiloxane) To Be Airtight and Resistive against Absorption of Small Molecules, *Anal Chem*, 82(2010) 5965-71.
- [336] M.S. Maria, P.E. Rakesh, T.S. Chandra, A.K. Sen, Capillary flow-driven microfluidic device with wettability gradient and sedimentation effects for blood plasma separation, *Sci Rep*, 7(2017) 43457.
- [337] S.A. Oelmeier, F. Dimer, J. Hubbuch, Application of an aqueous two-phase systems high-throughput screening method to evaluate mAb HCP separation, *Biotechnol Bioeng*, 108(2011) 69-81.
- [338] P. Novo, D.M. Prazeres, V. Chu, J.P. Conde, Microspot-based ELISA in microfluidics: chemiluminescence and colorimetry detection using integrated thin-film hydrogenated amorphous silicon photodiodes, *Lab Chip*, 11(2011) 4063-71.
- [339] A. Joskowiak, N. Stasio, V. Chu, D.M. Prazeres, J.P. Conde, Integrated detection of intrinsic fluorophores in live microbial cells using an array of thin film amorphous silicon photodetectors, *Biosens Bioelectron*, 36(2012) 242-9.
- [340] A.T. Pereira, A.C. Pimentel, V. Chu, D.M.F. Prazeres, J.P. Conde, Chemiluminescent Detection of Horseradish Peroxidase Using an Integrated Amorphous Silicon Thin-Film Photosensor, *Sensors Journal, IEEE*, 9(2009) 1282-90.
- [341] A.C. Pimentel, A.T. Pereira, D.M.F. Prazeres, V. Chu, J.P. Conde, Detection of fluorescently labeled biomolecules immobilized on a detachable substrate using an integrated amorphous silicon photodetector, *Appl Phys Lett*, 94(2009) 164106.

[342] A.C. Pimentel, D.M.F. Prazeres, V. Chu, J.P. Conde, Comparison of amorphous silicon photodiodes and photoconductors for detection of quantum dot biomolecular tags, *J Appl Phys*, 106(2009) 104904.

[343] J.C. Frisvad, 10 - Rationale for a polyphasic approach in the identification of mycotoxigenic fungi A2 - Saeger, Sarah De, *Determining Mycotoxins and Mycotoxigenic Fungi in Food and Feed*, Woodhead Publishing 2011, pp. 279-97.

[344] F. Munaut, F.V. Hove, 11 – Molecular identification of mycotoxigenic fungi in food and feed, *Determining mycotoxins and mycotoxigenic fungi in food and feed*, Woodhead Publishing Limited, Cambridge, 2011.

[345] M. Santamaria, 13 - DNA barcoding of toxigenic fungi: a perspective A2 - Saeger, Sarah De, *Determining Mycotoxins and Mycotoxigenic Fungi in Food and Feed*, Woodhead Publishing 2011, pp. 349-56.

[346] Y. Luo, W. Gao, M. Doster, T.J. Michailides, Quantification of conidial density of *Aspergillus flavus* and *A. parasiticus* in soil from almond orchards using real-time PCR, *Journal of Applied Microbiology*, 106(2009) 1649-60.

[347] Z.Y. Yang, W.B. Shim, J.H. Kim, S.J. Park, S.J. Kang, B.S. Nam, et al., Detection of aflatoxin-producing molds in Korean fermented foods and grains by multiplex PCR, *J Food Prot*, 67(2004) 2622-6.

[348] F. Degola, E. Berni, E. Spotti, I. Ferrero, F.M. Restivo, Facing the problem of "false positives": re-assessment and improvement of a multiplex RT-PCR procedure for the diagnosis of *A. flavus* mycotoxin producers, *Int J Food Microbiol*, 129(2009) 300-5.

[349] M. Godet, F. Munaut, Molecular strategy for identification in *Aspergillus* section Flavi, *FEMS Microbiol Lett*, 304(2010) 157-68.

[350] Y. Suanthie, M.A. Cousin, C.P. Woloshuk, Multiplex real-time PCR for detection and quantification of mycotoxigenic *Aspergillus*, *Penicillium* and *Fusarium*, *J Stored Prod Res*, 45(2009) 139-45.

[351] S. Sadhasivam, M. Britzi, V. Zakin, M. Kostyukovsky, A. Trostanetsky, E. Quinn, et al., Rapid Detection and Identification of Mycotoxigenic Fungi and Mycotoxins in Stored Wheat Grain, *Toxins*, 9(2017).

Appendix A

This appendix describes the preliminary methodology and instrumentation developed to perform the photoluminescence signal acquisition of a miniaturized immunoassay, aimed at detecting the mycotoxin deoxynivalenol (DON) in spiked buffer samples as a model system. These developments were performed within the scope of a course on sensors and instrumentation lectured by Prof. Agostinho Cláudio da Rosa and Prof. Luís Joaquim Pina da Fonseca at Instituto Superior Técnico, Lisbon. The light acquisition was performed using a commercial 2.4 by 2.4 mm c-Si photodiode covered with an a-SiC:H filter, the latter deposited on a 700 μm thick glass slide. The photodiode was addressed using a prototype transimpedance amplifier circuit mounted on a breadboard. The circuit design was based on that developed in collaboration with Lumisense Lda. as discussed in **Chapter 5**. The voltage signal acquisition was performed using a commercial Arduino Mega microcontroller board and the data processing was performed in real time using a MATLAB program. The proof of concept for the signal acquisition was performed for a DON immunoassay performed in a single bead microcolumn according to **Chapter 10**.

Circuit components and assembly

All components used to prototype the transimpedance circuit according to **Figure A 1-A** were purchased from RS components including the 1 $\text{G}\Omega$ resistor, 100 pF capacitor, 330 nF capacitor and LMC6482 CMOS high precision opamp. The c-Si photodiode (S1226-5BQ), operated at 0 V bias was purchased from Hamamatsu Photonics. The opamp and highly resistive negative feedback loop provide a total gain of 180 dB, meaning that a current output of 1 nA from the photodiode results in a voltage of 1 V between the output of the opamp and the ground. The opamp was powered by the 5 V pin of the microcontroller board, resulting in an output swing between 0 and approximately 5 V. An extra capacitor of 100 pF was added in the feedback loop to minimize oscillations and ringing by overcompensating the internal capacitance of the photodiode (160 pF). The higher capacitance 330 nF ceramic capacitors and decoupling capacitors aim at further minimizing high frequency noise in the power supply of the opamp circuit. The assembly of the breadboard, Arduino board and photosensor is shown in **Figure A 1-B** and C. The voltage output from the opamp is acquired by the 10-bit ADC

(resolution of ≈ 5 mV) of the Arduino board and further processed continuously, at 0.1 s intervals, using a MATLAB program. The program outputs the voltage measurement over time and respective 30 s linear slope (V/s) of the previous 300 readings.

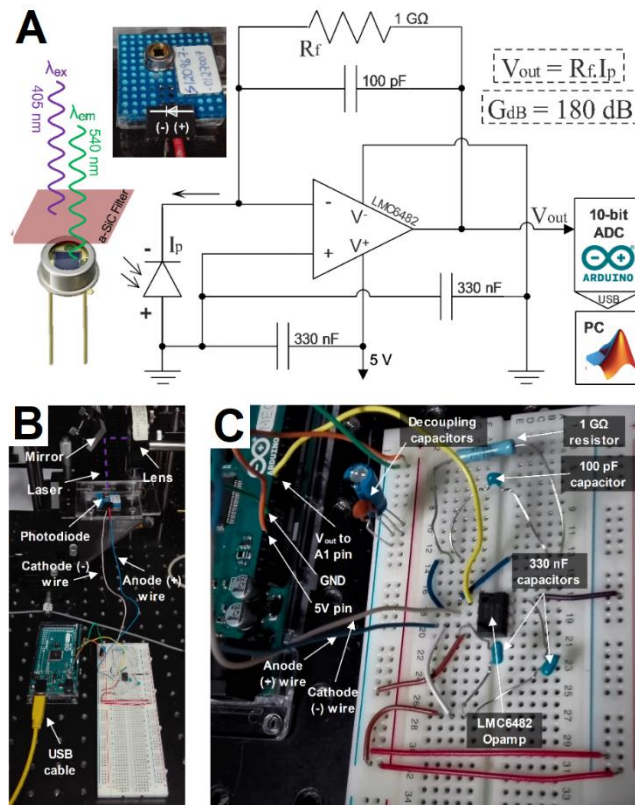


Figure A 1 - A- Schematics of the transimpedance amplification circuit used to address the c-Si photodiode, covered by the absorption filter. The LMC6482 opamp with a $1\text{ G}\Omega$ feedback resistor (R_f) provides a gain of 180 dB on the input current generated by the photodiode (I_p), meaning that a 10 pA current generates an output of 10 mV (V_{out}). The voltage signal over time is acquired with an Arduino board with a 10-bit ADC, meaning that the resolution is 4 mV considering an output swing of $+5\text{ V}$. The acquired voltage signals sent through the serial port with an interval of 0.1 s are continuously processed using a MATLAB program. **B** and **C-** photographs of the transimpedance circuit prototype connected to the Arduino board and addressing the photodiode mounted on an optical table and aligned with a focused 405 nm laser beam (diameter $\approx 1\text{ mm}$).

Arduino IDE and MATLAB programs

The programs written to acquire the voltage input at the A1 pin on the Arduino board (open source integrated development environment (IDE)) and in MATLAB to process the data are transcribed below with relevant comments in each line of code.

```
void setup() {
  // initialize serial communication at 9600 bits per second:
  Serial.begin(9600);
}
```

```

void loop() {
// read the input on analog pin A1:
  int sensorValue = analogRead(A1);
  // convert the analog reading (ranging from 0 to 1023) to a voltage
(raging from 0 to 5V):
  float voltage = sensorValue * (5.0 / 1023.0);
  // print out the value you read through the serial port:
  Serial.println(voltage);
  // wait 0.1 s before repeating the loop section, meaning that the
voltage readings will be performed at 0.1 s intervals
  delay(100);
}

clc % clear any previously plotted data
clear all % clear all stored objects in workspace and reset all
assumptions

rt = 0.1; % set sampling rate of arduino in seconds
m = 3; % set total measurement time in minutes
s = m*60*(1/rt); % parameter to define the size and spacing of the x-
axis vector

s1=serial('COM3'); % select COM port for the USB connection to the
arduino board
set(s1, 'DataBits' , 8 , 'StopBits' , 1 , 'terminator' , 'LF'
,'BaudRate' ,9600,'Parity' , 'none');
% set MATLAB to receive binary information from the serial port with
one
% stop bit and a baudrate of 9600 to match the information sent by the
% arduino board
fopen(s1); %open file where the binary voltage readings are being
written on
x=linspace(1,s,s); %create a vector of "s" linearly spaced points
between 1 and "s", which is the size of the x axis
set(gcf,'CurrentCharacter','@'); % set a dummy character, in this case
"@"

for i=1:length(x) % loop function to plot the voltage readings
  k=get(gcf,'CurrentCharacter'); % attribute current character as
the variable "k"
  clf; % clear information in the current plot
  y1(i)=fscanf(s1,'%f'); % in each loop, add to the vector "y1" the
voltage value written in file "s1"
  yyaxis left; % position the first y axis on the left of the plot
  plot((x(1:i))/(1/rt),y1); % make the plot of each voltage value vs
time in seconds
  xlabel('Time (s)'); % label for the x-axis of the plot
  ylabel('Voltage (V)'); %label for the left axis of the plot
  if i>=301 % after acquiring 300 voltage values, perform the loop
function to calculate the linear slope
    ym=polyfit((x(i-300:i))/(1/rt),y1(i-300:i),1); % in each loop,
calculate the linear slope of the last 300 voltage reads

```

```

        y2(i)=ym(1); % attribute to the variable "y2" only the slope
of the vector "ym", which contains the m and the b
        yyaxis right; % position the second y axis on the right of the
plot
        plot((x(1:i))/10,y2); % make the plot of each slope value vs
time in seconds
        ylabel('Slope(V/s)'); % label for the right axis of the plot
    end
    drawnow; % draw the plot on the screen at the end of each loop,
meaning each time a voltage is read
    % below is the function used to abort the real-time voltage
plotting if necessary
    if k~='@' % in each loop check if the dummy character is still "@"
        set(gcf,'CurrentCharacter','@'); % if it is not "@", set it
back to "@"
        if k=='q'; % if the character is equal to "q", meaning "quit",
execute the function below
            clf; % clear all data from the plot
            fclose(s1); % close the serial port communication
            return; % return control to keyboard
        end
    end
end
end
clf; % after acquiring all voltage readings for "m" minutes, clear
data and make a final voltage and slope plot
yyaxis left;
plot(x/10,y1);
xlabel('Time (s)');
ylabel('Voltage (V)');
yyaxis right;
plot(x/10,y2);
ylabel('Slope(V/s)');
fclose(s1); % close the serial port communication

```

Photodiode characterization using the transimpedance circuit

The photodiode measurements were first tested by impinging the laser light directly on the sensor through the absorption filter to assess the response measured in terms of voltage against the intensity of light. The intensity of light in this case was adjusted by placing different neutral density (ND) filters in front of the laser beam, ranging from 1% (ND 2.0) to 100% (no ND filter) transmittance. The raw data that was continuously acquired using the MATLAB program while changing the ND filters can be seen in **Figure A 2-A**. The plateau of voltage using each filter was subsequently plotted against the relative light intensity of the laser and a linear relation was obtained as expected (**Figure A 2- B**).

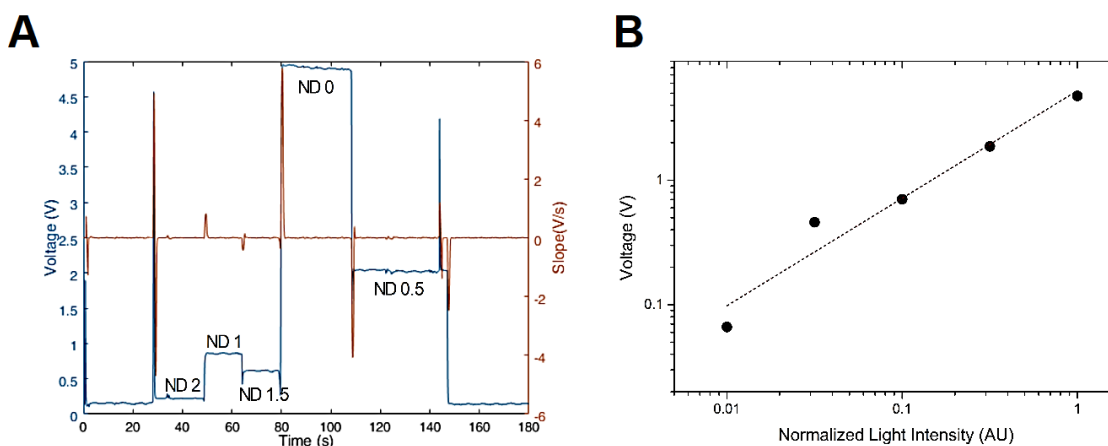


Figure A 2 - **A**- Continuous measurement of voltage over time while impinging the laser light on top of the photodiode through the a-SiC:H absorption filter. The initial and final voltage plateaus correspond to the measurement performed in the dark with the laser turned OFF. Different ND filters were placed in front of the laser light, providing a light transmission ranging from 1 to 100% (0.01 to 1 AU). For this measurement, the slope was calculated as the linear voltage slope of the last 10 points (1 s). **B**- Average voltage reading at increasing light intensities impinging on the photodiode through the absorption filter.

On-line fluorescence sensing and signal processing

Having in account the relatively low photoluminescence emitted from the 700 μm wide microchannel and the relatively large size of the commercial photodiode (2.4 x 2.4 mm), it was necessary to minimize all possible electromagnetic sources of interference and maximize the specific signal. Therefore, the transimpedance circuit and Arduino board were enclosed inside a grounded metal box to serve as a Faraday cage as shown in **Figure A 3**. The measurements were then performed in the dark while impinging the laser on the beads, previously aligned with the center of the photodiode. The raw voltage data acquired over time in Arduino and processed using the MATLAB program for the reference (0 ng/mL DON) and contaminated (100 ng/mL DON) samples are shown in **Figure A 4**. The data acquisition was started 2 s before turning on the laser and about 5 s before turning on the syringe pump, to first average the baseline (30 data points) provided by the excitation light. Comparing the reference and DON contaminated samples, the voltage values above the laser baseline at the end of 180 s were 0.040 V and 0.016 V, respectively, equating a DON-specific signal drop of $\approx 59\%$.

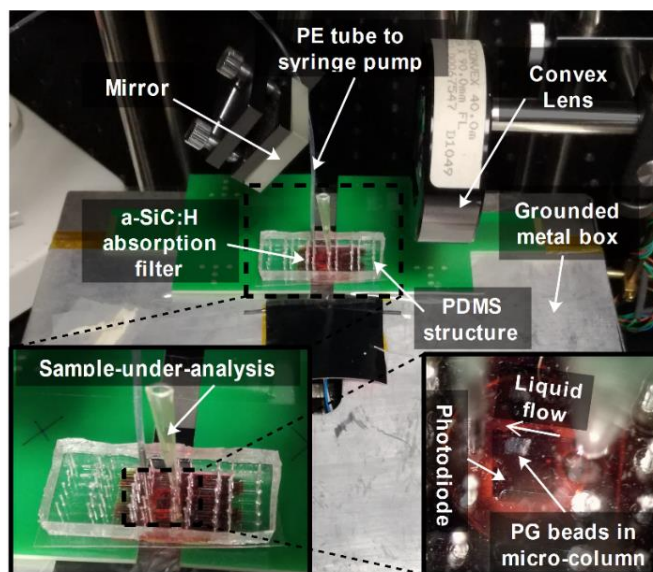


Figure A 3 - Experimental setup used to perform the fluorescence measurements of the competitive immunoassay. To minimize electromagnetic noise, the breadboard with the mounted circuit and Arduino were placed inside a grounded metal box. The photodiode was mounted through a hole in the box to leave only the photodiode exposed. The convex lens and mirror are used for the focusing and alignment of the laser light used for excitation. The a-SiC:H filter deposited on glass is placed in between the PDMS structure and the photodiode. The packed beads are first aligned with the photodiode and the box is then aligned with the laser beam, having a focal diameter of approximately 1 mm.

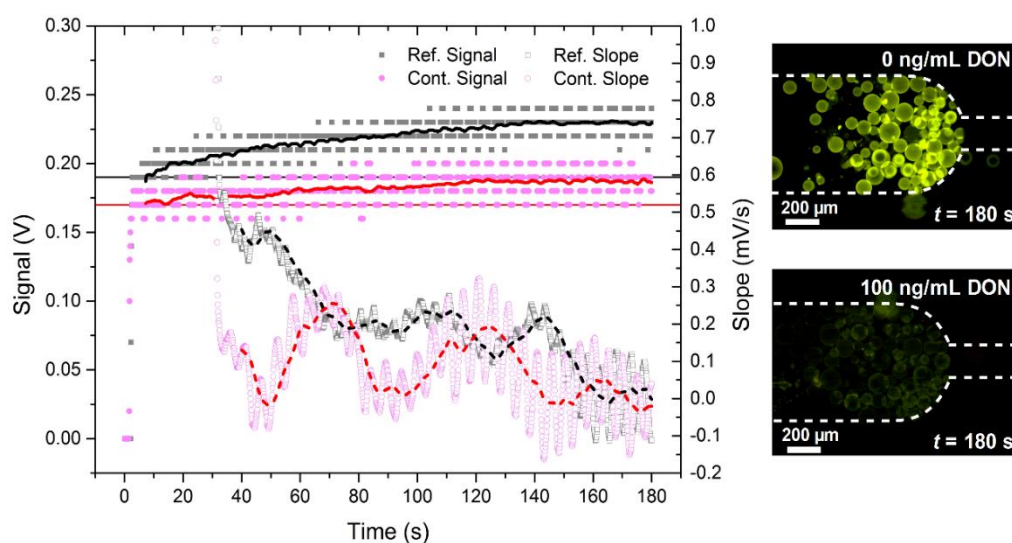


Figure A 4 - Fluorescence measurements performed using the photodiode addressed by the transimpedance amplification circuit. The voltage values and respective 30 s linear slopes were continuously acquired using the MATLAB program described above. The laser light passing through a ND 1.5 filter was turned ON 2 s after starting the signal acquisition. The baseline of the impinging laser light is highlighted as black and red horizontal lines for the reference (0 ng/mL DON) and contaminated (100 ng/mL DON) samples respectively. The square and round dots are the raw data and the continuous and dashed lines are the respective moving averages of 50 points (5 s) aimed at minimizing the periodic oscillations during the measurement. The fluorescence microscopy images on the right correspond to the structures measured using the photodiode, after 180 s of flowing the SUA containing 10 $\mu\text{g/mL}$ DON-BSA-Alexa 430 at 15 $\mu\text{L/min}$.

Curriculum Vitae

Personal address: Rua Pires Antunes n. 15 c/v DTA
(Monte Abraão, Sintra, Portugal) 2745-327 Queluz

Work address: INESC MN, Rua Alves Redol, 9
(Lisbon, Portugal) 1000-029 Lisbon

Contact (mobile phone, e-mail): +351 963481528,
ruben.soares@tecnico.ulisboa.pt

Nationality: Portuguese

Date of birth: September 16th, 1990

Personal URLs: ORCID (<https://orcid.org/0000-0001-5958-5232>)

LinkedIn (<https://www.linkedin.com/in/ruben-soares-94a1b94a/>)

ResearchGate (https://www.researchgate.net/profile/Ruben_Soares3)

Google Scholar (<https://goo.gl/e06NIv>)



1. Professional Experience

July 2014 to July 2018 (expected)

Research scientist and PhD student at INESC Microsystems and Nanotechnologies (INESC MN) and at the Institute of Bioengineering and Biosciences (IBB), Instituto Superior Técnico, Lisbon. Project title: “Development of a microfluidic mycotoxin screening chip for point-of-need food safety applications” (FCT Grant SFRH/BD/97354/2013).

Supervisors: Prof. João Pedro Conde, full Professor at Instituto Superior Técnico and co-director at INESC Microsystems and Nanotechnologies, and Prof. M. Raquel Aires-Barros, full Professor at Instituto Superior Técnico and group leader at the Bioseparations Laboratory from the Institute for Bioengineering and Biosciences (IBB).

November 2013 to July 2014

MSc research fellow at INESC Microsystems and Nanotechnologies (INESC MN).

Project title: "Microfluidic methods of extraction, purification and concentration" (FCT project EXCL/CTM-NAN/0441/2012).

July 2012 to November 2013

Research scientist and MSc student at INESC Microsystems and Nanotechnologies (INESC MN) and at the Institute of Bioengineering and Biosciences (IBB), Instituto Superior Técnico, Lisbon. Project title: “Integrated Extraction, Concentration and Quantification of Ochratoxin A in Wines using a Microfluidic Aqueous Two-Phase Extraction coupled to a Fluorescence-Linked Immunosorbent Assay”.

2. Education

September 2011 to November 2013

Master of Science (MSc) degree in Biotechnology awarded by Instituto Superior Técnico, University of Lisbon. Final classification of 19 out of 20 (GPA). ECTS grade A.

September 2008 to July 2011

Bachelor of Science (BSc) degree in Biochemistry awarded by the Faculty of Science, University of Lisbon. Final classification of 17 out of 20 (GPA). ECTS grade A.

3. List of Publications in International Peer-Reviewed Journals

3.1. Original Research Articles

[1] Pinto, I.F., Santos, D.R., Caneira, C.R.F., Soares, R.R.G., Azevedo, A.M., Chu V., Conde, J.P. *Optical biosensing in microfluidics using nanoporous microbeads and amorphous silicon thin-film photodiodes: quantitative analysis of molecular recognition and signal transduction.* **Journal of Micromechanics and Microengineering** 28, 094004 (2018).

[2] Soares, R.R.G., Santos, D.R., Pinto, I.F., Azevedo, A.M., Aires-Barros, M.R., Chu, V., Conde, J.P. *Multiplexed microfluidic fluorescence immunoassay with photodiode array signal acquisition for sub-minute and point-of-need detection of mycotoxins.* **Lab on a chip** 18 (11), 1569-1580 (2018).

- [3] Epifania, R., Soares, R.R.G., Pinto, I.F., Chu, V., Conde, J.P. *Capillary-driven microfluidic device with integrated nanoporous microbeads for ultrarapid biosensing assays*. **Sensors and Actuators B: Chemical**, 265, 452-458 (2018).
- [4] Pinto, I.F., Santos, D.R., Soares, R.R.G., Aires-Barros, M.R., Chu, V., Azevedo, A.M., Conde, J.P. *A regenerable microfluidic device with integrated valves and thin-film photodiodes for rapid optimization of chromatography conditions*. **Sensors and Actuators B: Chemical**, 255, 3636-3646 (2018).
- [5] Machado, J.M.D., Soares, R.R.G., Chu, V., Conde, J.P. *Multiplexed capillary microfluidic immunoassay with smartphone data acquisition for parallel mycotoxin detection*. **Biosensors and Bioelectronics**, 99, 40-46 (2018).
- [6] Santos, D.R., Soares, R.R.G., Chu, V., Conde, J.P. *Performance of Hydrogenated Amorphous Silicon Thin Film Photosensors at Ultra-Low Light Levels: Towards Attomole Sensitivities in Lab-on-Chip Biosensing Applications*. **IEEE Sensors Journal**, 17 (21), 6895-6903 (2017).
- [7] Brás, E.J.S., Soares, R.R.G., Azevedo, A.M., Fernandes, P., Arévalo-Rodríguez, M., Chu, V., Conde, J.P., Aires-Barros, M.R. *A multiplexed microfluidic toolbox for the rapid optimization of affinity-driven partition in aqueous two-phase systems*. **Journal of Chromatography A**, 1515, 252-259 (2017).
- [8] Soares, R.R.G., Azevedo, A.M., Fernandes, P., Chu, V., Conde, J.P., Aires-Barros, M.R. *A simple method for point-of-need extraction, concentration and rapid multi-mycotoxin immunodetection in feeds using aqueous two-phase systems*. **Journal of Chromatography A**, 1511, 15-24 (2017).
- [9] Pinto, I.F., Caneira, C.R.F., Soares, R.R.G., Madaboosi, N., Aires-Barros, M.R., Conde, J.P., Azevedo, A.M., Chu, V. *The application of microbeads to microfluidic systems for enhanced detection and purification of biomolecules*. **Methods**, 116 (1), 112–124 (2017).
- [10] Soares, R.R.G., Santos, D.R., Chu, V., Azevedo, A.M., Aires-Barros, M.R., Conde, J.P. *A point-of-use microfluidic device with integrated photodetector array for immunoassay multiplexing: detection of a panel of mycotoxins in multiple samples*. **Biosensors and Bioelectronics**, 87, 823-831 (2017).
- [11] Pinto, I.F., Soares, R.R.G., Rosa, S.A.S.L., Aires-Barros, M.R., Chu, V., Conde, J.P., Azevedo, A.M. *High-Throughput Nanoliter-Scale Analysis and Optimization of Multimodal Chromatography for the Capture of Monoclonal Antibodies*. **Analytical Chemistry**, 88 (16), 7959-7967 (2016).

- [12] Soares, R.R.G., Ramadas, D., Chu, V., Aires-Barros, M.R., Conde, J.P., Viana, A.S., Cascalheira, A.C. *An ultrarapid and regenerable microfluidic immunoassay coupled with integrated photosensors for point-of-use detection of ochratoxin A*. **Sensors and Actuators B: Chemical**, 235, 554-562 (2016).
- [13] Jolly, P., Damborsky, P., Madaboosi, N., Soares, R.R.G., Chu, V., Conde, J.P., Katrlík, J., Estrela, P. *DNA aptamer-based sandwich microfluidic assays for dual quantification and multi-glycan profiling of cancer biomarkers*. **Biosensors and Bioelectronics**, 79, 313-319 (2016).
- [14] Jacinto, M.J., Soares, R.R.G., Azevedo, A.M., Chu, V., Tover, A., Conde, J.P., Aires-Barros, M.R. *Optimization and miniaturization of aqueous two-phase systems for the purification of recombinant human immunodeficiency virus-like particles from a CHO cell supernatant*. **Separation and Purification Technology**, 154, 27-35 (2015).
- [15] Madaboosi, N., Soares, R.R.G., Chu, V., Conde, J.P. *A microfluidic immunoassay platform for the detection of free prostate specific antigen: a systematic and quantitative approach*. **Analyst**, 140 (13), 4423-4433 (2015).
- [16] Soares, R.R.G., Novo, P., Azevedo, A.M., Fernandes, P., Aires-Barros, M.R., Chu, V., Conde, J.P. *On-chip sample preparation and analyte quantification using a microfluidic aqueous two-phase extraction coupled with an immunoassay*. **Lab on a chip** 14 (21), 4284-4294 (2014).
- [17] Soares, R.R.G., Novo, P., Azevedo, A.M., Fernandes, P., Chu, V., Conde, J.P., Aires-Barros, M.R. *Aqueous two-phase systems for enhancing immunoassay sensitivity: simultaneous concentration of mycotoxins and neutralization of matrix interference*. **Journal of Chromatography A** 1361, 67-76 (2014).

3.2. Review Articles

- [1] Soares, R.R.G., Ricelli, A., Fanelli, C., Caputo, D., de Cesare, G., Chu, V., Aires-Barros, M.R., Conde, J.P. *Advances, challenges and opportunities for point-of-need screening of mycotoxins in foods and feeds*. **Analyst** 143 (5), 1015-1035 (2018).
- [2] Soares, R.R.G., Silva, D.F.C., Fernandes, P., Azevedo, A.M., Chu, V., Conde, J.P., Aires-Barros, M.R. *Miniaturization of aqueous two-phase extraction for biological applications: From micro-tubes to microchannels*. **Biotechnology Journal**, 11 (12), 1498–1512 (2016).

[3] Conde, J.P., Madaboosi, N., Soares, R.R.G., Fernandes, J.T.S., Novo, P., Moulas, G., Chu, V. *Lab-on-chip systems for integrated bioanalyses*. **Essays in Biochemistry**, 60 (1), 121-131 (2016).

[4] Soares, R.R.G., Azevedo, A.M., Van Alstine, J.M., Aires-Barros, M.R. *Partitioning in aqueous two-phase systems: Analysis of strengths, weaknesses, opportunities and threats*. **Biotechnology Journal**, 10 (8), 1158-1169 (2015).

3.3. Conference Proceedings

[1] Soares, R.R.G., Santos, D.R., Pinto, I.F., Azevedo, A.M., Aires-Barros, M.R., Chu, V., Conde, J.P. *Multiplexed microfluidic platform coupled with photodetector array for point-of-need and sub-minute detection of food contaminants*. **Micro Electro Mechanical Systems (MEMS), 2018 IEEE**, pp. 6-9 (2018).

[2] Pinto, I.F., Santos, D.R., Caneira, C.R.F., Soares, R.R.G., Chu, V., Conde, J.P. *Quantitative analysis of optical transduction in microfluidic biosensing platforms: Nanoporous microbeads coupled with thin-film photodiodes*. **Micro Electro Mechanical Systems (MEMS), 2018 IEEE**, pp. 278-281 (2018).

[3] Santos, D. R., Soares, R. R. G., Chu, V., Aires-Barros, M. R., Conde, J. P., 2016. *A multiplexed integrated a-Si:H photosensor for simultaneous detection of mycotoxins for point-of-use food safety applications*. **Euroensors 2016**, 168 pp. 1422-1425 (2016).

[4] Pinto, I. F., Soares, R. R. G., Santos, D. R., Aires-Barros, M. R., Chu, V., Azevedo, A. M., Conde, J.P., 2016. *Integration of photosensors in a nano-liter scale chromatography column for the online monitoring of adsorption/desorption kinetics of a fluorophore-labeled monoclonal antibody*. **Euroensors 2016**, 168 pp. 1426-1429 (2016).

[5] Soares, R.R.G., Santos, D. R., Pinto, I. F., Azevedo, A. M., Chu, V., Aires-Barros, M. R., Conde, J. P., 2016. *Point-of-use ultrafast single-step detection of food contaminants: a novel microfluidic fluorescence-based immunoassay with integrated photodetection*. **Euroensors 2016**, 168 pp. 329-332 (2016).

[6] Tzouvadaki, I., Madaboosi, N., Soares, R.R.G., Chu, V., Conde, J.P., Micheli, G.D., Carrara, S., 2015. *Bio-functionalization study of Memristive-Biosensors for early detection of prostate cancer*. **Ph.D. Research in Microelectronics and Electronics (PRIME), 2015 11th Conference on**, pp. 17-20 (2015).

[7] Madaboosi, N., Pedrosa, C.R., Reis, M.F., Soares, R.R.G., Chu, V., Conde, J.P., 2014. *Microfluidic ELISA for sensing of prostate cancer biomarkers using integrated a-Si:H p-i-n photodiodes*. **Sensors, 2014 IEEE**, pp. 881-884 (2014).

4. Contributed Presentations in Scientific Conferences

- [1] Soares, R. R. G., Santos, D. R., Pinto, I. F., Azevedo, A. M., Aires-Barros, M. R., Chu, V., Conde, J. P. *Multiplexed microfluidic platform coupled with photodetector array for point-of-need and sub-minute detection of food contaminants* (Oral Presentation). **MEMS 2018 - IEEE International Conference on Micro Electro Mechanical Systems**, Belfast, Northern Ireland (January 2018).
- [2] Soares, R.R.G., Azevedo, A.M., Fernandes, P., Chu, V., Conde, J.P., Aires-Barros, M.R. *Aqueous two-phase systems as a green and simple sample preparation procedure: simultaneous extraction and concentration of mycotoxins for subsequent immunodetection* (Oral Presentation). **European Society of Biochemical Engineering Sciences (ESBES) Workshop ABC² - Anything But Conventional Chromatography**, Lisbon, Portugal (November 2017).
- [3] Soares, R.R.G., Caneira, C.R.F., Pinto, I.F., Madaboosi, N., Chu, V., Azevedo, A.M., Conde, J.P., Aires-Barros, M.R. *Analytical affinity chromatography-on-a-chip for selective capture and sensitive detection of protein and polynucleotide biomarkers* (Oral Presentation). **ECI Separations Technology IX**, Albufeira, Portugal (March 2017).
- [4] Soares, R.R.G., Pinto, I. F., Santos, D. R., Azevedo, A. M., Chu, V., Aires-Barros, M. R., Conde, J. P. *A novel point-of-use, ultrafast and sensitive fluorescence immunoassay for the simultaneous detection of multiple mycotoxins using nanoporous agarose beads confined in microchannels* (Poster Presentation). **MicroTAS - Miniaturized Systems for Chemistry and Life Sciences 2016**, Dublin, Ireland (October 2016).
- [5] Soares, R.R.G., Ramadas, D., Azevedo, A.M., Fernandes, P., Chu, V., Cascalheira, A.C., Conde, J.P., Aires-Barros, M.R. *Simple sample preparation method coupled to microfluidic immunoassays for point-of-use screening of mycotoxins in foodstuffs* (Poster Presentation). **11th European Symposium on Biochemical Engineering Sciences**, Dublin, Ireland (September 2016).
- [6] Soares, R. R. G., Santos, D. R., Pinto, I. F., Azevedo, A. M., Chu, V., Aires-Barros, M. R., Conde, J. P. *Point-of-use ultrafast single-step detection of food contaminants: a novel microfluidic fluorescence-based immunoassay with integrated photodetection* (Oral Presentation). **Euroensors XXX**, Budapest, Hungary (September 2016).
- [7] Soares, R.R.G., Azevedo, A.M., Fernandes, P., Chu, V., Conde, J.P., Aires-Barros, M.R. *Exploring the versatility of aqueous two-phase systems: Toxin biosensing*

applications (Oral Presentation). **Congress of Microbiology and Biotechnology (MicroBiotec) 2015**, Évora, Portugal (December 2015).

[8] Soares, R.R.G., Azevedo, A.M., Fernandes, P., Chu, V., Conde, J.P., Aires-Barros, M.R. *Aqueous two-phase systems as a simple and effective means of sample processing: A novel approach for enhanced analyte quantification* (Poster Presentation). **Biopartitioning and Purification Conference (BPP) 2015**, Vienna, Austria (June 2015).

[9] Soares, R.R.G., Novo, P., Azevedo, A.M., Fernandes, P., Chu, V., Conde, J.P., Aires-Barros, M.R. *Integration and Simplification of Sample Preparation for Point-of-use Immunodetection of Mycotoxins in Foods and Feeds* (Poster Presentation). **4th Elsevier International Conference on Bio-Sensing Technology**, Lisbon, Portugal (May 2015).

[10] Soares, R.R.G., Novo, P., Azevedo, A.M., Fernandes, P., Chu, V., Conde, J.P., Aires-Barros, M.R. *Polymer-salt aqueous two phase systems for enhanced immunoassay sensitivity: Interference-free detection of mycotoxins in liquid food matrices* (Oral Presentation). **10th European Symposium on Biochemical Engineering Sciences**, Lille, France (September 2014).

[11] Soares, R.R.G., Novo, P., Azevedo, A.M., Fernandes, P., Chu, V., Conde, J.P., Aires-Barros, M.R. *Integrated extraction, concentration and quantification of ochratoxin a in wines using a microfluidic aqueous two phase extraction coupled to a fluorescence-linked immunosorbent assay* (Poster Presentation). **Congress of Microbiology and Biotechnology (MicroBiotec) 2013**, Aveiro, Portugal (December 2013).

5. Participation in other Scientific Activities

- **Co-Supervision Activities at INESC MN and Instituto Superior Técnico, Portugal: (November 2017 – February 2018)** Madeleine Born, BSc student in Applied Life Sciences at Hochschule Kaiserslautern University of Applied Sciences, Germany, with a project entitled "*Integration and characterization of an immunoassay for troponin I detection into a microfluidic lab-on-a-chip platform*";

(September 2017 – Currently) Mariana São Pedro, MSc student in Biotechnology at Instituto Superior Técnico, Lisbon, with a project entitled "*Development of novel monoclonal antibody purification strategies using microfluidic high-throughput screening tools*";

(August 2017 – September 2017) Susy Hammer, summer intern BSc student in Applied Life Sciences at Hochschule Kaiserslautern University of Applied Sciences, Germany, with a project entitled “*Selective capture and concentration of rolling circle amplification products in a microfluidic device*”;

(July 2017 – September 2017) Katarzyna Jaszczuk, summer intern MSc student in Applied Chemistry at Maria Curie Skłodowska University in Lublin, Poland, with a project entitled “*Microfluidic mycotoxin immunodetection: miniaturized solid phase extraction for red wine sample preparation*”.

(February 2017 – August 2017) Roberta Epifania, MSc student in Biomedical Engineering at University of Rome “La Sapienza” in Rome, Italy, with a project entitled “*Capillary-driven microfluidic device with integrated nanoporous microbeads for ultrarapid and single-step biosensing assays*”.

(September 2015 – November 2016) Jessica Machado, MSc student in Biotechnology at Instituto Superior Técnico, Lisbon, with a project entitled “*Autonomous Capillary Biochip to perform multiplexing immunoassays*”;

(February 2015 – November 2015) Catarina Caneira, MSc student in Biomedical Engineering at Instituto Superior Técnico, Lisbon, with a project entitled “*Anion exchange agarose beads enclosed within a microchannel towards pM detection of circulating micro-RNAs*”;

(February 2015 – October 2015) Joana Chim, MSc student in Biomedical Engineering at Instituto Superior Técnico, Lisbon, with a project entitled “*Capillary-driven PDMS biochips for Ochratoxin A detection using colorimetry*”.

(July 2014 – September 2014) Teresa Machado, summer intern MSc student in Biological Engineering at Instituto Superior Técnico, Lisbon, with a project entitled “*Optimization of a microfluidic immunoassay for the detection of ochratoxin A*”.

- Peer-review of more than 35 manuscripts submitted to the following journals: (1) Biotechnology and Bioengineering, Wiley Online Library; (2) Separation and Purification Technology, Elsevier; (3) Process Biochemistry, Elsevier; (4) Separation Science and Technology, Taylor & Francis Online; (5) Industrial Crops and Products, Elsevier; (6) Biochemistry and Biophysics Reports, Elsevier; (7) Biotechnology Journal, Wiley Online Library; (8) Journal of Chromatography A, Elsevier.

Publons profile URL: <https://publons.com/a/1230195/>

- **Responsible for routinely tutoring several undergraduate and MSc students in experimental activities** involving microfabrication of microfluidic structures including mask CAD design and fabrication via optical direct write lithography, SU-8 mold fabrication, polydimethylsiloxane (PDMS) soft-lithography, fluorescence microscopy and general microfluidic device operation.

- **Innovate, Connect, Transform (ICT) 2015 Lisbon, MAGNETRODES Exhibition Stand (October 2015)** - Active participation in organizing and engaging the public in an exhibition dedicated mainly at presenting the MAGNETRODES EU FP7 project and also the (1) provided services and (2) research developed at INESC Microsystems and Nanotechnologies, focusing particularly on microfluidics and biosensing. The presentation was directed at (1) general public, (2) potential clients and (3) potential collaborators.

- **NANODEM Workshop on fluorescence for biosensing (September 2015)** - Attendance of the NANODEM (NANOphotonic DEvice for Multiple therapeutic drug monitoring) EU FP7 project workshop on fluorescence for biosensing, held in the Complutense University of Madrid, Spain. The workshop was focused on the fundamentals of fluorescence and applications of fluorescence for advancing the field of biosensing.

- **Tech Days Aveiro (Portugal) INESC MN Exhibition (September 2015)** - Active participation in organizing and engaging the public at an exhibition dedicated at promoting the provided services and developed research at INESC Microsystems and Nanotechnologies, focusing mainly on microfluidics and biosensing. The stand was directed at high school students, the general public and potential clients/collaborators.

- **PROSENSE project (FP7-PEOPLE-2012-317420) microfabrication and biosensing workshop (July 2015)** - Active contribution for the organization and demonstrations performed for the Marie Skłodowska-Curie PROSENSE project fellows in INESC Microsystems and Nanotechnologies, Lisbon, including: (1) Planning of experiments and organization of demonstrations, (2) Introductory session on biosensing in microchannels, (3) Tutorial and demonstrations of PDMS soft lithography (SU-8 mold

and channel fabrication), (4) Tutorial and demonstrations of microfluidic immunoassays for free PSA detection.

- **DEMOTOX Project - (FP7-SME-2013-604752) (March 2014 to June 2015)** – Participated actively in the development, optimization and client demonstrations (wine producers in Minho, north of Portugal) of a prototype immunoassay-based sensing platform (Myconix Bio) for the point-of-need detection of ochratoxin A in beverages and solid foods and feeds. This was achieved in collaboration with the Portuguese SME Lumisense Lda. I participated also in the final project meeting, held at the Sapienza University in Rome, Italy, on June 23rd, 2015.

6. Honors and Awards

(January, 2018) Travel grant to deliver an oral presentation at the 31st IEEE International Conference on Micro Electro Mechanical Systems (MEMS 2018), held in Belfast, Northern Ireland, from the 21st to the 25th of January, 2018.

(October, 2017) Winner of the 2017 Life Science Award of Merck for Food and Beverage Safety awarded by Merck KGaA. International awards competition to recognize postgraduate students from universities in the U.S., Canada and Europe who demonstrate outstanding achievement, skill and commitment to excellence in the life science field through innovative, cutting-edge research. The winning project was chosen among 4 finalists after an oral presentation in Burlington, MA, USA, based on level of innovation, impact on the industry, scientific rigor and communication. Presentation title: “Single-step and sub-minute point-of-need device for the screening of mycotoxins in foods and feeds”.

(February 2015) Academic Merit Prize in 2011/2012 awarded by Instituto Superior Técnico, University of Lisbon. Prize awarded to the top-5 students of all MSc courses in 2011/2012.

(September, 2014) Individual PhD Student Fellowship Grant awarded by Fundação para a Ciência e Tecnologia (FCT) (September 2014). PhD Fellowship awarded to the top 14% (18/128) of candidates in the field of Biotechnology and Bioengineering. The evaluation

was based on (1) academic merit of the candidate; (2) impact, feasibility and novelty of the project and; (3) merit of the supervisors and institutions hosting the candidate.

(September, 2011) Academic Merit Scholarship in 2010/2011 awarded by the Faculty of Science of the University of Lisbon (September 2011). Prize awarded to all students with an average grade above 16 out of 20 in the respective academic year.

(September 2010) Academic Merit Scholarship in 2009/2010 awarded by the Faculty of Science of the University of Lisbon (September 2010). Prize awarded to all students with an average grade above 16 out of 20 in the respective academic year.

(September 2009) Prize for the Best 1st Year Students in 2008/2009 awarded by the Faculty of Science of the University of Lisbon (September 2009). Prize awarded to all first year undergraduate students with an average grade above 16 out of 20 in the respective academic year.
